Optical Remote Sensing of Water Quality in the Wadden Sea

Behnaz Arabi

OPTICAL REMOTE SENSING OF WATER QUALITY IN THE WADDEN SEA

DISSERTATION

to obtain
the degree of doctor at the University of Twente,
on the authority of the rector magnificus,
prof.dr. T.T.M. Palstra
on account of the decision of the Doctorate Board,
to be publicly defended
on Thursday, 23th of May 2019 at 14:45

by

Behnaz Arabi

Born on 15 February 1985
In Markazi Province, Iran

This thesis has been approved by
Prof.dr.ing. W. Verhoef (supervisor)
Dr.ir. S. Salama (co-supervisor)

ITC dissertation number 355
ITC, P.O. Box 217, 7500 AE Enschede, The Netherlands

ISBN: 978-90-365-4774-1
DOI: 10.3990/1.9789036547741
Printed by: ITC Printing Department

Cover designed by Behnaz Arabi and Benno Masselink
The used photo was taken from http://www.carringtonwest.com/uu-invests-40m-in-water-quality-improvement-scheme/

ITC
UNIVERSITY OF TWENTE.
FACULTY OF GEO-INFORMATION SCIENCE AND EARTH OBSERVATION

Graduation committee:

Chairman/Secretary

Prof.dr.ir. A. Veldkamp	University of Twente

Supervisor

Prof.dr.ing. W. Verhoef	University of Twente

Co-supervisor

Dr.ir. S. Salama	University of Twente

Members

Prof.dr. D. van der Wal	University of Twente,
Prof.dr.ir. K.M. Wijnberg	University of Twente
Prof.dr. O. Zielinski	University of Oldenburg, Germany
Prof.dr.ir. M. Chen	Free University Brussels, Belgium
Dr. M. Eleveld	Deltares
Dr.ir. C.M.M. Mannaerts	University of Twente

“With every drop of water you drink, every breath you take, you are connected to the sea.”

Sylvia Earle

To my parents

Acknowledgments

Writing this thesis was a challenging and fascinating journey for me. There have been many people who have walked alongside me during this journey. I would like to express my sincere appreciation to all these people:

First and foremost, I would like to express my special appreciation and thanks to my main supervisor (promotor) Prof.dr.ing Wouter Verhoef, who provided me with the opportunity to do my PhD in his research group at the Faculty of Geo-information Science and Earth Observations (ITC). I consider myself very fortunate to have had the chance to pursue my PhD with him. He has been truly a dedicated mentor and has always showed trust and confidence in me through my research. I could not have maintained interest in my work without his profoundly impressive elegant and clearness of his work, guidance, radiating enthusiasm, endless support, kindness, and unbelievable patience. His open office policy for my questions, being so quick response for my emails, generous in sharing his knowledge, work, and experience are all greatly appreciated.

My sincere thanks go to my co-supervisor, Dr.ir. Suhyb Salama, who always supported me during my PhD journey. His friendly advice, constructive comments, notes, and very smart suggestions were always a spark for considering the new ways to improve and rationalize the work. I deeply thank him for all his advice and guidance to help me to rise myself in both of my research and future career.

I thank Dr. Bayat who was all the time positive for sharing scientific ideas and having fruitful discussions during this work.

I thank Royal Netherlands Institute for Sea Research (NIOZ) for providing the additional in-situ measurements of my research. Special thanks go to Dr. Jaime Pitarch Portero from NIOZ who was always very quick response toward my questions and inquiries. Moreover, I would like to express my continuing respect and admiration to deceased Dr. Marcel Wernand from NIOZ for his quick responses, great assistance and helpful discussions in my research.

I would like to thank the European Space Agency (ESA) for providing the satellite dataset of my research.

I am thankful to ITC which provided me with a nice working environment and facilities. My big thanks also go to all the staff, colleagues, officemates and friends in ITC department for their support and company during these years, although it is hard to mention all of them. Most importantly, I would like to especially thank Prof.dr. Bob Su for his excellent management of the

Department of Water Resources (WRS) and providing a comfortable academic environment where I could focus only on my research.

I would like to thank the department secretaries, Anke, Tina, and Lindy, for being always so kind, supportive and helpful during my PhD and also Loes Colenbrander for the assistance of my PhD application and the support during my stay at ITC.

I am grateful that there was a lovely and supportive Iranian community in Enschede, where I could always found assistance when I needed that, and I thank all of my Iranian friends.

My deepest thanks go to my beloved family. Nothing more than their emotional and mental support, presence and sincere belief in my potential could give me the courage of doing what I like to do, and my love and respect for them are beyond the words. I owe all the achievements of my life to my wonderful parents, now and forever, and this thesis is dedicated to them.

Last but not least, I would like to especially thank all those people who made me here feel like home with their smiles, kindness, politeness, and understanding. They have given me a feeling of being so lucky to do my PhD in this beautiful country. Thank you, Nederland and Nederlanders!

Table of Contents

List of Figures

List of Tables

Abbreviations and Symbols

a	Total absorption
[a_{CDOM}(440)]	CDOM absorption at 440 nm
a_{Chla}	Chla absorption
a_{NAP}	NAP absorption
a^*_{NAP}	Specific absorption of non-algae particles
a_w	Absorption coefficients of water molecules
a_0 and a_1	Absorption and backscattering coefficients of water molecules taken from Lee
B	Total backscattering
b_b	Backscattering coefficient
b_{bw}	Backscattering coefficients of water molecules
b_{NAP}	NAP backscattering
b^*_{NAP}	Specific scattering coefficient of NAP
BEAM	A satellite data viewing and processing software, developed by Brockmann Consult
BEI	Bottom effect index
BIM	Bias In Mean values
CDOM	Coloured Dissolved Organic Matter
Chla	Chlorophyll-a
[Chla]	Concentrations corresponding to Chla
CZCS	Coastal Zone Color Scanner
C2R	Case-2 regional processor; a software tool for satellite data processing
DOY	Day Of Year
DHRF	Directional-Hemispherical Reflectance Factor
ESA	European Space Agency
E	Downward diffuse flux
E^+	Upward diffuse flux
E_d^- (0)	Diffuse downward irradiance incident
E_S	Direct solar flux/ Down-welling irradiances
E_S (0)	Direct solar irradiance
E_S - UV	Down-welling irradiances at ultraviolet
ENVI	A software application used to process and analyze geospatial imagery for remote sensing professionals and image analysts.
FAI	Floating Algae Index
FWHM	Full Width at Half Maximum
G	Overall gain factor
GOCI	Geostationary Ocean Color Imager
GSVs	Global Soil Vectors
H_2O	Water Vapor
Hydrolight	A radiative transfer model, developed by Dr. Mobley

IOPs	Inherent Optical Properties
IV	Inverse Visibility
K	The diffuse extinction coefficients for direct light
L_0	Total radiance for zero surface albedo
L_{sfc}(South-East)	Surface radiance sensor looking to South-East
L_{sfc}(South-West)	Surface radiance sensor looking to South-West
L_{sky}	Ramses-ARC sensors for measuring sky radiance values
L_{sky}(South-East)	Sky radiance sensor looking at the South-East
L_{sky}(South-West)	Sky radiance sensor looking at the South-West
L_{TOA}	Simulated TOA radiance using MODTRAN parameters
LOC	Lack Of Correlation
LUTs	Look Up Tables
m	Meter
MATLAB	A multi-paradigm numerical computing environment and proprietary programming language developed by MathWorks
MERIS	MEdium Resolution Imaging Spectrometer
MIT	MODTRAN Interrogation Technique
MODIS	Moderate Resolution Imaging Spectroradiometer
MODTRAN	MODerate resolution atmospheric TRANsmission
MSE	Mean Squared Error
MSI	Multispectral Instrument
NAP	Non-Algae Particles/ Normal Amsterdam Level
nm	Nanometer
NIBEI	The Near-Infrared Bottom Effect Index
NIOZ	Royal Netherlands Institute for Sea Research
NIR	Near-Infra-Red
NNs	The Neural Networks
NRMSE	Normalized Root Mean Square Error
OLCI	Ocean and Land Colour Instrument
O_3	Ozone
r	Hemispherical reflectance (= π R_{rs}) leaving the water surface
RAA	Relative Azimuth Angle
R_{rs}	Water-leaving remote sensing reflectance
$R(0)^+$	Irradiance reflectance above the water surface
$R(0)^-$	Irradiance reflectance beneath the water surface
R^2	Determination coefficient
RT	Radiative Transfer
RMSE	Root Mean Square Error
RRMSE	Relative Root Mean Square Error
S	Spherical albedo of the atmosphere
S_{CDOM}	Spectral slope of CDOM
SDGs	Sustainable Development Goals

SeaWiFS	Sea-Viewing Wide Field-of-View Sensor
SIOPs	Specific Inherent Optical Properties
SNAP	A common architecture for all Sentinel Toolboxes developed by Brockmann Consult, Array Systems Computing, and C-S
SPM	Suspended Particulate Matter
[SPM]	Concentrations corresponding to SPM
SZA	Solar Zenith Angles
TOA	Top Of Atmosphere
TRIOS	Name of a company producing sensors: commonly “TriOS” refers to their sensors
USD	Unequal Standard Deviations
UTC	Coordinated Universal Time
VZA	View Zenith Angle
ω	Transformed single scattering albedo
W	Water molecules
WCCs	Water Constituent Concentrations
wd	Water depth
WFD	Water Framework Directive
WSB	The Water - Sea Bottom model
λ	Wavelength
χ^2	Chi□square
x	Ratio of backscattering to absorption coefficients (x = bb/a)
μ_w	Cosine of the SZ A below the (flat) water surface.
z	Metrical depth

Summary

Deterioration of estuarine and coastal water quality has become a worldwide issue of substantial concern as anthropogenetic actions increase and climate change tends to cause main changes to the hydrological cycle. The acquisition of water quality information using radiometric measurements of the water's optical properties has developed quickly in recent years. Developments in algorithms and results improvement, sensor technology and reliability, and data availability have led to established practices in remotely-sensed observations with potential implications to water resources management. Using remotely sensed observations have played a significant role to develop satellite-derived products for providing vital information on most important water quality variables such as Chlorophyll-a (Chla), Suspended Particulate Matter (SPM), and Coloured Dissolved Organic Matter (CDOM) with the required accuracies for management organizations. This study investigates how these water quality variables can be estimated from remote sensing observations by means of a quantitative approach in complex coastal areas. This is important with respect to the Sustainable Development Goals (SDGs) to better understand the capability of the state of art of remote sensing technology to monitor long-term spatio-temporal variation of water quality in estuarine and coastal waters as a consequence of climate change, global warming, pollution and population increase, transportation changes and human activities.

The thesis presents how remote sensing techniques and observations can be employed to accurately retrieve water quality variables in complex coastal waters at both the water surface and Top Of Atmosphere (TOA) levels in the frame of proposing and evaluating the latest remote sensing methods and techniques established based on radiative transfer modeling, advanced retrieval methods, developed algorithms and optimal instruments and sensors. This dissertation is composed of six chapters: Chapter 1 is introductory and describes the optical remote sensing of water quality, the challenges and requirements to apply the remote sensing techniques in the coastal waters, the importance of the study area and the proposed methods and algorithms in this study. Chapter 2 deals with application and validation of a new and developed radiative transfer hydro-optical model (i.e., the 2SeaColor model) to accurately retrieving water quality variables at water surface level under various Solar Zenith Angles (SZAs) and water turbidity conditions by using in-situ hyperspectral measurements. Chapter 3 deals with application and validation of a proposed radiative transfer atmospheric-hydro-optical model (i.e., the coupled 2SeaColor- MODerate resolution atmospheric TRANsmission (MODTRAN) model) to simultaneously retrieve water quality variables and atmospheric properties (i.e., visibility and aerosol type) at TOA level by using MEdium Resolution Imaging Spectrometer (MERIS) images. Chapter 4 deals

with 15-years water quality monitoring in complex coastal waters of the Dutch Wadden Sea by using time series of diurnal in-situ hyperspectral measurements and multi-sensor satellite images of MERIS, Sentinel-2 Multispectral Instrument (MSI) and Sentinel-3 Ocean and Land Colour Instrument (OLCI) images. Chapter 5 deals with the problem of the sea-bottom effect in the shallow coastal waters and develops a refined hydro-optical model (i.e., the Water-Sea Bottom (WSB) model) to evaluate the sea-bottom effect on remote sensing observations in these areas. Further analysis and investigations in this chapter lead to proposing a new near-infrared bottom effect index (i.e., the NIBEI) to distinguish optically shallow waters from optically deep waters. Chapter 6 discusses the main objectives of this dissertation and explains how these objectives are achieved and provide research recommendations for future studies.

Samenvatting

De achteruitgang van de waterkwaliteit van rivierdelta's en kustgebieden heeft zich wereldwijd ontwikkeld tot een punt van aanzienlijke zorg, daar de antropogenetische activiteit toeneemt terwijl klimaatverandering grote veranderingen in de waterkringloop dreigt te veroorzaken. Het verzamelen van informatie over de waterkwaliteit via radiometrische metingen van de optische eigenschappen van water heeft zich snel ontwikkeld in de laatste jaren. Ontwikkelingen in algoritmen en verbeteringen in de resultaten, de sensortechnologie en de betrouwbaarheid, en de beschikbaarheid van gegevens hebben geleid tot een gevestigde praktijk in het verrichten van remote sensing waarnemingen, met mogelijke implicaties voor het waterbeheer. Het gebruik van remote sensing waarnemingen heeft een grote rol gespeeld bij het ontwikkelen van uit satellietdata afgeleide producten voor het verschaffen van vitale informatie over de belangrijkste waterkwaliteitsvariabelen zoals Chlorofyl-a (Chla), Zwevend stof (SPM), en Gekleurd opgeloste organische stoffen (CDOM), met een nauwkeurigheid zoals gewenst door bestuursorganisaties. In deze studie wordt onderzocht hoe men deze waterkwaliteitsvariabelen kan afleiden uit remote sensing waarnemingen door middel van een kwantitatieve benadering geschikt voor complexe kustgebieden. Dit is belangrijk in verband met de Water en Duurzame Ontwikkelingsdoelstellingen en voor het verkrijgen van een beter begrip over het vermogen van de huidige stand van de remote sensing technologie om lange-termijn ruimtelijke en temporele variaties in de waterkwaliteit van rivierdelta's en kustwateren te monitoren in relatie tot klimaatverandering, globale opwarming, de bevolkingsdichtheid en de toename ervan, veranderingen in de scheepsvaart en menselijke activiteit in het algemeen.

De dissertatie laat zien hoe remote sensing technieken en waarnemingen kunnen worden ingezet voor het nauwkeurig bepalen van waterkwaliteitsvariabelen in complexe kustwateren via metingen zowel op zeeniveau als met satellieten vanuit de ruimte. Dit vindt plaats vanuit het perspectief van het voorstellen en evalueren van de nieuwste remote sensing methoden en technieken gebaseerd op stralingstransportmodellen, geavanceerde bepalingsmethoden, ontwikkelde algoritmen en optische instrumenten en sensoren.

Dit proefschrift bestaat uit zes hoofdstukken. Hoofdstuk 1 is een inleiding en beschrijft de optische remote sensing van de waterkwaliteit, de uitdagingen en voorwaarden waaraan moet worden voldaan om de remote sensing technieken toe te kunnen passen in kustwateren, het belang van het gekozen studiegebied en de voorgestelde methoden en algoritmen in deze studie. Hoofdstuk 2 behandelt de toepassing en de validatie van een recent ontwikkeld hydro-optisch stralingstransportmodel (genaamd 2SeaColor) voor het nauwkeurig schatten van waterkwaliteitsvariabelen uit in-situ hyperspectrale metingen op

zeeniveau onder diverse zonnestanden en waterturbiditeitscondities. In Hoofdstuk 3 is dit model gekoppeld met het MODTRAN atmosfeermodel voor het simultaan afleiden van waterkwaliteitsvariabelen en atmosfeereigenschappen (horizontaal zicht en aerosoltype) uit MERIS satellietbeelden. Hoofdstuk 4 gaat over het monitoren van de waterkwaliteit in de complexe kustwateren van de Waddenzee door het gebruik van tijdreeksen van dagelijkse in-situ hyperspectrale metingen tezamen met diverse satellietbeelden afkomstig van MERIS, de Sentinel-2 MSI en de Sentinel-3 OLCI instrumenten. Hoofdstuk 5 behandelt het probleem van het zeebodemeffect in ondiepe kustwateren en de ontwikkeling van een verfijnd hydro-optisch model genaamd WSB waarin dit effect is opgenomen en waarmee men het effect van dit fenomeen op remote sensing waarnemingen in deze gebieden kan onderzoeken. Verdere analyses en onderzoeken in dit hoofdstuk leiden tot het voorstellen van een nieuwe nabij-infrarode bodemeffect index (NIBEI) om optisch ondiepe wateren te kunnen onderscheiden van optisch diep water. Hoofdstuk 6 bediscussieert de voornaamste doelstellingen van deze dissertatie en verklaart hoe deze doelstellingen zijn bereikt en geeft aanbevelingen voor toekomstige onderzoekstudies.

Chapter 1 **General Introduction**

The core idea of the dissertation is to exploit multiple observations including time-series of in-situ hyperspectral measurements and multi-sensor satellite images for optical remote sensing of water quality in complex shallow coastal areas. To understand the importance and scope of this subject, we have to return to the origin of ocean-colour remote sensing from space. The Coastal Zone Color Scanner (CZCS), the first satellite sensor to monitor ocean color, was launched by NASA in 1978. At that time, the main objectives of the mission were moderate: to record water-leaving radiance values at a limited number of bands in the visible region of the spectrum, and then retrieve the concentrations of phytoplankton pigments from the recorded signal at the water surface level. The regular water retrieval algorithms were established based on the assumption that the water components (*e.g.,* phytoplankton pigments) and the atmospheric effect on the received signal at TOA level could be separated by using radiative transfer models of the atmosphere. Then the atmospherically corrected signals were used in standard empirical algorithms to retrieve phytoplankton pigment concentrations. Aside from the sensor name as the Coastal Zone Color Scanner, it was soon recognized and acknowledged that these standard methods are not reliable enough in coastal, and other optically-complex areas, in which the presence of other water quality variables (*e.g.,* SPM and CDOM) plays a role in the amount of the received signal from water surface level to the TOA level. As a result, the reliability of retrieving phytoplankton pigment concentrations from remote sensing observations remained questionable in these complex waters.

With respect to the CZCS experience, and after learning from extensive theoretical studies and observations collected from in-situ platforms and aircraft, the requirements and scope of the remote sensing of coastal waters have been improved dramatically over the years. As more knowledge was obtained about the optical properties of aquatic constituents and their effect on the ocean color, it became more feasible to realize an accurate retrieval of water components other than phytoplankton from remote sensing observations.

Investigating these possibilities required sensors with the higher spectral resolution, higher signal-to-noise ratio and improved calibration than the CZCS sensor. Therefore, new ocean-color sensors have emerged with different types of instruments and capabilities. New algorithms were developed in parallel, to tackle these new challenges in remote sensing of coastal waters. For example, there has been a progress in treating the water-atmosphere interaction as a coupled system, and explaining the measured signal simultaneously in terms of atmospheric and water properties; using regular empirical algorithms for the retrieval of water quality variables has been replaced by algorithms that are established based on theoretical considerations and radiative transfer modeling; novel and influential statistical and mathematical methods capable of dealing with a nonlinear multi-variable system are now applied to tackle the problem. Most of these improvements are focused on developing remote sensing of water quality in coastal, turbid, shallow and other optically-complex water, and this dissertation has the same objective. This chapter gives a short general introduction and describes the importance of water quality in coastal areas, application of remote sensing techniques and observations, challenges and problems, available methods and techniques, proposed new solutions and the sub-objectives of this dissertation.

1.1. Why monitoring of water quality in coastal areas

In a world where coastal areas are home to approximately one-third of the world's population (UNEP, 2006), monitoring is essential to discover whether there are significant changes taking place in these natural environments (Burt et al., 2014; Zielinski et al., 2009). Coastal waters are the critical habitat for many marine species and are the basis for many economic concerns important to society and local economies, including fisheries, coastal recreation, and tourism activities (Halliday et al., 2014; Van der Wal and Pye, 2003; Zielinski et al., 2002). Monitoring water quality in coastal areas is crucial considering coastal resource consumption and aquatic resources management. Maintaining water quality in a decent condition is also vital for other sectors, including fisheries and the aquaculture industry.

Global urbanization of coastal regions, massive discharges of sewage, effluents, industrial and agricultural run-off have a significant influence on the quality of coastal waters by changing the nutrient components, triggering toxic algal blooms influencing biodiversity, recreation, tourism fisheries, and other activities (Mishra et al., 2015). Therefore water sector decision-makers and coastal planners must monitor the quality of water to protect these vital areas while having obligations to avoid deterioration under some of the European instruments. In December 2000, the European Parliament adopted the Water Framework Directive (WFD) (WFD, 2000). Based on the WFD regulations, all Member States are responsible for the safeguarding of good environmental quality by 2015 while a monitoring programme was established to observe the quality of the water in coastal and inland waters. Accordingly, the Marine Strategy Framework Directive followed the same objective in order to monitor and protect coastal waters aiming to maintain them in a suitable ecological status (Mélin et al., 2011).

1.1.1. Why the Wadden Sea?

One of the crucial European coastal ecosystems that has drawn great attention in Europe is the Wadden Sea. With an area of almost 8000 km^2 and a length of about 500 km, the Wadden Sea is considered as being the largest mudflat area in the world. Conservation of this tidal ecosystem as the largest unbroken system of intertidal mudflats in the world, and as one of the 193 natural World Heritage sites, has become compulsory since July 2009 (Sijtsma et al., 2015). Accordingly, particular attention has been paid by the Netherlands, Denmark, and Germany to protect this area (Bartholdy and Folving, 1986; Brockmann and Stelzer, 2008; Staneva et al., 2009). Therefore, following the WFD regulations and considering the importance of the Wadden Sea, home to more than 10 percent of 29 species and also a breeding and wintering area for up to 12 million birds per annum (Allan, 2008; CWSS, 2008), this research focused on monitoring of water quality in this unique coastal area.

1.2. Challenges and problems of remote sensing approaches

Maintaining coastal areas in a healthy state requires a continuous approach to capture information on dynamic events which might have a substantial impact on ecosystems such as unexceptional phytoplankton blooms or changes caused by storms and by tracking the spatio-temporal variations of water quality variables (Brando and Dekker, 2003; Bukata et al., 1995; Garaba and Zielinski, 2015). SPM, Chla, and CDOM concentrations (referred to as water constituent concentrations, WCCs) are amongst the most important water quality variables that need to be monitored to understand the process of such dynamic events and their impact on aquatic ecosystems. Reliable estimates of SPM are crucial for many water quality studies, as SPM is responsible for most of the scattering, which affects the water reflectance by modifying the light field (Kirk, 1994). Accurate estimation of SPM concentration and its variation is considered as a factor of great interest for sediment transport and may indicate the transport of organic toxins (e.g., Malmaeus and Håkanson, 2003; Ruddick et al., 2008). Hydro-chemical and ecological models need reliable SPM values to use as a proxy for terrestrial input, re-suspension or the sedimentation of particles (Blaas et al., 2007; Fettweis and Van Den Eynde, 2003; Lindstrom et al., 1999). SPM contains both inorganic and organic fractions. The inorganic fraction consists mostly of mineral particles originating from river discharge and erosion. The organic part of SPM consists of organic detritus, phytoplankton, and bacteria (Bowers and Binding, 2006; Bukata et al., 1995; Jerlov, 1976). Accurate estimation of Chla concentration, as the main proxy measure of phytoplankton abundance, is also a key factor to the understanding of the planetary carbon cycle as a crucial indicator of eutrophication in marine ecosystems (Murphy et al., 2001; Werdell et al., 2009). Chla amounts are influenced by anthropogenic nutrients of agricultural and industrial origin, whereby fisheries and aquaculture can be affected by Chla abundance (Peters et al., 2004). In addition to Chla and SPM, CDOM is another relevant component in water quality studies since it controls the functioning of ecological processes and biogeochemical cycles of marine ecosystems. CDOM is produced by phytoplankton degradation and bacterial decomposition while riverine discharge is another main source of CDOM in most coastal waters (Yu et al., 2016b; Zielinski and Brehm, 2007). Long-term tracking of variations in these WCCs reveals important patterns, which allow trends, cycles, and rare events to be identified (Burt et al., 2014).

Monitoring of WCCs using field measurements and laboratory analysis requires conventional cruise surveys with satisfactory temporal and spatial coverage. Unfortunately, this is often not feasible for most coastal regions due to lack of financial resources and technical equipment while it is impossible in practice to collect in-situ measurements for large regions using cruise measurements.

Remote sensing is an efficient technique that provides information on WCCs on high spatio-temporal scales and can considerably overcome some of these deficits in the current in-situ monitoring programs (Kirk, 1994; Philippart et al., 2013; Watson and Zielinski, 2013). Satellite remote sensing of coastal water quality is especially important since it is the only remotely sensed property that directly identifies a biological component of the ecosystem (Casal et al., 2015). Regarding the spatial and temporal sampling capabilities of satellite data, remote sensing of coastal waters is considered as the principal source of data for investigating spatio-tempral WCC variations and phytoplankton biomass in many coastal areas' estuaries (Le et al., 2013b). In many coastal waters, like the Wadden Sea, remote sensing has often been applied to produce tidal flat maps (*e.g.,* sediment type maps or finding locations with seagrass) (Niedermeier et al., 2005; Wang, 1997; Wimmer et al., 2000). However, there is still a pressing need on optical remote sensing for quantitative monitoring of WCCs in complex coastal waters (Hommersom, 2010). Recent studies show that remote sensing of the coastal area seems both possible and beneficial. Nevertheless, ocean color products in these areas may comprise errors of up to 50% due to the following major problems:

1.2.1. Atmospheric correction methods

Eliminating the effect of the atmosphere and performing a suitable atmospheric correction method is the most challenging task to translate remote sensing observations to reliable water quality products in remote sensing of ocean colours, especially in coastal waters (Salama et al., 2004; Wang, 2007; Wang et al., 2009, 2007; Wang and Gordon, 1994; Wang and Shi, 2007). Different atmosphere correction methods aim to exclude the effects of the atmosphere on the received TOA signal as the result of atmospheric scattering and absorption (Schroeder et al., 2007). Indeed, in many cases, less than 10% of the received TOA radiance at satellite images carries information on the optical properties of water components while 90% of the received signal is produced by the atmospheric scattering. Therefore, the accuracy of the atmospheric correction approach to remove the effect of the atmosphere is the most important and critical issue affecting the reliability of generated water products by using remote sensing techniques. Once an appropriate atmospheric correction has been applied, water-leaving reflectance can be linked to water optical properties and retrieved water quality variables. As a result, many different researches have been conducted to improve the accuracy of atmospheric correction methods in remote sensing of ocean color. For example, Gordon and Wang (1994) proposed the standard atmospheric correction of the black pixel approach by assuming zero water-leaving reflectance due to the high absorption by seawater in the Near-Infra-Red (NIR). This method can be performed by extrapolating the aerosol optical properties to the visible from the NIR spectral region of wavelength (Goyens et al., 2013). Although this method works well over open oceans, it does not necessarily lead to accurate results over turbid coastal waters (Jamet et al., 2011) where higher concentrations of Chla and SPM can cause a significant water-leaving reflectance in the NIR (Siegel et al., 2000). Consequently, the black pixel assumption tends to overestimate the aerosol scattered radiance and thus underestimates the water-leaving radiance in these areas (IOCCG, 2000). Indeed, most of the atmospheric correction methods fail in coastal waters due to the complexity of the recorded TOA radiance signals by satellite sensors (Carpintero et al., 2015) as these signals are associated with aerosols from continental sources (Mélin et al., 2007). Besides, in coastal waters, photons from nearby land areas can enter the field-of-view of the sensor (the adjacency effect) and contribute to total NIR backscatter (Santer and Schmechtig, 2000), whereas in shallow waters, TOA radiances can also be influenced by the bottom effect (Hommersom, 2010a). In recent years, some studies have been conducted to improve the atmospheric correction over turbid waters (Hu et al., 2000; Ruddick et al., 2006; Wang and Shi, 2007). For example, some efforts were made to improve the atmospheric correction method by assuming a zero water-leaving reflectance in the shortwave infrared, even in the case of highly turbid waters (Wang, 2007; Wang and Shi, 2005). However, in further studies, researchers found that for extremely high turbidities, even in the shortwave infrared region, the water-leaving reflectance was not negligible (Wang et al., 2011). In addition, other studies focused on the non-negligible water-leaving reflectance assumption in the NIR (Doxaran et al., 2014; Salama and Shen, 2010). For example, Carder et al. (2002) investigated the ratio of water-leaving reflectance at two NIR bands. This ratio was either assumed constant (Gould et al., 1999) or estimated from neighboring pixels of open oceans (Ruddick et al., 2000). Although the assumption of a known relationship between the values of water-leaving reflectance in two NIR bands is necessary, it is not sufficient. Indeed, accurate information about visibility and aerosol type is still needed (Salama and Shen, 2010). Shen et al. (2010) used the radiative transfer model MODTRAN to perform atmospheric correction for MERIS images over highly turbid waters. As shown by Verhoef and Bach (2007), for assumed visibility and aerosol type, MODTRAN can be used to extract the necessary atmospheric parameters to remove the scattering and absorption effects of the atmosphere and to obtain calibrated surface reflectance, as well as correcting the adjacency effects. However, this technique assumes a spatially homogeneous atmosphere (Shen and Verhoef, 2010), while in reality not only visibility but also the aerosol type may vary spatially within the extent of satellite images (in the presence of local haze variations). For example, in the case of coastal waters, some aerosol types (*e.g.,* urban or rural) might exist in the regions close to the land, and other pixels might have the maritime aerosol type. Consequently, the assumption of a homogeneous atmosphere may lead to the wrong establishment of visibility and aerosol model in different parts of the image and may result in overestimation or underestimation of WCCs from ocean-color observations. This case is even more complicated in the Wadden Sea. Therefore, regular atmospheric correction algorithms have a higher probability of failure in this complex turbid water, where not only substantial SPM concentrations can occur but also the atmosphere is mostly heterogeneous over the region due to local haze variations (Creutzberg, 1961; Arabi et al., 2016; Hu et al., 2000; Ruddick et al., 2000; Shen et al., 2010; Shen and Verhoef, 2010; Siegel et al., 2000; Wang et al., 2009; Wang and Shi, 2005; Pasterkamp et al., 2003; Peters et al., 2004; Salama et al., 2012; Van der Woerd et al., 2003). In this dissertation, we propose a coupled atmospheric-hydro-optical radiative transfer model (i.e.*,* the 2SeaColor-MODTRAN model) to treat the non-homogeneous atmosphere in highly turbid waters of coastal areas. This method is based on a TOA radiance approach, where atmospheric correction is not needed since the sensor radiances are simulated and compared to the measured TOA radiances in the spectral bands of the sensor to retrieve surface and atmospheric properties simultaneously. Chapters 3 and 4 are directed towards this issue, while the proposed method is also implemented in multi-sensor satellite images of MERIS, MSI and OLCI and its capabilities are validated against in-situ measurements, since water-leaving reflectance is obtained as a by-product in this approach.

1.2.2. Water quality retrieval algorithms

A suitable water quality retrieval algorithm is the key step to link the water leaving reflectance to the water quality variables in remote sensing of ocean color. Especially in coastal waters, where not only high concentrations of SPM can occur but also there may be a mixing of Chla, SPM, and CDOM (Hommersom, 2010; Pitarch et al., 2016), it is crucial to implement and validate a self-consistent, generic and operational hydro-optical model that can be applied to these complex water bodies. Although there are already many available empirical water retrieval algorithms for accurate retrieval of water quality variables (Matthews, 2011), these algorithms are not practical to be used for different coastal waters. Accordingly, many studies have focused on developing different hydro-optical models. For example, Gordon et al. (1988) developed a semi-analytical optical model which predicts the upwelling spectral radiance as a function of the phytoplankton pigment concentration at the sea surface level for open oceans. Based on Gordon's model, the variations in the phytoplankton backscattering and absorption, and the associated detrital material determine the radiance values variations. Lee et al. (2002) developed a multiband quasi-analytical algorithm based on Gordon's model to retrieve backscattering and absorption coefficients from remote sensing reflectance spectra for both open oceans and coastal waters. However, both the Gordon and Lee models suffer from early saturation at high turbidities (Salama and Shen, 2010). Fettweis et al. (2007) developed a semi-analytical algorithm to investigate the relationships between the backscattering coefficient, the absorption coefficient, water leaving reflectance and WCCs in the Belgian/Dutch coastal area. However, also their model was only appropriate for low turbidity waters. Indeed, most hydro-optical models are not capable enough to simulate water leaving reflectance values under the condition of high WCCs in turbid waters. Therefore, saturation occurs when modeling water turbidities at high turbidity, and consequently retrieving WCCs from remote sensing measurements over turbid waters will often fail.

In this dissertation, in Chapter 2, we introduce a new hydro-optical model (i.e., 2SeaColor model) which comprises an analytical forward model including an inversion scheme for the simultaneous retrieval of WCCs from in-situ hyperspectral measurements of remote sensing reflectance. This model has been developed while maintaining a relative simplicity by applying the two-stream approach including direct sunlight, based on Duntley (1942). The model considers multiple scattering, which delays the saturation of water reflectance under high turbidity conditions. Most hydro-optical models consider only single scattering (Salama and Verhoef, 2015), and therefore saturate in producing water leaving reflectance (R_{rs}) values already at moderate turbidity conditions. Moreover, the 2SeaColor model includes incident direct sunlight while it computes the Directional-Hemispherical Reflectance Factor (DHRF) as a function of the SZA. Consequently, by analyzing a time series of nearly continuous high quality in-situ hyperspectral measurements recorded over multiple years at the Dutch Wadden Sea, we explore and test the model-based retrievals under various SZAs using the 2SeaColor model.

1.2.3. Bottom effect

In many coastal areas, in addition to the concentration of water constituents present in the water column, the sea-bottom effect can contribute to the observed water leaving reflectances at the water surface level and accordingly to the TOA radiances at satellite level when the water is sufficiently shallow and is sufficiently clear (i.e., optically shallow waters) (Lee and Carder, 2002;

IOCCG, 2000). The effect of the sea bottom on water color differs with respect to the water depth, water clarity, the type of water constituents, and the type of sea-bottom. The sea-bottom can be sandy or rocky and can be covered by a combination of benthic organisms (*e.g.,* molluscs, algae). The occurrence of these factors can interfere with the correct retrieval of WCCs from hyperspectral measurements or satellite images depending on local water depth and transparency of the water (Lee et al., 1999; Martinez and Calway, 2012). Accordingly, water retrieval algorithms have a higher probability of failure in shallow coastal waters in which not only a mixture of WCCs may occur, but also the sea-bottom affects the watercolor. Therefore, it is important to identify optically shallow areas in coastal areas to establish where water retrieval algorithms may fail, and how we can improve the reliability of ocean-colour products, and extend their domain of applicability (Sathyendranath and others, 2000). Although bathymetry maps can be used to determine the shallowness of water in remote sensing studies of coastal areas (Pattanaik et al., 2015), these maps are not always available for all regions (Giardino et al., 2012).

On the other hand, the effect of the sea-bottom varies depending on water turbidity and/or on water depth variation in tidal areas (Giardino et al., 2014; Maritorena et al., 1994; Mgengel, 1991). Therefore, using bathymetry maps cannot always help to improve the accuracy of WCC products over turbid tidal areas. As a result, hydro-optical models should include the sea-bottom effect in order to accurately retrieve WCCs from atmospherically corrected water-leaving reflectance (Gitelson et al., 2008; Lee et al., 2002a). In this dissertation, in Chapter 5, we develop a new hydro-optical model termed Water - Sea Bottom (WSB), by incorporating the sea-bottom effect for modeling of the above water reflectance to better understand the effect of bottom albedo on field and satellite observations of ocean color. Using the developed WSB model, we define a novel near-infrared bottom effect index (i.e.*,* NIBEI) to distinguish optically shallow waters (contaminated by sea-bottom effects) from optically deep waters. We use the NIBEI to improve the reliability of generated WCC maps from MERIS and OLCI.

1.2.4. Availability of remote sensing observations

Using remote sensing techniques for monitoring of water quality in complex coastal waters requires the availability of high-quality remote sensing observations in water surface and/or satellite levels which might not be readily available in many cases. At the water surface level, availability of proximal sensing observations is dependent on many factors such as having access to advanced instruments/sensors, doing a consistent survey on the automatic sensors, performing regular calibration/validation on instruments and having a suitable meteorological condition (Wernand et al., 2006). Moreover, it is vital to apply suitable data quality control and to flag the recorded dataset to extract high-quality observations (Arabi et al., 2016; Cadee and Hegeman, 2002; Hommersom et al., 2010; Philippart et al., 2013, 2010; Van der Woerd and Pasterkamp, 2008). At TOA level, availability of observations is even more difficult. Only a limited number of satellites are practical to be used for water quality monitoring (Niedermeier et al., 2005; Wang, 1997; Wimmer et al., 2000). Moreover, not only all satellites images are not free, but also many satellite images are not usable due to the occurrence of series cloud/rain or local haze at the time of satellite overpass (Arnone et al., 2006). With the unique opportunity of having access to the full archive of 15 years of daily in-situ hyperspectral measurements and multi-sensor satellite images of MERIS, MSI, OLCI between 2003 and 2018 over the Dutch Wadden Sea, Chapter 4 aims to apply quantitative remote sensing techniques for long-term monitoring of WCC variations at both water surface and TOA levels for the Dutch Wadden Sea.

1.3. Objectives

The main objective of this dissertation is remote sensing monitoring of water quality in the complex shallow tidal waters of the Dutch Wadden Sea. To achieve this main objective, four sub-objectives have been defined, as listed below. Further, each of these sub-objectives is addressed in various chapters of this dissertation.

1. Evaluation and validation of the 2SeaColor model's performance to retrieve WCC retrievals from in-situ hyperspectral measurements under various SZAs and water turbidity conditions. (This topic is published in the journal Remote Sensing of Environment (RSE) in 2018).
2. Evaluation and validation of the proposed coupled 2SeaColor-MODTRAN model's performance to retrieve WCCs from MERIS images (This topic is published in the journal Remote Sensing in 2016).
3. Implications of the 2SeaColor and coupled 2SeaColor-MODTRAN models for 15-years of monitoring of WCC variations in the Wadden Sea using time series of in-situ hyperspectral measurements and multi-sensor satellite images (MERIS, MSI, and OLCI), respectively (This topic is under review in the journal of Remote Sensing of Environment).
4. Improving the reliability of generated WCC maps using the coupled 2SeaColor-MODTRAN model over the Wadden Sea from MERIS and OLCI images by applying the proposed NIBEI (This topic is under review in the journal of Remote Sensing of Environment).

1.4. Dissertation outline

This dissertation consists of six chapters following the objectives. Besides the "general introduction (**Chapter 1**)" and "concluding remarks and prospects (**Chapter 6**)", four chapters are published in, or under review, to peerreviewed ISI journals. Each of the published (submitted) chapters addresses one of the research sub-objectives described above.

In **Chapter 2**, the radiative transfer model 2SeaColor is inverted against time series of in-situ hyperspectral measurements. The 2SeaColor-retrievals of Chla, SPM are validated against time series of in-situ Chla and SPM concentrations collected in the NIOZ Jetty Station (the NJS), Texel, at the inlet to the Dutch Wadden Sea. Moreover, the performance of this model is evaluated under conditions of various SZAs and water turbidity while the effect of the tide on the variation of WCC retrievals is also evaluated.

In **Chapter 3**, the validated 2SeaColor model's simulations are coupled with the atmospheric radiative transfer model MODTRAN and the coupled hydro-optical-atmospheric model named 2SeaColor-MODTRAN is proposed to retrieve Chla from time series of MERIS images under local haze variations and high turbidity. The capabilities of the 2SeaColor-MODTRAN model in doing the atmospheric correction and WCC retrievals are then validated against in-situ measurements and are compared with retrievals of the standard MERIS Case 2 regional (C2R) model at the location of the NJS, Dutch Wadden Sea.

In **Chapter 4**, The 2SeaColor and coupled 2SeaColor-MODTRAN model are applied to 15 years of time series of in-situ hyperspectral measurements and multi-sensor satellite images of MERIS, MSI, and OLCI, respectively. The long-term variations of WCC retrievals at the water surface and TOA level are compared, and simultaneous maps of WCCs over the Dutch Wadden Sea using MERIS and OLCI images are generated.

In **Chapter 5**, a new hydro-optical model called WSB is developed to deal with the sea-bottom effect in the shallow waters of the Dutch Wadden Sea. As the results of WSB simulations, the new bottom-effect index NIBEI is defined to distinguish optically shallow waters from deep ones for the shallow waters of the study area. The proposed NIBEI is applied to the generated WCC maps using the 2SeaColor-MODTRAN model to exclude the optically shallow waters from consideration and to improve the reliability of these maps.

In **Chapter 6**, concluding remarks and prospects related to this dissertation are described. It provides the main conclusions, implications, and recommendations for further research.

Chapter 2 Remote sensing of water quality at water surface level using in-situ hyperspectral measurements*

* This chapter is based on:
Arabi, B., Salama, M.S., Wernand, M.R., Verhoef, W., 2016. Remote Sensing of Water Constituent Concentrations Using Time Series of In-situ Hyperspectral Measurements in the Wadden Sea. Remote Sensing of Environment Journal, 216 (2018) 154–170, https://doi.org/10.1016/j.rse.2018.06.040.

Arabi, B., Salama, M.S., Verhoef, W., 2018. Evaluation of Tidal Effect on Water Constituent Variations Using Optical Observations and Tide Gauge Recordings in the Dutch Wadden Sea. The 2018 IEEE International Geoscience and Remote Sensing Symposium (IGARSS 2018), Valencia, Spain, 22-27 July 2018.

ABSTRACT

This study aimed to investigate the capability of the two-stream radiative transfer model 2SeaColor for the simultaneous retrieval of Chla, SPM and CDOM concentrations from remote sensing measurements under various conditions (i.e., SZAs and water turbidity levels). For this evaluation, a time series of diurnal in-situ hyperspectral measurements of remote sensing reflectance (R_{rs}) concurrent with in-situ measured Chla and SPM concentrations between 2008 and 2010 by the NJS, located in the Dutch part of the Wadden Sea, was used. Validation of the model retrievals against in-situ measurements showed an acceptable accuracy (Chla: R^2 = 0.80 and RMSE = 2.98 (mg m^{-3}); SPM: R^2 = 0.89 and RMSE = 2.53 (g m^{-3})) with good agreement between the temporal trends of measured and retrieved concentration values over multiple years. However, the model inversion results yielded less good estimates at SZAs > 60° during winter.

Furthermore, the effect of the tide on the variation of daily time series of Chla and SPM concentrations was analyzed. At the particular NJS location, the tidal effects on the concentrations of SPM and Chla were found to be small. The capability of the 2SeaColor model to retrieve reliable estimates, and the favorable location of the NJS, which is little influenced by tidal phase variations, contribute to a better understanding of the long-term variability of Chla and SPM concentrations.

2.1. Introduction

Conservation of European coastal waters in a healthy environmental state has become a high priority as regulated in the "Marine Strategy Framework Directive, 2008/56/EC" (Mélin et al., 2011). One of the most important coastal ecosystems, which has drawn great attention in Europe, is the Wadden Sea. Conservation of this tidal ecosystem as the largest unbroken system of intertidal mudflats in the world, and as one of the 193 natural World Heritage properties, has become compulsory since July 2009 (Sijtsma et al., 2015). Accordingly, particular attention has been paid by the Netherlands, Denmark, and Germany to protect this area since the early years of the last century (Bashir, 2016). Maintaining this coastal area in a healthy state requires a continuous monitoring approach that can capture the dynamics of WCCs. Remote sensing is an efficient technique that provides information on these constituents on high spatio-temporal scales (Kirk, 1994; Philippart et al., 2013). In the Wadden Sea, remote sensing has often been applied to produce tidal flat maps (*e.g.,* sediment type maps or finding locations with seagrass). For example, radar and laser data have been used to detect the land-water boundaries (Niedermeier et al., 2005; Wang, 1997; Wimmer et al., 2000). However, there are only a few studies available on remote sensing algorithms of optical properties that can be applied for continuous monitoring of WCCs in this area (Hommersom, 2010). Recent studies show that remote sensing of this complex coastal area seems both possible and beneficial. Nevertheless, ocean color products may comprise errors of up to 50% due to the following major problems (Arabi et al., 2016; Cadee and Hegeman, 2002; Hommersom et al., 2010; Philippart et al., 2013, 2010; Van der Woerd and Pasterkamp, 2008) :

2.1.1. Atmospheric correction methods

Satellite images are widely used for remote sensing of WCCs in coastal areas. However, performing an accurate atmospheric correction is a most challenging task which may cause significant errors especially in coastal waters studies (Salama et al., 2004; Wang, 2007; Wang et al., 2009, 2007; Wang and Gordon, 1994; Wang and Shi, 2007). One possible approach to minimize the problem of atmospheric effects on remote sensing of coastal waters is using ground-based water leaving reflectance measurements which are collected at the study site (Loisel et al., 2013; Salama et al., 2012; Wernand and Woerd, 2010). In the present study, we had the opportunity to work with a unique dataset of time series of diurnal in-situ hyperspectral water leaving reflectance concurrently with in-situ measured Chla and SPM concentrations collected on a regular basis (noon time) throughout multiple years at the NJS. By using this continuous in-situ dataset, the effect of the atmosphere on the remote sensing dataset could be minimized. Accordingly, it was feasible to have the best validation of the hydro-optical model using this dataset, which was collected over different seasons and conditions. On the other hand, eliminating the effect of the atmosphere as the most important source of models' retrieval errors makes it better possible to evaluate the contribution of other factors (*e.g.,* water turbidity and SZAs) to the model's retrieval accuracy.

2.1.2. Hydro-optical models

Most hydro-optical models are not capable enough to simulate water leaving reflectance values under the condition of high WCCs in turbid waters. Therefore, saturation occurs when modeling R_{rs} at high turbidity, and consequently retrieving WCCs from remote sensing measurements over turbid waters will often fail. For example, Gordon et al. (1988) developed a semi-analytical optical model which predicts the upwelling spectral radiance as a function of the phytoplankton pigment concentration at the sea-surface level for open oceans. Based on Gordon's model, the variations in the phytoplankton backscattering and absorption, and the associated detrital material determine the radiance values variations. Lee et al. (2002) developed a multiband quasi-analytical algorithm based on Gordon's model to retrieve backscattering and absorption coefficients from remote sensing reflectance spectra for both open oceans and coastal waters. However, both the Gordon and Lee models suffer from early saturation at high turbidities (Salama and Shen, 2010). Fettweis et al. (2007) developed a semi-analytical algorithm to investigate the relationships between the backscattering coefficient, the absorption coefficient, water leaving reflectance and WCCs in the Belgian/Dutch coastal area. However, also their model was only appropriate for low turbidity waters. Since the Wadden Sea is considered a high turbidity coastal area (Hommersom, 2010), it is crucial to select a reliable hydro-optical model that does not saturate too soon for modeling of water leaving reflectance values under high water turbidity conditions.

In this study, we implemented a new hydro-optical model which comprises an analytical forward model including an inversion scheme known as the 2SeaColor model (Salama and Verhoef, 2015) for the simultaneous retrieval of WCCs from in-situ hyperspectral measurements of remote sensing reflectance, R_{rs}. The 2SeaColor model was developed while maintaining a relative simplicity by applying the two-stream approach including direct sunlight, based on Duntley (1942). The model considers multiple scattering, which delays the saturation of water reflectance under high turbidity conditions. Most hydro-optical models consider only single scattering (Salama and Verhoef, 2015), and therefore saturate in producing R_{rs} values already at moderate turbidity conditions.

2.1.3. SZA effect

High SZA values can affect the quality of remote sensing data and accordingly the accuracy of WCC retrievals using different hydro-optical models. Geostationary satellites (*e.g.,* GOICI which observes a region eight or more times a day) provide observations from the early morning to the late afternoon, and many data can be obtained under large SZA conditions (Chen, 2017). In addition, at the location of the Wadden Sea, high SZA variations can be found in winter around noon and in summer early in the morning or evening. Therefore, it is essential to use a hydro-optical model that includes the SZA effect when working with time series of optical measurements covering the whole year in this area. So far, a few studies have evaluated the effect of SZA on the accuracy of WCC retrievals using remote sensing measurements. For example, Volpe et al. (2007) assessed the uncertainties of Chla retrievals in the Mediterranean Sea using the OC4V4 algorithm and concluded that this algorithm was not capable enough to retrieve Chla concentration values at this region due to the weak light intensity. Chaves et al. (2015) assessed the ocean color products (*e.g.,* Chla and spectral marine IOPs) from the Moderate Resolution Imaging Spectroradiometer (MODIS) AQUA data in the Western Arctic Ocean. They found that the empirical algorithms were positively biased in comparison with in-situ measurements due to weak light and high latitudes. Li et al. (2017) investigated the performances of seven widely used Chla retrieval algorithms (i.e., OC2, OC3M, OC3V, OC4V4, Clark, ocean-color index, and Yellow Sea Large Marine Ecosystem Ocean Color Work Group) under high SZA conditions using the global in-situ ocean color dataset (NASA bio-optical marine algorithm dataset). The results showed that the performances of all seven algorithms decreased significantly under high SZA values compared with those under low to moderate SZA values. They later investigated the possibility of improving these models by adjusting the coefficients of the algorithms using the in-situ dataset under the condition of high SZA values. They showed that the results could not be significantly improved by adjusting the models for high SZA conditions. In this study, for the first time, we evaluated the effect of SZA on WCC retrievals using remote sensing measurements in the Wadden Sea. The 2SeaColor model includes incident direct sunlight while it computes the directional-hemispherical reflectance factor (DHRF) as a function of the SZA. Therefore the SZA effect on R_{rs} measurements is considered into this hydro-optical model while doing WCC retrievals (Salama and Verhoef, 2015), although no effects of VZA are considered in this model. Consequently, by analyzing a time series of nearly continuous high-quality in-situ hyperspectral measurements recorded over multiple years at the NJS, it was feasible to explore and test the model-based retrievals under various SZAs using the 2SeaColor model.

2.1.4. Reliability of local Specific Inherent Optical Properties

One of the challenges associated with applying remote sensing techniques in coastal waters is that the SIOPs show high spatial and temporal variability in different coastal areas (Babin, 2003; Babin et al., 2003). These variations are due to numerous factors, including changes in the water source, sediment type, phytoplankton species composition, and CDOM sources. Since the Wadden Sea is a vast coastal area with numerous sources of water inputs, it is crucial to evaluate the reliability of local SIOPs over the location and time in this region. (Salama and Su, 2010). However, for this area, detailed information about seasonal SIOPs is still lacking. For example, Peters (2001) documented SIOPs estimates for Chla, SPM and CDOM measurements for this region. However, these SIOPs were measured only at the Marsdiep inlet and only on two days in May 2000. Later, Babin et al. (2003) added SIOPs estimated in the Wadden Sea, but they merged them with the North Sea SIOPs. However, the Wadden Sea SIOPs are different from those of the North Sea (Hommersom, 2010). In this study, we used a set of measured SIOPs, which have been collected by Hommersom et al. (2009) at 37 locations between 2006 and 2007 at the Wadden Sea. At the time when this study was conducted, these measured SIOPs were the only available ones as representative of WCCs in the Wadden Sea. However, some analysis was performed to ensure the reliability of these measured SIOPs to be implemented for the 2SeaColor parametrization during different seasons at the NJS.

2.1.5. Tidal variation

In remote sensing studies in coastal regions, tidal phase variations might interfere with time series of optical measurements and consequently with retrieved WCCs using hydro-optical models (Hu et al., 2016; Wal et al., 2017). Many studies have been conducted to evaluate the effect of tide on retrieved WCCs from remote sensing observations in different coastal areas. For example, Eleveld et al. (2014) investigated the relationship between the tidal phase and retrieved SPM concentration values using MERIS images in the Western Scheldt located in the southwest of the Netherlands. They concluded that tide is one of the leading factors, affecting the variations in estimated surface SPM concentrations for this tidal area. He et al. (2013) generated hourly SPM concentration maps from the Geostationary Ocean Color Imager (GOCI) observations. They showed that various regions had different diurnal variations concerning tidal phases in Hangzhou Bay. Wang et al. (2013) investigated the effect of the tide on the diurnal variation of ocean optical properties using GOCI images in the western Pacific region. Doxaran et al. (2009) used a one-year time series of in-situ measurements to show the tidal phase effect on turbidity variations in the upper part of a micro-tidal estuary using MODIS images. Valente and da Silva (2009) investigated the effect of tide on water turbidity and circulation in the Tagus estuary using multi-sensor satellite observations.

The Wadden Sea is also a tidal area, which is connected to the North Sea by a series of tidal inlets (Ridderinkhof et al., 1990). Like anywhere else, at the NJS location there is a daily shift of about one hour in the tidal phase so that all phases pass by in about one month. Thus, the tidal phase variation might interfere with the time series of measurements since the in-situ R_{rs} measurements concurrent with WCCs are taken around noon local time on all days. Therefore, the effect of tide needs to be considered carefully when interpreting time series of water quality products in this region. In this study, for the first time, we did a brief analysis to verify whether the time series analysis of WCCs at the NJS is affected by tidal phase variations. Although this assessment is not intended as an in-depth study of tidal effects, its conclusion plays a vital role in following the long-term temporal courses of WCCs at the NJS.

After mentioning the main problems of remote sensing of water quality at the Wadden Sea, we defined the main objectives of this study as evaluation and validation of the 2SeaColor model performance for WCC retrievals under different SZAs and water turbidity conditions at the NJS. Finally, we will discuss the application of this validated hydro-optical model to be implemented on the ground-based remote sensing measurements and satellite images.

2.2. Study area

The study area of this work is the Dutch Wadden Sea. This is the area located between the North Sea in the northwest and the mainland of the Netherlands in the southeast, and between the Eems-Dollard estuary in the northeast and the Marsdiep in the southwest (Ridderinkhof et al., 1990). This area is considered as a shallow, well-mixed tidal region with a surface area of 2500 km^2 and consists of several tidal basins (Ridderinkhof et al., 1990). The satellite image in Figure 2.1 shows the south-western part of the Wadden Sea, with parts of the Dutch mainland on the right and the island of Texel at the bottom left, and Vlieland and Terschelling to the north. As this SPOT satellite image (spatial resolution 20 m) shows, the bottom can be seen in large parts of the Dutch Wadden Sea, illustrating clearly that the sea bottom effect can influence remote sensing of optical measurements in this shallow coastal area (Lee et al., 1999). However, this was not the case for the NJS data due to the moderate turbidity and the depth of the water (> 5 m) at that location, so that the bottom effect on measured reflectance values is negligible.

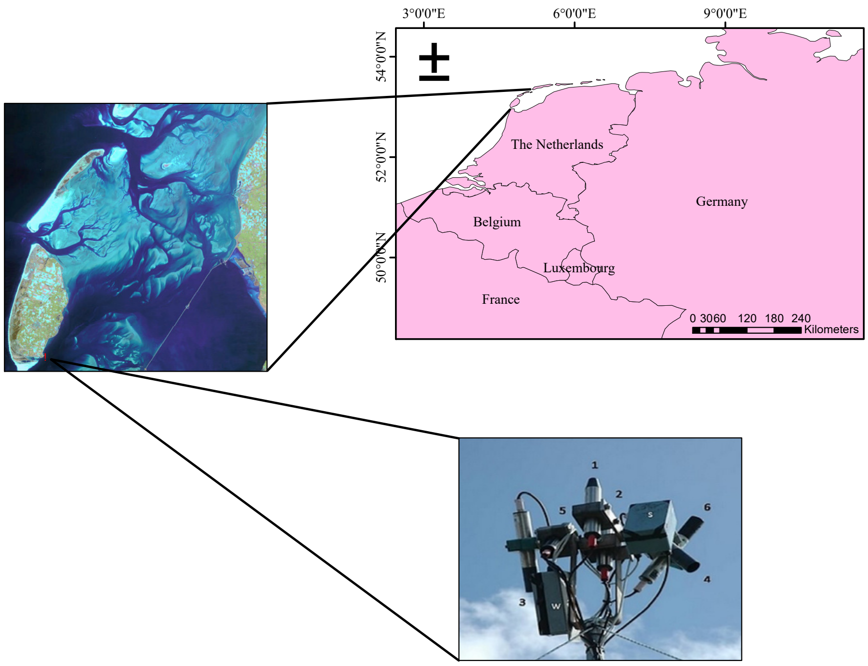

Figure 2.1 Upper-right: the Southwestern part of the Dutch Wadden Sea in Europe; Upper-left: one SPOT satellite image covering the Dutch Wadden Sea and parts of IJsselmeer lake (8th of May 2006); bottom: the optical sensors installed on the NJS with the VZA of 35° (w: looking at water, s: looking at sky, 1: down-welling irradiance sensor at ultraviolet (E_S - UV), 2: down-welling irradiance sensor (E_S), 3: the surface radiance sensor looking to South East (L_{sfc} (South East)), 4: the surface radiance sensor looking to South West (L_{sfc} - South West), 5: the sky radiance sensor looking at the South East (L_{sky} - South East), 6: the sky radiance sensor looking at the South West (L_{sky} - South West)).

This study focused on measurements taken at the NJS located nearby the Marsdiep inlet (53°00′06″N; 4°47′21″E) to the Dutch part of the Wadden Sea (Fig. 1). The Marsdiep inlet is located at the western border and consists of a deep tidal channel flanked by shallow sand and mud flats. The inlet is bordered by the island Texel to the north and by the town of Den Helder to the south on the mainland.

2.3. Dataset

2.3.1. Time series of in-situ measurements at the NJS

The NJS provided the dataset of the present study. This dataset contained the time series of in-situ hyperspectral measurements of R_{rs} concurrent with Chla and SPM concentrations (collected at noon time almost every day) from 2008 to 2010. Fig 2.2 presents the spectral variations of the in-situ R_{rs} measurements at the NJS for this study.

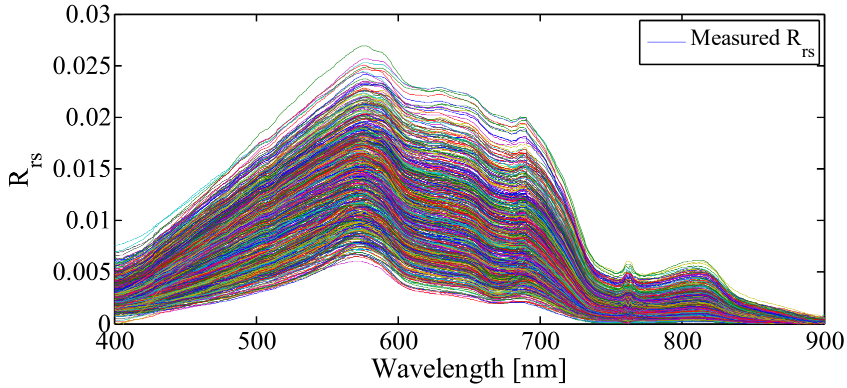

Figure 2.2. The in-situ spectral measurements of R_{rs} between 2008 -2010 at the NJS.

The NJS has been in operation since 2001 by the Royal Netherlands Institute for Sea Research (NIOZ) on the Texel Island. Every fifteen minutes in-situ hyperspectral measurements (surface, sky, and sun) including meteorological data are being collected using the newest generation of TRIOS Ramses hyperspectral radiometers (Fig 2.1 bottom) for "autonomous" monitoring of seawater since August 2001 until present (Wernand, 2011). For more detailed information on the measurement setup of the NJS, the readers are referred to Wernand (2002).

2.3.2. Time series of tidal information at the Den Helder station

Simultaneously with recording R_{rs} measurements at the NJS, tidal measurements (water depth values, ebb and flood measurements) are recorded at Den Helder (52.9667° N, 4.7500° E) located only 3.7 km away from the NJS. Therefore, we had the opportunity to investigate the possible correlation between the tidal phase and the variation of WCCs at the NJS. In this study, three-years (2008 - 2010) of diurnal tidal measurements containing the water depth values in Normal Amsterdam Level (NAP) (cm) units, ebb, and flood tidal phase information, besides sunrise and sunset time were extracted from the Den Helder station to make this evaluation.

2.4. Method

This study followed the below steps to meet the main objectives of this research:

(a) Perform data quality control of the NJS dataset.
(b) Evaluate the 2SeaColor model accuracy under different SZA conditions.
(c) Evaluate the 2SeaColor model accuracy under different water turbidity conditions.
(d) Evaluate the reliability of SIOPs measured by Hommersom et al. (2009).
(e) Analyze the effect of tide on WCC variations at the NJS.

2.4.1. Data quality control and R_{rs} calculations at the NJS

Ship-borne and unsupervised optical measurements collected by sensors installed on jetties, freighters or ferries can be hampered by factors like meteorological conditions, precipitation or the sun-glint effect. These factors can significantly influence the radiance and irradiance measurements and consequently the accuracy of the retrieved WCCs from calculated water leaving reflectance values. Performing data quality control by data flagging (based on the knowledge under which meteorological conditions the optical measurements were collected) is crucial in water quality studies using remote sensing measurements. In this study, three different kinds of data flagging, i.e., related to "weather conditions (*e.g.,* precipitation, wind speed)", "spectral shape" and "sun-glint contamination" were implemented to select the high-quality measurements automatically. This implemented data flagging approach was proposed by Wernand (2002), based on thousands of measurements of incident solar irradiance as well as coastal watercolor, and the meteorological dataset collected at the NJS. By implementing the precipitation flag, we indicated whether any precipitation occurred during the time of the measurements. Next, the spectral shape flag detected those spectra, which were possibly influenced by specific dusk or dawn radiation (red coloring of the sky) using the band ratio of down-welling solar irradiance (E_S) values. By implementing these two data flaggings, all unacceptable spectra were removed from the dataset. However, sun-glint contamination might still influence the quality of measured R_{rs} data (Wang and Bailey, 2001). To minimize the sun-glint effect, the NJS was equipped with three optical hyperspectral sensors consisting of two down-looking water leaving radiance sensors (L_{sfc}), 90 degrees apart in the horizontal plane (under azimuth angles of 135° and 225° from north), instead of the conventional single sensor measurement, as well as one down-welling irradiance (E_S) sensor (Fig. 2.1 bottom). In this way, one of the two water-leaving radiance signals was always available with a minimum of sun-glint (Table 2.1), and the effect of sun-glint contamination was removed from the dataset (Wernand, 2002). After performing the mentioned data quality control process and extracting the high-quality spectra from all three sensors, the water leaving reflectance values were calculated following Wernand (2002), as explained in Table 2.1:

Table 2.1. Water-leaving reflectance calculations at the NJS (Wernand, 2002).

Variable	Formula	Eq.
Select East/West L_{sfc} sensors	L_{sfc} *(min) = minimum of* L_{sfc} *sensors*	(2.1)
Calculate L_w	$L_w = L_{sfc}\,(\mathrm{min}) - (f_{sky} \times L_{sky})$	(2.2)
Calculate R_{rs}	$R_{rs} = L_w \,/\, E_s$	(2.3)

[1] When L_{sfc} West was minimum, L_{sky} west was used to do sun-glint contamination correction and vice versa.

The calculated in-situ R_{rs} values using the equations mentioned above in Table 1 were later used to perform WCC retrievals using the 2SeaColor model as described below.

2.4.2. The 2SeaColor model

Table 2.2 presents the employed algorithms for the 2SeaColor parameterization in this study. The same set-up of Table 2.2 was successfully used in previous studies for the 2SeaColor model to retrieve WCCs from remote sensing observations at the NJS (Arabi et al., 2016). Some of the employed parameterizations are empirical and therefore only valid for given ranges of the independent variables (WCCs). For instance, the Lee et al. (1999) model (Eq. 2.5), is not valid for very low values of Chla (< 0.4 (mg m^{-3})). Therefore, special care was taken to ensure that each variable stayed within its valid range, and outside these ranges, the border value was taken. To do this, we implemented an automatic truncation function in MATLAB to stay within the valid ranges of WCCs in this study.

Table 2.2. Summary of the used parameterizations (Arabi et al., 2016).

Variable	Parameterization	Ref.	Eq.
Chla absorption[1] at λ_1	$a_{Chla}(\lambda_1) = 0.06 \times ([Chla])^{0.65}$	(Lee et al., 1999)	(2.4)
Chla absorption[2]	$a_{Chla}(\lambda) = \{[a_0(\lambda) + a_1(\lambda) \times \ln a_{Chla}(\lambda_1)] \times a_{Chla}(\lambda_1)\}$	(Lee et al., 1999)	(2.5)
CDOM absorption[3]	$a_{CDOM}(\lambda) = a_{CDOM}(\lambda_2) \times \exp[-S_{CDOM}(\lambda - \lambda_2)]$	(Bricaud et al., 1981)	(2.6)
NAP absorption[4] at λ_2	$a_{NAP}(\lambda_2) = a^*_{NAP}(\lambda_2) \times [SPM]$	(Lee et al., 1998)	(2.7)
NAP absorption[5]	$a_{NAP}(\lambda) = a_{NAP}(\lambda_2) \times \exp[-S_{NAP} \times (\lambda - \lambda_2)]$	(Lee et al., 1998)	(2.8)
Chla backscattering at λ_3	$b_{b,Chla}(\lambda_3) = 0.416 \times [Chla]^{0.766}$	(Morel and Maritorena, 2001)	(2.9)
Chla backscattering	$b_{b,Chla}(\lambda) = \{0.002 + 0.01 \times [0.5 - 0.25 \times \log_{10}[Chla] \times (\lambda/\lambda_3)^n]\} \times b_{b,Chla}(\lambda_3)$	(Morel and Maritorena, 2001)	(2.10)
NAP backscattering[6] at λ_3	$b_{NAP}(\lambda_3) = b^*_{NAP}(\lambda_3) \times I \times [SPM]$	(Doxaran et al., 2009)	(2.11)
NAP scattering[7]	$b_{NAP}(\lambda) = b_{NAP}(\lambda_3) \times (\lambda_3/\lambda)^{\gamma} - [1 - \tanh(0.5 \times \gamma^2)] \times a_{NAP}(\lambda)$	(Doxaran et al., 2009)	(2.12)
Water molecules absorption[8]	$a_w(\lambda)$: listed values	(Pope and Fry, 1997)	(2.13)
Water molecules scattering	$b_{bw}(\lambda)$: listed values, table (3.8), page 104.	(Mobley, 1994)	(2.14)
Total absorption coefficient	$a(\lambda) = a_W(\lambda) + a_{Chla}(\lambda) + a_{NAP}(\lambda) + a_{CDOM}(\lambda)$	(IOCCG, 2000)	(2.15)
Total backscattering coefficient	$b_b(\lambda) = b_{bw}(\lambda) + b_{b,Chla}(\lambda) + b_{b,NAP}(\lambda)$	(Arnone et al., 2006)	(2.16)
Backscattering to absorption coefficients ratio	$x = b_b/a$	(Salama and Verhoef, 2015)	(2.17)
The directional-hemispherical reflectance of the semi-infinite medium[9]	$r^{\infty}_{sd} = (\sqrt{1+2x} - 1)/(\sqrt{1+2x} + 2\mu_w)$	(Salama and Verhoef, 2015)	(2.18)
Irradiance reflectance beneath the surface[10]	$R(0^-) \simeq r^{\infty}_{sd}/Q$	(Mobley et al., 1993)	(2.19)
Above-surface remote sensing reflectance	$R_{rs} = (0.52 \times R(0^-))/(1 - 1.7 \times R(0^-))$	(Lee et al., 2002)	(2.20)

1 λ_1, λ_2 and λ_3 are reference wavelengths at 443 nm, 440 nm, and 550 nm, respectively.
2 a_0 and a_1 are the absorption and backscattering coefficients of water molecules taken from Lee et al. (1998).
3 S_{CDOM} = 0.013 (nm^{-1}) is the spectral slope of CDOM taken from Hommersom et al. (2009).
4 $a^*_{NAP}(\lambda_2)$= 0.036 ($m^2\ g^{-1}$) is the specific absorption of non-algae particles taken from Hommersom et al. (2009).
5 S_{NAP} = 0.011 (nm^{-1}) is the spectral slope of non-algae particles (NAP) taken from Hommersom et al. (2009).
6 $b^*_{NAP}(\lambda_3)$= 0.282 ($m^2\ g^{-1}$) is the specific scattering coefficient of NAP taken from Hommersom et al. (2009) and I = 0.019 for the North Sea was taken from Petzold (1972).
7 γ = 0.6 for the North Sea was taken from Doxaran et al. (2009).
8 a_w and b_{bw} are the absorption and backscattering coefficients of water molecules and were taken from Mobley (1994) and Pope and Fry (1997).
9 μ_w is the cosine of the SZA below the (flat) water surface.
10 Q = 3.25 was taken from Mobley (1994).

In Table 2.2, the symbols a and b_b represent the absorption and backscattering coefficients. The subscripts Chla, SPM, CDOM, NAP, and W, denote Chlorophyll-a, Suspended Particulate Matter, Colored Dissolved Organic Matter, Non-Algae Particles (NAP) and water molecules, respectively. [Chla], [SPM] are the concentrations corresponding to Chla and SPM, respectively. It should be noted that the predicted reflectance from the water by the 2SeaColor model (r_{sd}^{∞}) is dependent on the SZA values (Eq. 2.18), although the range in the cosine of the SZA (μ_w) is quite moderate since the maximum SZA underwater is Brewster's angle, 53° for water. The calculated IOPs using the parameterizations in Table 2.2 and the set of measured SIOPs valid for the Dutch Wadden Sea were used to model R_{rs} spectra by the 2SeaColor model (Eqs. 2.17 – 2.20). Next, an iterative optimization technique was applied for the model inversion to retrieve the WCCs. Within the constraints mentioned in Table 2.2, there are three WCCs in Eq. 2.18, Chla (mg m^{-3}) concentration, SPM (g m^{-3}) concentration and CDOM absorption at 440 nm (m^{-1}), which uniquely determine the modeled R_{rs} spectra. These unknown variables can be retrieved by minimizing the differences between R_{rs} curves that are modeled by the 2SeaColor model calculated in Eq. 2.20 and the measured ones calculated in Eq. 2.3 (Lee et al., 1999). The "Trust Region" algorithm, implemented in the MATLAB (The MathWorks, Inc. Natick, MA, USA) function "lsqnonlin", was used to minimize the cost function. The program calculated the Root Mean Square Error (RMSE) between the measured and modeled values over the whole wavelength range of the reflectance spectra.

Table 2.3. The initial guess of WCCs used in the model inversion.

Parameter	Unit	Lower/upper boundary	Border values	Initial Guess
Chla concentration	mg m^{-3}	0 - 50	0 , 50	0.1
SPM concentration	g m^{-3}	0 - 100	0 , 100	20
CDOM absorption	m^{-1}	0 - 3	0 , 3	0.25

To avoid local minima, we did the minimization in numerous loops starting with different WCCs initial guesses as recommended by Salama and Shen (2010). We changed the model's initial values and modeled the R_{rs} spectra. The results (data are not shown) showed that initial values had no significant effects on the minimization and thus on the retrieved parameters.

2.4.3. The 2SeaColor model's evaluation for various SZAs and turbidities

To investigate the SZA variation effect, we categorized the time series of in-situ R_{rs} measurements into different SZA groups. Considering the yearly SZA variation (from 30° to 75°) at the measurement site (located at 53° North) with an average change of almost 7.5° per month, we created six SZA groups (SZAs < 37.5°, 37.5° ⩽ SZAs < 45°, 45°⩽ SZAs < 52.5°, 52.5° ⩽ SZAs < 60°, 60° ⩽ SZAs < 67.5° and 67.5° ⩽ SZAs ⩽ 75°). Regarding different water turbidity conditions, we extracted the concentration ranges of in-situ Chla (mg m^{-3}) and SPM (g m^{-3}) measurements between 2008 and 2010 at the NJS corresponding to each SZA group separately. Then a Mean Squared Error (MSE) decomposition analysis was performed for different SZA groups and water turbidity conditions at the NJS. The MSE is one of the most widely used criteria for evaluation of models against in-situ measurements. We decomposed the MSE into three contributions due to i) unequal standard deviations (USD), ii) bias in the mean values (BIM), and iii) lack of (positive) correlation (LOC), following (Gupta et al., 2009) as expressed in Eq. 2.21.

$$\mathrm{MSE} = (\sigma_1 - \sigma_2)^2 + (\mu_1 - \mu_2)^2 + 2\sigma_1\sigma_2(1 - \mathrm{R}) \tag{2.21}$$

where 1 and 2 indicate the variables (modeled and measured values), σ and μ are standard deviations and means, respectively, and R is the correlation coefficient. The results of the MSE decomposition analysis results are presented in sections 2.5.1 and 2.5.2. Finally, we analyzed the reliability of measured SIOPs to be implemented in the 2SeaColor model parametrization at the NJS. For this evaluation, the occurrence of any systematic errors between modeled and measured R_{rs} spectra in different parts of the spectrum by using the spectral difference criteria for different SZA groups was investigated. Results of this evaluation are also presented in section 2.5.3.

2.4.4. The 2SeaColor's validation

The 2SeaColor model accuracy was evaluated at two different levels: (i) validating the modeled spectra against in-situ R_{rs} measurements at the four reference wavelengths of 443 nm, 490 nm, 550 nm, and 665 nm and (ii) validating the retrieved concentrations of Chla and SPM against in-situ measurements. The statistical measures of the determination coefficient (R^2) and RMSE were used to quantify the goodness-of-fit between modeled and measured R_{rs}, and retrieved and measured in-situ Chla and SPM concentrations. The results of these assessments are presented in section 2.5.4.

2.4.5. Tidal effect evaluation

For the tidal effect evaluation, two different approaches were used in this study. In the first approach, the temporal variation of in-situ SPM and Chla concentrations corresponding to their water depth values within the yearly tidal cycles between 2008 and 2010 at the NJS were plotted (Figs. 2.4 and 2.5). Next, the correlation between time series of in-situ Chla and SPM concentrations at the NJS and the corresponding water depth values at the Den Helder station for different SZA groups were calculated to investigate the possible correlation between these two parameters (Table 2.10). For the second approach, a complete dataset of ebb and flood tidal information (including water depth values during the ebb and flood, ebb and flood occurrence times and sunrise and sunset time per day) between 2008 to 2010 were obtained for the Den Helder station (flood: 1076 measurements, ebb: 1065 measurements). For times concurrent with tidal events, in-situ R_{rs} measurements at the NJS were extracted. After performing the data quality control process, 508 and 383 reliable in-situ R_{rs} measurements were selected under conditions of flood and ebb, respectively. Then, the 2SeaColor model was inverted to retrieve Chla and SPM concentrations per each R_{rs} measurement of the quality-controlled dataset. Then the differences between mean values of retrieved SPM and Chla concentration during flood and ebb for different SZA groups were evaluated as an indicator to investigate whether the tide causes any significant change in the WCCs (Table 2.11).

2.5. Results

2.5.1. SZA effect on the 2SeaColor model's accuracy

Fig. 2.3 presents the daily variation of SZA over the year at the NJS. The spectral residuals (RMSE) between in-situ and modeled R_{rs} values over the whole wavelength region as a function of time (Day Of Year: DOY) are also presented in this figure.

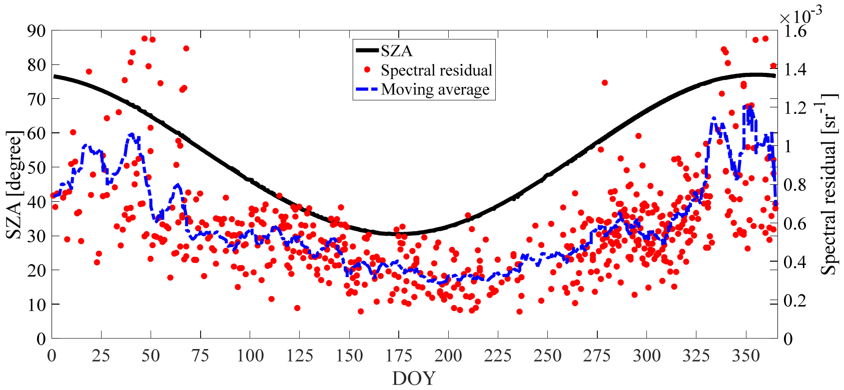

Figure 2.3. The spectral residual (RMSE between the best fits of modeled and measured Rrs) and the yearly SZA variation versus DOY for the quality-controlled meteorological, shape and sun-glint effect dataset between 2008 and 2010 at the NJS.

The X-axis in this figure shows DOYs for three years (between 2008 and 2010). The left Y-axis shows the SZA values corresponding to each day (black line). The spectral residual (RMSE) values for each measurement are presented with red dots while a moving average with a span of 5 days is also used (blue dashed-line) to show the variation of RMSE with SZA variation better. As the figure shows, the spectral residual values increase (from 0.0001 to 0.0016 (sr^{-1})) nearly in parallel with SZA (from 10° to 80°). By evaluating the rising trend of spectral residual amounts at high SZAs (SZAs > 60°), it can be concluded that the 2SeaColor model inversion yields worse spectral fitting results under high SZAs in this region. As to the effect of SZA variation on the accuracy of the 2SeaColor model retrievals, the results of MSE decomposition analysis for all SZA groups are computed in Tables 2.4 and 2.5. In these tables, the distribution of the three error sources (i.e., USD: unequal standard deviations (second column), BIM: bias in the mean values (third column) and LOC: lack of correlation (fourth column) is calculated as the percentages (%) of total MSE. In addition, the calculated R^2 values (first column) are attached to the MSE decomposition tables as follows:

Table 2.4. The statistical measures used for evaluation of the SZAs effect on the retrieved Chla (mg m^{-3}) concentrations by the 2SeaColor model.

SZAs	R^2	USD (%)	BIM (%)	LOC (%)	Total MSE
[30° - 37.5°)	0.81	18.15	0.150	81.69	06.61
[37.5° - 45°)	0.78	18.17	02.15	79.68	07.43
[45° - 52.5°)	0.74	28.67	04.72	66.61	11.44
[52.5° - 60°)	0.72	14.77	20.00	65.23	08.80
[60° - 67.5°)	0.03	50.12	43.93	15.95	08.40
[67.5° - 75°]	0.08	42.30	43.40	14.30	10.07

As the results of Tables 2.4 show, the calculated R^2 values between the measured and retrieved Chla estimates significantly decrease (from 0.81 to 0.08) when SZAs becomes higher than 60°. The R^2 value of Chla is around 0.80 for 30° < SZAs < 52°, decreasing to 0.75 for 52° < SZAs < 60° and it is dropping to < 0.2 for SZAs > 60°. Therefore, the SZA of 60° might be considered as a threshold which leads to less accurate retrievals in case R_{rs} measurements are collected at SZAs > 60°. However, the total MSE values for all SZA groups are relatively small (between 6 and 12) and do not increase in parallel with the SZA. The very low R^2 values (< 0.1) of Chla retrievals by the model in winter (SZAs > 60°) do contribute little (< 15%) to the total MSE and therefore cannot be considered a major source of error. This also means that R^2 as an error measure is rather meaningless in this case. Improving the correlation would not help much here since the greatest contributions to the MSE decomposition for Chla estimates in winter (SZAs > 60°) come from the bias in the mean values (~ 45%) and the unequal standard deviations (~ 50%) while the lack of positive correlation plays the smallest role (~ 15%) in the total MSE. The results of the calculated R^2 values, as well as the MSE decomposition analysis for all SZA groups for SPM estimates, are presented in Table 2.5.

Table 2.5. The statistical measures used for evaluation of the SZAs effect on the retrieved SPM (g m^{-3}) concentrations by the 2SeaColor model.

SZAs	R^2	USD (%)	BIM (%)	LOC (%)	Total MSE
[30° - 37.5°)	0.89	01.69	21.01	77.29	4.14
[37.5° - 45°)	0.84	01.54	10.57	87.89	8.42
[45° - 52.5°)	0.83	01.46	10.41	88.13	10.28
[52.5° - 60°)	0.87	01.52	14.35	84.14	11.85
[60° - 67.5°)	0.23	0.580	31.97	67.45	36.25
[67.5° - 75°]	0.42	0.740	41.20	58.06	65.09

Like for the Chla estimates, the calculated R^2 values between the measured and retrieved SPM estimates significantly decrease (from 0.89 to 0.42) in winter when SZAs becomes higher than 60°. On the other hand, the total MSE values of SPM estimates also increase (from 4 to 65) with the SZA increase in winter. The total MSE values are ~ 12 for SZAs < 60°, and they increase dramatically to ~ 65 for SZAs > 60°. Moreover, the lack of positive correlation does have the most significant contribution (~ 70%) to the total MSE for SPM estimates in winter. Therefore, the seasonal variation of higher SPM concentrations in winter might be another factor besides the SZA effect that leads to the sudden increase of total MSE at SZAs > 60°. In the following section, the 2SeaColor model's performance with respect to the variation range of in-situ Chla and SPM concentrations at different SZA groups is investigated.

2.5.2. Turbidity affect the 2SeaColor's accuracy

The ranges of in-situ Chla and SPM concentrations for the various SZA groups at the NJS are presented in Table 2.6:

Table 2.6. The concentration ranges of in-situ Chla (mg m^{-3}) and SPM (g m^{-3}) measurements corresponding to each SZA group between 2008 and 2010 at the NJS.

SZAs	Chla (mg m^{-3})	SPM (g m^{-3})
[30° - 37.5°)	0.22 - 22.04	3.06 - 30.54
[37.5° - 45°)	1.37 - 18.92	5.60 - 31.39
[45° - 52.5°)	0.84 - 26.52	7.64 - 32.08
[52.5° - 60°)	0.19 - 20.96	2.84 - 39.46
[60° - 67.5°)	0.19 - 09.37	3.63 - 43.48
[67.5° - 75°]	0.40 - 08.51	1.17 - 51.65

As can be seen from Table 2.6, the maximum levels of in-situ SPM concentrations (~ 50 (g m^{-3})) occur during winter (SZAs > 60°) while these amounts are considerably higher than the maximum levels of SPM concentration (~ 30 (g m^{-3})) during spring and summer (30° ⩽ SZAs < 52.5°). Conversely, the maximum levels of in-situ Chla concentration (~ 30 (mg m^{-3})) occur in spring and summer, while these amounts reach their minimum values (~ 0.1 (mg m^{-3})) during winter. Therefore, the substantial variations in the concentration of in-situ measured Chla and SPM in different seasons in the NJS might be another reason for the model's deterioration in winter, especially for the SPM estimates. Figs. 2.4 and 2.5 present the temporal variation of retrieved Chla and SPM concentration versus their corresponding in-situ measurements at the NJS. In these figures, the retrieved values between March and October (SZAs < 60°) are shown by red triangles. Blue stars show the retrieved values during winter (SZAs > 60°), and black dots indicate the in-situ Chla and SPM measurements at the NJS. In addition, the water depth values at the Den Helder station corresponding to each in-situ Chla and SPM measurement at the NJS are presented in grey bars to support the further analysis given in section 2.5.5.

(a)

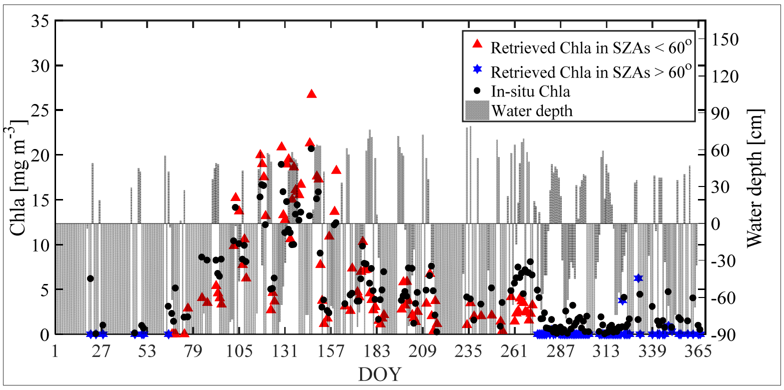

(b)

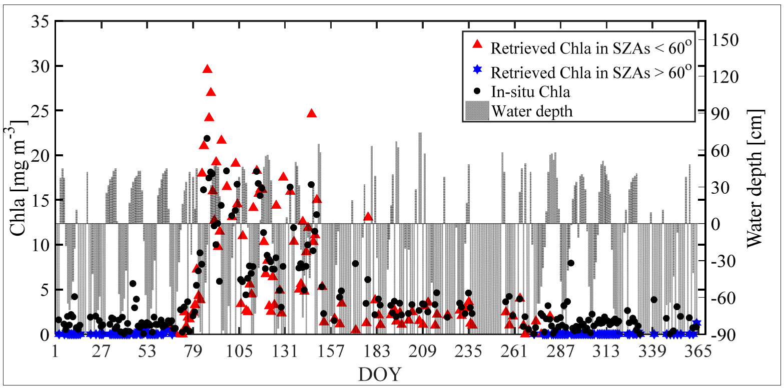

(c)

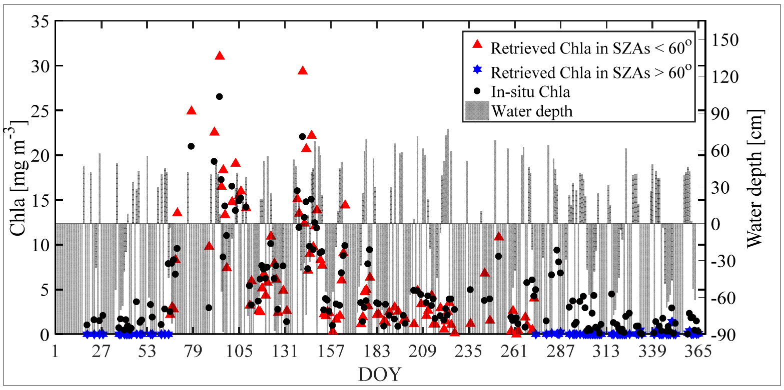

Figure 2.4. Temporal variation of retrieved Chla concentrations (mg m^{-3}) by the 2SeaColor model versus in-situ Chla concentrations (mg m^{-3}) for the flagged meteorological, shape and sun-glint effect dataset at the NJS in (a): 2008; (b): 2009 and (c): 2010.

As can be seen in Fig. 2.4, the temporal trends of retrieved and in-situ Chla concentrations (mg m^{-3}) are in good agreement (between 0 and 35 (mg m^{-3}))

with the daily Chla concentration variations between 2008 and 2010 at the NJS. The highest values of retrieved and measured Chla concentrations are mainly observed in the spring period (April, May, and June) ~ 30 (mg m^{-3}). After the spring period, Chla values start to decrease in July (~ 5 (mg m^{-3})) with a slight increase in September (~ 10 (mg m^{-3})), and they reach their lowest values during winter (~ 0 (mg m^{-3})) (blue stars). However, underestimation of retrieved Chla concentrations in comparison to in-situ measurements in winter (SZAs > 60°) can be observed in all three years (Figs 2.4. (a), (b) and (c)). Indeed, the low concentration of in-situ Chla measurements during the winter makes the water leaving the spectrum less sensitive to changes in Chla values. That is why the model underestimates Chla concentration retrievals by tending to take the lower boundaries (~ 0 (mg m^{-3})) of the Chla concentration variable through optimization techniques (Table 2.3). On the other hand, in-situ Chla concentrations occur in very low ranges (~ 0 to 5 (mg m^{-3})) during winters. Consequently, reasonable temporal agreement occurs between the retrieved and in-situ Chla concentrations in winter, with relatively low total MSE (~ 10) in the high SZA groups (SZAs > 60°) (Table 2.4), which also means that the low R^2 (< 0.1) is harmless in wintertime, since the low Chla concentrations in winter (between 0 and 5 (mg m^{-3})) were predicted correctly. Therefore, it can be concluded that the 2SeaColor model is capable enough to retrieve Chla concentrations under different water turbidity conditions at the NJS. The temporal variations of retrieved SPM concentrations versus in-situ ones at the NJS are presented in Fig. 2.5.

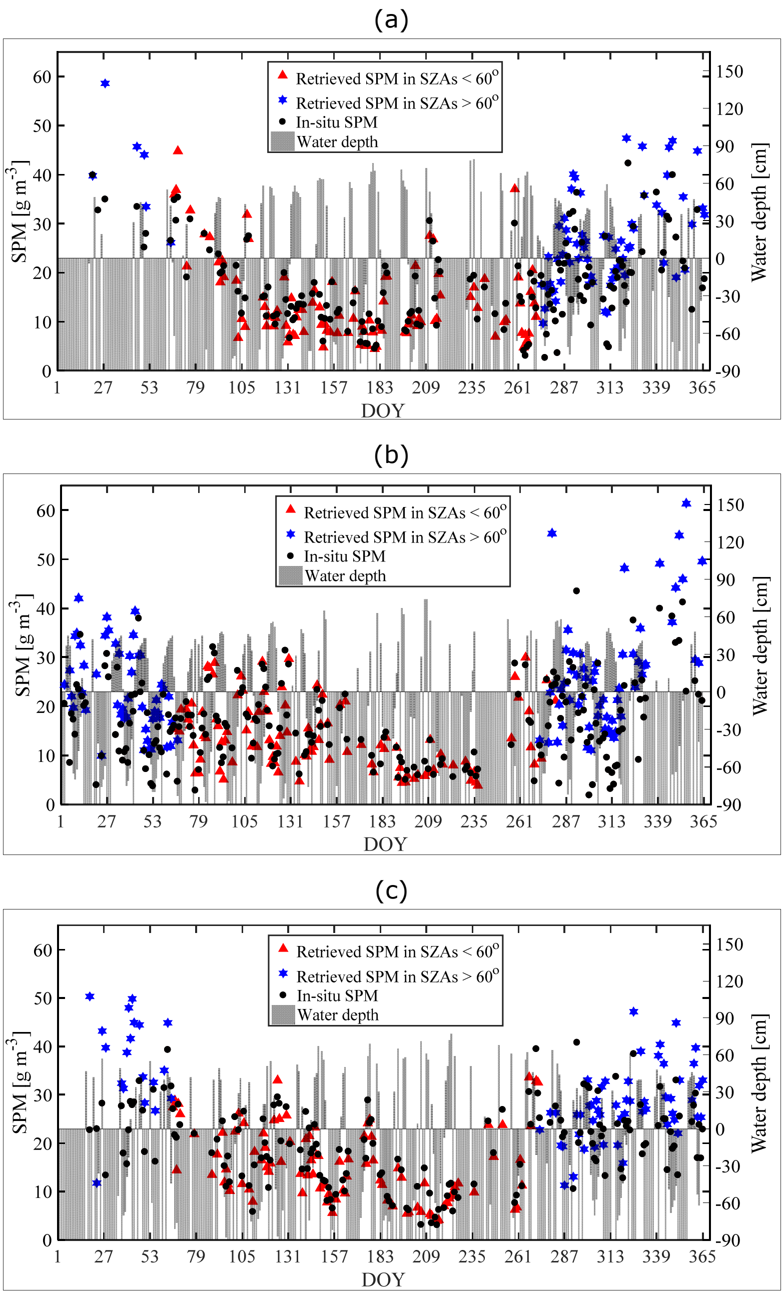

Figure 2.5. Temporal variation of retrieved SPM concentrations (g m^{-3}) by the 2SeaColor model versus in-situ SPM concentrations (g m^{-3}) for the flagged meteorological, shape and sun-glint effect dataset at the NJS (a): 2008; (b): 2009 and (c) : 2010.

As can be seen in Fig. 2.5, the temporal trends of retrieved and in-situ SPM concentrations (g m^{-3}) are in good agreement (between 0 and 60 (g m^{-3})) with the daily water turbidity variation between 2008 and 2010 at the NJS. Both retrieved and in-situ SPM concentrations show their highest values (between 10 and 60 (g m^{-3})) from January to February, they start to decrease (from 0 to 30 (g m^{-3})) from April to July and they increase again at the beginning of October (between 10 and 35 (g m^{-3})), until they reach their highest level in November and December (between 40 and 60 (g m^{-3})). On the other hand, some overestimation of retrieved SPM concentrations in comparison to in-situ measurements can be observed during winters (SZAs > 60°) in all three years. As the results of the MSE analysis also showed (Table 2.5), the total MSEs significantly (from 4 to 65 (g m^{-3})) increase in winter, in parallel with SZA increase (from 30° to 75°) while the most significant contribution to this error at SZAs > 60° is due to lack of correlation (~ 90%). Therefore, the higher level of SPM concentrations in winter in comparison to summer level (SZAs < 60°) might be another reason (besides SZA increase) that the total MSE values considerably increase during winter for SPM retrievals (from 4 to 65 (g m^{-3})). However, as explained before in section 2.1.2, and following recent studies (Arabi et al., 2016; Salama and Verhoef, 2015; Yu et al., 2016a), the 2SeaColor model has been developed to deal with high turbidity. Therefore, this SPM overestimation might be related to the unreliability of the SIOPs implemented in the 2SeaColor model’s parametrization for SPM retrievals during winter. The main reason is that the SPM concentration levels follow a certain seasonal pattern over different years (Figs. 2.5 (a), (b), (c)) while there is no information about seasonal SIOPs at this moment for the NJS. Indeed, the implemented SIOPs in this study have been collected only during spring and summer (Hommersom et al., 2010). However, even this model overestimation in winter still shows fairly reasonable agreement with the trend of in-situ SPM concentrations for all three years. Therefore, from the results of this evaluation, it can be concluded that the 2SeaColor model is capable enough to retrieve SPM concentrations under various water turbidity conditions at the NJS. However, the results of winter retrievals (SZAs > 60°) show a considerable model overestimation in this season. It should be noted that the 2SeaColor model also retrieves CDOM absorption at 440 nm (m^{-1}) simultaneously with Chla and SPM concentration values. The trend of retrieved CDOM by the 2SeaColor model is presented in Fig. 2.6. However, there were no in-situ CDOM measurements to evaluate the agreement between the temporal variation of measured and retrieved CDOM absorptions.

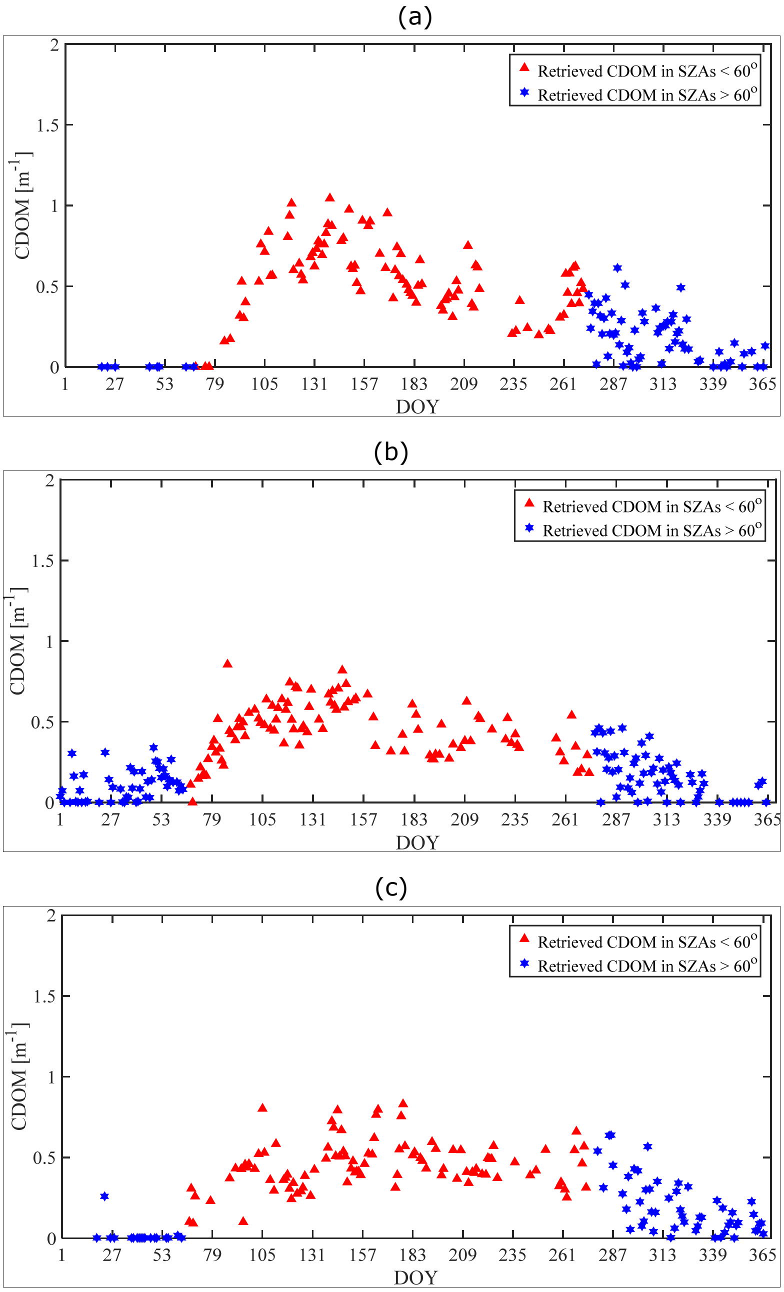

Figure 2.6. Temporal variation of retrieved CDOM absorption at 440 nm (m^{-1}) by the 2SeaColor model for the flagged meteorological, shape and sun-glint effect dataset at the NJS (a): 2008; (b): 2009 and (c) : 2010.

As Fig. 2.6 shows, the temporal variability of CDOM is independent of that of Chla (Yu et al., 2016b). In general, the retrieved values of CDOM (blue stars) are low (~ 0.5 m^{-1}) during winter (SZAs > 60°) and increasing to ~ 1.2 (m^{-1}) in spring and summer (red triangles) during three years at the NJS. Moreover, the temporal CDOM absorption variations follow similar trends (between 0 and 2 (m^{-1})) over the years between 2008 and 2010 at the NJS.

2.5.3. Evaluation of the reliability of SIOPs

The reliability of the measured SIOPs by Hommersom et al. (2009) used in the 2SeaColor model parametrization, are evaluated as explained in Fig. 2.7.

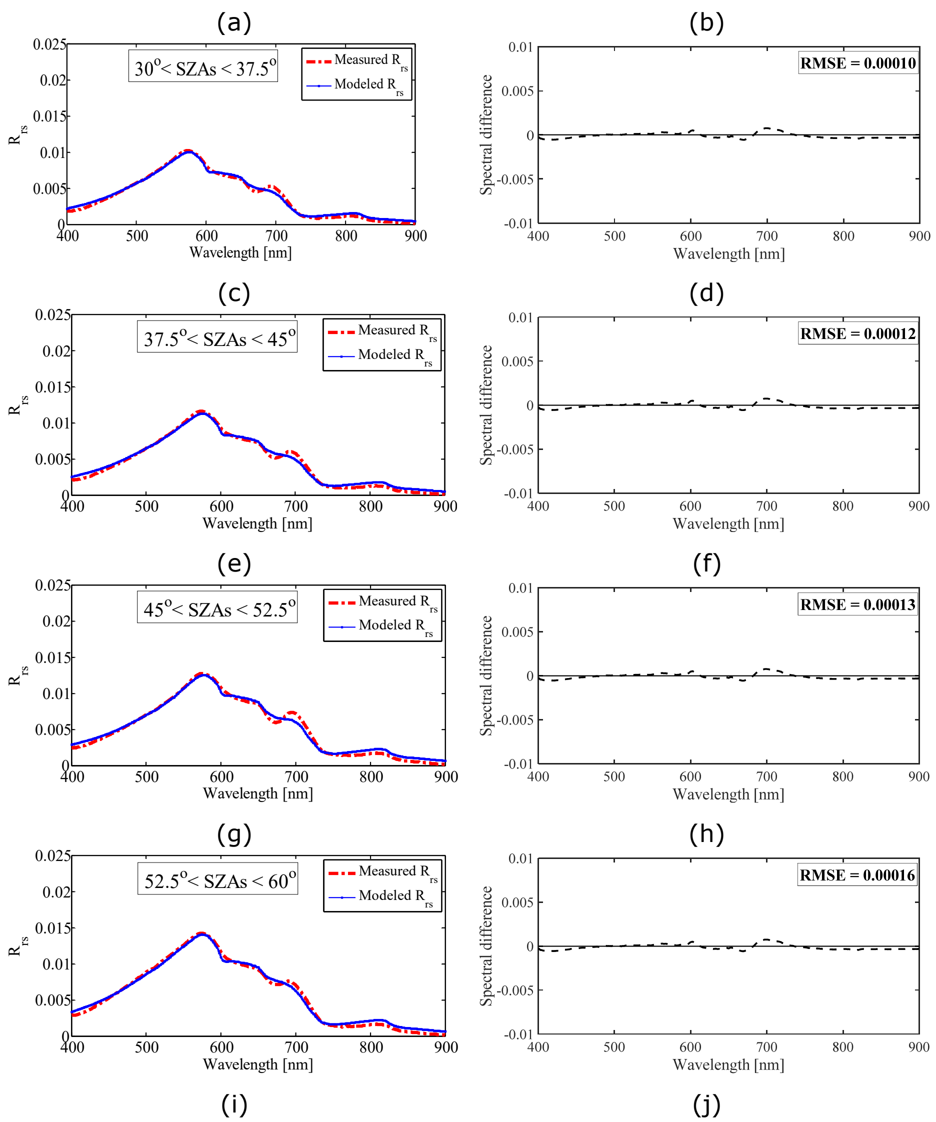

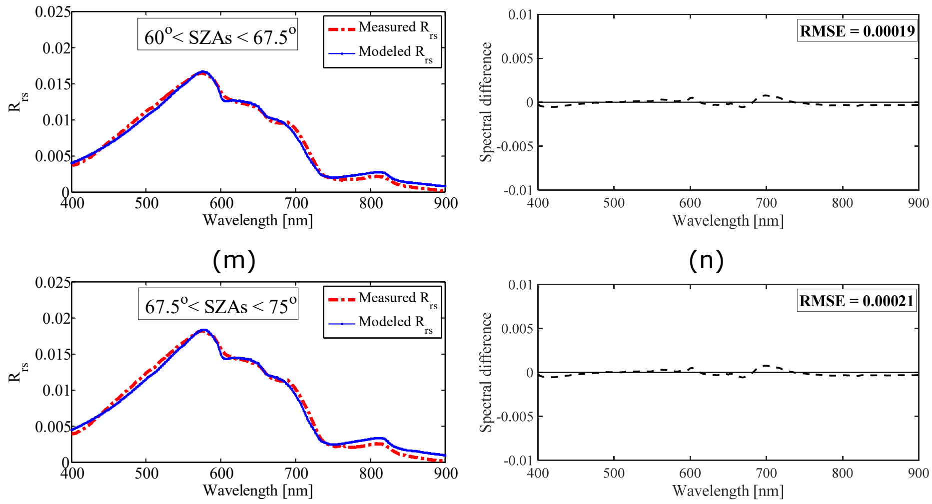

Figure 2.7. The spectral differences between in-situ and model's best fit R_{rs} corresponding to the different SZA groups versus wavelength for the quality-controlled meteorological, shape and sun-glint effect dataset between 2008 and 2010 at the NJS. Left: red dashed-lines present the spectral average of in-situ R_{rs} values, and the blue lines present the spectral average of the models best fits R_{rs} values; right: the spectral differences (RMSE) between in-situ and model's best fit R_{rs} for the whole wavelength region. (a,b): data collected at SZAs [30° - 37.5°); (c,d): data collected at SZAs [37.5° - 45°); (e,f): data collected at SZAs [45° - 52.5°); (g,h):data collected at SZAs [52.5° - 60°); (i,j): data collected at SZAs [60°- 67.5°); (m,n): data collected at SZAs [67.5°- 75°].

As the left panels of this figure show, by using Hommersom's SIOPs, good fits are found between measured and modeled R_{rs} spectra while the calculated RMSE are in very low range groups (0.0001 < RMSE < 0.00022) for all SZAs. However, as the right panels of this figure show, many zero-crossings occur constantly at nearly the same spectral positions. For example, there are systematic R_{rs} underestimations around 410 nm and 600 nm for all SZA groups. In addition, another systematic R_{rs} overestimation can be observed in the Near Infrared Red (NIR) part of the spectrum (between 780 and 900 nm). Regarding the similar patterns of zero-crossings as well as the very low spectral residuals (0.0001 < RMSE < 0.00022) for all SZA groups (Fig. 2.7 right panel), it can be stated that the SIOPs measured by Hommersom et al. (2009) is suitable to be implemented for the 2SeaColor model parametrization at the NJS. However, there is a slight mismatch between the real and implemented SIOPs for the 2SeaColor model parametrization at this region. Therefore, modifying these SIOPs with respect to the seasonal patterns of WCCs at the NJS may lead to improved retrieval results. On the other hand, the right panels of Fig. 2.7 show, the calculated RMSE values between the measured and modeled R_{rs} spectra increase (from 0.00010 to 0.00021) in parallel with the SZA increase (from 30° to 75°). The RMSE values are around 0.00013 for 30° < SZAs < 52°, increasing to 0.00016 for 52° < SZAs < 60° and rising to around 0.0002 for SZAs > 60°. On the other hand, the amplitudes of R_{rs} values also increase (from 0.01 to 0.02) (Fig. 2.7, left panels) in parallel with the SPM level increase from spring to winter (Table 2.6). The R_{rs} amplitude values are around 0.012 for 30° < SZAs < 52°, increasing to 0.015 for 52° < SZAs < 60° and are rising to around 0.02 for SZAs > 60°. This can be other evidence of the lower reliability of the retrieved WCCs during winter under high SZA conditions at the NJS (Table 2.5). However, it is uncertain whether the higher spectral residuals and consequently the worse retrieval results during winter are caused by the seasonal pattern of SPM concentrations and lack of seasonal SIOPs, or by the SZA effect.

2.5.4. Validation of the 2SeaColor model performance

The results of the 2SeaColor model validation for modeling R_{rs} spectra and retrieving Chla and SPM concentrations are provided in Figs. 2.8, 2.9 and 2.10, respectively.

(a) (b) (c) (d)

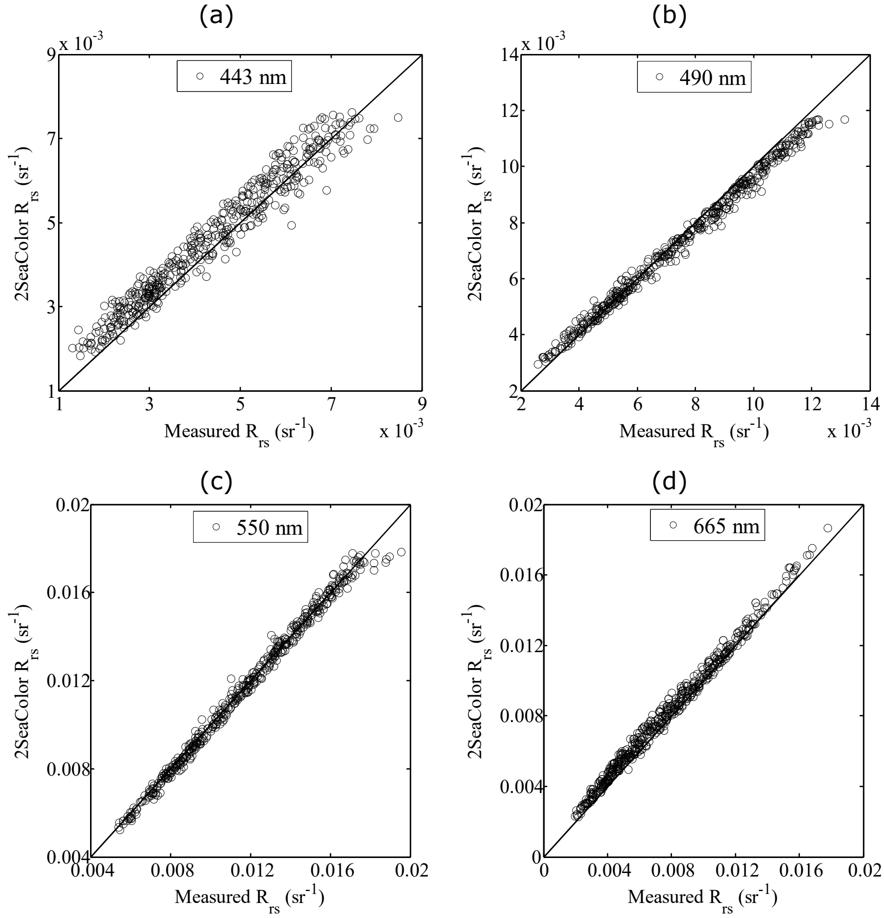

Figure 2.8. Comparison between the 2SeaColor model's best-fit spectra and in-situ R_{rs} measurements for the quality-controlled dataset between 2008 and 2010 at the NJS for wavelengths: (a) 443 nm; (b) 490 nm; (c) 550 nm and (d) 665 nm.

Fig. 2.8 presents the results of the 2SeaColor model validation for modeling R_{rs} spectra for the four wavelengths at 443 nm, 490 nm, 550 nm and 665 nm for the flagged meteorological, shape and sun-glint effect dataset between 2008 and 2010 at the NJS. As this figure shows, the modeled best fitting spectra agree very well with measured spectra at the selected wavelengths. The related error statistics are also presented in Table 2.7.

Table 2.7. The model's performance evaluation for R_{rs} model's best-fit spectra against in-situ ones for the quality-controlled dataset between 2008 and 2010 at the NJS for wavelengths at 443 nm, 490 nm, 550 nm, and 665 nm.

Wavelength / statistical measures	R^2	RMSE (sr^{-1})
443 nm	0.95	0.00032
490 nm	0.99	0.00019
550 nm	0.99	0.00028
665 nm	0.99	0.00032

The high R^2 values ($R^2 > 0.95$ for all selected wavelengths) and small RMSE values ($0.00015 < \text{RMSE} < 0.00035$) for all the quality-controlled datasets show that the 2SeaColor model is capable of accurately reproducing the measured reflectance spectra for varying WCC values at the NJS. The accuracy of the 2SeaColor model for retrieving Chla and SPM concentrations for the NJS dataset with and without winter retrievals are also illustrated in Figs. 2.9 and 2.10, respectively.

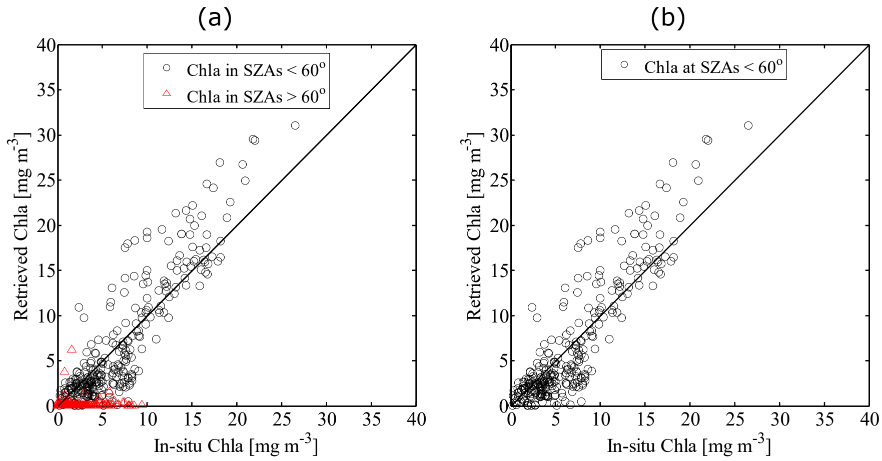

Figure 2.9. Left: comparison between retrieved and in-situ measurements of Chla concentration (mg m^{-3}) for the quality-controlled dataset between 2008 and 2010 at the NJS; right: the same after removing winter retrievals.

Fig. 2.9 presents the results of the 2SeaColor model validation for retrieving Chla concentrations from a time-series of daily quality-controlled R_{rs} measurements for three years at the NJS. As Fig. 2.9 left shows, the model is less successful in achieving reasonable retrievals in winter under high SZAs. However, by removal of the winter retrievals, the retrieved-measured Chla scatter plot shows significant improvement (Fig. 2.9 right). The related error statistics are also presented in Table 2.8.

Table 2.8. The model's performance evaluation of Chla retrievals for the quality-controlled dataset with and without winter retrievals between 2008 and 2010 at the NJS.

SZA groups / statistical measures	R^2	RMSE (mg m^{-3})
All dataset (Fig. 9 left)	0.79	2.57
SZAs < 60° (Fig. 9 right)	0.80	2.98

As Table 2.8 presents, the calculated R^2 and RMSE values of the Chla estimates slightly improve (R^2 from 0.79 to 0.80; RMSE: from 2.57 to 2.98) when the winter retrievals are removed. However, for both groups (with and without winter data), the statistical measures still indicate a reasonable agreement between the retrieved and in-situ Chla concentrations for three years at the NJS.

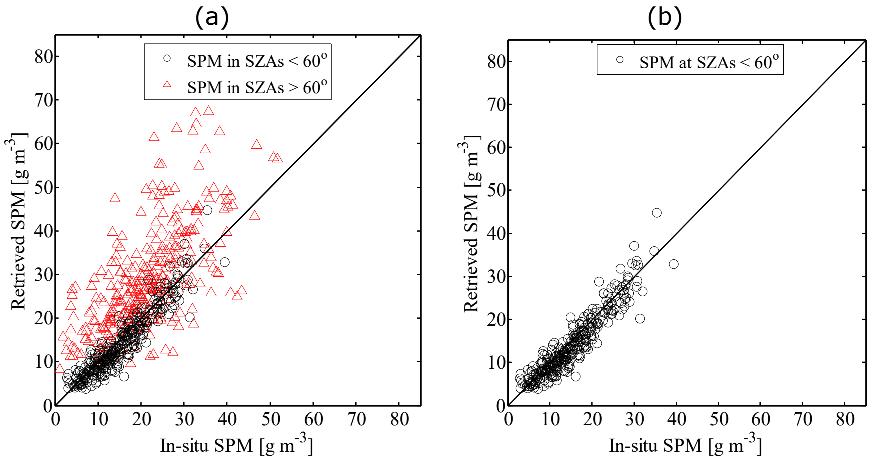

Figure 2.10. Left: comparison between retrieved and in-situ measurements of SPM concentration (g m^{-3}) for the quality-controlled dataset between 2008 and 2010 at the NJS; right: the same after removing winter retrievals.

Fig. 2.10 also presents the results of the 2SeaColor model validation for retrieving SPM concentrations from a time-series of daily quality-controlled R_{rs} measurements for three years at the NJS. As Fig. 2.10 left shows, retrievals are less successful in winter under high SZAs. However, by removal of the winter retrievals, the retrieved-measured SPM scatter plot shows improvement (Fig. 2.10 right). The related error statistics are also presented in Table 2.9.

Table 2.9. The model's performance evaluation of SPM retrievals for the quality-controlled dataset between 2008 and 2010 at the NJS.

SZA groups / statistical measures	R^2	RMSE (g m^{-3})
All dataset (Fig. 2.10 left)	0.66	7.65
SZAs < 60° (Fig. 2.10 right)	0.89	2.53

As Table 2.9 shows, the calculated R^2 and RMSE values of the SPM estimates improve significantly when the winter retrievals are removed. Indeed the model shows much better performance to retrieve SPM concentrations after removing the winter retrievals (R^2 = 0.89, RMSE = 2.57 (g m^{-3})). However, as explained before in section 2.5.3, it is uncertain whether this model's deterioration in winter is due to the seasonal pattern of SPM concentrations or due to the SZA effect. Moreover, the accuracy of the 2SeaColor model to retrieve SPM concentration is, as expected, (Salama et al., 2011; Salama and Stein, 2009), better than that for Chla after removal of winter retrievals. The R^2 values are 0.89, and 0.80 and the RMSE values are 2.98 and 2.53 for retrieved Chla and SPM estimates, respectively.

2.5.5. Tidal effect

To investigate the possible correlation between WCC variations and the tidal cycles over the year at the NJS, the two figures that were produced in section 2.5.2 to present the time series (Fig. 2.4: Chla concentrations versus water depth values, Fig. 2.5: SPM concentrations versus water depth values) can be used. These figures show the temporal variation of the in-situ Chla and SPM concentrations (black dots) in comparison with their water depth values (grey bars), respectively. As these figures show, no temporal relationship can be found to prove that the concentration of Chla and SPM values at the NJS are affected by the level of water depth. The scatter plots of in-situ Chla and SPM concentrations at the NJS, and their corresponding water depth values at the Den Helder station are also presented in Fig. 2.11.

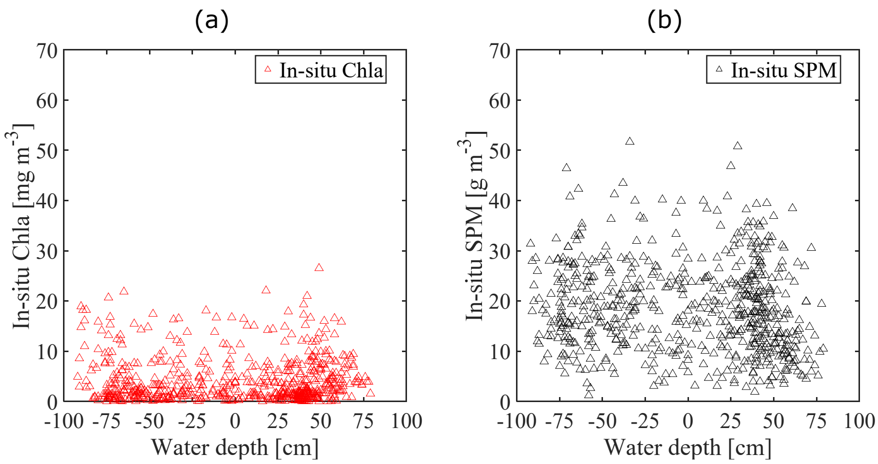

Figure 2.11. Left: scatter plot of in-situ Chla concentrations (mg m^{-3}) at the NJS versus water depth values (cm) at the Den Helder station for the quality-controlled dataset between 2008 and 2010; right: the same, for in-situ SPM concentrations (g m^{-3}).

As can be seen from these figures, no relationships are found between in-situ Chla and SPM concentrations and their corresponding water depth values. The calculated correlation estimates between time series of in-situ Chla and SPM concentrations at the NJS corresponding to their water depth values at the Den Helder station at different SZA groups are also presented in Table 2.10.

Table 2.10. The calculated correlation between in-situ Chla (mg m^{-3}) and SPM (g m^{-3}) concentration values between 2008 and 2010 at the NJS and their water depth values (cm) corresponding to different SZA groups.

SZAs / water constituents	Chla (mg m^{-3})	SPM (g m^{-3})
[30° - 37.5°)	-0.02	-0.12
[37.5° - 45°)	-0.34	-0.41
[45° - 52.5°)	-0.14	-0.30
[52.5° - 60°)	0.09	-0.01
[60° - 67.5°)	0.03	0.07
[67.5° - 75°]	-0.01	-0.04

As shown in this table, there are no explicit relationships between measured measurements (i.e., Chla and SPM) and their corresponding water depth values. Table 2.11 presents the mean values of retrieved Chla and SPM concentrations by the 2SeaColor model during the flood and ebb tide for different SZA groups between 2008 and 2010.

Table 2.11. The mean values of retrieved Chla and SPM concentrations for the flood and ebb groups corresponding to their SZA degrees for the quality-controlled dataset between 2008 and 2010 at the NJS.

SZA / water constituent	Chla (mg m^{-3})		SPM (g m^{-3})	
	flood	ebb	flood	ebb
[30°- 37.5°)	07.02	07.10	17.25	19.15
[37.5° - 45°)	09.77	08.66	17.66	20.61
[45° - 52.5°)	09.93	08.78	20.39	22.86
[52.5°- 60°)	08.10	07.93	24.60	26.01
[60°- 75°]	04.87	04.97	25.94	28.86

As Table 2.11 shows, there is no large difference between the mean values of retrieved Chla and SPM concentrations under the conditions of flood and ebb for different SZAs, since the mean differences are less than 1.15 (mg m^{-3}) and less than 3 (g m^{-3}) for Chla and SPM, respectively, for all groups. Only for SPM, we found that the mean values at flood tend to be slightly lower, which might be due to the inflow of relatively clear water from the North Sea.

2.6. Discussion

In-situ hyperspectral measurements recorded from fixed offshore platforms can be a cost-effective solution to provide continuous observations for long-term water quality monitoring (Zibordi et al., 2009, 2006). In this study, the two-stream radiative hydro-optical modeling of 2SeaColor was applied for the simultaneous retrieval of Chla, SPM and CDOM absorption from a time-series of in-situ R_{rs} measurements recorded between 2008 and 2018 at the NJS located at the Dutch Wadden Sea. Based on the results of this study, the 2SeaColor model shows a good performance in modeling water leaving reflectance spectra (Table 2.7) and retrieving Chla and SPM concentration values (Tables 2.8 and 2.9) using the implemented parameterization in this work (Table 2.2). The trends of retrieved Chla and SPM values (Figs. 2.4 and 2.5) show higher values of Chla (between 10 and 35 (mg m^{-3})) in spring and lower ones in winter (between 0 and 5 (mg m^{-3})), as well as low values of SPM in spring and summer (between 5 and 30 (g m^{-3})), and higher values (between 10 and 60 (g m^{-3})) in winter. These results are in agreement with previous studies for the long-term monitoring of Chla and SPM concentration variations during cruise measurements in the Dutch Wadden Sea (Hommersom, 2010; Hommersom et al., 2009).

Furthermore, the performed analysis in the present study revealed that the accuracy of the model deteriorates during winter when the SZA effect and seasonal pattern of WCCs play a role in the quality of in-situ R_{rs} measurements, affecting thereby the accuracy of the retrievals. The results of this study have significant implications for the assessment of the causes and the consequences of long-term WCC dynamics in the complex turbid waters of the Dutch Wadden Sea using ground-based measurements and satellite images as follows:

2.6.1. Water quality monitoring using in-situ measurements

The tidal effect evaluation of this study shows that the NJS is located at a favorable location at the Dutch Wadden Sea, where tides do not significantly influence WCCs (Table 2.10). This conclusion helps to investigate the monthly, seasonal and annual variation of WCCs retrieved by the 2SeaColor model from time series of in-situ R_{rs} measurements at the NJS, without concerns about the tidal effect on the variation of these WCCs. Otherwise, the studying of the temporal course would become very complicated. In other words, it is fortunate that tidal effects were small, since otherwise, we could hardly follow the seasonal courses. Once a hydro-optical model is considered sufficiently valid for WCC retrievals, its temporal predictions can be used for the long-term water quality monitoring at the Dutch Wadden Sea. The validated 2SeaColor model was applied to every fifteen minutes of in-situ R_{rs} measurements collected for more than one decade (from 2002 till present) at the NJS for the simultaneous retrieval of WCCs. These long-term retrievals can later be used to conduct the phenological analysis of Chla concentration and investigation of SPM variation at this area. Of particular interest when conducting Chla phenological analysis, is whether any significant decreasing trend from 2002 until present might indicate the influence of prior nutrient reduction management actions. This has remarkable applications for identifying positive anomaly occurrences and may operate as a warning for water management actions (Arabi et al., 2016). In addition, considering the fair accuracy of the 2SeaColor model (Tables 2.8 and 2.9), these accurate long-term observational baselines of SPM and Chla can be used as an indicator to check the accuracy of retrieved WCCs using other water retrieval algorithms in the complex Dutch Wadden Sea.

2.6.2. Water quality monitoring using satellite images

Using a hyperspectral optical model like 2SeaColor, which has been validated under different conditions, and coupling its output to an atmospheric Radiative Transfer (RT) model like MODTRAN following Arabi et al. (2016), allows generating TOA radiance signals for any hyperspectral or multispectral sensor, thus creating a flexible solution that can be applied with any given optical sensor system. The modeled TOA radiance data can next be used in an optimization loop to retrieve all relevant WCCs. Then we will be able to produce retrieved WCCs using satellite images of the Dutch Wadden Sea. Regarding the atmospheric correction, two approaches can be followed: either the atmospheric parameters (aerosol type and visibility) for the whole image are estimated first, and next applied to the whole image, or the atmospheric correction parameters are retrieved pixel by pixel, along with the WCCs, in which case the spatial variation of atmospheric properties is accommodated (Arabi et al., 2016; Shen and Verhoef, 2010). At present, there is a full archive of MERIS images of the Dutch Wadden Sea which have been captured from 2002 to 2012. In addition, there is free access to OLCI Sentinel-3 images of the Dutch Wadden Sea since February 2016 (Harvey et al., 2014). Therefore, producing WCC maps retrieved from time series of MERIS (from 2002 to 2012) and OLCI (2016 till present) images will be the next objective of this research. These maps can be used as baseline data for the long-term spatio-temporal monitoring of the area. However, due to the shallowness of large parts of the Dutch Wadden Sea, considering the bottom effect into the hydro-optical retrieval model to produce more reliable WCC maps from satellite images is recommended for these further studies.

2.7. Conclusion

From the performed analysis and evaluation of this study, we conclude that: (1) the 2SeaColor model is accurate enough to retrieve the concentrations of Chla and SPM during spring and summer for a period of three years (from 2008 to 2010) at the NJS located in the Dutch part of the Wadden Sea; (2) the 2SeaColor model's retrievals of Chla and SPM deteriorate in winter. For Chla, the levels of Chla during winter are too low to be well detectable, and for SPM the concentrations in winter are higher than in the rest of the year. It is therefore uncertain whether the worse results during winter are caused by the seasonal pattern of the concentrations, or by an SZA effect; (3) the SIOPs measured by Hommersom et al. (2009) were found valid for the retrieval of Chla and SPM concentrations. However, measuring seasonally varying SIOPs is recommended for further studies; (4) at the NJS the tide has little observable effects on the diurnal changes of SPM concentration.

Chapter 3 Remote sensing of water quality at the top of atmosphere level using satellite images*

* This chapter is based on:
Arabi, B., Salama, M.S., Wernand, M.R., Verhoef, W., 2016. MOD2SEA: A Coupled Atmosphere-Hydro-Optical Model for the Retrieval of Chlorophyll-a from Remote Sensing Observations in Complex Turbid Waters. Remote Sensing. 2016, 8(9), 722., https://doi.org/10.3390/rs8090722.

Arabi, B., Salama, S., Bayat, B., and Verhoef, W., 2016. Monitoring of Water Quality in High Turbid Waters Using Coupled Atmospheric-hydro-optical Models and Remote Sensing Observations (Case study: The Wadden Sea). AGU Ocean Science Meeting 2016, New Orleans, Louisiana, USA, 21-26 February 2016.

ABSTRACT

An accurate estimation of Chla concentration is crucial for water quality monitoring and is highly desired by various government agencies and environmental groups. However, using satellite observations for Chla estimation remains problematic over coastal waters due to their optical complexity and the critical atmospheric correction. In this study, we coupled an atmospheric and a water optical model for the simultaneous atmospheric correction and retrieval of Chla in the complex waters of the Wadden Sea. This coupled model called 2SeaColor-MODTRAN combines simulations from MODTRAN and the two-stream radiative transfer hydro-optical model 2SeaColor. The accuracy of the coupled 2SeaColor-MODTRAN model was validated using a matchup data set of MERIS observations and four years of concurrent in-situ measurements (2007–2010) at the NJS location in the Dutch part of the Wadden Sea. The results showed that MERIS-derived Chla from 2SeaColor-MODTRAN explained the variations of measured Chla with a determination coefficient of R^2 = 0.88 and an RMSE of 3.32 (mg m^{-3}), which means a significant improvement in comparison with the standard MERIS Case 2 regional (C2R) processor. The proposed coupled model might be used to generate a time series of reliable Chla maps, which is of profound importance for the assessment of causes and consequences of long-term phenological changes of Chla in the turbid Wadden Sea area.

3.1. Introduction

Effective management of water quality in coastal regions and turbid waters requires accurate information about WCC changes on prolonged time scales. Although this may sound simple, it is an extremely challenging task. One of the most important WCCs is Chla concentration, which is an important factor controlling light attenuation in the water column and is used as a measure of the eutrophic state (Le et al., 2013). Chla concentration is a very crucial factor to understanding the planetary carbon cycle (Casal et al., 2015) and is considered as an important indicator of eutrophication in marine ecosystems that may influence human life (Moradi and Kabiri, 2015; Werdell et al., 2009). Chla abundance can be affected by anthropogenic nutrient supply from industrial and agricultural sources, where simultaneously the aquaculture industries and fisheries are influenced by Chla abundance (Peters et al., 2004).

Long-term monitoring of Chla concentration using field measurements and laboratory analysis requires conventional cruise surveys with satisfactory temporal and spatial coverage. Unfortunately, this is often not feasible for most coastal regions due to lack of financial resources and technical equipment while it is impossible in practice to collect in-situ measurements for the whole regions using cruise measurements.

The spatio-temporal coverage provided by remote sensing can considerably overcome some of these deficits in the current in-situ monitoring programs for WCCs (Van der Woerd and Pasterkamp, 2004). Satellite ocean color is especially important since it is the only remotely sensed property that directly identifies a biological component of the ecosystem (Casal et al., 2015). Regarding the spatial and temporal sampling capabilities of satellite data, remote sensing of ocean color is considered as the principal source of data for investigating long-term changes in Chla concentration and phytoplankton biomass in many coastal areas' estuaries (Le et al., 2013b).

The maintenance of a good environmental status in European coastal regions and sea has become a crucial concern embodied in European regulations (Marine Strategy Framework Directive, Directive 2008/56/EC of the European Parliament and the Council, "establishing a framework for community action in the field of marine environmental policy") (Mélin et al., 2011). One of the most important European coastal zones which have aroused increasing attention from all of Europe is the Wadden Sea. For the assessment of the current role of the Wadden Sea as a source of Chla and organic matter, and for the ongoing discussion on eutrophication problem areas, it is of great interest to obtain more detailed knowledge on the phytoplankton and Chla changes and their regulating factors in this turbid coastal region of the North Sea (Hommersom et al., 2010). In addition, monitoring of this area is mandatory due to its nature reserve status and its July 2009 inclusion on the UNESCO World Heritage List (Hommersom, 2010a). Recently some research into the analysis of long-term variations and trends in the optically active substances (Chla, SPM, CDOM) and watercolor changes using in-situ measurements have been conducted over different parts of the Wadden Sea (Hommersom et al., 2009; Philippart et al., 2013, 2007; Poremba et al., 1999). However, using satellite observations for Chla estimation remains problematic in this area due to its optical complexity and the critical application of an accurate atmospheric correction. Recent efforts show that researchers are confronted with two main problems in improving the accuracy of derived water parameter concentration using remote sensing techniques in the Wadden Sea. First, most atmospheric correction methods fail in this region (Bartholdy and Folving, 1986; Gemein et al., 2006). Second, the general water property retrieval models do not work well in this complex turbid water (Hommersom and Researcher, 2015). Thus, the main purpose of this research is to tackle these two problems aiming to increase the accuracy of Chla concentration retrieval from earth observation data in this area.

3.1.1. Atmospheric correction

Quality of the atmospheric correction is one of the most limiting factors for the accurate retrieval of water constituents from earth observation data in coastal waters (Schroeder et al., 2007). The standard atmospheric correction method by Gordon and Wang (Gordon and Wang, 1994) assumes a zero water-leaving reflectance due to high absorption by seawater in the NIR and can be performed by extrapolating the aerosol optical properties to the visible from the NIR spectral region (Goyens et al., 2013). This is not always the case when in turbid waters (which often are optically complex) (Jamet et al., 2011), higher concentrations of Chla and SPM can cause a significant water-leaving reflectance in the NIR (Siegel et al., 2000). Indeed, most of the atmospheric correction methods fail in these areas due to the complexity of the recorded TOA radiance signal at satellite images (Carpintero et al., 2015) as these signals are associated with aerosols from continental sources (Mélin et al., 2007). In addition, in coastal waters, photons from nearby land areas can enter the field-of-view of the sensor (the adjacency effect) and contribute to total NIR backscatter (Santer and Schmechtig, 2000), whereas in shallow waters, TOA radiances can also be influenced by the bottom effect.

Consequently, the black pixel assumption tends to overestimate the aerosol scattered radiance and thus underestimates the water-leaving radiance in these areas (IOCCG, 2000). In recent years, some studies have been conducted to improve the atmospheric correction over turbid waters (Hu et al., 2000; Ruddick et al., 2006; Wang et al., 2009). For example, some efforts were made to improve the atmospheric correction method by assuming a zero water-leaving reflectance in the shortwave infrared, even in the case of highly turbid waters (Wang, 2007, 2005). However, in further studies, researchers found that for extremely high turbidities, even in the shortwave infrared region, the water-leaving reflectance was not absolutely equal to zero (Wang et al., 2011). In addition, other studies focused on the non-negligible water-leaving reflectance assumption in the NIR (Carder et al., 2002; Doxaran et al., 2014; Salama and Shen, 2010). For example, Carder et al. (2002) investigated the ratio of water-leaving reflectance at two NIR bands. This ratio was either assumed constant (Gould et al., 1999) or estimated from neighboring pixels of open oceans (Ruddick et al., 2000). Although the assumption of a known relationship between the values of water-leaving reflectance in two NIR bands is necessary, it is not sufficient. Indeed, accurate information about visibility and aerosol type is still needed (Salama and Shen, 2010). Shen et al. (2010) used the radiative transfer model MODTRAN to perform atmospheric correction for MERIS images over highly turbid waters. As shown by Verhoef and Bach (2007), for assumed visibility and aerosol type, MODTRAN can be used to extract the necessary atmospheric properties to remove the scattering and absorption effects of the atmosphere and to obtain calibrated surface reflectance, as well as correcting the adjacency effects. However, this technique assumes a spatially homogeneous atmosphere (Shen and Verhoef, 2010), while in reality not only visibility but also the aerosol type may vary spatially within the extent of satellite images (in the presence of local haze variations). For example, in the case of coastal waters, some aerosol types (*e.g.,* urban or rural) might exist in the regions close to the land, and other pixels might have the maritime aerosol type.

Consequently, the assumption of a homogeneous atmosphere may lead to the wrong establishment of visibility and aerosol model in different parts of the image and may result in overestimation or underestimation of WCCs from ocean-color observations. The C2R processor provided by ESA for MERIS L1 products in the MERIS regional coastal and case 2 water projects (Koponen et al., 2007), performs atmospheric correction pixel by pixel and contains procedures for determining inherent optical properties that are delivered as MERIS L2 products, including reflectance, inherent optical properties (IOPs), and water quality parameters . However, the C2R processor may be invalid for very Chlorophyll-rich waters like some eutrophic lakes (Duan et al., 2012) and for highly turbid waters (Shen et al., 2010). In this paper, by applying radiative transfer modeling for the non-homogeneous atmosphere and comparing the results with the C2R processor, we tried to improve the atmospheric correction technique over this coastal area.

3.1.2. Hydro-Optical model

After improving the atmospheric correction technique, WCC-dependent optical modeling of turbid waters is the next step. Improving the accuracy of water properties retrievals in coastal waters requires generic models that can be applied to these complex water bodies. For open oceans, estimation of Chla from earth observation data is well established (O'Reilly et al., 1998). An empirical algorithm is in use that, with slight modifications for the actual band settings, has proven to work well for instruments like SeaWiFS (Sea-Viewing Wide Field-of-View Sensor), MODIS and MERIS (Arnone et al., 2006; Dasgupta et al., 2009; O'Reilly and Maritorena, 2000). However, satellite estimation of Chla concentration is still difficult for coastal waters, where Chla, SPM, and CDOM occur in various mixtures which complicate the derivation of their concentrations from reflectance observations (Salama et al., 2012). Therefore, there is a pressing need to develop, implement and validate a self-consistent, generic and operational retrieval model of water quality in turbid waters.

In this study, the forward analytical model of 2SeaColor (Salama and Verhoef, 2015) was applied for the first time to retrieve Chla concentration in the Wadden Sea. The 2SeaColor model is based on the solution of the two-stream radiative transfer equations for incident sunlight and also performs well for turbid waters, while the commonly applied water quality algorithms might suffer from saturation in the presence of high turbidity.

After defining the main problems of remote sensing of coastal waters described above, and motivated by the need for a high-quality, satellite-based long-term Chla retrieval in the turbid waters of the Wadden Sea, this research focused on the following objectives: (1) improving the accuracy of Chla concentration (mg m^{-3}) retrieval from MERIS data by applying the coupled 2SeaColor-MODTRAN model for the Wadden Sea and (2) comparing the accuracy of the coupled 2SeaCoLoR-MODTRAN in performing atmospheric correction and retrieving Chla concentration values with the ESA standard C2R processor. The paper is arranged as follows: the case study is described first. Then, the datasets used for C2R and MODTRAN simulations as well as the 2SeaColor model are briefly introduced. Next, we validate the derived Chla concentration and water-leaving reflectance values for both 2SeaColo-MODTRAN and C2R processor against the in-situ measurements at the NJS. Then, we evaluate the remote sensing (2SeaColor-MODTRAN and C2R) retrievals and compare the variation of 2SeaColor-MODTRAN results with similar in-situ studies in the Wadden Sea. Finally, we suggest some recommendations for further remote sensing studies in complex turbid waters like the Wadden Sea and discuss the applicability of this approach to other estuaries and satellite ocean color missions.

3.2. Materials and methods

3.2.1. Study area

The Dutch Wadden Sea is a coastal area located between the mainland of the Netherlands and the North Sea. The area is located between the Marsdiep near Den Helder in the southwest and the Dollard near Groningen in the northeast and comprises a surface area of 2,500 km^2 (Figure 3.1). This region is a shallow, well-mixed tidal area that consists of several separated tidal basins. Each basin comprises tidal flats, subtidal areas, and channels. Basins are connected to the adjacent North Sea by relatively narrow and deep tidal inlets between the barrier islands (Zimmerman, 1976).

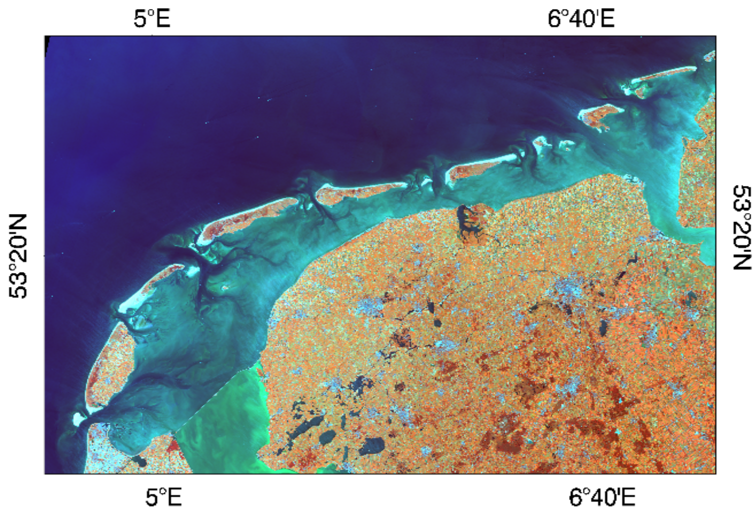

Figure 3.1. One Landsat-8 OLI image covering the Dutch Wadden Sea and parts of IJsselmeer lake acquired on 20 July 2016 (Color composite of red: band-5, green: band-3 and blue: band-1).

The high near-surface concentrations of water constituents, as well as the spatial, tidal and seasonal variations of the optically active substances (Chla, SPM, and CDOM), make this region an optically very complex area and a good representative for remote sensing studies in turbid coastal waters (Hommersom, 2010a).

3.2.2. In-situ dataset

The in-situ data have been extensively used to investigate the accuracy of remote sensing radiometric products (i.e., the remote sensing reflectance) from the recorded TOA radiance in satellite observations like MERIS images (Zibordi et al., 2011). In this study, the in-situ above-water radiometric dataset was provided by the research jetty of the Royal Netherlands Institute for Sea Research (NIOZ) at Texel, located in the Dutch part of the Wadden

Sea. Every quarter of an hour, radiometric color measurements of the water, sun, and sky (including meteorological conditions), as well as Chla and mineral concentration, were recorded for over a decade. The data were collected at the NJS (53°00’06”N; 4°47’21”E) (Ly et al., 2014), where the newest generation of hyperspectral radiometers was installed for “autonomous” monitoring of the Wadden Sea from 2001 until the present (Wernand, 2011). The footprint size of the radiometer is less than a meter, and the viewing direction is not nadir but oblique, so the measurements on the ground are only partially representative of the nadir water reflectance from 300 m pixels as sensed by MERIS.

(a)

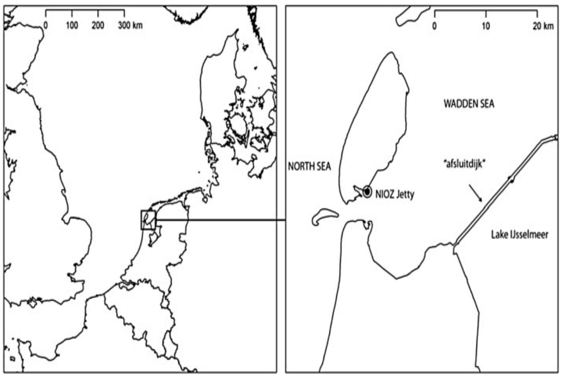

(b)

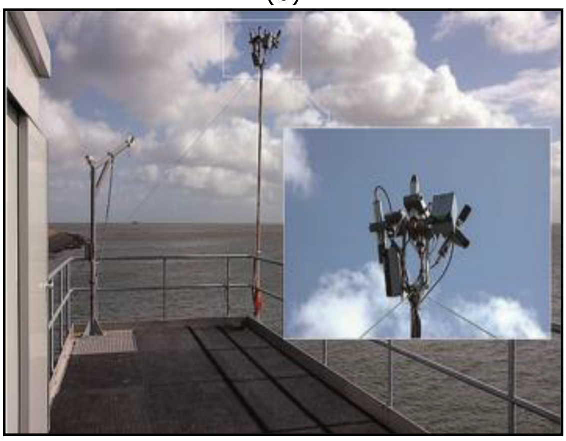

Figure 3.2 (a) The location at the NJS sampling station in the western part of the Dutch Wadden Sea; (b) The optical system mounted on a pole on the platform of the NJS in the Wadden Sea (Wernand, 2011).

In addition, SIOPs of water constituents in the Wadden Sea were obtained from Hommersom et al. (Hommersom et al., 2009), who documented SIOP measurements in 2007 at 37 stations in this area.

3.2.3. Satellite images

The MERIS sensor, operational on board the European environmental satellite ENVISAT between 2002–2012, was primarily intended for the ocean, coastal and continental water remote sensing. MERIS was an orbital sensor with 15 bands covering the spectral range from 400 nm to 950 nm and was succeeded by OLCI on board Sentinel-3 beyond 2015 (Zibordi et al., 2009). The high sensitivity and large dynamic range of the MERIS sensor have been widely used for ocean and coastal water remote sensing (Zibordi et al., 2013, 2006). In this study, ocean color data were obtained from ESA archive of MERIS images (full resolution: 300 m) covering the Wadden Sea during 2002–2012 (data provided by European Space Agency). MERIS has a revisit time of three days over the Dutch Wadden Sea at around 10:30 a.m. local time. The MERIS 1b image provides TOA radiance information and some environmental parameters for each pixel. Some of these environmental parameters (such as SZA, VZA, relative azimuth angle (RAA), water vapor (H_2O) and ozone (O_3)) were used as input parameters to perform MODTRAN simulations in this study.

3.2.4. In-situ and satellite images data matchups

Validation of ocean color products (i.e., IOPs and water-leaving radiance), theoretically, should be performed from in-situ measurements acquired simultaneously to the satellite overpass over the same location (the so-called matchup points) (Loisel et al., 2013). In this study, the following criteria were used to find matchup points between satellite observations and in-situ measurements: (1) all available MERIS images over the Dutch part of Wadden Sea between 2002 and 2012 were checked to select the cloud-free images; (2) a narrow time window of ±1 h was used; (3) five-by-five pixel kernels centered on the in-situ measurement coordinates were then extracted from the MERIS images using BEAM software (version 5.0) (no aggregation method was used to avoid possible spectral contamination); (4) finally, 35 suitable MERIS images were concurrent with in-situ-measured concentrations of Chla at the NJS during 2007–2010.

3.3. Methodology

The accuracy of the coupled 2SeaColor-MODTRAN model in doing the atmospheric correction and deriving Chla concentration values was evaluated against in-situ measurements and was compared with C2R results.

3.3.1. The Coupled 2SeaColor-MODTRAN model

The developed 2SeaColor-MODTRAN method combined two look-up tables (LUTs) from 2SeaColor and MODTRAN as schematically shown in Fig 3.3.

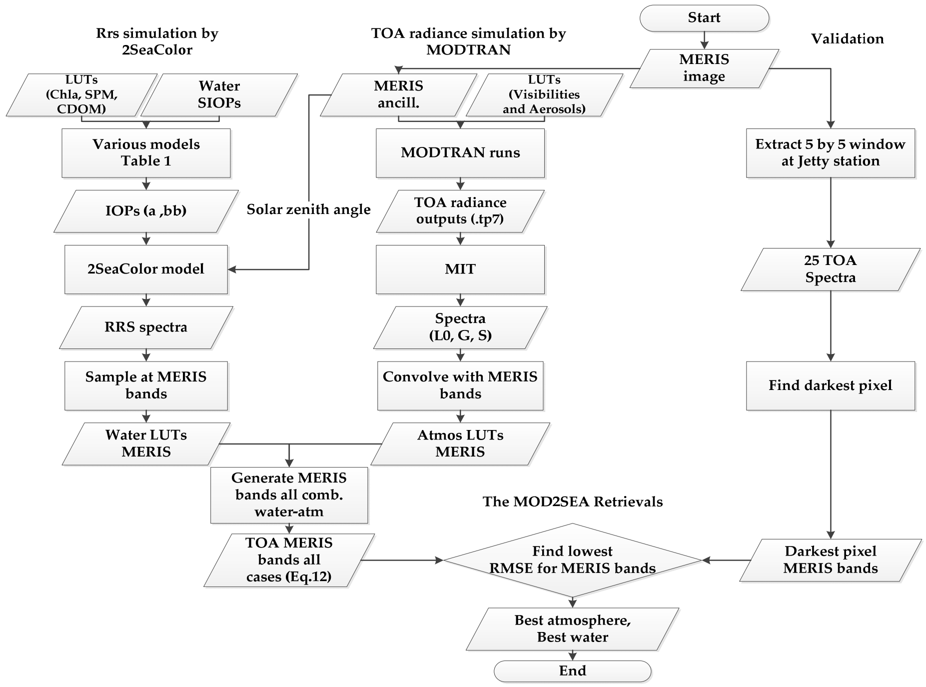

Figure 3.3. Diagram of the coupled 2SeaColor-MODTRAN model (pixel-based).

These LUTs were generated by simulating the water-leaving reflectance for varying ranges of the governing biophysical variables (with respect to the range of these WCCs at the NJS (Table 3.1)) and MODTRAN parameters based on different combinations of visibilities and aerosol models at specific viewing-illumination geometries for every MERIS image, separately. Table 3.1 presents the LUT composition of the 2SeaColor model and the MODTRAN input variables in this assessment.

Table 3.1. Lookup table composition of 2SeaColor-MODTRAN model.

LUT Variables	Range	Increment	Unit
Chla	0 - 150	5, 0.1	mg m^{-3}
SPM	0 – 150	5; 0.1	g m^{3}
CDOM absorption	0 – 2.5	1; 0.1	m^{-1}
Visibility	5 – 50	1	km
Aerosol type	Rural, Maritime, Urban	-	-

The details on the simulation of R_{rs} by the 2SeaColor model and TOA radiance by the MODTRAN radiative transfer code are described as follows:

3.3.1.1. Reflectance simulation by the 2SeaColor forward model

The 2SeaColor model is based on the solution of the two-stream radiative transfer equations including direct sunlight, as described by Duntley (1942, 1963) (Duntley, 1963, 1941). Both the analytical forward model and the inversion scheme are provided in detail in Salama and Verhoef (Salama and

Verhoef, 2015). The reflectance result predicted by the 2SeaColor model is r_{sd}^{∞}, the directional-hemispherical reflectance of the semi-infinite medium, which is linked to IOPs by Salama and Verhoef (2015):

$$r_{sd}^{\infty} = \frac{\sqrt{1+2x}-1}{\sqrt{1+2x}+2\mu_w} \tag{3.1}$$

where x is the ratio of backscattering to absorption coefficients ($x = b_b/a$), and μ_w is the cosine of the SZA beneath the water surface. The reflectance factor r_{sd}^{∞} can be approximated by $Q \times R(0^-)$ under sunny conditions, where Q = 3.25 and $R(0^-)$ is the irradiance reflectance beneath the surface (Maritorena et al., 1994), which can be converted to above-surface remote sensing reflectance (R_{rs}) by Lee et al. (2002).

$$R_{rs} = \frac{0.52R(0^-)}{Q-1.7R(0^-)} \tag{3.2}$$

Total absorption and backscattering coefficient of water constituents (a and b_b) were calculated using Eqs. (3.3) and (3.4) respectively (Hu et al., 2000; IOCCG, 2000).

$$a(\lambda) = a_W(\lambda)+a_{Chla}(\lambda) + a_{NAP}(\lambda) + a_{CDOM}(\lambda) \tag{3.3}$$

$$b_b(\lambda) = b_{bw}(\lambda) + b_{b,Chla}(\lambda) + b_{b,NAP}(\lambda) \tag{3.4}$$

where the subscripts W, Chla, NAP and CDOM stand for water molecules, Chlorophyll, non-algae particles and colored dissolved organic matter, respectively, as implemented in Suhyb Salama and Shen (2010), the absorption coefficients of the water constituents (*a*) are parameterized by Bricaud et al. (1981) and Lee et al. (1999, 1998). Also, the backscattering coefficients of the water constituents (b_b) were parametrized by Doxaran et al. (2009) and Morel and Maritorena (2001).

Table 3.2. Summary of the used parameterizations

Variable	Parametrization	Ref.	Eq.
Chla absorption	$a_{Chla}(\lambda) = [a_0(\lambda) + a_1(\lambda) \times ln\, a_{Chla}(443)] \times a_{Chla}(443)$ $a_{Chla}(443) = 0.06 \times [Chla]^{0.65}$	(Lee et al., 1999)	(3.5)
CDOM absorption	$a_{CDOM}(\lambda) = a_{CDOM}(440) \times exp[-S_{CDOM}(\lambda - 440)]$	(Bricaud et al., 1981)	(3.6)
NAP absorption	$a_{NAP}(\lambda) = a_{NAP}(440) \times exp[-S_{NAP} \times (\lambda - 440)]$ $a_{NAP}(440) = a^{*}_{NAP}(440) \times [SPM]$	(Lee et al., 1998)	(3.7)
Chla backscattering	$b_{b,Chla}(\lambda) = \{0.002 + 0.01 \times [0.5 - 0.25 \times log_{10}[Chla] \times \left(\frac{\lambda}{550}\right)^{n}]\} \times b_{b,Chla}(550)$ $b_{b,Chla}(550) = 0.416 \times [Chla]^{0.766}$	(Morel and Maritorena, 2001)	(3.8)
NAP backscattering	$b_{NAP}(\lambda) = b_{NAP}(550) \times (\frac{550}{\lambda})^{-\gamma} - [1 - tanh(0.5 \times \gamma^2)] \times a_{NAP}(\lambda)$ $b_{NAP}(550) = b^{*}_{NAP}(550) \times I \times [SPM]$	(Doxaran et al., 2009)	(3.9)
Scattering of water molecules	$b_{bw}(\lambda)$; Listed values, Table (3.8), page 104.	(Mobley, 1994)	(3.10)
Absorption of water molecules	$a_w(\lambda)$; Listed values	(Pope and Fry, 1997)	(3.11)

In Table 3.2, [Chla], [SPM] and $a_{CDOM}(440)$ stand for Chla concentration, SPM concentration and the CDOM absorption at 440 nm, respectively. The absorption and backscattering coefficients of water molecules (a_w and b_{bw}) were taken from previous studies (Lee et al., 1998; Mobley, 1994; Pope and Fry, 1997) and a_0 and a_1 were given in Lee et al. (1998). The initial values of non-algae particle absorption ($a^*_{NAP}(440)$ = 0.036 ($m^2\ g^{-1}$)), spectral slope of non-algae particles (S_{NAP}= 0.011 (nm^{-1})), spectral slope of CDOM (S_{CDOM}= 0.013 (nm^{-1})) and specific scattering coefficient of non-algae particles ($b^*_{NAP}(550)$ = 0.282) were taken from Hommersom et al. (2009) SIOP measurements at 37 stations in the Wadden Sea. Also, the initial values of γ and I (γ = 0.6 and I = 0.019) for the North Sea were taken from Doxaran et al. (2009) and Petzold (1972), respectively. In this study, we used the 2Seacolor forward model and the various parameterizations described in Table 3.2 to simulate the water-leaving reflectance (R_{rs} spectra) values for a series of combinations of Chla, SPM and CDOM concentration (Table 3.1) and for the given SZA associated with every MERIS image, separately. The simulated values of R_{rs} spectra for all MERIS bands were stored in a water LUT for the MERIS bands and then used as R_{rs} input parameters for MODTRAN to calculate the TOA radiances in the MERIS bands.

3.3.1.2. TOA radiance simulation by MODTRAN

MODTRAN is the successor of the atmospheric radiative transfer model LOWTRAN (Kneizys et al., 1988). It is publicly available from the Air Force Research Laboratory in the USA. The latest version of MODTRAN (5.2.1) contains large spectral databases of the extraterrestrial solar irradiance and the absorption of all relevant atmospheric gases at a high spectral resolution. The accurate calculation of multiple atmospheric scattering makes it a very appropriate tool for reliable simulation and interpretation of remote sensing problems in the optical and thermal spectral regions (Verhoef and Bach, 2003). To apply MODTRAN simulations, first of all, several parameters describing the real atmospheric conditions should be determined as inputs for this model. Table 3.3 shows the standard definition of MODTRAN inputs with respect to the ranges of average values of atmospheric and geometric variables variation over one image for four years of all available MERIS images between 2007 and 2010 over the Dutch part of the Wadden Sea. In the MERIS image, some of the local atmospheric (O_3, H_2O) and geometric variables (VZA, SZA, and RAA) can be used as input for MODTRAN. Note that for every MERIS image a separate input file was created by establishing the local atmospheric (O_3, H_2O, CO_2) and geometric variables (VZA, SZA, RAA) of that specific run to MODTRAN (Fig 3.3). These parameters could be retrieved from MERIS ancillary data per pixel using Matlab.

Table 3.3. Input parameters for MODTRAN4 simulations.

Parameter	Range or Value	Unit
Atmospheric profile	Mid Latitude Summer	-
Correlated-k option	Yes	-
DISORT number of streams	8	-
Concentration of CO_2[1]	380 – 390	ppm
H_2O	0.5 – 4.5	g cm^{-2}
O^3	250 – 450	DU
SZA	30 – 80	degree
VZA	5 – 30	degree
RAA	0 – 150	degree
Visibility	5 – 50 (1 km increment)	km
Aerosol Model	Rural, Maritime, Urban	-
Surface height	0	km
Sensor Height	800	km
Molecular band model resolution	1.0	cm^{-1}
Start, ending wavelength	350−1000	nm

[1] Annual CO_2 concentration level can be in Global Greenhouse Reference Network Global Greenhouse Reference Network 2017. Available online: http://www.esrl.noaa.gov/gmd/ccgg/.

In this study, we varied the aerosol type (rural, maritime and urban) and visibility (5 to 50 km with 1 km step) and thus made a total of 135 scenarios for each LUT and given atmospheric state and angular geometry, which were extracted from the MERIS image ancillary data per image. For each scenario, the MODTRAN Interrogation Technique (MIT) was applied by using surface albedos of 0.0, 0.5 and 1.0 (the MIT technique is explained in detail by Verhoef and Bach, (2003)). The output .tp7 file of MODTRAN quantified the TOA radiance spectrum for each simulated wavelength from 350 nm to 1000 nm. Then in the MIT, the .tp7 file was used as input to derive three MODTRAN parameters (gain factor (G), path radiance (L_0), and spherical albedo (S)). These parameters are spectral variables depending on various atmospheric conditions Verhoef and Bach (2003). The spectral response functions (SRF) of the MERIS bands were convolved with the MODTRAN parameters to compute L_0, G and S for every MERIS band and these simulations were stored in the atmospheric LUTs (Atmos LUTs MERIS).

3.3.1.3. The 2SeaColor-MODTRAN retrievals

The simulated TOA radiance of MERIS data in the MODTRAN output file, L_{TOA} (Wm^{-2} sr^{-1} μm^{-1}), Can be expressed in surface reflectance r by the following equation (Berk et al., 2011):

$$L_{\mathrm{TOA}} = L_0 + \frac{Gr}{1 - Sr} \qquad (3.12)$$

where r is the hemispherical reflectance (= πR_{rs}) leaving the water surface, L_0 is the total radiance for zero surface albedo (Wm^{-2} sr^{-1} μm^{-1}), S is the spherical albedo of the atmosphere and G is the overall gain factor. In this study, the LUTs of water-leaving reflectance generated by the 2SeaColor model were used as R_{rs} input parameters of Equation (3.12) to calculate TOA radiance for all combinations of water properties and atmospheric conditions and then organized in a water-atmosphere LUT (water-atmosphere). The simultaneous retrieval of Chla, SPM, CDOM concentration, aerosol type, and visibility was then performed by spectrally fitting the 2SeaColor-MODTRAN-simulated TOA radiances (using RMSE) to MERIS TOA radiances for all MERIS bands except the band numbers 1, 2 and 11. Band 11 is located in the O_2-A absorption band and can give erroneous results due to sampling errors of MERIS. Bands 1 and 2 gave systematic deviations in R_{rs} after atmospheric correction. The cause of this problem is presently still unknown. In this retrieval, Chla retrieval using the coupled 2SeaColor-MODTRAN model was performed in two steps. First the increments of 5, 5 and 1 were taken for Chla concentration (mg m^{-3}), SPM concentration (g m^{-3}) and CDOM absorption at 440 nm (m^{-1}), respectively, to find an approximate solution. Later, in the refined step, the step size of the LUTs composition was reduced to 0.1 for all water constituents in the identified rough range resulting from the first step. Applying this approach led to speeding up the running of the Matlab code and to obtain more precise results. Although Fig. 3.3 suggests the storage of a fixed LUT for water R_{rs} for each MERIS image, this LUT was only generated in a loop, and not stored, in order to reduce memory requirements. The best fitting combination of water properties and atmospheric conditions was found during the generation of the water LUT, but this water LUT was never stored as such, contrary to the atmospheric LUT, which was actually stored. This approach also allowed greater flexibility by applying the two-step procedure in finding the best-fitting water properties, by first applying a rough search in the first round with large steps in the three concentrations, and in the next round a refined search with small steps over much smaller ranges. It should be noted that the current procedure applied to a single pixel per matchup date is not suitable to be applied pixel by pixel, and this issue is left for a future study.

3.3.2. MERIS Case-2 regional processor

The C2R (Doerffer and Schiller, 2007), available in the Basis ERS and ENVISAT (A) ATSR and MERIS Toolbox (BEAM) software, has been widely used to derive WCCs from MERIS images (Ambarwulan et al., 2012; Attila et al., 2013; Beltrán-Abaunza et al., 2014; Smith et al., 2013). The C2R processor consists of two procedures, one for atmospheric correction and one for the bio-optical part for retrieving the IOPs of water columns. The Neural Networks (NNs) in C2R were trained with Hydrolight (Mobley, 1994) simulations and in-situ measurements in the German bight and from other cruises in European seas. More details can be found in (Doerffer and Schiller, 2007). The output of the C2R processor, including IOPs: the absorption coefficient of Chla at wavelength 443 nm (a_{Chla} (443)), the absorption coefficient of CDOM (a_{CDOM} (443)), the total absorption (a_{tot} (443)), and the scattering coefficient of SPM (b_{SPM} (443)) were then used to define WCCs such as Chla and SPM. Equations to relate

BEAM processor IOPs to water quality concentrations of Chla and SPM are presented as follows:

$$[Chla] = 21 \times a_{Chla}(443)^{1.04} \qquad (3.13)$$

$$[SPM] = 1.72 \times b_{SPM}(443) \qquad (3.14)$$

where [Chla], [SPM], $a_{chla}(443)$ and $b_{SPM}(443)$ stand for Chla concentration, SPM concentration, the Chla absorption at 443 nm and SPM scattering coefficient at 443 nm, respectively.

3.3.3. Validation

To evaluate the accuracy of the coupled 2SeaColor-MODTRAN model and the C2R processor, we applied these two models to the 35 matchup moments of MERIS observations and four years of concurrent Chla measurements (2007–2010) at the NJS, separately. The validation of model simulations was performed in two different levels of atmospheric correction and water retrieval models. Since the NJS is located close to the land, for every image, the darkest pixel from 5 by 5 pixels around the location of this station was extracted first. By selecting the darkest pixel from the 5 × 5 neighborhood centered on the jetty station, we exclude cloudy and land pixels, as well as water pixels close to the shore that are possibly influenced by an adjacency effect due to the near land area. Of course, an underlying assumption in our approach is that the water of the darkest pixel has the same composition as found at the location of the jetty station. However, since the water current is mostly strong near the inlet to the Wadden Sea, we are confident that the water is well-mixed, and local gradients in water properties are small.

3.3.3.1. Atmospheric correction

The accuracy of atmospheric correction methods using the coupled 2SeaColor-MODTRAN model and C2R processor was evaluated against the in-situ water-leaving reflectance for all 35 matchups between 2007 and 2010 at the NJS. Four statistical parameters, the RMSE, R^2, the normalized root mean square error (NRMSE) and relative root mean square error (RRMSE) were used to quantify the goodness-of-fit between derived and measured water-leaving reflectance values at the NJS data where near-concurrent (±1 h) MERIS measurements were available. To do this, three MERIS bands 3, 5 and 7 were selected. Finally, the accuracy of the proposed 2SeaColor-MODTRAN model in doing atmospheric correction was compared against C2R processor products. The results of this assessment are presented in section 3.4.2.

3.3.3.2. Water model inversion

The accuracy of retrieved Chla concentration values using the coupled 2SeaColor-MODTRAN model and the C2R processor were evaluated against in-situ Chla measurements for all 35 matchup points at the NJS between 2007 and 2010. The results of this evaluation are presented in section 3.4.3. It should be mentioned that in view of the main objective of this study (retrieval of Chla concentration), investigation of changes in other water constituents (SPM and CDOM concentration) was considered to fall outside of the scope of this study, although these were retrieved along with Chla using 2SeaColor-MODTRAN. In addition, the visibility and aerosol type were retrieved simultaneously with WCCs which were used in the model to simulate water-leaving reflectance values based on the best matching TOA radiance by 2SeaColor-MODTRAN coupled model.

3.4. Results

3.4.1. The MODTRAN simulations

The case of the three aerosol types (i.e., rural, maritime and urban) for visibility of 20 km on 7 October 2007 was used as an example to display the result of applying MODTRAN to the MERIS bands for three atmospheric conditions. We used the MIT method (Verhoef and Bach, 2003) to derive L_0, G and S values using surface albedos of 0.0, 0.5 and 1.0 for the mentioned visibilities and aerosol types in these figures.

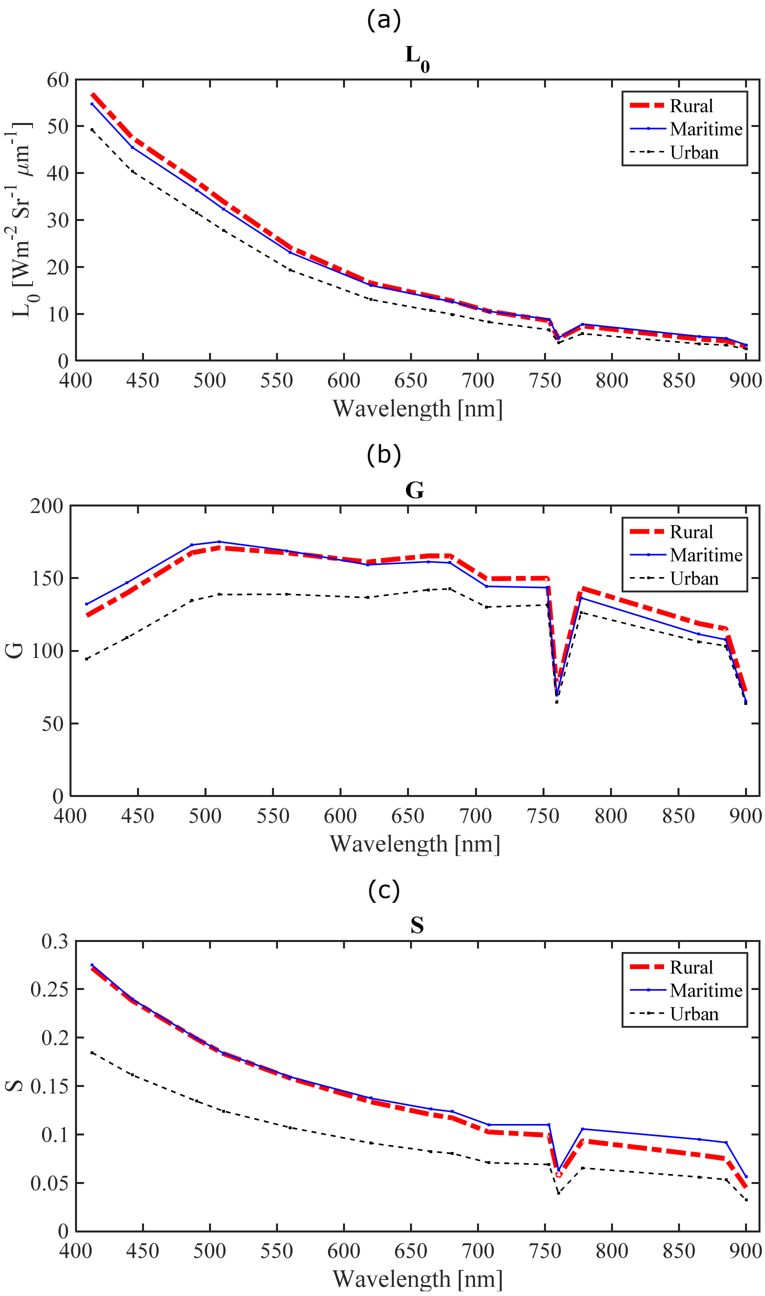

Figure 3.4. (a to c) L_0, *G* and *S* values at the visibility of 20 km and different aerosol types; (d) The atmospheric parameters L_0, *S,* and *G* for the maritime aerosol type and a visibility of 20 km.

The atmospheric path radiance L_0 represents the case when the surface reflectance is zero, and the radiance at the top of the atmosphere comes from atmospheric scattering alone. As Fig. 3.4 shows, L_0 values decrease with wavelength, which means at longer wavelengths the atmosphere scatters less. The S presents the spherical albedo values which are not large and show a similar trend to L_0. The gain factor G contains the product of the extraterrestrial solar irradiance and the total two-way transmittance through the atmosphere and shows a maximum at about 500 nm. L_0, G and S vary with different combinations of aerosol types and visibilities, while for maritime and rural aerosol types, they have similar values. The urban aerosol model has a stronger absorption and always has lower values when compared to the other two aerosol models. Examples of the MODTRAN path radiance simulations (L_0) from 7 October 2007, for visibilities of 5, 10 and 40 km while water-leaving reflectance is zero as representative for a range of haze conditions and three different aerosol models are presented in Fig. 3.5.

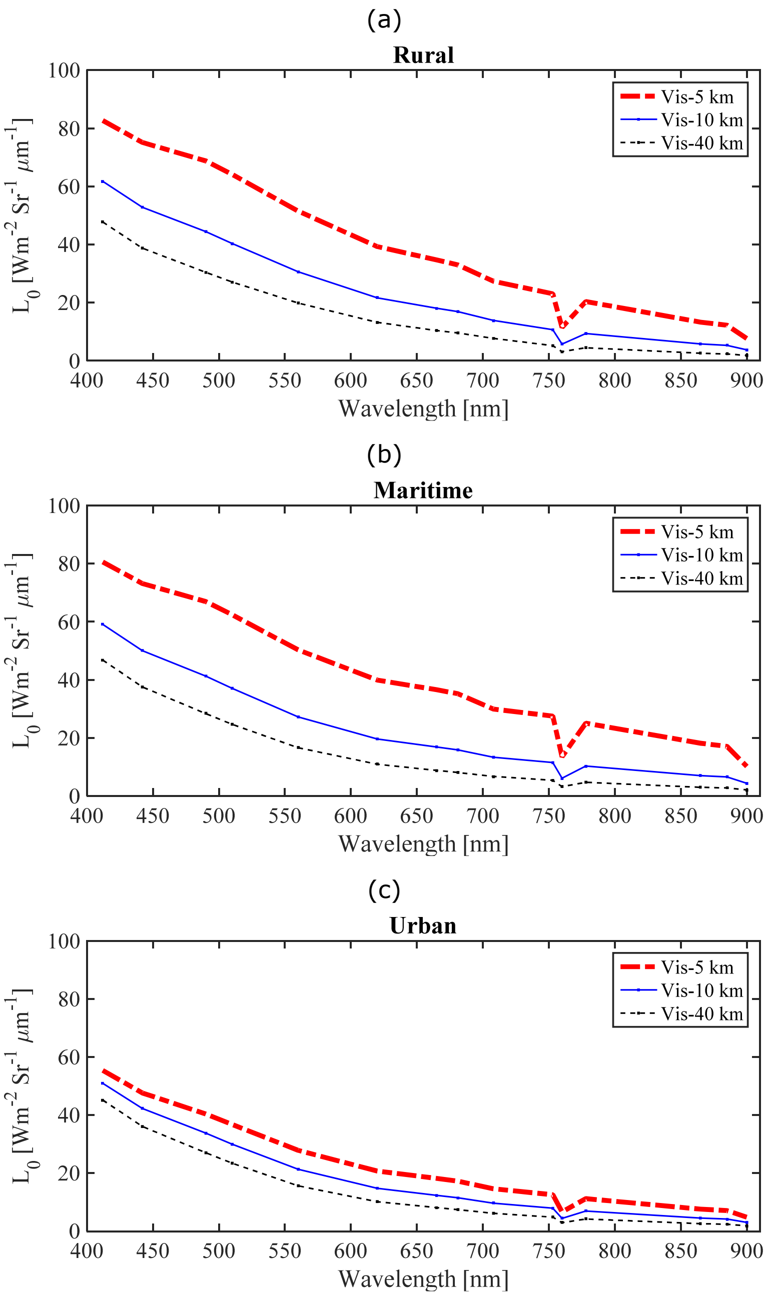

Figure 3.5. TOA radiance simulated by MODTRAN for (a) rural, (b) maritime and (c) urban aerosol types respectively.

As this figure shows, the calculated TOA radiances for the urban aerosol type show a lower range of variation compared to the maritime and rural cases. All the values of TOA radiance for the urban aerosol type are between 0 and 60

(Wm^{-2} sr^{-1} μm^{-1}), while these values for maritime and rural ones vary between 0 and 80 (Wm^{-2} sr^{-1} μm^{-1}). On the other hand, the simulated TOA radiances by MODTRAN differ significantly not only with the aerosol type but also with visibility. Lower visibility gives higher TOA radiances. Consequently, a wrong assumption about visibility or aerosol type leads to a wrong calculation of water-leaving reflectance and as a result, the water parameter concentrations may be overestimated or underestimated.

3.4.1.1. Atmospheric correction validation

The results of performing of the coupled 2SeaColor-MODTRAN model and the ESA MERIS standard C2R processor to derive water-leaving reflectances for MERIS bands of 3, 5 and 7 against in-situ measurements are shown in Fig. 3.6. The statistical analysis regarding this assessment is presented in Table 3.4.

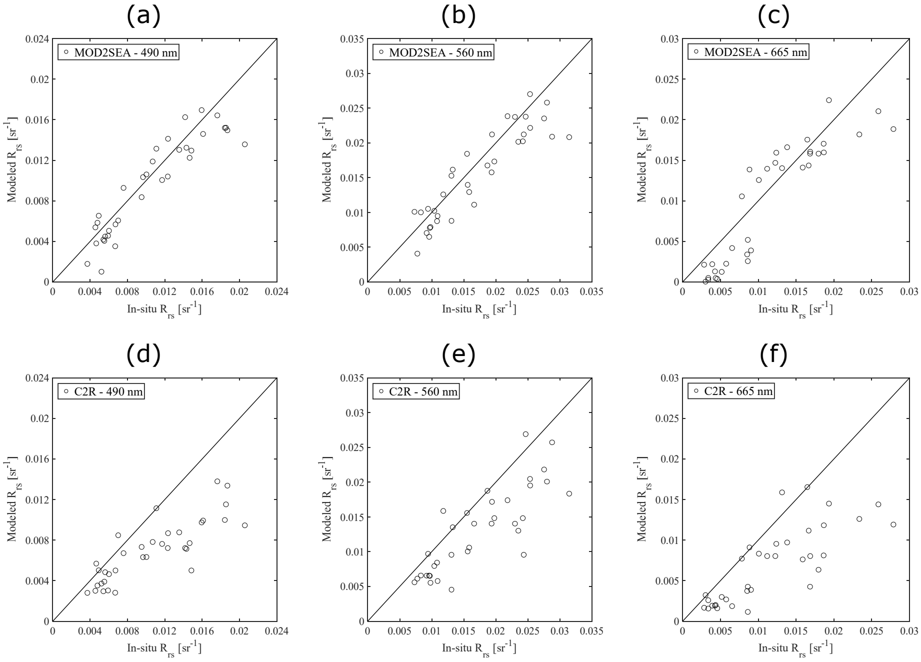

Figure 3.6 Comparison between MERIS-retrieved values and in-situ measurements for R_{rs} for 35 matchups in 2007−2010 at the NJS; (a to c) represent the retrieved R_{rs} using the coupled 2SeaColor-MODTRAN model against in-situ measurements for MERIS band of 3, 5 and 7 (band centers: 490, 560 and 665 nm), respectively; (d to f) represent the retrieved R_{rs} values using C2R processor against in-situ measurements for MERIS bands centers of 3, 5 and 7 (band centers: 490, 560 and 665 nm), respectively.

As can be seen from Fig. 3.6, the coupled 2SeaColor-MODTRAN model provides significant improvements in the atmospheric correction and the resulting water-leaving reflectance in comparison with C2R processor in all MERIS bands of 3, 5 and 7. More details of this evaluation are presented in Table 3.4.

Table 3.4. Models' performance evaluation in atmospheric correction part.

Statistical Measures	R^2			RMSE (%)			NRMSE (%)			RRMSE (%)		
Model/bands	3	5	7	3	5	7	3	5	7	3	5	7
Coupled model	0.84	0.81	0.80	0.2	0.3	0.3	13	14	39	21	20	30
C2R	0.69	0.68	0.62	0.4	0.5	0.6	28	24	25	44	33	54

As the statistical measures show, performing atmospheric correction by applying the MODTRAN lookup table proposed in the coupled 2SeaColor-MODTRAN model resulted in a reasonable accuracy against in-situ above the water radiometric dataset for 35 matchups between 2007−2010 at the NJS for bands 3, 5 and 7 respectively. In addition, the 2SeaColor-MODTRAN coupled model shows significant improvement especially in band 3 with R^2 = 0.84, RMSE = 0.0022, NRMSE = 13.18% and RRMSE = 21.08% in comparison with C2R. The standard C2R processor also shows higher accuracy for band 3 (R^2 = 0.69, RMSE = 0.0047) in comparison with bands 5 (R^2 = 0.68, RMSE = 0.0058) and 7 (R^2 = 0.62, RMSE = 0.0063), respectively.

3.4.2. Water retrieval validation

The comparisons of C2R and 2SeaColor-MODTRAN Chla retrieval against in-situ measurements are shown in Fig. 3.7 and related statistical analysis are presented in Table 3.5.

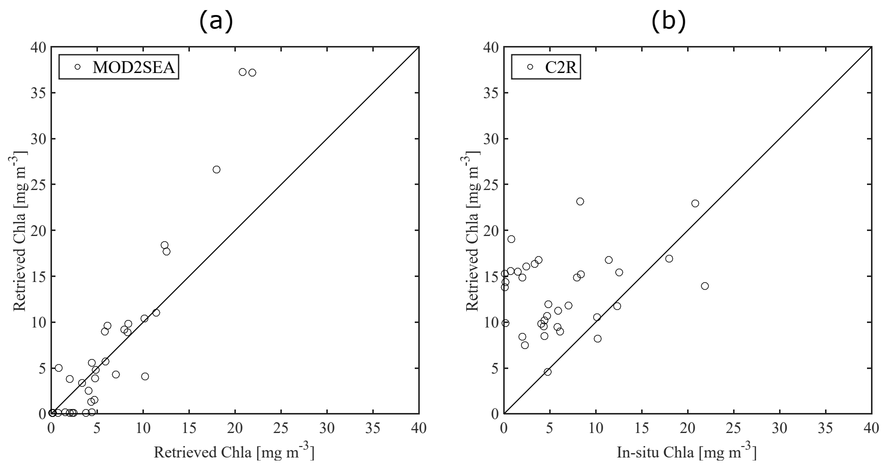

Figure 3.7. Comparison between MERIS-derived and measured log Chla (mg m^{-3}) for 35 matchup moments.

Assessing the model accuracy using R^2 and RMSE shows the reasonable agreement between the measured and retrieved Chla (mg m^{-3}) for all the matchup points during 2007–2010 at the NJS with a significant regression (Fig. 3.7: R^2 = 0.88 and RMSE = 3.32 (mg m^{-3})) during the period of four years. In addition, the comparison of this model with the C2R processor shows significant improvement in the retrieval of Chla. The result of this comparison is presented in Table 3.5.

Table 3.5. Models performance evaluation Chla retrieval.

Statistical Measures	R^2	RMSE	NRMSE (%)	RRMSE (%)
Coupled 2SeaColor-MODTRAN model	0.88	3.32	15.25	53.31
C2R	0.17	4.42	20.30	70.98

There are several possible reasons for the improvement of 2SeaColor in the retrieval of Chla in comparison with the C2R procedure, but the most obvious one is probably that the SIOPs used in the training of the C2R neural networks might be more generic and thus different from the ones used in this study and which are more applicable to the Wadden Sea. In addition, the derived Chla data for 35 matchups between 2007–2010 by the coupled 2SeaColor-MODTRAN model was examined to see how well the in-situ values (mg m^{-3}) agreed with those derived from the MERIS images (mg m^{-3}) at the NJS (Fig. 3.8). In this figure, the X-axis presents the date while the Y-axis presents the Chla concentration for in-situ data (in blue), the coupled 2SeaColor-MODTRAN model (in red) between 2007 and 2010.

(a)

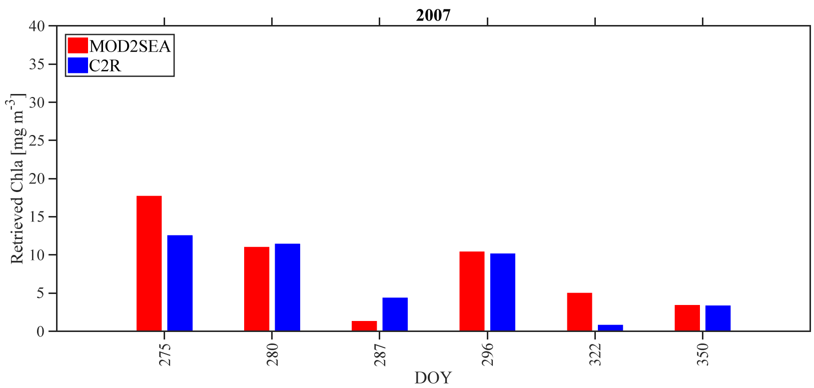

(b)

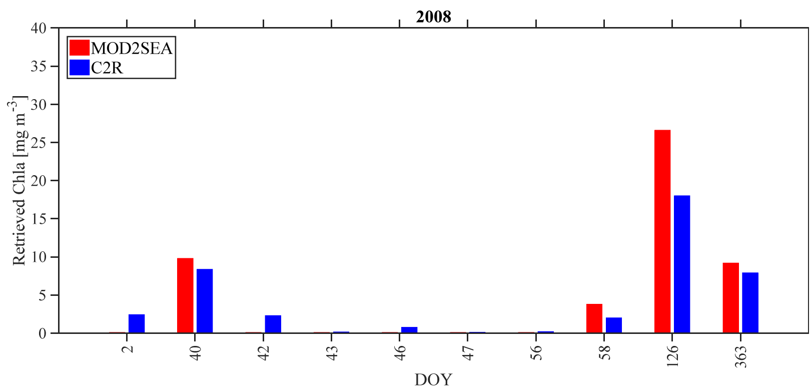

(c)

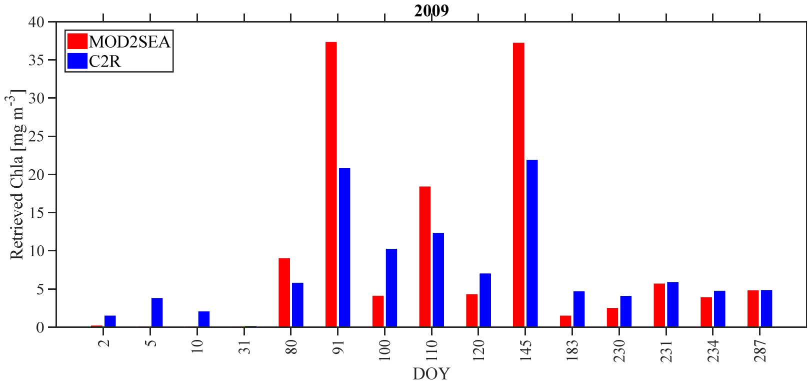

(d)

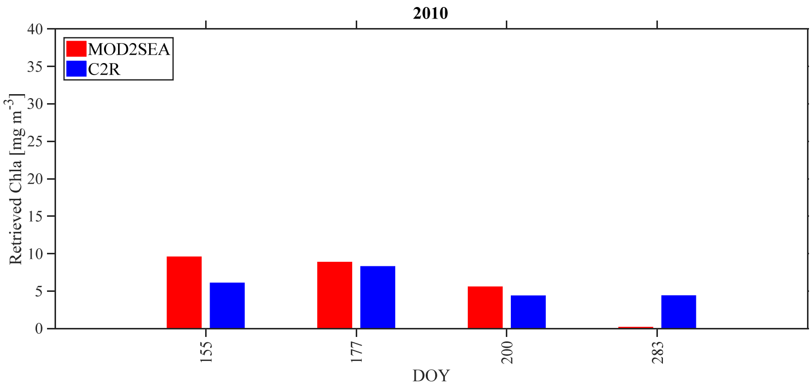

Figure 3.8. (a to d) The four-year comparison of derived Chla values using the coupled 2SeaColor-MODTRAN model (red line) and in-situ measurements (blue line) (mg m^{-3}) from 2007−2010 at matchup moments.

As Fig. 3.8 shows, the derived Chla concentration values using the coupled 2SeaColor-MODTRAN model shows reasonable agreement during 2007–2010, with maximum retrieved values of around 40 (mg m^{-3}) and minimum values just above zero. However, despite the agreement between MERIS-derived and in-situ Chla in a four-year period, systematic overestimations at high Chla concentration values (during April and May) (mg m^{-3}) were also identified. Chla products, particularly during the phytoplankton bloom seasons of spring and summer, require further development. This overestimation might be explained by the Chla parametrization of the Lee et al. (1999) model since it appears that the Chla model calibration based on that model does not fit that well for the Wadden Sea. This Chla overestimation using satellite images was also in agreement with a Chla retrieval overestimation in most of the European seas studies by Zibordi et al. (2013).

3.5. Discussion

Accurate estimation of water-leaving reflectance from satellite sensors is a fundamental goal for ocean color satellite missions Zibordi et al. (2012). The commonly applied atmospheric correction methods based on zero water-leaving reflectance in the near-infrared bands fail when applied to turbid waters since the high concentrations of water constituents lead to a detectable water-leaving reflectance in the near-infrared region in the satellite image. In this study, we focused on the long-term retrieval of Chla concentration from MERIS images in the Wadden Sea, and the coupled 2SeaColor-MODTRAN model is proposed as a tool to improve the retrieval of Chla concentration from earth observation data in this area.

Calculating accurate water-leaving reflectance spectra to translate them into Chla concentration under different atmospheric conditions is a crucial part of this study, since the atmosphere, in most cases, contributes more than 90% of the TOA radiance signal (Shen and Verhoef, 2010). We can attribute the success of the coupled 2SeaColor-MODTRAN model to its capability of combining simulations from 2SeaColor with the MODTRAN radiative transfer model for different combinations of aerosol type, visibility, and water constituent concentrations for all MERIS bands to simulate TOA radiances, instead of applying the routine atmospheric correction and water retrieval algorithms, separately. Furthermore, based on a heterogeneous atmosphere assumption of the coupled 2SeaColor-MODTRAN model, this technique can help suppress the influence of local haze variations in satellite images. Thus, applying this method results in a considerable improvement of the accuracy of the atmospheric correction, which is the most problematic part of remote sensing data processing for turbid waters like the Wadden Sea.

However, satellite estimation of Chla concentration is still difficult for coastal waters, where Chla, SPM, and CDOM occur in various mixtures which complicate the derivation of their concentrations from reflectance observations. The 2SeaColor model performed well while the commonly applied water quality algorithms might fail in water constituent retrieval. Fig. 3.9 shows an example of coupled 2SeaColor-MODTRAN model spectral matchings for 2 October 2007.

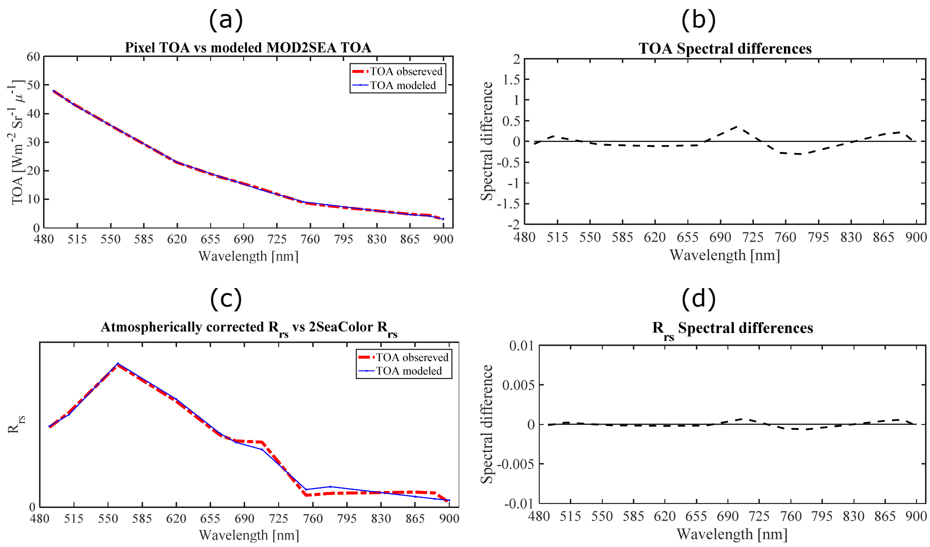

Figure 3.9. (a) the best match identified by the coupled model between simulated TOA radiances vs. pixel TOA radiance; (b) the spectral differences between observed and simulated TOA radiance; (c) the simulated R_{rs} (extracted from the best TOA radiance match) vs. the simulated 2SeaColor R_{rs}; (d) the spectral differences between simulated R_{rs} by 2SeaColor and atmospherically corrected R_{rs} from observed TOA radiance by 2SeaColor-MODTRAN.

As this figure shows, good matches are found between modeled and observed TOA radiance as well as modeled and atmospherically corrected water-leaving reflectance with respect to identified visibility and aerosol type by the coupled model. All in all, assessing the 2SeaColor-MODTRAN Chla retrievals from MERIS data at one location (the NJS) for a period of four years (2007–2010) shows reasonable agreement with in-situ measurements (R^2 = 0.88, RMSE = 33.2%). The 33.2% RMSE appears reasonable enough, as compared with the validation of the SeaWiFS Chla data product for global open ocean waters with a relative RMSE of about 58% (Le et al., 2013a). In addition, this model shows considerable improvement to retrieve Chla concentration from satellite images in comparison with similar studies for the Wadden Sea (Hommersom, 2010b; Hommersom et al., 2009; Philippart et al., 2013, 2007; Poremba et al., 1999). The results of retrieved Chla concentration using this coupled model are within the range of measured Chla concentration (mg m^{-3}) on the ground reported by other researchers, while a clear seasonal pattern is observed with the peak values during spring (in May). For example, Hommersom (2010b) reported Chla concentration range variations in the Wadden Sea during eight surface water sampling campaigns in 2006−2007 in 156 stations while Chla also showed a strong seasonal pattern with the highest values during spring in May. Chang et al. (2006) showed the higher Chla concentrations occurred in May. Reuter et al. (2009) provided continuous data on Chla concentration of the Wadden Sea at a time series station established in autumn 2002 by the

University of Oldenburg. They reported a clear seasonal pattern in Chla concentration between 2007 and 2008 which has the highest values in May and the lowest values in November. Tillmann et al. (2000) showed a large variability of Chla concentration over the year in the Wadden Sea. Winter concentrations were much lower than summer concentrations while in spring a phytoplankton bloom with peak concentrations occurs. Cadée (1996) showed that yearly patterns of Chla concentration were similar in the Wadden Sea, although the overall inter-annual variability is large, as well as the maxima measured during spring bloom (in May). All in all, regarding the reasonable agreement of the 2SeaColor-MODTRAN results with in-situ measurements and considering the turbid nature and complex heterogeneity in the turbid Wadden Sea, the performance of this coupled model should be regarded as encouraging and satisfactory enough.

It is also worth mentioning that in shallow coastal waters like the Wadden Sea the bottom might influence the reflected signal to the sensor. This is not the case for the NJS where, due to the depth of > 5 m and the high turbidity of the water (Table 3.1) near the NJS and the surrounding area, the bottom effect on observed reflectance is negligible. This has been confirmed in the quality check of the NJS data and the corresponding MERIS pixels. However, in the other shallower parts of the Wadden Sea, the bottom effect might contribute substantially in the visible region of the spectrum. As can be seen in Fig. 3.1, the effect of the bottom is visible in large areas of the Wadden Sea satellite image. Thus, for shallow waters, it is recommended in future studies to develop water constituent retrieval algorithms by incorporating sea bottom effects in the hydro-optical model. We speculate that developing a hydro-optical model including the bottom effect may lead to significant improvements in the derived WCCs from earth observation data in this shallow coastal region. That is why, in the next phase of this research, we are going to include the bottom effect contribution into the TOA radiance calculation to derive and provide Chla concentration maps over the Wadden Sea.

For the Wadden Sea, and many other estuaries, knowledge of local SIOPs to locally calibrate retrieval algorithms is often lacking, and more research is still needed. For the Wadden Sea, Peters (2001) reported a complete set of SIOPs for Chla, SPM and CDOM measurements. However, the data of Peters were all collected at one location (the Marsdiep inlet) and only for two days (in May 2000). After that, the only published set of SIOP measurements in the Wadden Sea was constructed by Hommersom et al. (2009). Using Hommersom's measurements, SIOPs increased the accuracy of the derived Chla concentration significantly in comparison to previous efforts in this region. However, Hommersom's measurements lack seasonal information on the SIOPs while there is currently not much information on the SIOPs to be the basis for a hydro-optical model for the Wadden Sea. Without any doubt, having seasonal SIOPs may lead to improved accuracy of retrieved Chla using this coupled model. Thus, more in situ data (especially on SIOPs) is still necessary for the model calibration.

Although our current efforts are centered on validating the proposed coupled atmospheric-hydro-optical model in the highly turbid Wadden Sea using MERIS satellite images, it is unclear how broadly applicable this coupled model will be and to what extent these findings could be generalized. Thus, we suggest extending this study to other parts of the world using various ocean color remote sensors. However, to apply this method to other regions, first, the availability of valid SIOPs (water quality constituent's absorption and backscattering coefficient), in addition to the accurate ecological and geophysical knowledge of the interest area (i.e., the ranges of WCCs) are needed. Furthermore, spectral response functions of the desired sensor as well as atmospheric parameters and illumination geometry of the satellite image to run MODTRAN are required. As a consequence, access to accurate in-situ water-leaving reflectance and WCC is essential for the assessment of primary data products from satellite ocean color missions (Zibordi et al., 2009) using the proposed approach.

The Water Framework Directive regulations from the European Union force member states to monitor all their coastal areas (Environment Directorate-General of the European Commission, 2000). Availability of one decade of MERIS images (2002–2012) over the Wadden Sea, allows providing long-term Chla distribution maps using this coupled model with reasonable accuracy and to conduct a one-decade phenological analysis in this area. To provide Chla concentration maps with reasonable accuracy, the proposed method should be applied pixel by pixel for the whole region of interest. To speed up the pixel-based approach, a filter can be introduced to remove those combinations of visibilities and aerosol types from the MODTRAN LUT which result in negative water-leaving reflectance values in any band, by considering the recorded TOA signal per pixel. On the other hand, other WCCs like SPM and CDOM as well as visibility and aerosol model maps can be produced as the output of the 2SeaColor-MODTRAN code. Of particular interest when analyzing the variability in the MERIS-derived Chla data trend for the Wadden Sea is whether any significant decreasing trend from 2002–2012 would indicate the effect of prior nutrient reduction management actions. This has significant implications for identifying positive anomaly events and may act as an alert for management actions. Clearly, climatic variability needs to be considered carefully when interpreting the long-term data trends and when making management decisions (Le et al., 2013a).

Furthermore, this established MERIS-based Chla data record may serve as baseline data to continuously monitor the estuary's eutrophic state, and the validated algorithm may extend such observations to the future using various satellite continuity missions. The OLCI, embedded on the Sentinel-3 platform, is a sensor especially adapted for aquatic remote sensing (Harvey et al., 2014) and succeeded the MERIS sensor in 2015 (Saulquin et al., 2016). The launch of Sentinel-3 and OLCI will secure future consistent operational monitoring by medium resolution data for water quality assessment also of coastal zones and bays (Harvey et al., 2014). OLCI is designed mainly for global biological and biochemical oceanography, which constrains its spatial resolution. On the other hand, the asymmetric view of OLCI will offer sun-glint free images in 21 spectral bands (from ultraviolet to near-infrared wavelengths) with improved spatial coverage and temporal frequency. OLCI will provide high quality optical ocean observations (*e.g.,* normalized water-leaving radiance, inherent optical properties, spectral attenuation of down-welling irradiance, photosynthetically active radiation, particle size distribution) and allow more accurate retrieval of the ocean color variables (*e.g.,* Chla, SPM and CDOM concentrations) (Malenovský et al., 2012) where the OLCI bands are optimized to measure ocean color over open ocean and coastal zones. Sentinel-3 was successfully launched in February 2016 and will give free access to satellite data of the Wadden Sea. It is expected that the 2SeaColor-MODTRAN coupled model will also operate successfully to derive Chla concentration using OLCI images for highly turbid waters and that it will result in an accuracy improvement in atmospheric correction and Chla retrieval aspects in comparison with the MERIS sensor. Thus, applying this method for further studies using OLCI data over the Wadden Sea is recommended.

3.6. Conclusions

A coupled atmospheric-hydro-optical model (2SeaColor-MODTRAN) has been proposed and validated to derive long-term Chla concentration (mg m^{-3}), visibility and aerosol type from MERIS observations for the turbid coastal area of the Wadden Sea. At one location, the model validation showed a good agreement between MERIS-derived and measured Chla concentration for a period of four years (2007–2010). We attribute the success of this approach to the simultaneous retrieval of atmosphere and water properties. In addition, we have found that water and atmospheric properties have different effects on TOA radiance spectra and therefore these are separately retrievable from MERIS data if the coupled 2SeaColor-MODTRAN model is used. Using this coupled atmospheric-hydro-optical model led to considerable improvement for the simultaneous retrieval of water and atmosphere properties using earth observation data, with significant results in the accuracy in comparison with other algorithms applied to derive Chla in the Wadden Sea.

Chapter 4 **Long-term variability of water constituent concentrations in the Wadden Sea: integration of in-situ and satellite observations**[*]

[*] This chapter is based on:
Arabi, B., Salama, M.S., Pitarch, J., Verhoef, W., 2020. Integration of in-situ and multi-sensor satellite observations for long-term water quality monitoring in coastal areas. Remote Sensing of Environment Journal, 239 (2020) 111632. https://doi.org/10.1016/j.rse.2020.111632.

ABSTRACT

Recently, there is a significant effort in the integration of in-situ and satellite observations for effective monitoring of coastal areas, as stated by Copernicus: the European Earth Observation Programme. In this study, 15-years diurnal variation of water constituent concentrations (WCCs) retrieved from the integration of in-situ and multi-sensor satellite images was tracked by using Radiative Transfer (RT) modeling in the Dutch Wadden Sea, The Netherlands. First, the existing RT model of 2SeaColor was applied for simultaneous retrieval of WCCs (i.e., Chla, SPM, CDOM) from time series of in-situ hyperspectral measurements collected in a daily basis between 2003 and 2018 at the NIOZ jetty station (the NJS) located in the Dutch part of the Wadden Sea. Second, the existing coupled RT model of coupled 2SeaColor-MODTRAN was applied, in the same area for the same period, to retrieve WCCs from time series of multi-sensor satellite images of MERIS, Multispectral Instrument on board Sentinel-2 (MSI), and Ocean and Land Colour Instrument on board Sentinel-3 (OLCI). At the location of the NJS, a direct comparison of retrievals (Taylor diagram and statistical analysis) from in-situ and satellite observations showed that both RT models of the 2SeaColor and coupled 2SeaColor-MODTRAN are comparable in terms of obtained coherent results at water surface and TOA level: (the Coefficient of Determination: $R^2 \sim 0.70$ for Chla, SPM and CDOM; the Correlation Coefficient: $R > 0.80$ for Chla, SPM and CDOM and the Root Mean Square Error (RMSE): 8 (mg m^{-3}), 5.5 (g m^{-3}), 0.18 (m^{-1}) for Chla, SPM and CDOM, respectively). Finally, the coupled 2SeaColor-MODTRAN model was applied to MERIS and OLCI images to generate WCCs over the study area. The established long-term WCCs data and the generated maps of this research have remarkable applications for recognizing anomaly events and can be served as a warning for management actions at the complex coastal waters of the Wadden Sea.

4.1. Introduction

In a world where coastal areas are home to approximately one-third of the world's population (UNEP, 2006), monitoring is essential to discover whether there are significant changes taking place in these natural environments (Burt et al., 2014; Zielinski et al., 2009). Coastal waters are the critical habitat for many marine species and are the basis for many economic concerns important to society and local economies, including fisheries, coastal recreation, and tourism activities (Halliday et al., 2014; Van der Wal and Pye, 2003; Zielinski et al., 2002). Monitoring of these essential global resources is a key feature of a sustainable future considering the provided facts (i.e., Goal-14: Conserve and sustainably use the oceans, seas and marine resources) by the recent Sustainable Development Goals' (SDGs) report (McInnes, 2018) which says (the facts are taken from the SDGs report directly):

- "Over three billion people depend on marine and coastal biodiversity for their livelihoods."
- "Globally, the market value of marine and coastal resources and industries is estimated at $3 trillion per year or about 5 percent of global GDP."
- "Marine fisheries directly or indirectly employ over 200 million people."
- "Coastal waters are deteriorating due to pollution and eutrophication. Without concerted efforts, coastal eutrophication is expected to increase in 20 percent of large marine ecosystems by 2050."

Moreover, as it is reported in Goal-6 (i.e., Ensure access to water and sanitation for all) of SDGs, it is crucial to have effective and global water quality monitoring since inadequate water quality directly influence peoples' lives by having negative impacts on their livelihood choices, food security, etc., (McInnes, 2018). However, at the current time, there is a continuous deterioration of coastal waters owing to global urbanization of coastal regions, massive discharges of sewage, effluents, industrial and agricultural run-off which causes a significant impact on the quality of coastal waters. This may lead to change the nutrient components and triggering toxic algal blooms and influence biodiversity, recreation, tourism fisheries, and other activities (Mishra et al., 2015). In recent decades, water sector decision-makers and coastal planners have been urged to establish regulations for effective monitoring of these vital areas in order to avoid more deterioration and to sustainable conservation of these natural resources. With this respect, in December 2000, the European Parliament adopted the Water Framework Directive (WFD) (WFD, 2000) to force all members' states to observe the quality of the water in coastal and inland waters. Accordingly, the Marine Strategy Framework Directive (MSFD) followed the same objective to monitor and protect coastal waters aiming to maintain them in a suitable ecological status (Mélin et al., 2011). One of the most important European coastal areas, which has drawn great attention in Europe, is the Wadden Sea. Conservation of this tidal ecosystem as the largest unbroken system of intertidal mudflats in the world, and as one of the 193 natural World Heritage properties, has become compulsory since July 2009 (Sijtsma et al., 2015). Accordingly, particular attention has been paid by the Netherlands, Denmark, and Germany to protect this area since the early years of the last century (Bartholdy and Folving, 1986; Brockmann and Stelzer, 2008; Staneva et al., 2009).

Maintaining this area in a healthy state requires a continuous approach to track the spatio-temporal variation of water quality variables in order to capture information on dynamic events which might have a substantial impact on ecosystems such as changes caused by storms or unexceptional phytoplankton blooms (Brando and Dekker, 2003; Bukata et al., 1995; Garaba and Zielinski, 2015). SPM, Chla, and CDOM concentrations are amongst the most important water quality variables that need to be monitored to understand the process of such dynamic events and their impact on aquatic ecosystems. Tracking of long-term variation of these water constituents reveals important patterns, which allows trends, cycles, and rare events to be identified (Burt et al., 2014).

The first constituent to be monitored is Chla. Accurate estimation of Chla concentration, as the main proxy measure of phytoplankton abundance, is a key factor to the understanding of the planetary carbon cycle as a crucial indicator of eutrophication in marine ecosystems (Murphy et al., 2001; Werdell et al., 2009). Chla amounts are influenced by anthropogenic nutrients of agricultural and industrial origin, whereby fisheries and aquaculture can be affected by Chla abundance (Peters et al., 2004). The second constituent to be monitored is SPM. A reliable estimate of SPM concentration is crucial for many water quality studies, as SPM is responsible for most of the scattering, which affects the water reflectance by modifying the light field (Kirk, 1994). Accurate estimation of SPM concentration and its variation are considered as factors of great interest for sediment transport and may indicate the transport of organic toxins (e.g., Malmaeus and Håkanson, 2003; Ruddick et al., 2008). Moreover, hydrochemical and ecological models need reliable SPM values to be used as a proxy for terrestrial input, re-suspension or the sedimentation of particles (Blaas et al., 2007; Fettweis and Van Den Eynde, 2003; Lindstrom et al., 1999). SPM contains both inorganic and organic fractions. The inorganic fraction consists mostly of mineral particles originating from river discharge and erosion. The organic part of SPM consists of organic detritus, phytoplankton, and bacteria (Bowers and Binding, 2006; Bukata et al., 1995; Jerlov, 1976). In addition to Chla and SPM, CDOM is another relevant component in water quality studies since it controls the functioning of ecological processes and biogeochemical cycles of marine ecosystems. CDOM is produced by phytoplankton degradation and bacterial decomposition while riverine discharge is another main source of CDOM in most coastal waters (Yu et al., 2016b; Zielinski and Brehm, 2007).

One way to obtain information on Chla, SPM and CDOM concentrations and variations is to direct water sampling and to collect in-situ measurements. Indeed using in-situ measurements provide most accurate and reliable information. However, monitoring of WCCs using in-situ measurements and direct water sampling needs conventional cruise surveys with satisfactory spatial and temporal coverage. Unfortunately, this is not often practical for various coastal waters due to lack of technical equipment and financial resources (Friedrichs et al., 2017; Philippart et al., 2013; Vries et al., 1998).

Remote sensing is an efficient technique that can provide information on WCC variations on high spatio-temporal scales (Harvey et al., 2014; Kirk, 1994; Philippart et al., 2013; Salama et al., 2012a; Shen et al., 2010; Van der Wal et al., 2005). Optical remote sensing of water quality using satellite images is the backbone of aquatic ecosystem studies as it can provide a long-term spatio-temporal determination of WCC patterns, although operational applications are still limited by deficits of in-situ verification. That is why the integration of in-situ and satellite observations is a great step to reduce uncertainties in long-term water quality studies (Chen et al., 2007, 2004) Indeed, combination of WCCs data obtained from in-situ and satellite observations is an optimal remote sensing approach to provide high temporal resolution information on water surface properties with the final aim of generating more accurate WCC maps for effective monitoring of coastal regions (Lawford et al., 2013). However, this is a challenging task due to the main problems of i) availability of long-term observations and ii) reliability of retrieved information (Doerffer and Fischer, 1994; Eleveld et al., 2014; Lee et al., 2011; Reid et al., 1990; Ryu et al., 2008; Van Raaphorst et al., 1998; Wang et al., 2007; Zibordi et al., 2012) as follows:

First, in water-surface level, availability of long-term remote sensing observations is dependent on many factors such as having access to advanced instruments/sensors, doing a consistent survey on the automatic sensors and performing regular calibration/validation on instruments (Wernand et al., 2006). Moreover, it is vital to apply suitable data quality control approach on the recorded dataset to extract high-quality observations (Arabi et al., 2016; Cadee and Hegeman, 2002; Hommersom et al., 2010; Philippart et al., 2013, 2010; Van der Woerd and Pasterkamp, 2008). Availability of long-term observations in TOA level is even more difficult. Only a limited number of satellites are practical to be used for water quality monitoring where some of them may not cover the region of interest (Niedermeier et al., 2005; Wang, 1997; Wimmer et al., 2000). Moreover, not only all satellites images are not free, but also many satellite images are not usable due to the occurrence of series cloud/rain or local haze at the time of satellite overpass (Arnone et al., 2006).

Second, retrieving reliable information from the high-quality in-situ dataset or clear satellite images is complicated due to high turbidity, the mixture of WCCs and local haze variations in the atmosphere. As a result, most of the regular atmospheric correction methods and water retrieval algorithms fail for accurate retrieval of WCCs in these areas (Albert and Mobley, 2003; Salama et al. 2004; Ceyhun and Yalçin, 2010; Garcia et al., 2018; Gitelson et al., 2008; Lee et al., 2001; Maritorena et al., 1994; Salama et al., 2012a; Sathyendranath and others, 2000; Shen and Verhoef, 2010; Shi and Wang, 2007; Siegel et al., 2000). With the unique opportunity of having access to the full archive of 15-years of diurnal in-situ hyperspectral measurements and multi-sensor satellite images (MERIS, MSI, OLCI), and having access to developed RT models of 2SeaColor (Salama and Verhoef, 2015) and coupled 2SeaColor-MODTRAN (Arabi et al., 2016), evaluated and validated over the Dutch Wadden Sea, the main objective of the research was to combine in-situ and satellite observations for long-term water quality monitoring in this complex study area. Following the mentioned objective, the current paper is arranged as follows: the study site and the used datasets are described in sections 4.2 and 4.3. The methodology is described in section 4.4, and the results, implications and some recommendations for further studies are described in sections 4.5 and 4.6.

4.2. Study area

The case study of this research is the Dutch Wadden Sea. This region covers a surface area of approximately 2500 km^2 and is located in the north of the Netherlands. The area is shallow, leading to surfacing mudflats with low tide and re-suspension due to tidal currents. The region contains 11 islands, which extend from west to east (Dube, 2012). Fig. 4.1 shows an OLCI satellite image covering the parts of the Dutch mainland and the island of Texel at the bottom left and the islands Vlieland and Terschelling to the northeast from Texel. The location of the NJS (53°00’06”N; 4°47’21”E) is shown by a red dot in the Western-South of the image.

Figure 4.1. One OLCI image covering the Dutch Wadden Sea and parts of Ijsselmeer lake (5th of March 2018); the location of the NJS is shown in red dot; image color composition using OLCI bands: red: band-18; green: band-9; blue: band-4.

The climatological condition of the Dutch Wadden Sea, by having mostly cloudy and rainy days, fair concentrations of WCC besides the shallowness of the water, make this region as a complex case study for water quality monitoring using remote sensing approaches (Hommersom, 2010).

4.3. Dataset

The used dataset in this research contained three groups of in-situ Chla and SPM concentrations, in-situ hyperspectral measurements and multi-sensor satellite images as follows:

4.3.1. In-situ Chla and SPM concentrations

The first used dataset of this study was a time series of in-situ measurements of Chla (mg m^{-3}) and SPM (g m^{-3}) concentrations collected in a daily basis under the condition of SZAs < 60° between 2008 and 2010 at the NJS. This dataset was taken from other study conducted by Arabi et al. (2018) and was used to show the temporal agreement of retrieved Chla and SPM concentrations from in-situ hyperspectral measurements and satellite images with in-situ ones at the NJS (Fig. 4.13).

4.3.2. In-situ hyperspectral measurements

In this study, we used a time series of in-situ hyperspectral measurements collected between 2003 and 2018 at the NJS. There is a radiometric setup mounted 5 meters above the water surface at this station which is responsible for the automatic recording of every fifteen minutes of hyperspectral measurements between 350 nm between 950 nm (increment: 1 nm) since 2002 till present (Wernand, 2011). This radiometric setup contains six TRIOS sensors which includes one Ramses-ACC sensor for measuring down-welling irradiance values (E_s), one Ramses-ACC-UV sensor for measuring down-welling irradiance values at ultraviolet (E_s - UV), and two pairs of Ramses-ARC sensors for measuring sky radiance values (L_{sky}) and surface radiance values (L_{sfc}) looking to South-West and South-East, separately (Fig. 4.2).

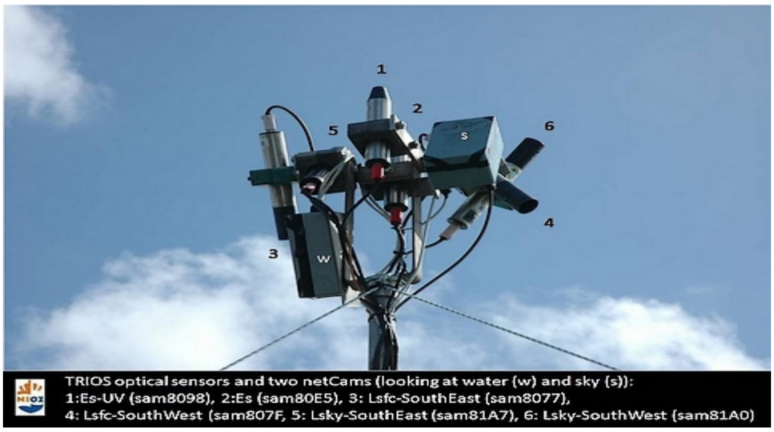

Figure 4.2. The optical sensors with the VZA of 35° installed on the NJS, Marsdiep inlet (53°00′06″N; 4°47′21″E), the Dutch Wadden Sea (Wernand, 2011); w: looking at water; s: looking at sky; 1: down-welling irradiance sensor at ultraviolet (E_S - UV); 2: down-welling irradiance sensor (E_S); 3: the surface radiance sensor looking to South-East ($L_{sfc\ (South\text{-}East)}$); 4: the surface radiance sensor looking to South-West ($L_{sfc\ (South\text{-}West)}$); 5: the sky radiance sensor looking at the South-East ($L_{sky\ (South\text{-}East)}$); 6: the sky radiance sensor looking at the South-West ($L_{sky\ (South\text{-}West)}$).

For this study, we used those hyperspectral measurements which were recorded from 9:30 a.m. to 11:30 p.m. (UTC) per day. The reason for this time selection was to select those measurements which were in concurrent with the time of MERIS, MSI and OLCI overpass, simultaneously, at the study area. Moreover, we excluded those hyperspectral measurements which were recorded during winter time and under the condition of SZAs > 60° from the dataset. As Arabi et al. (2018) showed, these measurements are not reliable enough for doing retrievals by hydro-optical models. They pointed the effect of high SZA, higher sensitivity of the measurements to sun-glint and skylight and lack of information about the seasonal SIOPs, as the main reasons behind the model's deterioration during winter (Arabi et al., 2018). Accordingly only the hyperspectral measurements collected from March to September (SZAs < 60°) were selected for further analysis.

4.3.3. Satellite images

We used three multispectral satellite images of MERIS, MSR, and OLCI in this study. We did data quality control check on satellite images by exclusion all cloudy and hazy images. Also, as it was explained above, we used only those images which were captured from March to September over the study area (SZAs < 60°). Below the description of these satellites and the number of the used images per each satellite is described in details:

4.3.3.1. MERIS images

We used a full archive of MERIS images captured between 2003 and 2012. The MERIS sensor (full resolution: 300 m) was operational on the board of the European environmental satellite ENVISAT in March 2002 (Shen et al., 2010). The high sensitivity and extensive dynamic range of the MERIS sensor have been widely used for ocean and coastal water remote sensing studies (Majozi et al., 2014; Pasterkamp et al., 2003; Pitarch et al., 2017). The MERIS sensor had a revisit time of three days on average at around 10:30 a.m. (UTC) over the study area with 15 bands covering the spectral ranges from 400 nm to 950 nm (Salama et al., 2009). In this study, we used 207 cloud-free MERIS images (SZAs < 60°) from which 145 images were in concurrent with in-situ hyperspectral measurements at the NJS (MERIS-matchups).

4.3.3.2. MSI images

European Space Agency (ESA) launched MSI on board Sentinel-2 in June 2015 which opened a potential in remote sensing of coastal waters (Orlandi et al., 2018; Pahlevan et al., 2017). The MSI sensor has a revisit time of five days at around 11 a.m. (UTC) over the study area with 13 bands covering the spectral ranges from 400 nm to 2400 nm. The MSI spatial resolution is much higher than MERIS and OLCI images (10 m, 20 m, and 60 m) and varies in different bands (Table 4.1). At the time this study was conducted, there were 24 cloud-free MSI images over the Dutch Wadden Sea between 2015 and 2018 (SZAs < 60°) while 20 images were in concurrent with in-situ hyperspectral measurements at the NJS (MSI-matchups).

4.3.3.3. OLCI images

MERIS was put out of operation in April 2012 and was succeeded by OLCI, embedded on the Sentinel-3 on platform A in February 2016 and was continued on Sentinel-3 on the platform B since April 2018 (Saulquin et al., 2016). OLCI is designed mainly for global biological and biochemical oceanography, which constrains its spatial resolution (full spatial resolution: 300 m). The asymmetric view of OLCI offers sun-glint free images with 21 bands covering the spectral ranges from 400 nm to 1020 nm which are optimized to measure ocean color over open ocean and coastal zones (Woerd and Wernand, 2015). The OLCI sensor has a revisit time of two-three days at around 10 a.m. (UTC) over the study area. The first available OLCI product was observed in November 2017, and there were in total 20 cloud-free OLCI images (SZAs < 60°) available over the Dutch Wadden Sea till the end of 2018 from which 17 images were in concurrent with in-situ hyperspectral measurements at the NJS (OLCI-matchups). An overview of the MERIS, MSI and OLCI bands is presented in Table 4.1.

Table 4.1. MERIS, MSI and OLCI configuration.

	Band centre (nm)			Band width (nm)			Spatial resolution (m)		
Sensor/ band number	MERIS	MSI	OLCI	MERIS	MSI	OLCI	MERIS	MSI	OLCI
1	412.5	443.9	400	10	27	15	300	60	300
2	442.5	496.9	412.5	10	98	10	300	10	300
3	490	560	442.5	10	45	10	300	10	300
4	510	664.5	490	10	38	10	300	10	300
5	560	703.9	510	10	19	10	300	20	300
6	620	740.2	560	10	18	10	300	20	300
7	665	782.5	620	10	28	10	300	20	300
8	681.2	835.1	665	7.5	145	10	300	10	300
8a	-	864.8	-	-	33	-	-	20	-
9	708.7	945	673.7	10	26	7.5	300	60	300
10	753.7	1373	681.2	7.5	75	7.5	300	60	300
11	761.8	1613	708.7	2.5	143	10	300	20	300
12	778.7	2202	753.7	15	242	7.5	300	20	300
13	865	-	761.2	20	-	2.5	300	-	300
14	885	-	764.3	10	-	3.7	300	-	300
15	900	-	767.5	10	-	2.5	300	-	300
16	-	-	778.7	-	-	15	-	-	300
17	-	-	865	-	-	20	-	-	300
18	-	-	885	-	-	10	-	-	300
19	-	-	900	-	-	10	-	-	300
20	-	-	940	-	-	20	-	-	300
21	-	-	1020	-	-	20	-	-	300

4.4. Methodology

The flowchart in Fig. 4.3 depicts the methodology used to conduct this research.

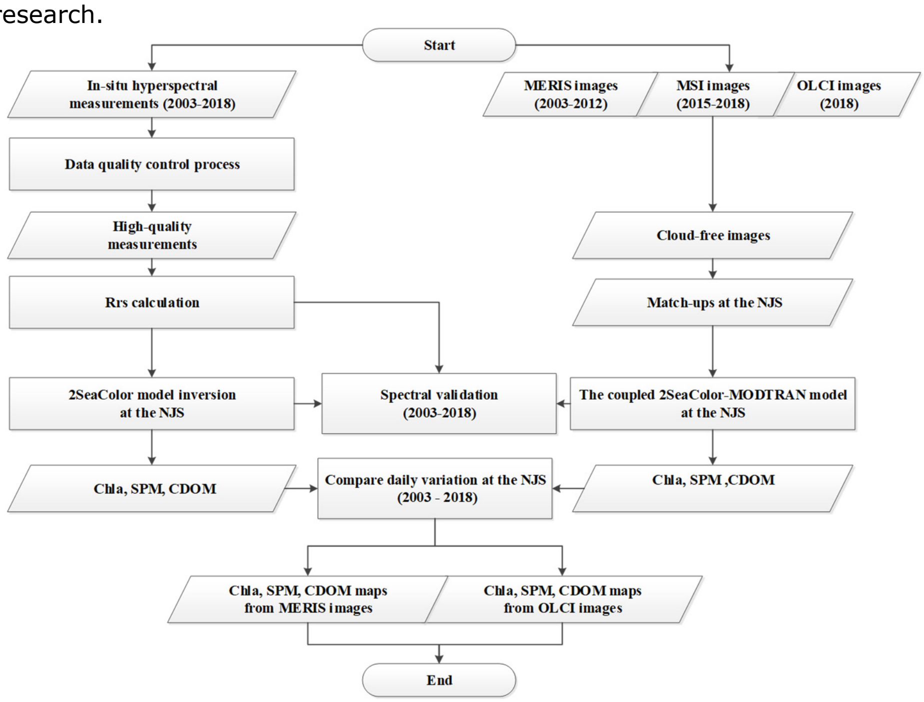

Figure 4.3. The flowchart of the implemented approach in this research.

The methodology of this work can be briefly explained within below main steps:

a) Select high-quality in-situ hyperspectral measurements and cloud-free multi-sensor satellite images under the condition of SZAs < 60°.
b) 15-years WCC retrievals from daily in-situ hyperspectral measurements using the RT model of 2SeaColor at the NJS.
c) 15-years WCC retrievals from MERIS, MSI and OLCI images using the coupled RT model of coupled 2SeaColor-MODTRAN at the NJS.
d) Comparison between retrieved WCCs from in-situ hyperspectral measurements and multi-sensor satellite images at the NJS.
e) Generate retrieved WCC maps using the coupled 2SeaColor-MODTRAN model from satellite images over the Dutch Wadden Sea.

The details of the methodology of our study are described in details as follows:

4.4.1. Data quality control approach

The in-situ hyperspectral measurements of this study were recorded automatically by the sensors mounted on the NJS (Fig. 4.2). Therefore, we needed to perform a suitable data quality control approach to extract the high-quality measurements from the full archive of the dataset. To do this, we used an advanced data quality control approach proposed by Marcel Wernand (2002). He developed and improved his proposed approach based on thousands of incident solar irradiation as well as coastal colour measurements and meteorological dataset collected at the NJS containing four steps of 1) sun-glint effect (2) meteorological, (3) spectral shape and (4) minimal solar light flagging as follows:

4.4.1.1. Sun-glint effect flagging

We applied the sun-glint flagging to the automatic selection of those measurements which were affected by the least effect of sun-glint contamination (Wernand, 2002). To perform this data flagging, the NJS was equipped with two pairs of sky radiance (L_{sky}) and surface radiance (L_{sfc}) sensors, looking at South-East ($L_{sky\ (South\text{-}East)}$, $L_{sfc\ (South\text{-}East)}$) and South-West, ($L_{sky\ (\mathrm{South\text{-}West})}$, $L_{sfc\ (\mathrm{South\text{-}West})}$), separately (Fig. 4.2). Per each pair, L_{sky} and L_{sfc} sensors were 90° apparat in the horizontal plane (under azimuth angles of 135° and 225°). One down-welling irradiance sensor (E_s) was also installed per each pair. This way one of the two water-leaving radiance signals was always available with a minimum of sun-glint. The selection was made by comparing the spectral values at the wavelength of 550 nm between $L_{sfc\ (South\text{-}West)}$ and $L_{sfc\ (South\text{-}East)}$ per each pair of spectra recorded at the same time. Then the spectrum with lower L_{sfc} amplitude was selected for further analysis assuming that this spectrum was affected the least amount of sun-glint (Wernand, 2002).

4.4.1.2. Meteorological data flagging

We applied the meteorological data flagging to the automatic selection of those measurements which were recorded under favorable meteorological circumstances (i.e., no precipitation and/or high humidity) (Wernand, 2002). Based on this meteorological data flagging, the values of E_s measurements at two wavelengths of 940 nm (water vapor absorption wavelength) and 370 nm (ultraviolet (UV)) were selected per each spectrum. Then the band ratio of $r_2 = E_S\,(\lambda = 940\text{ nm})/E_S\,(\lambda = 370\text{ nm})$ was calculated per each spectrum. In case r_2 was equal to or smaller than 0.2 (mW m^{-1} nm^{-1} sr^{-1}), the precipitation condition was detected, and the spectrum was removed from the dataset. In case r_2 was between 0.2 and 0.25 (mW m^{-1} nm^{-1} sr^{-1}), high humidity condition was detected, and the spectrum was removed from the dataset. Otherwise ($r_2 > 0.25$ (mW m^{-1} nm^{-1} sr^{-1})), the dry condition was detected at the time of data collection, and the spectrum was used for further analysis (Wernand, 2002).

4.4.1.3. Spectral shape flagging

We applied the spectral shape flagging to the automatic detection of those measurements which were possibly influenced by specific dusk (red coloring of the sky) or down radiation. To perform this spectral shape flagging, the values of E_S measurements in two wavelengths of 470 nm and 680 nm were selected per each spectrum. Then the band ratio of $r_3 = E_S\,(\lambda = 470\text{ nm}) / E_S\,(\lambda = 680\text{ nm})$ was calculated per each spectrum. In case, in normal daylight, r_3 was greater than one ($r_3 > 1$) the spectrum was used for further analysis (Wernand, 2002).

4.4.1.4. Minimal data flagging

We applied the minimal data flagging to set the minimum incoming E_S level from which was expected a detectable signal back from the water column. To perform this minimal data flagging, the values of E_S measurements at a wavelength of 480 nm, $r_4 = E_s\,(\lambda = 480\text{ nm})$ were extracted per each spectrum. In case $r_4 > 20$ (mW m^{-2} nm^{-1}), the measurement was used for further analysis (Wernand, 2002). The implemented data flagging of this research are summarized in Table 4.2:

Table 4.2. The implemented flags for doing data quality control (Wernand, 2002).

Flag name[1]	SZA	Sun-glint	Meteorology	Spectral shape	Solar light
Threshold[2]	SZA<60°	minimal value of r_1	$r_2 > 0.25$	$r_3 > 1$	$r_4 > 20$
Status	accepted	accepted	accepted	accepted	accepted

[1] More detailed information on this proposed data flagging can be found in Wernand (2002).
[2] $r_1 = (L_{sfc\ (South\text{-}West;\ South\text{-}East)}(550\text{ nm}))$; $r_2 = E_S(940\text{ nm})/E_S(370\text{ nm})$; $r_3 = E_S(470\text{ nm})/E_S(680\text{ nm})$; $r_4 = E_s(480\text{ nm})$.

In this study we applied the above-mentioned data quality control approach to the full archive of the NJS data to extract high-quality measurements for further analysis as follows:

4.4.2. R_{rs} measurements of the NJS

The extracted high-quality hyperspectral measurements were used to simulates in-situ water leaving reflectance values (R_{rs}) as follows:

$$R_{rs} = \frac{L_{sfc} - (f_{sky} \times L_{sky})}{E_S} \tag{4.1}$$

where R_{rs} is the water leaving reflectance values, L_{sfc} is water surface radiance values, and E_s is down-welling irradiance values. f_{sky} = 0.0265 is the average value of the sky correction factor which was taken from the NASA report by Mueller et al. (2004). It should be noted that concerning the sun-glint contamination, the $L_{sfc\ (South\text{-}West)}$ was used when its values at 550 nm were minimum and accordingly $L_{sky\ (South\text{-}West)}$ was used for the sky correction and vice-versa. The simulated high-quality R_{rs} values were later used for the retrieval of WCCs using the 2SeaColor model as is described in the following sections:

4.4.3. The 2SeaColor model

In this study, we applied the 2SeaColor model developed by Salama and Verhoef (2015) for simultaneous retrieval of WCCs retrieval from simulated R_{rs} values at the NJS. This model has already shown high accuracy for the retrieval of water optical properties in turbid waters in the Dutch Wadden Sea and other coastal areas in previous studies (Arabi et al., 2018; Ambarwulan et al., 2011; Arabi et al., 2016; Yu et al., 2016a). The 2SeaColor model simulates R_{rs} values defined by the solution of the two-stream radiative transfer equations containing direct sunlight, as explained by Salama and Verhoef (2015):

$$r_{sd}^{\infty} = \frac{\sqrt{1+2x}-1}{\sqrt{1+2x}+2\mu_w} \tag{4.2}$$

$$R_{rs} = \frac{0.52 \times R(0^-)}{1 - 1.7 \times R(0^-)} \tag{4.3}$$

Where $\boldsymbol{r_{sd}^{\infty}}$ is the directional-hemispherical reflectance of the semi-infinite medium, μ_w is the cosine of the SZA beneath the water surface. $R(0^-)$ is the irradiance reflectance beneath the water surface which is equal to $\boldsymbol{r_{sd}^{\infty}}$/Q under the sunny condition and Q = 3.25. R_{rs} is the calculated water-leaving reflectance values. The ratio of x is based on the simple equation of x = b_b/a while b_b is total backscattering coefficient and, a is to the total absorption coefficient as follows (Salama et al., 2009):

$$a(\lambda) = a_W(\lambda) + a_{Chla}(\lambda) + a_{NAP}(\lambda) + a_{CDOM}(\lambda) \tag{4.4}$$

$$b_b(\lambda) = b_{bw}(\lambda) + b_{b,Chla}(\lambda) + b_{b,NAP}(\lambda) \tag{4.5}$$

where the subscripts of W, Chla, NAP and CDOM stand for water molecules, Chlorophyll-a, Nan-algae Particles, and Coloured Dissolved Organic Matter, respectively. In this study, we applied the same parametrization approach proposed in Table 4.3 by Arabi et al. (2018) to calculate the absorption and backscattering coefficients of WCCs in the study area.

4.4.3.1. Applying the 2SeaColor model on in-situ R_{rs} measurements

We applied the 2SeaColor model inversion for simultaneous retrieval of Chla, SPM concentrations and CDOM absorption from the time series of quality-controlled R_{rs} measurements collected every fifteen minutes from 9:30 a.m. to 11:30 p.m. (UTC) between 2003 and 2018 at the NJS. To do the model inversion, we used a spectral optimization technique by minimizing the differences between the simulated and measured R_{rs}. Table 4.3 presents the initial values of Chla, SPM concentrations beside CDOM absorption to perform the optimization as follows:

Table 4.3. The initial guess of WCCs used in the model inversion (Arabi et al., 2018).

Variable	Unit	Lower/upper boundary	Border values
Chla concentration	mg m^{-3}	0 - 100	0 - 100
SPM concentration	g m^{-3}	0 - 100	0 - 100
CDOM absorption	m^{-1}	0 - 1.5	0 - 1.5

To show the diurnal variation of WCC retrievals, per each day, the daily average of retrieved Chla (mg m^{-3}), SPM (g m^{-3}) and CDOM absorption (m^{-1}) were computed, separately. The results of the 2SeaColor model's WCC retrievals are presented in Fig. 4.5.

4.4.3.2. Evaluation of the 2SeaColor performance

We evaluated the performance of the 2SeaColor model to simulate R_{rs} spectra against in-situ R_{rs} measurements at the three reference wavelengths of 490 nm, 550 nm, and 665 nm. Four statistical parameters of R^2, RMSE, Normalized Mean Square Error (NRMSE), and Relative Root Mean Square Error (RRMSE) were used to quantify the goodness-of-fit between simulated and measured R_{rs} values for the quality-control NJS dataset. The results of this statistical analysis are presented in Fig. 4.6 and Table 4.7.

4.4.4. The coupled 2SeaColor-MODTRAN model

In this study, we applied the coupled TOA radiance approach of 2SeaColor-MODTRAN proposed by Arabi et al. (2016) for the simultaneous retrieval of WCCs from multi-sensor satellite images of MERIS, MSI, and OLCI. This model has already shown high accuracy for the retrieval of WCCs from MERIS images over the Dutch Wadden Sea under various condition of water turbidity and atmospheric local haze variations with considerable improvement in comparison to MERIS regional Case 2 water algorithm (C2R) (Doerffer and Schiller, 2007) in previous studies (Arabi et al., 2016).

Following Arabi et al. (2016), per each image, a LUT of R_{rs} simulations generated based on different combinations of WCCs by using 2SeaColor model were combined with a LUT of atmospheric parameters generated based on different combinations of aerosol types and visibilities by using the RT model of MODTRAN (Berk et al., 2011). As a result, a bigger LUT of TOA radiances were generated based on different combinations of water turbidity and atmospheric conditions per each image, separately. By finding the best spectral fit (RMSE) between the TOA radiances LUTs and the pixel TOA radiance, the simultaneous concentrations of WCC were retrieved from satellite images.

Moreover, by applying this coupled 2SeaColor-MODTRAN model, the atmospheric properties of visibility and aerosol type were also retrieved simultaneously besides the WCCs. However, evaluation of the retrieved atmospheric properties by this model was outside the scope of this research and, therefore, was not presented in this manuscript. In the following sections, more details on applying the coupled 2SeaColor-MODTRAN model on multi-sensor satellite images of this research are presented.

4.4.4.1. LUT processing for generating R_{rs} values

The 2SeaColor model was used to model R_{rs} values for the different combinations of Chla, SPM, and CDOM concentration values per given SZA at the recording time of each R_{rs} measurement at the NJS, separately. Table 4.4 shows the LUT composition of the 2SeaColor model in this study.

Table 4.4. The input variables to build-up the LUTs of calculated R_{rs} spectra using the 2SeaColor model.

Variable	Source	Unit	Values	Step[2]	Step
Chla	case study status	mg m^{-3}	0 - 100	0.1	5
SPM	case study status	g m^{-3}	0 - 100	0.1	5
CDOM	case study status	m^{-1}	0 - 1.5	0.1	0.5
SZA[1]	SZA formula	degree	30 - 60	-	-

[1] SZA can be calculated concerning the date, time, zone and the geographical location (the NJS) of each measurement, separately, using SZA formulas.
[2] The WCC steps varied while the coupled 2SeaColor-MODTRAN model was applied to the single location of the NJS and the study area.

The calculated R_{rs} values by Eq. (4.3) using the 2SeaColor model were stored as an R_{rs} LUTs and was later combined with the modeled atmospheric parameters LUTs using MODTRAN as follows:

4.4.4.2. LUT processing for generating atmospheric parameters

We used the radiative transfer model MODTRAN 5.2.1 (Berk et al., 2011) to calculate the MODTRAN parameters describing the atmospheric effect, which comprise the atmospheric path radiance (L_0), the total gain factor (G) and the spherical albedo (S). MODTRAN needs several input variables including aerosol type, visibility, environmental variables (*e.g.,* carbon dioxide, ozone, water vapor) and illumination geometry (i.e., SZA, VZA, RAA) to describe the real condition of the atmosphere at the time of satellite image overpass.

In this study, we ran a MODTRAN programme for modeling atmospheric parameters for a given atmospheric state and angular geometry, per each image, separately. We obtained the environmental variables from Global Reference Networks concerning the location of the study area and each satellite image capturing date, separately. We defined the visibility steps considering that a change in lower visibilities (*e.g.,* 4 km) has much more effect on the TOA radiances than a change at higher visibilities (*e.g.,* 40 km). Therefore, we used Inverse Visibility (IV) to obtain almost perfect linear increments in AOT (Aerosol Optical Thickness). Based on this method, values of IV were set equal to 100 divided by the actual visibility (100 / Vis). We ran MODTRAN with the values 1, 2, 3, ... , 25 for IV and, therefore, with the corresponding actual visibilities (100, 50, 33.3, …, 4 km). By varying the visibility, we were able to produce a series of corresponding atmospheric parameters (*e.g.,* atmospheric path radiance, transmittance) at all wavelengths. We used three aerosol types of urban, maritime and rural in this study. The Mid-Latitude Summer atmospheric vertical profile and the Full Width at Half Maximum (FWHM) of 10 nm were used to run MODTRAN. The summary of the input variables to run MODTRAN and their corresponding variations in the study are described in Table 4.5.

Table 4.5. The input variables, their used sources, units, ranges, and steps to run MODTRAN in this research.

Variable	Source	Unit	Range	Step
Atmospheric profile	study area status	-	Mid-Latitude Summer	constant per image
CO_2 [1, 2]	global websites	ppm	380 - 410	constant per image
O_3	global websites	DU	250 - 450	constant per image
H_2O	global websites	g cm^{-2}	0.5 - 4.5	constant per image
Surface height	water surface height	km	0	constant value
Sensor height[3]	sensor height	km	800/786/814	constant per image
Correlated-k option[4]	(Berk et al., 2011)	-	Yes	constant value
DISORT number of streams	(Berk et al., 2011)	-	8	constant value
Start, ending wavelength[5]	sensor band coverage	nm	350 - 1000	1
SZA[6]	satellite image	degree	30 - 60	constant per image
VZA	satellite image	degree	5 - 30	constant per image
RAA	satellite image	degree	0 -150	constant per image
Visibility	study area status	km	1 - 100	100, 50, 33.3, …, 4
Aerosol-type	study area status	-	maritime,urban,rural	-

[1] Environmental variables were found in Global Reference Networks concerning the geographic location of the study area and the satellite image capturing date.
[2] The ranges of environmental variables were determined with respect to their annual variations at the Dutch Wadden Sea between 2003 and 2018.
[3] The sensor height varied concerning the altitude of each satellite orbit (MERIS: 800 km, MSI: 786 km and OLCI: 814 km) from the Earth, separately.
[4] Detailed information on the correlated-k option and DISORT number of streams values can be found in MODTRAN user's manual 5.2.1 (Berk et al., 2011).
[5] Start and ending wavelengths varied concerning each satellite band coverage, separately.
[6] Illumination geometry (SZA, VZA, RAA) were extracted from MERIS, MSI and OLCI images directly.

MODTRAN obtained these input variables from a .tp5 text file and stored its simulation results as a .tp7 text file. This .tp7 file was used later as input to calculate the MODRAN atmospheric parameters of L_0, G and S. Finally, TOA radiances, L_{TOA} (Wm^{-2} sr^{-1} μm^{-1}), in the sensor's bands were calculated in surface reflectance r by the following equation (Verhoef and Bach, 2003):

$$L_{\mathrm{TOA}} = L_0 + \frac{Gr}{1-Sr} \tag{4.6}$$

where L_{TOA} is the modeled TOA radiance values (W sr^{-1} m^{-2} nm^{-1}), and r is the hemispherical water-leaving reflectance (=πR_{rs}). For making LUTs TOA radiances in the sensor's spectral bands, reflectance spectra generated by the 2SeaColor model at 1 nm resolution were convolved with the spectral response functions of MERIS, MSR, and OLCI, respectively, and the same was done with high-resolution MODTRAN spectra of the atmospheric parameters before applying Eq. (4.6). The simultaneous retrieval of WCCs was performed by finding the best fit (RMSE) between the pixel TOA radiance spectrum and the modeled TOA radiances (Eq. (4.6)). The spectral fitting was performed using lsq function in Matlab. To find the best TOA spectral fitting using the coupled model, for MERIS, all bands were used except the band numbers 1, 2 and 11 and 12, and for OLCI all bands were used except the band numbers 1, 2, 3, 13, 20 and 21. Bands 11 and 13 are located in the O_2-A absorption band for MERIS and OLIC, respectively, and can give erroneous results due to sampling errors. For MSI, all bands were used except the band numbers 2, 9, 10, 11. Per each sensor, other excluded bands gave systematic deviations in R_{rs} after atmospheric correction. The cause of this problem is presently still unknown.

4.4.4.3. Applying the coupled 2SeaColor-MODTRAN model on multi-sensor satellite images

The above approach was applied to the MERIS and OLCI images, directly, since they provide TOA radiances per pixel. The MSI image offers TOA reflectance information. Therefore, the MSI TOA reflectances were, first, inverted to MSI TOA radiances using ENVI 5.5. Moreover, the spatial resolution of each band of MSI sensor was resized to 300 m, separately, to provide the same spatial resolution with MERIS and OLCI sensors (full spatial resolution: 300 m). The reason to resize these MSI pixels was that the high spatial resolution of MSI images (10 m, 20 m, and 60 m) was not an advantage when comparing to in-situ measurements from the single location of the NJS.

We applied the coupled 2SeaColor-MODTRAN model on all available cloud-free satellite images of MERIS (207 images), MSI (24 images) and OLCI (20 images) between 2003-2018. First, we applied this coupled model one single location of the NJS. For this one pixel retrieval, the small steps of 0.1 were taken for Chla concentrations (mg m^{-3}), SPM concentration (g m^{-3}) and CDOM absorption at 440 nm (m^{-1}), respectively, to find the more accurate solution (Table 4.4). The results of these retrievals are presented in Fig. 4.8. However, the current procedure is not suitable to be applied pixel by pixel over the image. This issue is explained in detail in section 4.4.6.

4.4.4.4. Evaluation of the coupled 2SeaColor-MODTRAN model's performance

We validated the accuracy of the coupled 2SeaColor-MODTRAN model's atmospheric correction approach against in-situ R_{rs} measurements using 145 MERIS, 20 MSI, and 17 OLCI-matchups at the three band centers of 490 nm, 550 nm, and 665 nm. To do this, we first selected a narrow window (five by five pixels) around the NJS from every satellite image, separately. Next, following Arabi et al. (2016), we extracted the darkest pixel among these five by five pixels per image using Matlab assuming that this darkest pixel was the least contaminated by the adjacency effect from the neighboring coastal area (Bulgarelli and Zibordi, 2003). The simultaneous retrieval of WCCs was performed by spectrally fitting the coupled model-simulated TOA radiances (using RMSE) to TOA radiances as it was explained in section 4.4.4.2. Fig. 4.4 shows the general view of implication and validation of the coupled 2SeaColor-MODTRAN model at the NJS. However, it should bear in mind that this TOA coupling approach does not apply atmospheric correction directly and only compares the simulated TOA radiances with the ones recorded at satellite sensors. Therefore, to retrieve the water-leaving reflectances (r) at each band the inverse Eq. (4.6) was used as follows:

$$r = \frac{L_{TOA} - L_0}{G + (L_{TOA} - L_0)S} \tag{4.7}$$

where r the hemispherical water-leaving reflectances ($=\pi R_{rs}$), L_{TOA} is the modeled TOA radiances (W sr^{-1} m^{-2} nm^{-1}), L_0 is the atmospheric path radiance, G is the total gain factor and, S is the spherical albedo simulated by MODTRAN. The statistical parameters of R^2, RMSE, NRMSE, and RRMSE were applied to evaluate the goodness-of-fit between measured and derived R_{rs} values for all matchups. The results of this validation are presented in Fig. 4.9 and Table 4.8.

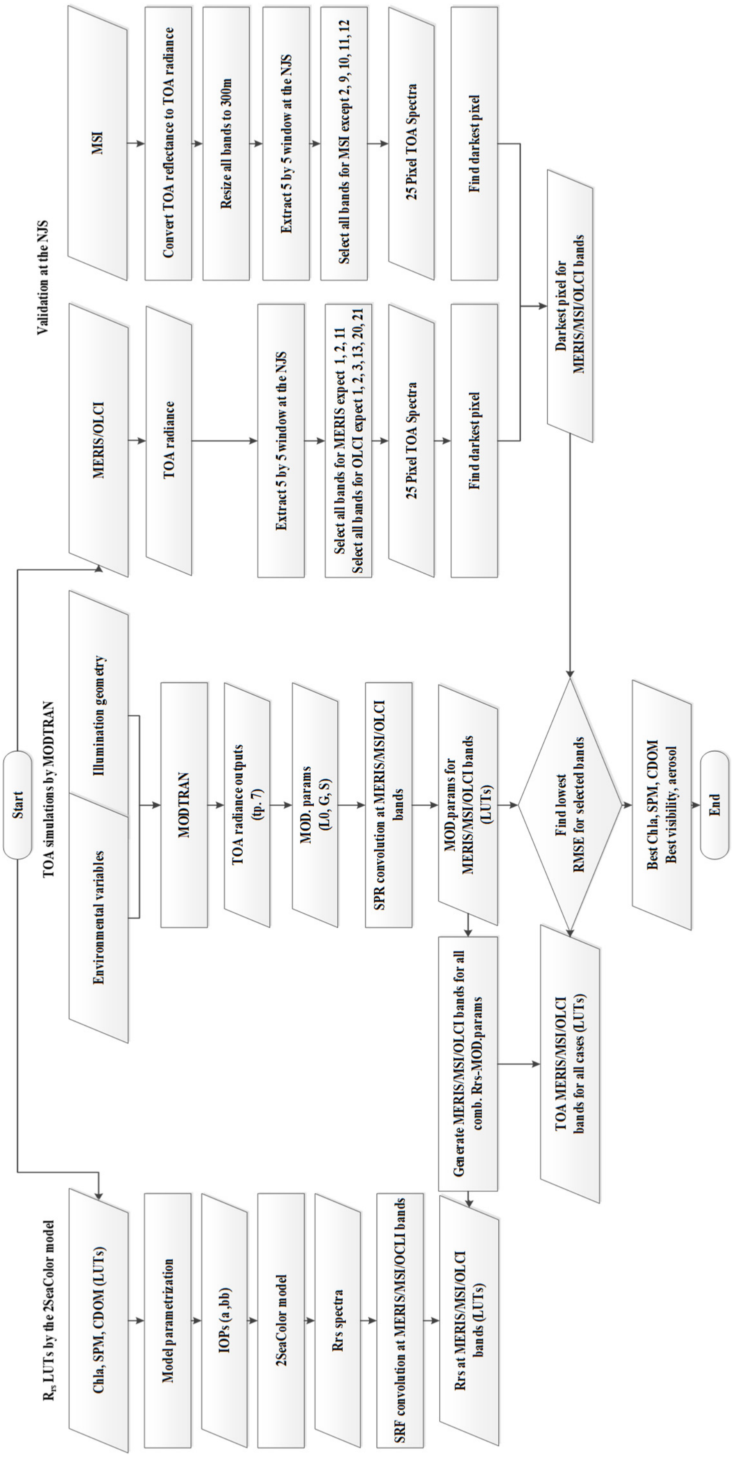

Figure 4.4. The flowchart for implementing and validating the coupled 2SeaColor-MODTRAN model using MERIS, MSI and OLCI images at the NJS.

4.4.5. Comparison of WCC-retrievals from in-situ measurements and multi-sensor satellite images

The statistical parameters of R^2, RMSE, NRMSE, and RRMSE besides the Taylor diagram (Taylor, 2001) were used to quantify the agreement of retrieved Chla concentration (mg m^{-3}), SPM concentration (g m^{-3}) and CDOM absorption (m^{-1}) by using the coupled 2SeaColor-MODTRAN model at TOA level from MERIS, MSI and OLCI images against the retrieved ones by using the 2SeaColor model at water surface level from in-situ R_{rs} measurements. The results of these evaluations are presented in Figs. 4.11 and 4.12 and Table 4.9.

4.4.6. Spatio-temporal variability of WCCs using satellite images over the study area

After evaluating the accuracy of the coupled 2SeaColor-MODTRAN model's simulations, we applied this model on MERIS, MSI and OLCI images over the study area to generate WCC maps. We presented these maps using two MERIS and OLCI images captured during high and low tidal phases, respectively. The reason to choose these images in different tidal phases was the location of the shallow waters of the Dutch Wadden Sea in a tidal area where the variation of WCCs is considerably affected by the tide. We obtained the corresponding tidal phase information (high or low tide) for each image overpass in the study area from the Den Helder station also located at the western inlet of the Dutch Wadden Sea. The date and tidal information of these images are provided in Table 4.6.

Table 4.6. Images dates, SZA and tidal phases at the study area.

Satellite	Date	Tidal phase[1]	SZA
MERIS	14-08-2002	high	41°
MERIS	19-04-2009	low	43°
OLCI	05-05-2018	high	39°
OLCI	06-06-2018	low	36°

[1] The phase of the tide (high: flood or low: ebb) at satellite overpass in the Dutch Wadden Sea.

To apply the model in a pixel-by-pixel approach for the whole region of interest, a small LUTs for WCCs and atmospheric properties of visibility and aerosol type were selected. For WCC retrievals, the steps of 5 were taken for Chla concentrations (mg m^{-3}) and SPM concentration (g m^{-3}), respectively. For CDOM absorption (m^{-1}), only steps of 0, 0.5, 1 and 1.5 were taken (Table 4.4). For atmospheric properties, the best spectral fitting match was found by considering only the first five visibilities that would generate non-negative reflectances in all selected bands and three aerosol types. This approach worked super-fast when applied using MatLabR2017B on a personal PC [Processor: Intel (R) cORE (tm) i7 - 4700 MQ, CPU: 2.40 GHz, RAM: 7.88 GB]. In total, the average number of pixels per image was equal to 70,000. The total number of LUT cases for each pixel is 15 (5 visibility, 3 aerosol types) times the number of water cases (in total 21 × 21 × 4 = 1764 cases). The computation time to generate each map was thirteen minutes. In this approach six output maps were generated, containing aerosol type, visibility, Chla concentration, SPM concentration, CDOM absorption, and the RMSE spectral error. The generated WCC maps are presented in section 4.4.5. It should be mentioned that applying the coupled 2SeaColor-MODTRAN model on MSI images did not lead to high-quality WCC maps. Therefore the generated maps by MSI images are not presented in this manuscript.

4.5. Results

4.5.1. Long-term variability of WCCs at water surface level using in-situ R_{rs} measurements

Fig. 4.5 presents a 15-year variation of retrieved WCCs by the 2SeaColor model (section 4.4.3) from the quality-controlled in-situ R_{rs} measurements collected every fifteen minutes between 2003 and 2018 at the NJS. As it was explained in section 4.4.3.1, per each day, the daily average of retrieved WCCs is computed, separately, to show the diurnal variation of these retrievals.

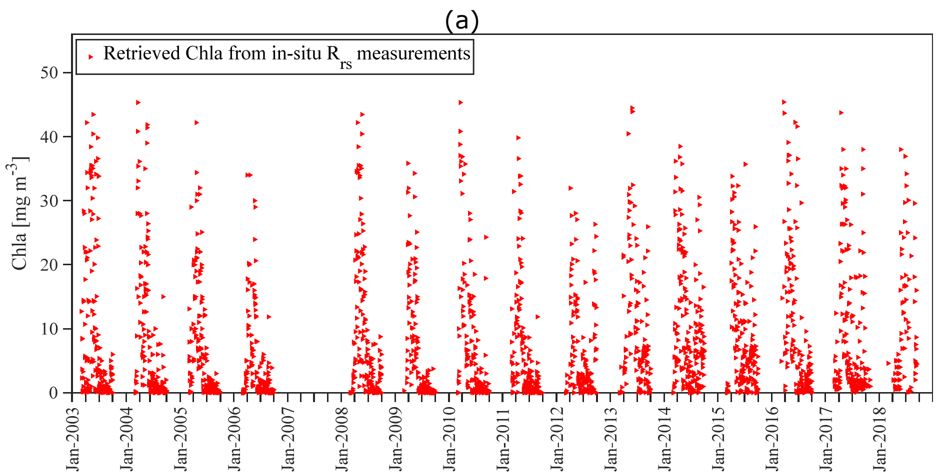

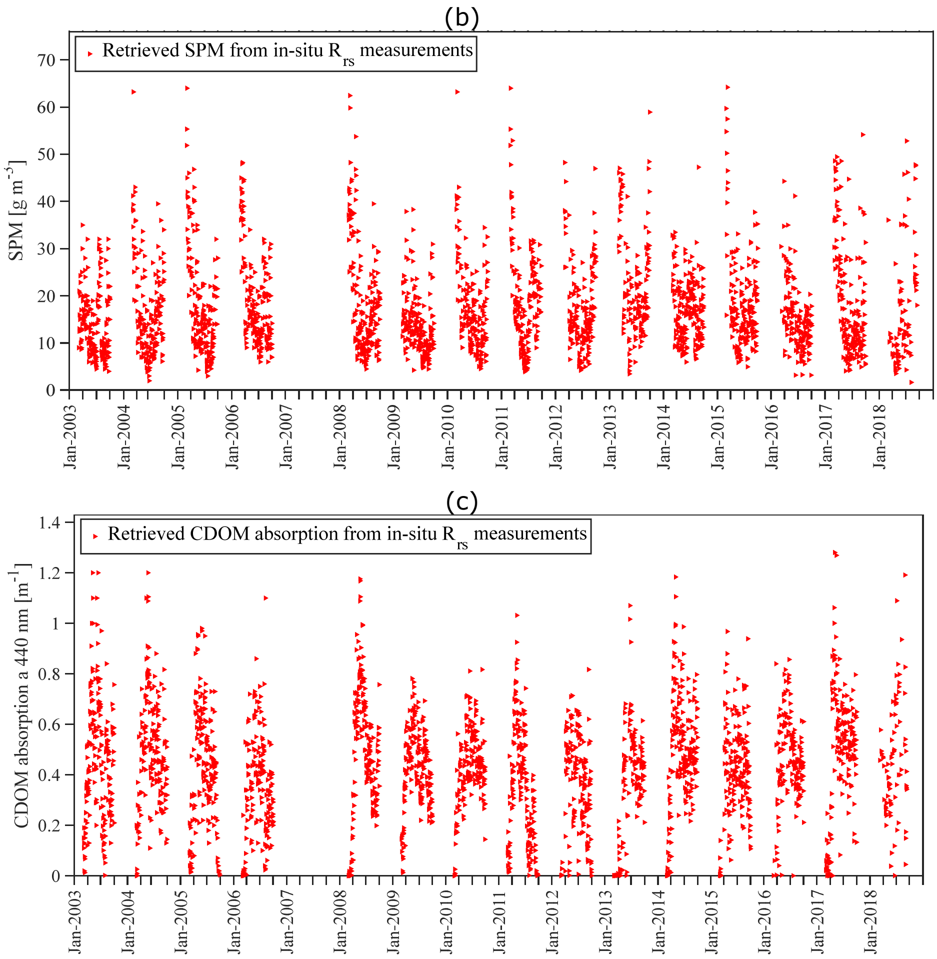

Figure 4.5. The diurnal variation of retrieved WCCs using the 2SeaColor model from time series of in-situ R_{rs} measurements collected between 2003 and 2018 at the NJS (SZAs < 60°); (a): Chla concentrations (mg m^{-3}); (b): SPM concentrations (g m^{-3}); (c): CDOM absorption at 440 nm (m^{-1}).

In Fig. 4.5 the x-axis shows the number of different years between 2003 and 2018. To have a better visual presentation, each year is divided to four sections concerning the occurrence of four seasons at the Dutch Wadden Sea: winter (from January to March), spring (from April to June), summer (from July to September) and autumn (from October to December). The y-axis shows the daily average values (from 9:30 a.m to 11:30 p.m.) of retrieved WCCs from in-situ R_{rs} measurements. As it was explained before, due to the SZA flagging data proposed by Arabi et al. (2018), only the WCC retrievals from March to September (SZAs < 60°) are presented per each year. Moreover, there was no data recorded during the spring and summer in 2007 at the NJS. That is why there is a gap to report the variation of retrieved WCCs in 2007.

As can be seen from Fig. 4.5 (a), the highest values of retrieved Chla concentrations (mg m^{-3}) are mainly reported during spring period (April, May, and June) ~ 45 (mg m^{-3}) with the similar temporal trend within multiple years. After the spring period, retrieved Chla concentration values start to decrease in July (~ 10 (mg^{-3})) and increase again in September (~ 30 (mg m^{-3})). This increase in the retrieved Chla concentration values is even more pronounced between 2014 and 2018 which cause the second peak of the retrieved Chla concertation values during September (~ 35 (mg m^{-3})) in these years. The retrieved SPM concentrations from in-situ R_{rs} measurements show their highest values (~ 65 (g m^{-3})) at the beginning of spring in March (Fig. 4.5 (b)). They start to decrease from May to July (~ 25 (g m^{-3})) and increase again between August and September (~ 40 (g m^{-3})). The retrieved CDOM absorptions (m^{-1}) show a slight decrease during July (~ 0.8 (m^{-1})) and reach their lowest values in September (~ 0.4 (m^{-1})) (Fig. 4.5 (c)).

Moreover, as can be seen in Figs. 4.5 (a) and (c), the temporal variation of CDOM absorptions (m^{-1}) is independent of that of the retrieved Chla concentrations values (mg m^{-3}) (Yu et al., 2016). Overall it can be concluded that the diurnal variation of retrieved WCCs at the NJS show almost the similar temporal trends over multiple years from 2003 to 2018 while these patterns slightly differ after 2014. Moreover, the provided information on variation ranges of retrieved WCC are within the ranges of in-situ ones measured by other researchers in the study area (Chla: 0 - 100 (mg m^{-3}); SPM: 0 - 100 (g m^{-3}); CDOM absorption at 440 nm: 0 - 2 (m^{-1})) (Cadée, 1996; Hommersom et al., 2009; Reuter et al., 2009; Tillmann et al., 2000).

4.5.1.1. Validation of the 2SeaColor model's simulations

Below we present the validation of the 2SeaColor model to simulate R_{rs} values against in-situ R_{rs} measurements at the three wavelengths of 490 nm, 550 nm, and 665 nm as follow:

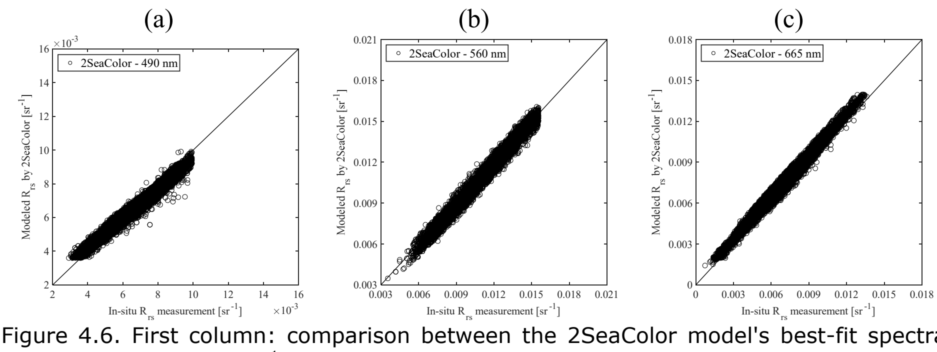

Figure 4.6. First column: comparison between the 2SeaColor model's best-fit spectra and in-situ R_{rs} values (sr^{-1}) for the quality-controlled dataset between 2003 and 2018 at the NJS; second column: comparison between MERIS-atmospheric corrected R_{rs} and in-situ R_{rs} values (sr^{-1}) for 145 matchups between 2003 and 2012 at the NJS; third column:

comparison between MSI-atmospheric corrected R_{rs} and in-situ R_{rs} values (sr^{-1}) for 20 matchups between 2015 and 2018 at the NJS; fourth column: comparison between OLCI-atmospheric corrected R_{rs} and in-situ R_{rs} values (sr^{-1}) for 17 matchups in 2018 at the NJS for band centers of the first row: 490 nm; second row: 560 nm and third row: 665 nm.

The related statistical analysis of this evaluation is presented in Table 4.7 as follows:

Table 4.7. Evaluation of the 2SeaColor models' best-fit spectra against in-situ R_{rs} values (sr^{-1}) for the quality-controlled dataset collected every fifteen minutes between 2003 and 2018 at the NJS (SZAs < 60°) for wavelengths of 490 nm, 560 nm, and 665 nm.

Statistical analysis	R^2	RMSE × 10^{-2}	NRMSE (%)	RRMSE (%)
490 nm	0.97	0. 02	03.1	03.3
560 nm	0.98	0. 03	02.6	02.8
665 nm	0.98	0. 02	01.8	03.2

As can be seen from Table 4.7, there is a robust agreement between the simulated and in-situ R_{rs} values for the quality controlled dataset which are recorded every fifteen minutes between 2003 and 2018 at the NJS. The calculated R^2 values are greater than 0.95, and RMSE values do not exceed 0.0003 for all three selected wavelengths. Moreover, the calculated NRMSE and RRMSE show reasonable estimates (NRMSE and RRMSE < 3.5%).

Moreover, the robust agreements between simulated and in-situ R_{rs} values can be considered as an approval that the implemented parametrizations of the 2SeaColor model (taken from Table 2 Arabi et al. (2018)) are suitable enough for these long-term WCC retrievals in this study. Therefore, it can be stated that the 2SeaColor model is capable enough to accurately simulate R_{rs} values for a period of 15-year in different dates, seasons (SZAs < 60°) and water turbidity conditions at the NJS. Moreover, as Arabi et al. (2018) showed 2SeaColor-WCC retrievals are in very good agreement (R^2 > 0.80 and RMSE < 3 for Chla and SPM) against in-situ WCC measurements collected in a daily basis at the NJS between 2008-2010 (Arabi et al., 2018).

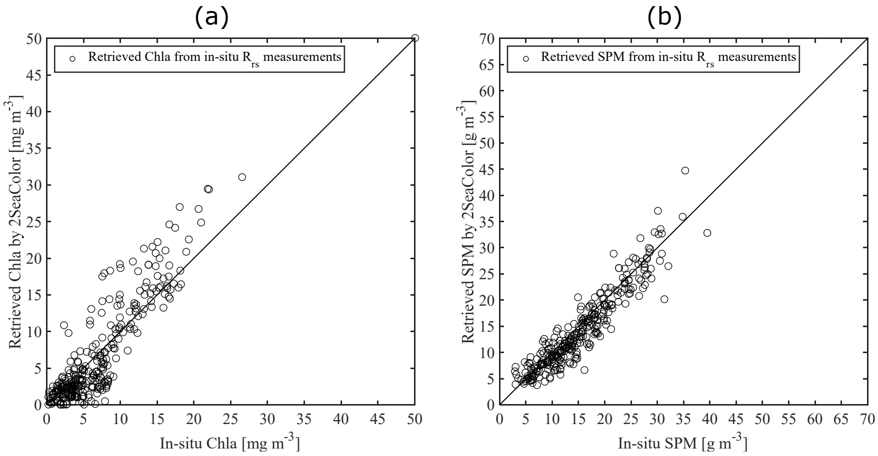

Figure 4.7. Comparison between the 2SeaColor-WCC retrievals against in-situ ones collected between 2008 and 2010 at the NJS (SZAs < 60°): (a) Chla (mg m^{-3}); and (b) SPM (g m^{-3}) (Arabi et al., 2018).

Therefore, with respect to high accuracy of the 2SeaColor model for accurately simulate R_{rs} spectra (Fig. 4.6 and Table 4.7) at this study and for accurately retrieve WCCs (Fig. 4.7) in previous studies (Arabi et al., 2018), these 15-years diurnal retrieved WCCs can be considered as the reliable representatives of actual values of WCC at the NJS.

These results are important to analyze temporal course (monthly, seasonal and annual variations) of WCCs at the study site. Of particular interest when analyzing the long-term variability in these constituents' trends, is whether any significant decreasing trend from 2003 to 2018 would indicate the effect of prior nutrient reduction management actions (Le et al., 2013). More importantly, since the in-situ R_{rs} measurements are contaminated the least by the effect of atmosphere at water surface level, these long-term in-situ R_{rs}-WCC retrievals can be considered as a reliable source of information to be compared with satellite-WCC retrievals.

4.5.2. Long-term variability of WCCs at TOA level using multi-sensor satellite images

Fig. 4.8 presents 15-year variations of retrieved WCCs at a single location of the NJS using the coupled 2SeaColor-MODTRAN model (section 4.4.4) from all available cloud-free multi-sensor satellite images of MERIS (2002-2012), MSI (2015-2018) and OLCI (2018).

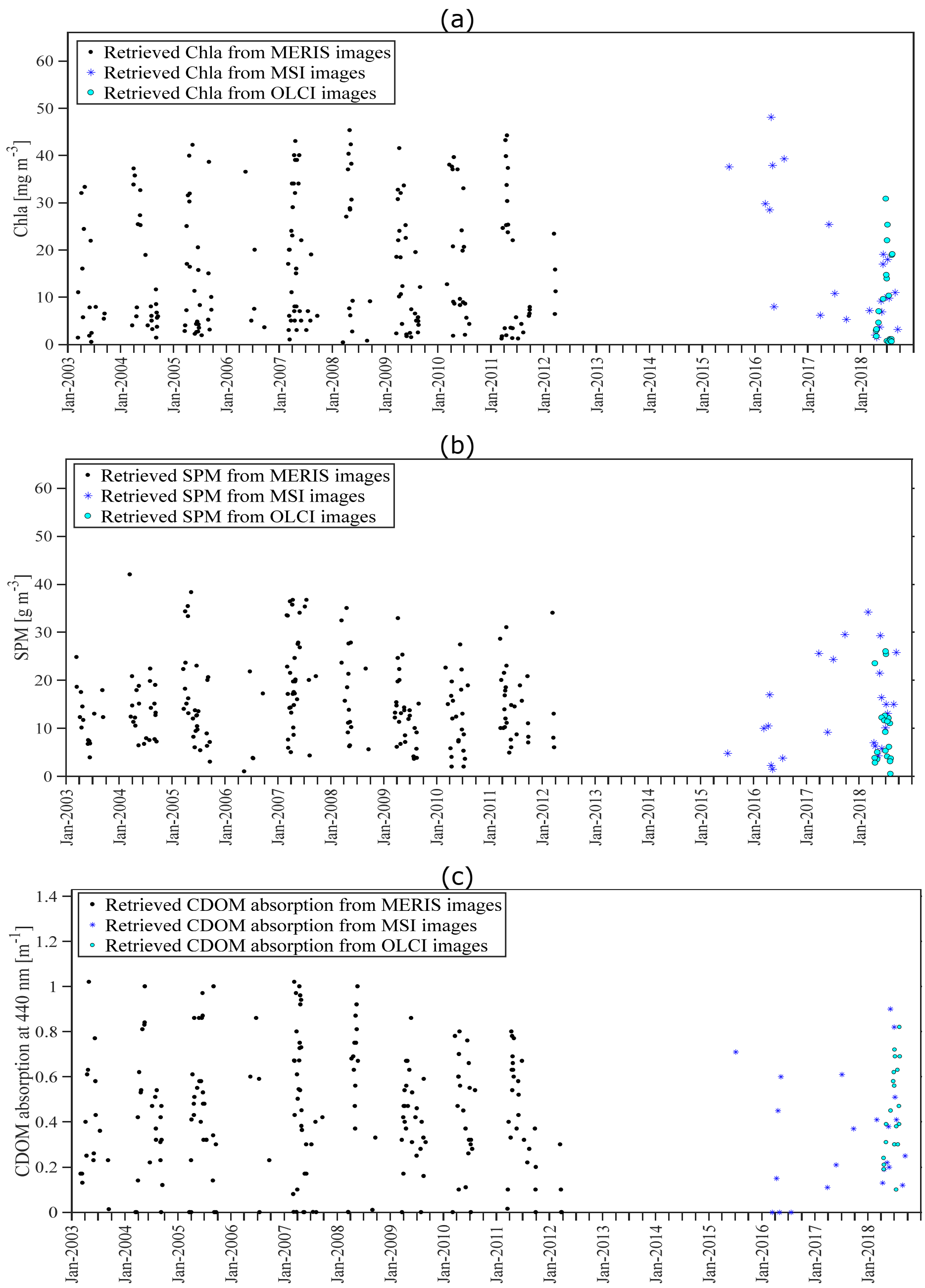

Figure 4.8. Variation of retrieved WCCs using the coupled 2SeaColor-MODTRAN model at the NJS (SZAs < 60°) from: black circle: 207 cloud-free MERIS images captured between 2003 and 2012; blue stars: 24 cloud-free MSI images captured between 2015 and 2018; cyan circle: 20 cloud-free OLCI images captured in 2018; (a): retrieved Chla concentrations (mg m^{-3}); (b): retrieved SPM concentrations (g m^{-3}); (c): retrieved CDOM absorption at 440 nm (m^{-1}).

Like before, the x-axis of Fig. 4.8 shows the number of different years between 2003 and 2018 and the y-axis shows the retrieved WCCs from MERIS (black circles), MSI (blue stars) and OLCI (cyan circles) images using the coupled 2SeaColor-MODTRAN model. As it was explained before, The MERIS sensor worked only between 2003 and 2012 and the first images of MSI and OLCI sensors were available since 2015 and 2018, respectively. Therefore, there is a gap to show the variation of WCC retrievals between 2012 and 2015 in these figures.

As can be seen in Fig. 4.8, due to a limited number of available cloud-free satellite images in comparison to in-situ R_{rs} measurements, it is more difficult to detect the temporal variations of retrieved WCCs from TOA level. Overall MERIS retrievals (207 images) show a denser temporal pattern in comparison to MSI (24 images) and OLCI retrievals (20 images) while almost similar temporal patterns can be seen from MERIS-WCC retrievals from 2003 to 2012. Moreover as Figs. 4.8 (a), (b) and (c) show, the retrieved WCCs from MERIS, MSI and OLCI are in similar ranges (Chla: 0 - 50 (mg m^{-3}), SPM: 0 - 45 (g m^{-3}) and CDOM absorption 0 - 1.2 (m^{-1}) while OLCI-retrievals slightly show lower amplitudes in comparison to MERIS and MSI retrievals.

4.5.2.1. Validation of the coupled 2SeaColor-MODTRAN model's simulations

Fig. 4.9 presents the evaluation of the coupled 2SeaColor-MODTRAN model's performance to do the atmospheric correction (Eq. (4.7)) against in-situ R_{rs} measurements at the three band centers of 490 nm, 550 nm, and 665 nm using MERIS, MSI, and OLCI matchups as follows:

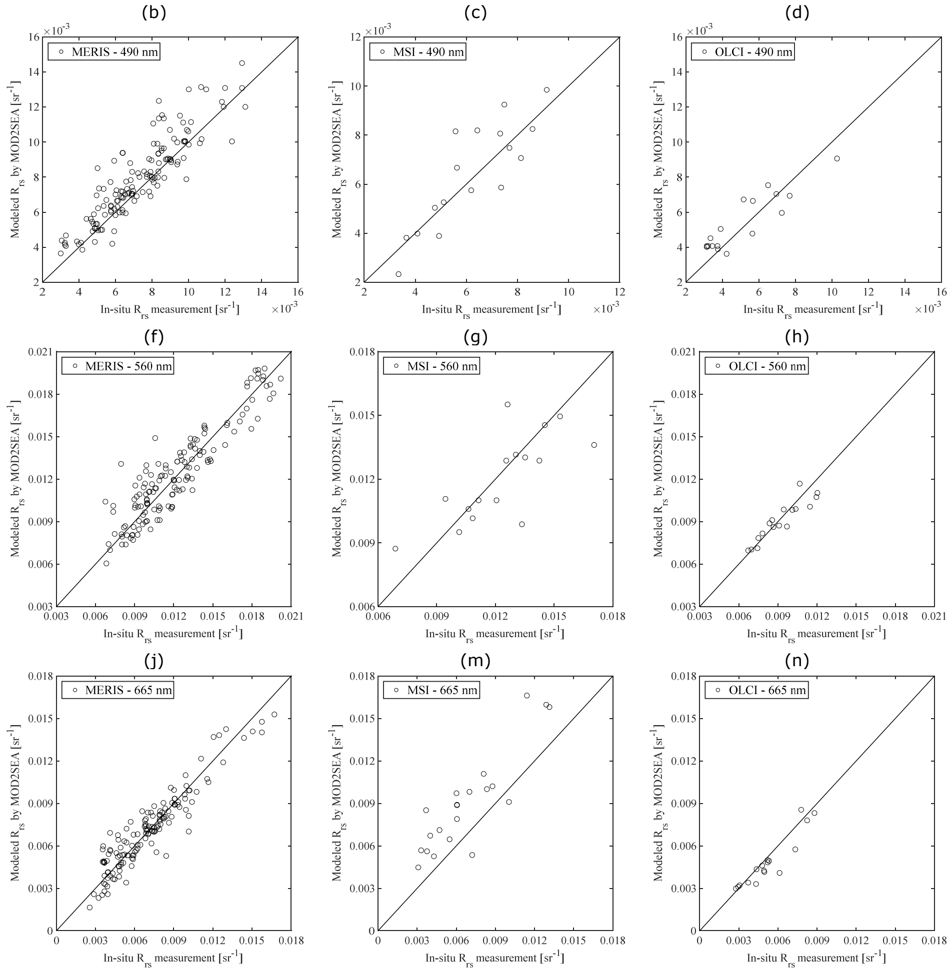

Figure 4.9. Comparison between the coupled 2SeaColor-MODTRAN-atmospheric corrected R_{rs} and in-situ R_{rs} values (sr^{-1}) at the NJS; first column: 145 MERIS-matchups between 2003 and 2012; second column: 20 MSI-matchups between 2015 and 2018 at the NJS; third column: 17 OLCI-matchups in 2018 for band centres of first row: 490 nm; second row: 560 nm and third row: 665 nm.

The related statistical analysis of this evaluation is presented in Table 4.8:

Table 4.8. Evaluation of the coupled 2SeaColor-MODTRAN model's best-fit spectra for 145 MERIS-matchups, 20 MSI-matchup and 17 OLCI-matchups against in-situ R_{rs} values (sr^{-1}) at the NJS between 2003-2018.

Statistical analysis	R^2			RMSE × 10^{-2}			NRMSE (%)			RRMSE (%)		
Band centre/ images	MERIS	MSI	OLCI	MERIS	MSI	OLCI	MERIS	MSI	OLCI	MERIS	MSI	OLCI
490 nm	0.79	0.73	0.80	0.10	0.26	0.07	09.4	09.8	09.7	13.6	14.4	13.6
560 nm	0.84	0.68	0.82	0.13	0.21	0.05	07.4	08.4	09.4	08.1	15.2	05.4
665 nm	0.87	0.74	0.86	0.09	0.17	0.03	06.3	09.9	09.2	12.6	14.6	10.1

As the results of this evaluation show, there is a reasonable agreement between in-situ and atmospherically-corrected R_{rs} values from MERIS, MSI and OLCI matchups at three band centers of 490 nm, 560 nm and 665 nm (R^2 ~ 0. 70, RMSE < 0.0035, NRMSE < 10% and RRMSE < 16%). However, OLCI atmospherically-corrected R_{rs} values show the most robust agreement (R^2 ≥ 80, RMSE ≤ 0.001) against in-situ R_{rs} measurements in comparison to the MERIS and MSI ones. This might be due to the higher signal-to-noise ratio and due to the availability of more number of spectral bands (16 bands in total) to be used for the WCC retrievals using the OLIC sensor in comparison to MERIS (i.e., 12 bands) and MSI (i.e., 8 bands) sensors (Table 4.1, Fig. 4.4). That is to say that more band information provides more WCCs accuracy. On the other hand, MSI atmospherically-corrected R_{rs} values show the lowest accuracy in comparison to OLCI and MERIS ones (R^2 ~ 70, RMSE ~ 0.002). The reason could be due to the usage of only limited numbers of spectral bands (i.e., 8 bands) for simultaneous retrieval of five variables (i.e., Chla, SPM, CDOM, visibility, and aerosol type) by the coupled 2SeaColor-MODTRAN model. Therefore, it is reasonable that the model's accuracy decreases in case of applying the coupled 2SeaColor-MODTRAN model on MSI images in comparison to MERIS and OLCI images.

Overall, considering the results of performed statistical analysis in Table 4.8, the capability of the coupled 2SeaColor-MODTRAN model can be considered good enough for doing atmospheric correction from all multi-sensor satellite images of MERI, MSI, and OLCI. Moreover, as Arabi et al. (2016) reported in previous studies, there is a reasonable agreement (R^2 > 80, RMSE < 4 for Chla and SPM) between the coupled 2SeaColor-MODTRAN WCC retrievals from MERIS-matchups concurrent with in-situ WCCs between 2008 and 2010 at the NJS with considerable improvement in comparison to standard C2R model (Arabi et al., 2016).

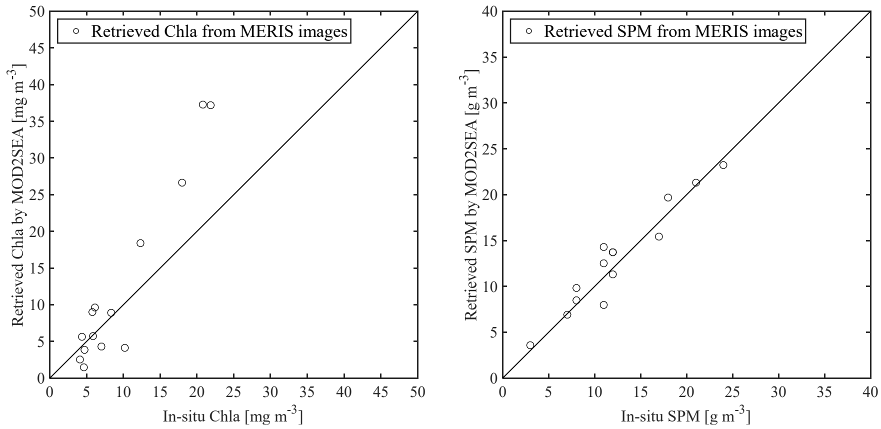

Figure 4.10. Comparison between the coupled 2SeaColor-MODTRAN model's retrievals against in-situ WCCs for 13 MERIS-matchups (SZAs < 60°) between 2008 and 2010 at the NJS: (a) Chla (mg m^{-3}); and (b) SPM (g m^{-3}) (Arabi et al., 2016)

So far, the validation of the coupled 2SeaColor-MODTRAN model's performance to retrieve WCC is only evaluated using MERIS images (Arabi et al., 2016) while there are no in-situ measurements of Chla and SPM concentrations since 2010 at the NJS to evaluate the WCC-retrievals from MSI and OLCI images. However, as it was shown in section 4.5.1, the WCC-retrievals from in-situ R_{rs} measurements can be used as reference indicators to evaluate the agreement of satellite retrievals with actual WCCs at water surface level at the NJS.

4.5.3. Correlation of WCC retrievals from satellite images and in-situ R_{rs} measurements

Below the agreement of retrieved WCCs from satellite images at TOA level with the ones retrieved from in-situ R_{rs} measurements at water surface level are presented:

(a)

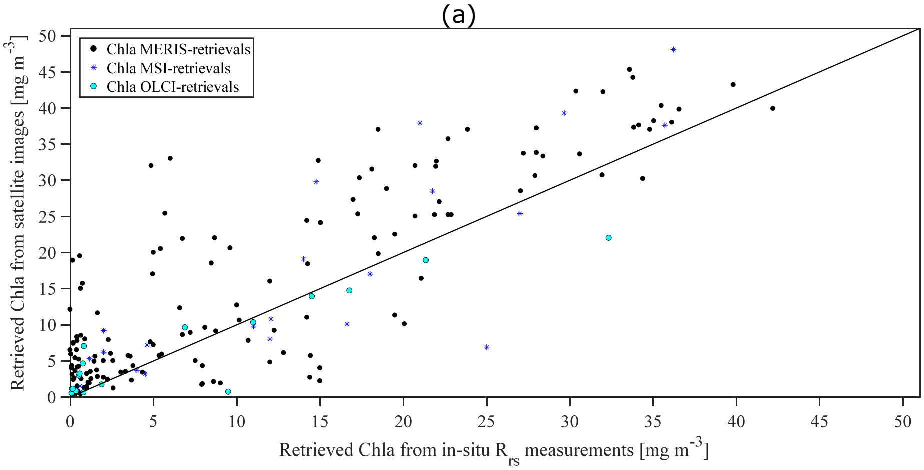

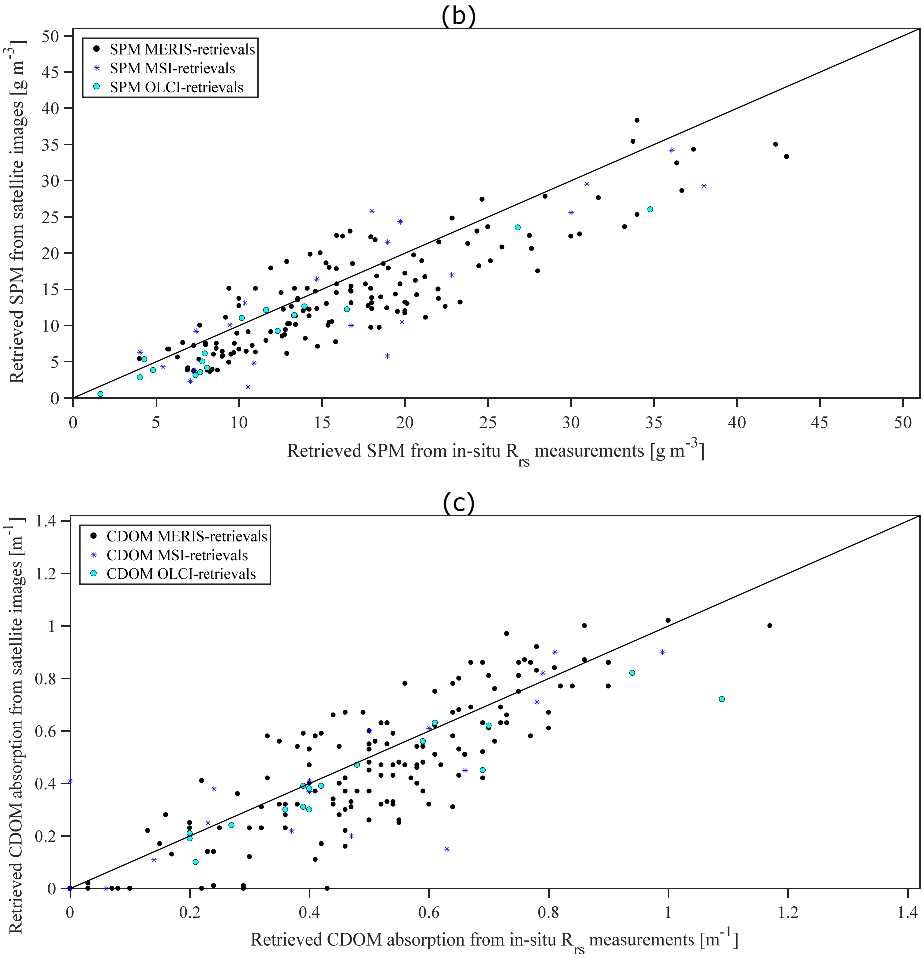

Figure 4.11 Comparison between the 2SeaColor-retrievals from in-situ R_{rs} measurements and the coupled 2SeaColor-MODTRAN retrievals from 145 MERIS-matchups (black circles), 20 MSI-matchups (blue stars) and 17 OLCI-matchups (cyan circles) at the NJS; (a): retrieved Chla concentrations (mg m^{-3}); (b) retrieved SPM concentrations (g m^{-3}); (c) retrieved CDOM absorption at 440 nm (m^{-1}).

Fig. 4.12 and Table 4.9 present the detailed statistical analysis of this evaluation:

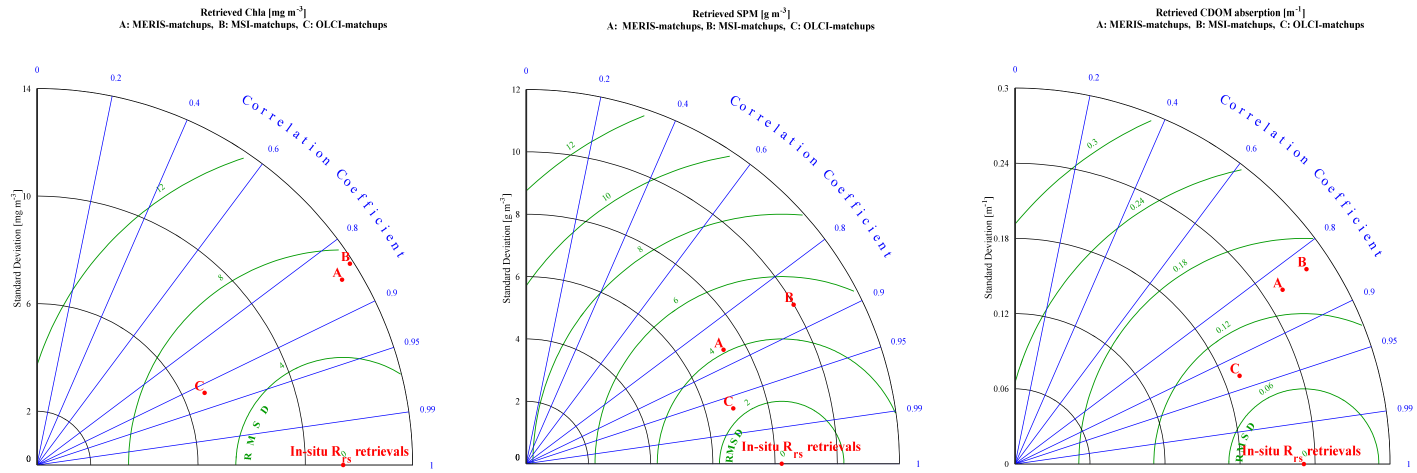

Figure 4.12. Taylor diagram showing the statistics between the 2SeaColor-retrievals from in-situ R_{rs} measurements and the coupled 2SeaColor-MODTRAN retrievals from A: MERIS-matchups, B: MSI-matchups, C: OLCI-matchups; (a) retrieved Chla concentrations (mg m^{-3}); (b): retrieved SPM concentrations (g m^{-3}); (c): retrieved CDOM absorption at 440 nm (m^{-1}).

Table 4.9. Statistical measures implemented in this study to evaluate the agreements between in-situ R_{rs} and satellite WCC-retrievals.

Constituent	Satellite-matchups	Standard deviation	Correlation coefficient	RMSE (RMSD)	R^2	NRMSE (%)	RRMSE (%)
Chla (mg m^{-3})	MERIS	13.29	0.85	06.89	0.72	16.44	52.63
	MSI	13.85	0.84	07.51	0.70	22.05	62.08
	OLCI	06.79	0.91	03.97	0.82	08.84	40.84
SPM (g m^{-3})	MERIS	07.32	0.86	03.92	0.73	05.50	11.00
	MSI	09.99	0.86	05.22	0.72	09.41	21.96
	OLCI	06.88	0.96	02.32	0.92	05.67	16.53
CDOM (m^{-1})	MERIS	0.255	0.83	0.139	0.68	11.96	27.38
	MSI	0.280	0.83	0.162	0.67	16.16	39.66
	OLCI	0.193	0.93	0.096	0.86	07.86	14.26

Taylor diagram in Fig. 4.12 presents a summary of the statistical measures and relationships between the retrieved WCCs from multi-sensor satellite images and the ones from in-situ R_{rs} measurements which are used as a reference indicator (named as in-situ R_{rs} retrievals in these diagrams). The statistical measures of retrieved WCCs from three different satellite sensors are presented by three different capital letters of A, B and C for MERIS, MSI, and OLCI, respectively. As can be seen Figs. 4.12 (a), (b) and (c), these statistical measures are simultaneously compared with each other for three different types of sensors. Moreover, in each diagram, the distance between the satellite indicator of A, B or C and the point labeled as "in-situ R_{rs} retrievals" is a measure of how realistically each satellite reproduces the retrievals at water surface level. To do this evaluation, for each retrieved water constituent of Chla (mg m^{-3}), SPM (g m^{-3}) and CDOM (m^{-1}), three statistical measures are calculated between the satellite and in-situ R_{rs} retrievals named as: (i) the standard deviation (black color), (ii): the Pearson Correlation Coefficient (blue color), and (iii) the Root Mean Square Deviation (RMSD = RMSE) (green color).

As can be seen from these Taylor diagrams, the OLCI retrievals (indicated by C) agree the best with in-situ R_{rs} retrievals for all three constituents of Chla, SPM and CDOM (correlation coefficient > 0.90, standard deviation estimates < 7) while for each retrieved-constituent the estimated RMSD values is less than 4 and lies the nearest with the "in-situ R_{rs} retrievals" on the x-axis. Moreover, as Table 4.9 shows, OLCI-WCC retrievals show the most robust agreements with the in-situ R_{rs} retrievals ($R^2 \geq 0.82$, NRMSE < 9%, RRMSE< 45%) in comparison to MSI and MERIS retrievals. Therefore, it can be stated that the OLCI is the most practical sensor to be used for the retrieval of WCCs in comparison to MERIS and MSI sensors in this study. The MERIS (indicated by A) and MSI (indicated by B) retrievals also agree well with in-situ R_{rs} retrievals with similar correlation coefficients ≥ 0.83. However, MERIS-retrievals have lower amplitudes of the variations (i.e., the standard deviation) in comparison to MSI-retrievals and accordingly smaller RMSD estimates for all three constituents of Chla, SPM, and CDOM. Further statistical analysis presented in Table 4.9 is also another evidence of the better agreement of MERIS-retrievals with in-situ R_{rs} retrievals ($R^2 \geq 0.68$, NRMSE < 17% and RRMSE < 55%) in comparison to MSI ones. Therefore, it can be concluded that the MERIS sensor can be rated as the second practical sensor to be used for WCC retrievals in this study. The last practical sensor for WCC retrievals in this study is MSI with highest RMSD estimates in comparison to MERIS and OLCI sensors while these estimates show larger variations with in-situ R_{rs} retrievals for all three Chla, SPM, and CDOM constituents. Furthermore, the lowest estimates of R^2 and the highest estimates of NRMSE and RRMSE (Table 4.9) show that MSI-retrievals have lower correlations and agreements with in-situ R_{rs} retrievals in comparison to MERIS and OLCI ones.

Overall, considering the reasonable accuracy of the coupled 2SeaColor-MODTRAN model for doing atmospheric correction (Fig. 4.9, Table 4.8) and reasonable agreement of 2SeaColor-MODTRAN WCC retrievals with the retrieved WCCs from in-situ R_{rs} measurements in different seasons (SZAs < 60°) and under different water turbidity and atmospheric conditions (Figs. 4. 11 and 4.12, Table 4.9), the retrieved WCCs from time series of multi-sensor satellite images of this study can be considered reliable enough. Below we present the long-term variations of retrieved WCCs from the integration of multi-sensor satellite images and in-situ R_{rs} measurements at the NJS.

4.5.4. Long-term variability of WCCs from the integration of in-situ measurements and satellite images

Fig. 4.13 presents the diurnal variation of retrieved WCCs by using the 2SeaColor model from quality-controlled in-situ R_{rs} measurements and by using the coupled 2SeaColor-MODTRAN model from cloud-free MERIS, MSI and OLCI images between 2003 and 2018 at the NJS. Moreover, the collected in-situ Chla and SPM concentrations between 2008 -2010 at the NJS (grey stars) are also presented in these figures. These in-situ of Chla and SPM concentrations are taken from Arabi et al. (2018).

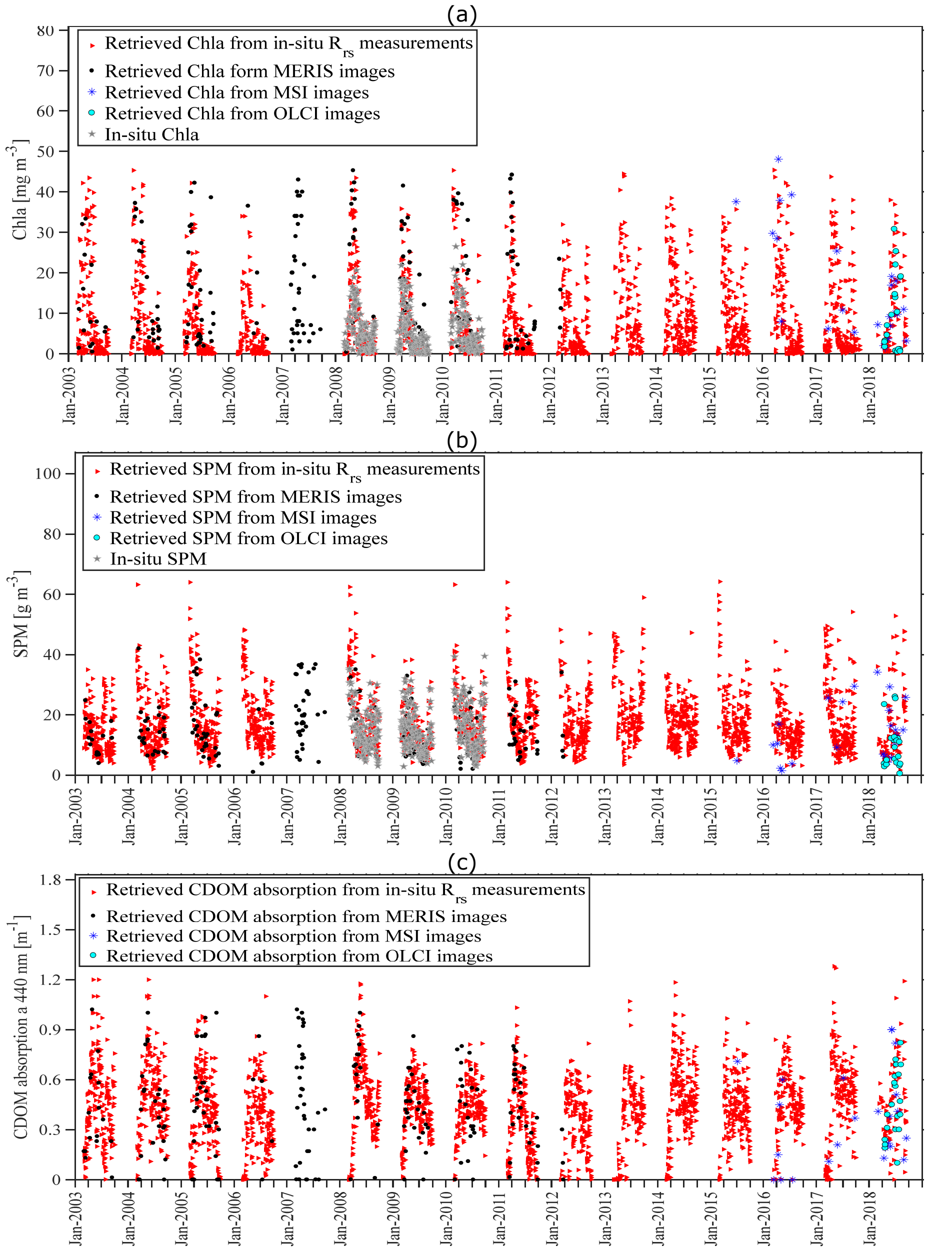

Figure 4.13 Diurnal variation of WCCs at the NJS: red dot: retrieved from in-situ R_{rs} measurements using the 2SeaColor model between 2003 and 2018; black circle: retrieved from 207 MERIS images using the coupled 2SeaColor-MODTRAN model between 2003 and 2012; blue stars: retrieved from 24 MSI images using the coupled 2SeaColor-MODTRAN model between 2015 and 2018; cyan circle: retrieved from 20 OLCI images using the coupled 2SeaColor-MODTRAN model in 2018; grey stars: measured in-situ values between 2008 and 2010; (a): Chla concentrations (mg m^{-3}); (b): SPM concentrations (g m^{-3}); (c): CDOM absorption at 440 nm (m^{-1});.

In these figures, the x-axis shows the number of different years and the y-axis shows diurnal values of retrieved WCCs from in-situ R_{rs} measurements using the 2SeaColor model (red triangles) besides the values of retrieved WCCs from MERIS (black circles), MSI (blue stars) and OLCI (cyan circles) images using the coupled 2SeaColor-MODTRAN model. As it was explained before, due to the SZA flagging data proposed by Arabi et al. (2018), only the WCC retrievals from March to September (SZAs < 60°) are presented per each year.

From Fig. 4.13 (a), it can be seen that the trends of retrieved Chla concentrations (mg m^{-3}) from MERIS, MSI and OLCI images follow almost similar temporal patterns with the ones retrieved from in-situ R_{rs} measurements within multiple years between 2003 and 2018. Moreover, these patterns agree well with the detected pattern of in-situ Chla concentrations collected between 2008 and 2010 at the NJS. However, slight overestimations can be observed for the MERIS-Chla retrievals in comparison with the retrieved ones from in-situ R_{rs} measurements and measured in-situ ones at the NJS. Similar temporal trends can also be detected between SPM-retrievals (g m^{-3}) from multi-sensor satellite images and from in-situ R_{rs} measurements for the period of 15-years while only, small underestimations are observed for the satellite-SPM retrievals in comparison with the ones retrieved from in-situ R_{rs} measurements. Moreover, the temporal patterns of satellite retrievals fit very well with the retrieved ones from in-situ R_{rs} measurements and measured ones at the NJS. The story is the same for retrieved CDOM absorption (m^{-1}) with similar temporal pattern and agreement between satellite and in-situ R_{rs} retrievals. However, there was no measured CDOM absorption (m^{-1}) at the NJS to be compared with remote sensing retrievals at this study.

Overall from the evaluation of these long-term retrievals, it can be concluded that the diurnal variation of retrieved WCCs from the integration of satellite images and in-situ measurements show similar temporal patterns, ranges and, good agreement for a period of 15-years. The combination of these retrievals from different satellite and in-situ sensors are important to fill gaps in time in order to long-term water quality studies, satellite validations and instruments calibrations. Moreover, they have significant applications to provide high-temporal resolution information to be used on multi-temporal analyses on a weekly, monthly, seasonal and annual basis of water quality monitoring and for frequently updating of the generated WCC maps at the study site.

4.5.5. Spatio-temporal variability of WCCs using satellite images in the study area

Figs. 4.14, 4.15 and 4.16 show the generated WCC maps using the MERIS and OLCI images described in Table 4.6. The date and tidal phase are indicated above each map. The location of the NJS (located at bottom-left of each map) and the North arrow (located at upper-right of each map) are presented in pink color. For each figure, the legend is shown in the last map considering the minimum and maximum level of the retrieved values for all dates.

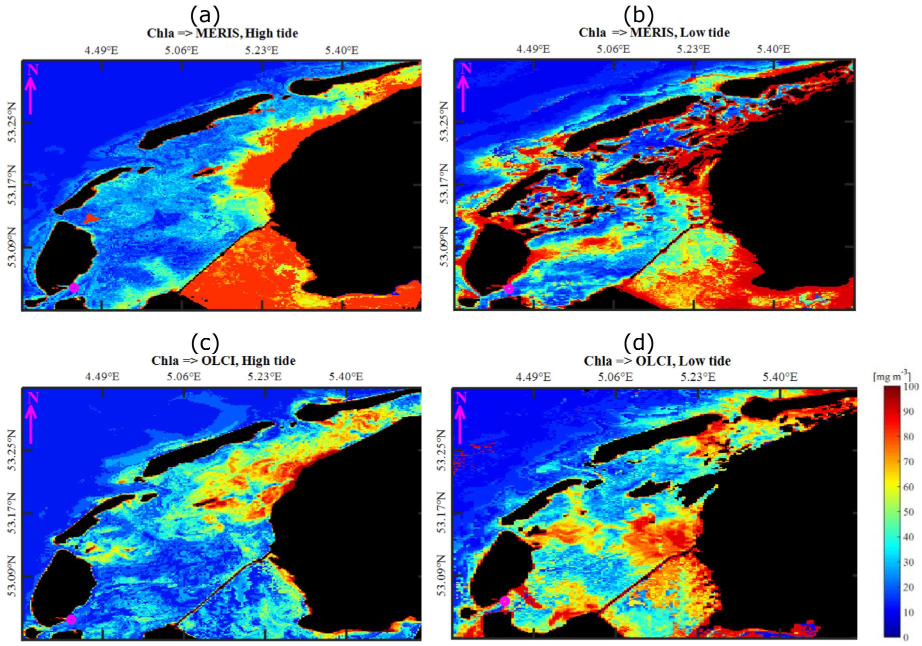

Figure 4.14. The generated Chla concentration (mg m^{-3}) maps using the coupled 2SeaColor-MODTRAN model over the Dutch Wadden Sea and the IJsselmeer lake from: (a) the MERIS image captured during high tidal phase on 14-08-2002; (b) the MERIS image captured during low tidal phase on 19-04-2009; (c) the OLCI image captured during high tidal phase on 05-05-2018; (d) the OLCI image captured during low tidal phase on 06-06-2018.

As can be seen from these maps, the variation ranges of the Chla concentration level are similar in all maps (0 to 90 (mg m^{-3})). However, the different spatial variability of Chla concentration level is observed on various dates. For example, the retrieved Chla level is ~ 80 (mg m^{-3}) in the IJsselmeer lake in the image captured in Fig. 4.14 (a), (b) and (d) while these values show a lower level (~ 50 (mg m^{-3})) for the same area in Fig. 4.14 (c).

The retrieved SPM concentration (g m^{-3}) maps, which are generated, simultaneously with the Chla concentrations maps from the same images are presented in the below figure.

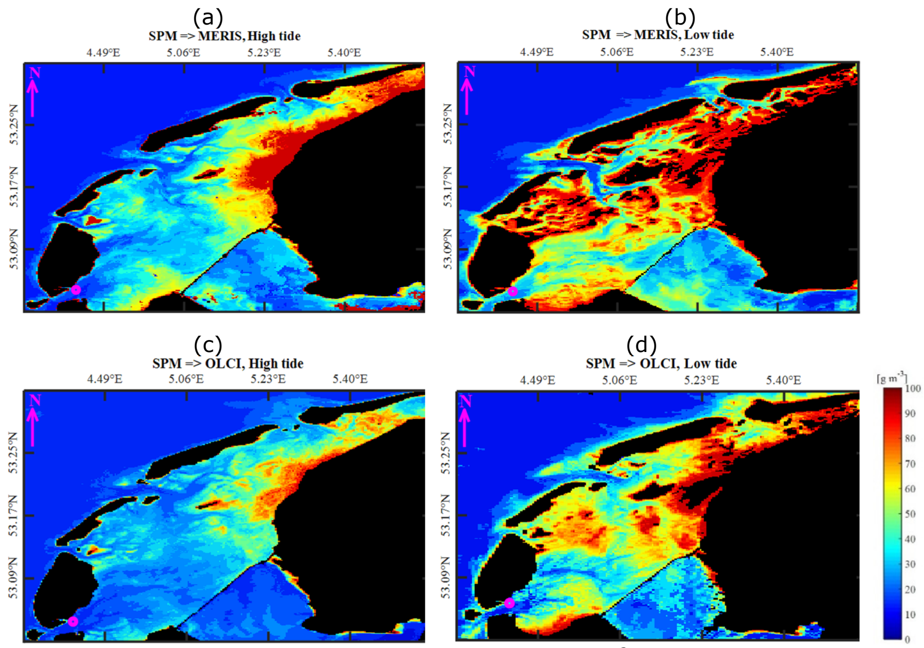

Figure 4.15. The generated SPM concentration (g m^{-3}) maps using the coupled 2SeaColor-MODTRAN model over the Dutch Wadden Sea and the IJsselmeer lake from (a) the MERIS image captured during high tidal phase on 14-08-2002; (b) MERIS image captured during low tidal phase on 19-04-2009; (c) OLCI image captured during high tidal phase on 05-05-2018 (d) OLCI image captured during low tidal phase on 06-06-2018.

As can be seen from Fig. 4.15, the retrieved SPM concentration maps show almost similar range (between 0 to 100 (g m^{-3})) and similar spatial pattern for all four dates. The SPM concentrations level are ~ 40 (g m^{-3}) in internal parts of the IJsselmeer lake and reach their highest level (~ 100 (g m^{-3})) around the inner islands of the Dutch Wadden Sea while show their lowest level in the external part of Texel island in the neighborhood of the North Sea (between 0 and 10 (g m^{-3})).

The maps of retrieved CDOM absorption (m^{-1}) for the same images are also presented in Fig. 4.16.

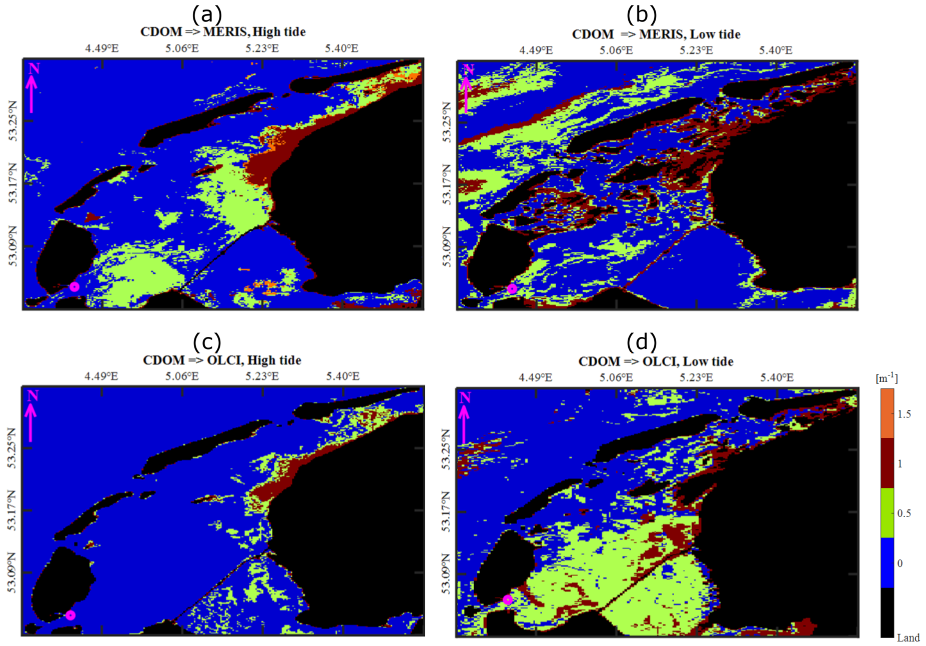

Figure 4.16. The generated CDOM concentration (m^{-1}) maps using the coupled 2SeaColor-MODTRAN model over the Dutch Wadden Sea and the IJsselmeer lake from: (a) the MERIS image captured during high tidal phase on 14-08-2002; (b) the MERIS image captured during low tidal phase on 19-04-2009; (c) the OLCI image captured during high tidal phase on 05-05-2018; (d) the OLCI image captured during low tidal phase on 06-06-2018.

As can be seen from Fig. 4.16, the CDOM absorption at 440 nm (m^{-1}) change between 0 to 1.5 (m^{-1}) over the study area for all four maps. However, high spatio-temporal variability of CDOM absorption is observed in different parts of each map. For example, the retrieved CDOM absorption shows a high level (~ 1.2 (m^{-1})) in the IJsselmeer lake in Fig 4.16. (d), but lower CDOM absorption level is observed for the same areas in the other three maps (Figs. 4.16 (a), (b) and (c)). It should be mentioned that regarding the small steps of CDOM in water properties LUT over the study area (Table 4.4), the generated maps show only four groups of CDOM absorption values (0, 0.5, 1, 1.5 (m^{-1})).

Fig. 4.17 shows the generated maps of spectral residual errors (RMSE) between the best fits of observed and modeled TOA radiances using the coupled 2SeaColor-MODTRAN (described in section 4.4.4):

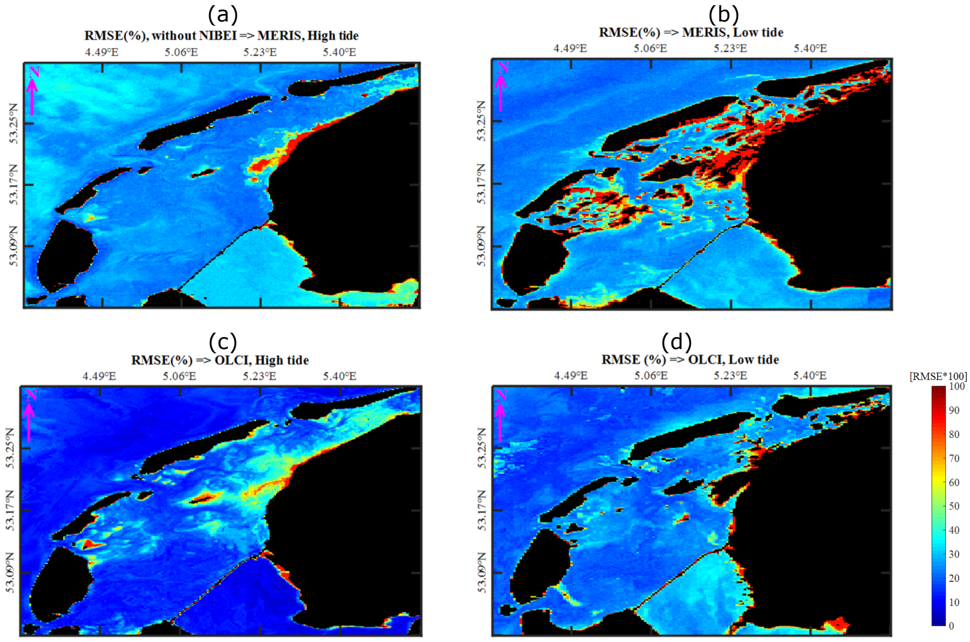

Figure 4.17. The generated maps of the TOA radiances spectral residual errors (RMSE) (W m^{-2} sr^{-1} μm^{-1}) between the best fits of 2SeaColor-MODTRAN modeled and observed TOA radiances over the Dutch Wadden Sea and the IJsselmeer lake; (a): the MERIS image captured during high tidal phase on 14-08-2002; (b): the MERIS image captured during low phase on 19-04-2009; (c): the OLCI image captured during high tidal phase on 05-05-2018; (e): the OLCI image captured during low tidal phase on 06-06-2018.

As Fig. 4.17 (a) shows, the estimated TOA radiances spectral residual errors (RMSE (W m^{-2} sr^{-1} μm^{-1})) for the MERIS image captured during the high tidal phase, do not exceed ~ 30% inside the study area for all maps. However, these errors reach their maxima (shown in bright-red color) of ~ 100% in the shallow areas close to the land during both high and low tidal phases (Figs. 4.17 (a) and (b)). This RMSE increase is even more apparent in the map which is generated from the MERIS image during low tidal phase (Fig. 4.17 (b)). The same applies to OLCI images captured during high and low tidal phases, respectively (Figs. 4.17 (c) and (d)). As a result, it can be concluded that the generated WCC maps can be considered satisfactory enough over the deep parts of the study area with low spectral RMSE (*e.g.,* external parts of the Dutch Wadden Sea close to the North Sea and the IJsselmeer lake). However, the retrieved WCCs are questionable over the areas with very high spectral residual errors mainly located in shallow parts of the study area. Further investigations showed that for each image similar aerosol types and visibilities are present over the regions with high spectral residual errors (results are not presented). On the other hand, some channels are visible in the generated maps. Thus it can be stated that the sea bottom effect plays significant role at the received signal at TOA level on satellite images and accordingly is the main reason for the model's failure to accurately simulate TOA radiances over the shallow waters of the study area (Arabi et al., 2018; Yu et al., 2016). Although it is not the case for the NJS data where, due to the depth of > 5 m, the bottom effect on observed reflectance is negligible. Therefore, to generate reliable WCC maps over the shallow parts of the Dutch Wadden Sea, the sea bottom impact should be taken into account in the retrievals. Otherwise one can never tell whether the retrieved spatial variations in WCCs are real or just artifacts caused by observation of the sea-bottom.

4.6. Discussion

Optical remote sensing of water quality is dramatically improving by developing new approaches for integration of earth observations data with in-situ measurements in support of critical activities such as the effective monitoring of complex coastal regions and aquatic ecosystems. Quantitative remote sensing of water quality benefits from observation complementarities and synergies by combining in-situ measurements and satellite images to provide more precise and higher temporal resolution monitoring (Teillet et al., 2002). In this study, we combined in-situ and remote sensing observations for long-term monitoring of multi-variate water constituent concentrations of Chla, SPM, and CDOM using radiative transfer modeling in complex coastal waters of the Dutch Wadden Sea.

In the first phase of this study, we used the RT model of the 2SeaColor for simultaneous retrieval of WCCs from time series of in-situ R_{rs} measurements collected in a daily basis between 2003 and 2018 at the NJS, Dutch Wadden Sea. The performed statistical analysis and model's validation showed that the 2SeaColor model is capable enough for accurate estimates of WCCs within different dates, seasons and water turbidity conditions for a period of 15-years at the NJS (Figs. 4.6 and 4.7, Table 4.7). Relying on the capability of the 2SeaColor model for an accurate estimate of WCCs, these retrievals were used as a reference indicator to evaluate the long-term variation of WCCs from TOA level using multi-sensor satellite images.

In the second phase of this study, we used the RT model of the coupled 2SeaColor-MODTRAN model for simultaneous retrieval of WCCs from multi-sensor satellite images of MERIS, MSI and OLCI between 2003 and 2018 at the same study site. Performed statistical analysis and model's validation showed that the atmospherically corrected-R_{rs} values from multi-sensor satellite images by using the coupled 2SeaColor-MODTRAN model were in reasonable agreement with in-situ R_{rs} measurements (Fig. 4.9 and Table 4.8) while OLCI images slightly showed better performance in comparison to MERIS and MSI images. Moreover, performed statistical analysis showed that there are a reasonable agreement and correlation between variations of retrieved

WCCs from satellite images with the ones retrieved from in-situ R_{rs} measurements in different dates, seasons (SZAs < 60°), water turbidity and atmospheric conditions within a period of 15 years at the NJS (Fig. 4.11 and Table 4.9).

Furthermore, the produced Taylor diagrams for three constituents of Chla, SPM and CDOM from MERIS, MSI and OLCI images showed that OLCI retrievals fit the best with in-situ R_{rs} retrievals in comparison to MERIS and MSI-retrievals (Fig. 4.12, Table 4.9). Accordingly, long-term variability of WCC retrievals from the integration of in-situ and satellite observations was presented while both WCC retrievals at TOA and water surface level were in good agreements and followed similar temporal patterns at the NJS (Fig. 4.13).

Finally, we applied the coupled 2SeaColor-MODTRAN model on MERIS and OLCI images to monitor the spatio-temporal variation of WCCs over the Dutch Wadden Sea (Figs. 4.14, 4.15 and 4.16). The results indicate that applying this model on MERIS and OLCI images lead to generating high-quality WCC maps while the quality of generated maps by MSI remains questionable. The reason might be due to this fact that applying the coupled 2SeaColor-MODTRAN model on MSI images requires to resize the sensor spatial resolution to 300 m. This could influence the quality of generated WCC maps although the model's validation at the single location of the NJS is fairly reasonable.

4.6.1. Implications

The established reliable long-term WCC variations in high temporal resolution obtained from integration of in-situ measurements and satellite images may be used as baseline information for sustainable management of water resources, and the validated algorithms may be served for the future satellite images using oncoming satellite missions. Moreover, a similar approach to exploit the integration of space and ground-based observations for quantitative water quality monitoring can be implemented in various critical coastal areas worldwide. Providing such information has great potential to empower decision makers and water managers to detect possible alert and supports the recent global goals (i.e., Goal 14: Conserve and sustainably use the oceans, seas and marine resources) by SDGs program (McInnes, 2018) which aims in (the goals are taken from the SDGs report directly):

- "14.2 By 2020, sustainably manage and protect marine and coastal ecosystems to avoid significant adverse impacts".
- "14.5 By 2020, conserve at least 10 percent of coastal and marine areas, consistent with national and international law and based on the best available scientific information".

- "14.A increase scientific knowledge, develop research capacity and transfer marine technology, taking into account the Intergovernmental Oceanographic Commission Criteria and Guidelines on the Transfer of Marine Technology ".
- "14.C Enhance the conservation and sustainable use of oceans and their resources by implementing international law as reflected in UNCLOS, which provides the legal framework for the conservation and sustainable use of oceans and their resources, as recalled in paragraph 158 of The Future We Want".

4.6.2. Recommendations

It is recommended to investigate the potential of integration of in-situ measurements with earth observation data obtained from recently launched and future satellite sensors to be served for automatic monitoring of water quality. The hyperspectral satellite mission of Environmental Mapping and Analysis Program (EnMAP) will be launched in 2020 by Germany with the main goal of global monitoring of Earth's environment and to model and measure the key dynamic processes of the Earth's ecosystems (Kaufmann et al., 2008). The EnMAP will provide earth observation data with a high radiometric, temporal (4 days) and spatial (30 m) resolution while covering a broad spectral range (420 nm-2450 nm). The integration of hyperspectral satellite images provided by EnMAP with in-situ hyperspectral measurements helps to exploit their synergies and complementarities to reduce uncertainties for effective and automatic monitoring of water quality monitoring and will provide information on the status and evolution of various terrestrial and aquatic ecosystems.

It is recommended to establish denser in-situ measuring stations in coastal waters to support and validate the spatio-temporal water quality information provided by satellite images. Although this might not be readily feasible due to lack of budget and facilities in many vast areas or underdeveloped countries, the density of measuring in-situ stations in time and space can be optimal by some factors: 1) detecting crucial sites of a coastal area with more necessity to be monitored due to risks of fishery, human activities, climate change; 2) considering the climatological condition of the study site for expecting more cloud-free images in specific seasons; 3) considering time tracking of available satellites covering the study site to reduce mismatch between in-situ measurements and satellite images; and 4) obtaining updated information about topography and ecosystem of the region for best establishment of spatio-temporal stationarity.

It is recommended to develop a hydro-optical model which includes the impact of the sea-bottom to improve in the derived WCCs from MERIS and OLCI images (Arabi et al., 2018; Yu et al., 2016). Although the spatial variation of retrieved using MERIS and OLCI images in deep waters of Dutch Wadden Sea are considered satisfactory enough (Fig. 4.17), in the shallow areas and the regions close to the land, the coupled model failed to simulate TOA radiances accurately (Fig. 4.11). The reason was due to this fact that in the shallower parts of the study area, the sea bottom might contribute significantly in the visible region of the spectrum and consequently is as the main reason for the model's failure to accurately simulate TOA radiances (Arabi et al., 2018; Yu et al., 2016). As a result, in the next chapter of this thesis, we will develop a WCCs retrieval algorithm by incorporating the sea bottom effect in the hydro-optical model and evaluate the reliability of generated WCC maps by using the new model.

4.7. Conclusion

15-years monitoring of WCCs from the integration of in-situ and satellite observations using radiative transfer modeling is studied in the Dutch Wadden Sea, the Netherlands. From the results of this research, it is concluded that:

1) The two-stream radiative transfer model of 2SeaColor accurately illustrates the temporal variation of WCCs retrieved from in-situ R_{rs} measurements between 2003 and 2018 at the NJS.
2) The coupled radiative transfer model of 2SeaColor-MODTRAN accurately illustrate the temporal variation of WCCs retrieved from MERIS (2003-2012), MSI (2015-2018) and OLCI (2018) images at the NJS.
3) There are similar temporal trends and good agreements between the retrieved WCCs by the 2SeaColor at water surface level and the ones by the coupled 2SeaColor-MODTRAN model at TOA level.
4) The provided high-temporal resolution information on water quality variables obtained from the integration of ground and space remote sensing observations in this study is vital for decision-makers to detect unexpected alters and effective monitoring of the study area.
5) Generating reliable WCC maps over the complex waters of the Dutch Wadden Sea require a water retrieval model which considers the sea bottom effect.

Chapter 5 **The sea - bottom effects on radiances and the retrievals***

* This chapter is based on:
Arabi, B., Salama, M.S., van der Wal, Daphne., Pitarch, J., Verhoef, W., 2020. The impact of sea bottom effects on the retrieval of water constituent concentrations from MERIS and OLCI images in shallow tidal waters supported by radiative transfer modeling. Remote Sensing of Environment Journal, 237 (2020) 111596. https://doi.org/10.1016/j.rse.2019.111596.

ABSTRACT

The Dutch Wadden Sea includes large areas of optically shallow water where the sea bottom is visible from above, and there may be a substantial influence on the water-leaving reflectance. If not treated, the effect of bottom reflectance will interfere with the correct retrieval of WCCs from hyperspectral and multispectral remote sensing data. To study this phenomenon in more detail, the semi-infinite 2SeaColor radiative transfer (RT) model was modified into a finite water layer model, bounded by a diffusely reflecting surface at the bottom. From simulations with the new model, called Water - Sea Bottom (WSB) model, it was observed that ratios of spectral bands in the near infrared can be employed as a bottom effect index (BEI), and to distinguish it from currently existing BEIs using visible light, it was called NIBEI, near infrared bottom effect index. The NIBEI from bands at 750 nm and 900 nm is nearly insensitive to the WCCs and increases with the shallowness of the water, and therefore can be used as a robust flag to detect optically shallow waters. This flag can be applied to exclude optically shallow waters from consideration in WCC retrieval algorithms. This concept has been tested on the MERIS and OLCI images of the Dutch Wadden Sea. A LUT of TOA radiance was generated using the 2SeaColor and MODTRAN models. The LUT was applied to MERIS and OLCI images to retrieve WCCs in the study area. The results indicate that flagging for optically shallow waters helps to improve the reliability of WCC retrievals, but it will remain a challenge to differentiate the combination of effects of the sea bottom, water constituents and atmospheric properties from TOA radiance spectra alone.

5.1. Introduction

The Wadden Sea is a UNESCO World Heritage (Hommersom, 2010) and is considered one of the most important coastal areas in Europe (Cadée, 1982). Monitoring this area is mandatory following the European Marine Strategy launched in 2002 and to adhere to the Marine Framework Directive (Long, 2011). Remote sensing data provide more cost-effective information than alternative field-survey methods for monitoring of this vast coastal area (Mumby et al., 1999). Using earth observation is a big step of change from the station-oriented monitoring to the system-oriented monitoring over this highly dynamic coastal area (WFD, 2000). Fortunately, this area is observed by the most operational satellites for water quality studies like the MERIS and OLCI (Ambarwulan et al., 2011; Matthews et al., 2012). At present, there is a full archive of MERIS images between 2002 and 2012 over the Wadden Sea. OLCI, on board of the Sentinel-3 mission series of satellites, is an improved successor of the MERIS sensor and in orbit since February 2016, with higher accuracy, greater wavelength region coverage, and more spectral bands. It is expected that products from the OLCI sensor can improve both the geographical and temporal coverage of WCC retrievals (Harvey et al., 2014). OLCI images are free for users to be downloaded. Therefore, there is a great opportunity to produce WCC maps of Chla, SPM, and CDOM using these satellite images and track the spatio-temporal variation of these concentrations for more than one decade over this coastal area. Such products can contain very significant information for the environmental decision makers concerning maintenance and conservation (Doerffer and Fischer, 1994; Eleveld et al., 2008; Peters et al., 2005; Pitarch et al., 2016). However, producing accurate and reliable WCC maps over this complex coastal area is a big challenge. Studies have reported three main problems, i) atmospheric correction issues, ii) WCC retrieval algorithms and iii) the effect of the sea-bottom on the observed remote sensing data, in the use of remote sensing techniques in this complex coastal area (Bartholdy and Folving, 1986; Dekker et al., 2001; Hommersom et al., 2010; Hommersom, 2010a, 2010b; Peters et al., 2004; Philippart et al., 2013; Salama and Shen, 2010; Staneva et al., 2009; Van der Woerd and Pasterkamp, 2004; Malthus and Mumby, 2003).

The Dutch Wadden Sea is a highly turbid coastal area located on the coast of northwestern continental Europe, with many rainy and cloudy days during a year (Creutzberg, 1961). That is also the reason why regular atmospheric correction algorithms have a higher probability of failure over these waters (Pasterkamp et al., 2003; Peters et al., 2004; Salama et al., 2012; Van der Woerd, Hans et al., 2003), where not only substantial SPM concentrations can occur but also the atmosphere is mostly heterogeneous over the region due to local haze variations (Arabi et al., 2016; Hu et al., 2000; Ruddick et al., 2000; Shen et al., 2010; Shen and Verhoef, 2010; Siegel et al., 2000; Wang et al., 2009; Wang and Shi, 2005). Besides the atmospheric correction problem, the accuracy of water retrieval algorithms remains problematic where Chla, SPM, and CDOM concentrations have high spatio-temporal variation over this coastal area (Arabi et al., 2018). These WCCs vary independently from each other, and their effect needs to be considered, separately, in water retrieval algorithms (Salama et al., 2012; Van der Woerd and Pasterkamp, 2008). Furthermore, depending on the local water depth, water transparency and the nature of the bottom surface, the sea-bottom may have a substantial influence on water leaving reflectances recorded at sensor level in this shallow coastal area (Casey, 2007; Ceyhun and Yalçin, 2010; Hommersom, 2010a; Mobley, 2003). This can interfere with the correct retrieval of WCCs from water leaving reflectances using different water retrieval algorithms. Therefore the hydro-optical algorithms should include the sea-bottom effect in order to accurately retrieve WCCs from atmospherically corrected water-leaving reflectance (Gitelson et al., 2008; Lee et al., 2002a). Although many studies have been conducted to improve the accuracy of atmospheric correction methods and hydro-optical models for water quality monitoring in this area, producing WCC maps is still a big challenge due to the complexity of this optically shallow water system (Hommersom et al., 2010; Philippart et al., 2013).

In their most recent effort, Arabi et al. (2018) evaluated the performance of a two-stream radiative transfer modeling with the 2SeaColor model (Salama and Verhoef, 2015) for the simultaneous retrieval of Chla, SPM and CDOM concentrations from time series of in-situ hyperspectral measurements collected on different dates, varying SZAs and water turbidity conditions for the Dutch Wadden Sea. They showed that the accuracy of the 2SeaColor model for WCC estimation against in-situ WCCs is reasonable enough at the location of the NJS located at the western inlet to the Dutch Wadden Sea. However, the effect of the bottom was not considered on the accuracy of WCC retrievals in their study. In another study, Arabi et al. (2016) coupled the 2SeaColor model with the MODTRAN atmospheric RT model to the simultaneous retrieval of WCCs and atmospheric properties (i.e., visibility and aerosol type) from MERIS images over the Dutch Wadden Sea. By applying this model, they succeeded to accommodate local haze variations over the MERIS images while the results showed significant improvements in both the atmospheric correction and WCC retrievals in comparison to the standard MERIS C2R processor (Doerffer and Schiller, 2007). However, the accuracy of generated maps using their proposed coupled model remained a concern due to the shallowness of the Wadden Sea and the significant effect of the sea-bottom on the satellite images.

Although there are some studies of bottom reflectance in shallow waters, most of these studies have focused on habitat classification mapping or bathymetry by establishing the statistical relationships between image pixel values and field measured water depth values, which requires a high level of spatial and spectral details (Bresciani et al., 2016; Chybicki, 2017; Giardino et al., 2014, 2012; McKinna et al., 2015; Mgengel and Spitzer, 1991; Pattanaik et al., 2015; Sari, 2013; Stumpf et al., 2003; Yanjiao et al., 2007). For example, Brando et al. (2009) applied an integrated physics-based mapping approach to retrieve bathymetry, substratum type and WCCs using airborne hyperspectral observations at Moreton Bay, Australia. Their investigations suggested that the quantitative identification and screening of the optically deep waters and the quasi-optically deep waters led to improved precision in the depth retrieval. Hu et al. (2010) and Hu (2009) proposed the Floating Algae Index (FAI) to detect cyanobacteria and macro-algae in the freshwater lake Taihu and the Yellow Sea (China) from MODIS images. Their investigations showed that the FAI was sensitive to turbid waters and shallow depths. Lee et al. (2002) used measured hyperspectral data from both optically deep and shallow environments and inverted the remote-sensing reflectance spectra to accomplish a simultaneous retrieval of WCCs, bottom depths, and bottom albedos by an optimization technique. However, one of the first steps in deriving WCCs from satellite images in shallow waters is the differentiation between optically shallow and optically deep waters. In clear shallow regions, the R_{rs} values will be enhanced by light reflected from the sea-bottom, depending on both water turbidity and metrical bottom depth. Regions with either low turbidity or a small depth or both are typically characterized as optically shallow waters, where regular water quality retrieval algorithms cannot detect WCCs. Note that the term "optically shallow" is also dependent on the wavelength of the incident light, since the effects of turbidity vary substantially with the total absorption coefficient, which is strongly spectrally dependent (Albert and Mobley, 2003; Cannizzaro and Carder, 2006; Carder et al., 1986; Durand, 2000; Lee et al., 1999, 1998; Li et al., 2003; Lyzenga, 1978; Maritorena et al., 1994; McKinna and Werdell, 2018; Volpe et al., 2011).

Using bathymetry maps or estimating water depth values in coastal areas using different retrieval algorithms may not always be beneficial in satellite remote sensing of shallow coastal waters. First, the water depth values vary in time and space, especially in tidal areas (Chybicki, 2017). Second, such products do not necessarily help to discriminate optically deep from shallow waters, which is also dependent water turbidity and absorption (Albert, 2004; Lee et al., 1998; Reichstetter et al., 2015; Yang and Yang, 2015). Until now, some limited studies have focused on this subject. In their most recent effort, Li et al. (2017) introduced a bottom effect index (BEI) to separate optically shallow waters from optically deep waters to retrieve CDOM concentrations in Saginaw Bay, in the U.S. However, applying their BEI required reliable bathymetry data, which are not available for all coastal waters. Later, McKinna and Werdell (2018) developed an approach to flag optically shallow waters using MODIS images at Great Barrier Reef, Australia. However, their approach was dependent on simultaneous input data such as bathymetry, water clarity and seafloor albedo which are not always available for all regions.

With respect to all problems mentioned above, a major objective of the present paper was to develop an image based flagging approach to detect optically shallow waters without the requirement of ancillary data (*i.g.,* bathymetry maps). To do this, we first evaluate the effect of the sea-bottom on remote sensing observations of water leaving reflectances and satellite images using radiative transfer modeling. Then we define an appropriate flagging index and show its application using MERIS and OLCI images. The paper is structured as follows: we describe the location of the Dutch Wadden Sea, its environmental characteristics and the water depth variation in different parts of this region (section 5.2). We introduce the characteristics of satellite images which were used in this study (section 5.3). Next, we explain the methodology of this research (section 5.4) and discuss the results (section 5.5) and come to conclusions in the final sections (5.6 and 5.7).

5.2. Study area

The Wadden Sea is the largest unbroken coastal tidal and mudflat system in the world and characterized by a mosaic of sand and mudflats, tidal channels, salt marshes, seagrass meadows, mussel banks, sandbars and barrier islands extending over a transboundary area (Hommersom, 2010b). Since July 2009, conservation of this tidal ecosystem has become compulsory due to its inclusion on the UNESCO World Heritage List. The Wadden Sea World Heritage property comprises the Dutch Wadden Sea conservation area and the German Wadden Sea National Parks of Lower Saxony and Schleswig-Holstein. The site represents over 66% of the whole Wadden Sea and is home to numerous plant and animal species. It is also a breeding and wintering area for up to 12 million birds per annum, and it supports more than 10 percent of 29 species (CWSS, 2008).

The case study of this research is the Dutch Wadden Sea. It is located in the north of the Netherlands and partly sheltered from the North Sea by a chain of barrier islands. It covers a total surface area of 2500 km^2 and extends to German and Denmark. The area is shallow, leading to surfacing mudflats with low tide and re-suspension due to tidal currents (Dube, 2012). Tides influence the water depth and therefore, determine which tidal flats surface and which are submerged (Van der Wal and Pye, 2003). The variation in tidal level depends on the location: the highest tidal ranges in the Wadden Sea are found in the corner of the German Bight (> 3 m), and the least differences are found near the islands Texel and Fanø (~ 1.5 m) (Postma, 1982; Dijkema et al., 1980). Tide also causes strong tidal currents in the Wadden Sea, which lead to high mixing (Hommersom, 2010a). The bottom level in this area varies from about 25 m in the tidal channels up to +1 m above mean sea level on the tidal flats (Vledder, 2008). Fig. 5.1, right, shows the bathymetry of the Dutch Wadden Sea while X- and Y-axes present the geographical coordinates of the Dutch RD (rijksdriehoek) -system in km, and the scale bar presents the water depth variations (m). Fig. 5.1, left, shows a SPOT satellite image covering the southern part of the Wadden Sea with parts of the Dutch mainland on the right and the island of Texel at the bottom left and the islands Vlieland and Terschelling to the northeast from Texel.

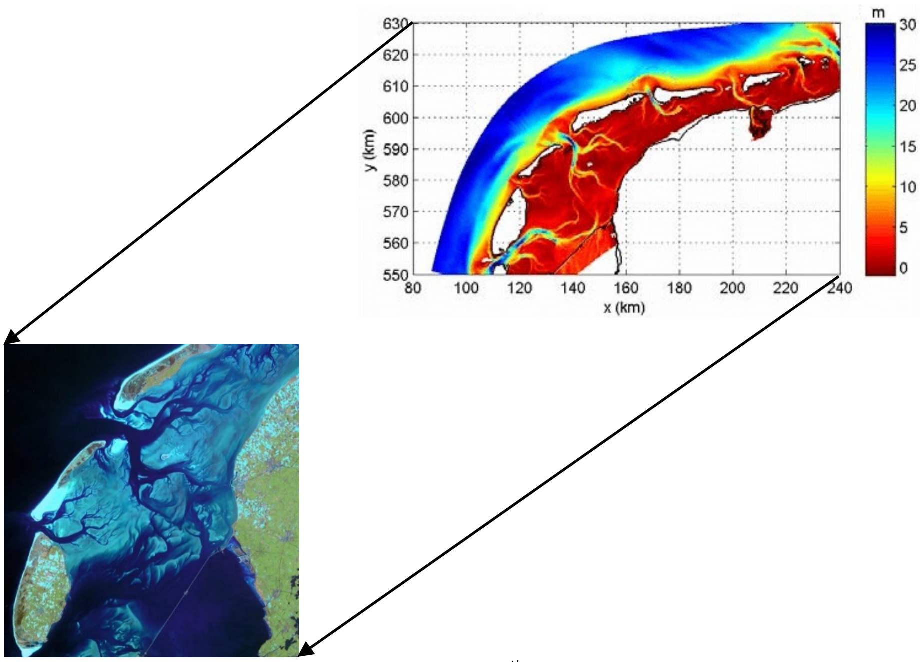

Figure 5.1. left: a SPOT- 4 image captured on 8th of May 2006 with a spatial resolution of 20 m covering the western part of the Dutch Wadden Sea (acquired from ESA official website: https://www.esa.int/ESA); right: the bathymetry map of the whole Dutch Wadden Sea (Vledder, 2008).

As can be seen from the bathymetry map (Fig. 5.1, right), the bottom depth relative to mean sea level is less than 5 m in most parts of the Dutch Wadden Sea. Therefore this area can be considered a good example of shallow coastal waters for remote sensing studies. Also since Fig. 5.1, left, shows that the bottom of the sea can easily be seen from space, influenced by water clarity and the tidal phase at the time of satellite overpass. Altogether, the fair concentrations of Chla, SPM, and CDOM, the influence of the tide, the occurrence of many cloudy days, and the shallowness of the water, make the Dutch Wadden Sea a very complex case study for remote sensing of coastal areas.

5.3. Dataset

In this study, we used MERIS and OLCI images. MERIS and OLCI are likely the optimal past and present sensors for near real-time frequent monitoring applications for spatially constrained inland and coastal waters (Matthews et al., 2012). MERIS was one of the instruments on board of the ENVISAT mission and monitored the Earth between 30 April 2002 and 8 April 2012. The high sensitivity and extensive dynamic range of the MERIS sensor (full spatial resolution: 300 m) have been widely used for ocean, lakes and coastal water remote sensing studies (Majozi et al., 2014; Odermatt et al., 2012; Pasterkamp et al., 2003; Pitarch et al., 2017). The MERIS sensor had a revisit time of three days on average at around 10:30 a.m. (UTC) over the Dutch Wadden Sea with 15 bands covering the spectral ranges from 400 nm to 950 nm. MERIS was put out of operation in 2012 and was succeeded by OLCI, embedded on the Sentinel-3 on platform A in February 2016 and was continued on Sentinel-3 on the platform B since April 2018 (Saulquin et al., 2016). OLCI has the same spectral bands as MERIS plus six extra bands at 400 nm, 673.75 nm, 764.37 nm, 767.5 nm, 940 nm, and 1020 nm. The OLCI sensor (full spatial resolution: 300m) has a revisit time of two-three days on average at around 10:00 a.m. (UTC) over the Dutch Wadden Sea. An overview of the MERIS and OLCI bands is presented in Table 5.1.

Table 5.1. MERIS and OLCI spectral band configurations.

	Band center (nm)		Band width (nm)	
Band number / Sensor	MERIS	OLCI	MERIS	OLCI
1	412.5	400	10	15
2	442.5	412.5	10	10
3	490	442.5	10	10
4	510	490	10	10
5	560	510	10	10
6	620	560	10	10
7	665	620	10	10
8	681.2	665	7.5	10
9	708.7	673.7	10	7.5
10	753.7	681.2	7.5	7.5
11	761.8	708.7	2.5	10
12	778.7	753.7	15	7.5
13	865	761.2	20	2.5
14	885	764.3	10	7.5
15	900	767.5	10	2.5
16	-	778.7	-	15
17	-	865	-	20
18	-	885	-	10
19	-	900	-	10
20	-	940	-	20
21	-	1020	-	40

5.4. Methodologies

In the following subsections, the methodology of this work will be discussed in detail.

5.4.1. The Water - Sea Bottom (WSB) model

We extended the 2SeaColor model by incorporating the sea bottom effect for modeling R_{rs} as a function of five independent variables, namely Chla, SPM, CDOM, bottom albedo (ba) of the sea-bottom, and water depth (wd). The improved model, called Water - Sea Bottom (WSB), was used to evaluate the sensitivity of R_{rs} values to the sea-bottom effect in different parts of the spectrum. The 2SeaColor model is based on a two-stream approach, first proposed by Duntley (1941), with direct solar radiation included as a source of incident flux. The model predicts the directional-hemispheric reflectance factor (DHRF) of a semi-infinite water layer as:

$$r_{sd}^{\infty} = \frac{\sqrt{1+2x}-1}{\sqrt{1+2x}+2\mu_w} \tag{5.1a}$$

where x is the ratio of the backscattering to the absorption coefficient ($x = b_b / a$), and μ_w is the cosine of the SZA beneath the water surface. The reflectance factor r_{sd}^{∞} can be approximated by $Q \times R(0^-)$ under sunny conditions, where $Q = 3.25$ and $R(0^-)$ is the irradiance reflectance beneath the surface (Morel and Gentili, 1993). The model also gives the reflectance for diffuse incident light, called the bi-hemispheric reflectance factor or BHRF, which is given by

$$r_{dd}^{\infty} = \frac{\sqrt{1+2x}-1}{\sqrt{1+2x}+1} \tag{5.1b}$$

If sunlight dominates over the diffuse incident flux from the sky, only Eq. (5.1a) is applied in practice. In the extensive literature on two-stream approximations of radiative transfer, particularly in Duntley (1941), one can find quite different expressions for these reflectance factors, but the ones presented above are particularly suitable for model inversion purposes since x can be derived easily from the reflectances. Derivations of Eqs. (5.1a-5.1b) are given in Appendix A. For more details on the 2SeaColor model, readers are referred to Salama and Verhoef (2015). To incorporate the sea-bottom effect in the 2SeaColor model, the semi-infinite water layer was replaced by a finite layer of given metrical depth d, and the number of model outputs was extended with extra reflectance and transmittance factors that enable calculating the effect of a sea-bottom with a given Lambertian reflectance r_b on the water-leaving reflectance. In Verhoef (1985) the adding equations for calculating the reflectance of the combination of a turbid medium layer and a background surface with a reflectance r_b were given by Eqs. (26a-b), slightly adapted here for a Lambertian background:

$$r_{dd} = \rho_{dd} + \frac{\tau_{dd}\, r_b\, \tau_{dd}}{1 - r_b \rho_{dd}} \tag{5.2}$$

$$r_{sd} = \rho_{sd} + \frac{(\tau_{ss} + \tau_{sd})\, r_b\, \tau_{dd}}{1 - r_b \rho_{dd}} \tag{5.3}$$

where the double subscripts indicate the types of flux on incidence and exit, respectively, and *s* stands for direct solar flux and *d* for semi-isotropic diffuse flux. Reflectances caused by volume scattering inside the layer have the symbol ρ, and transmittances have the symbol τ. The direct transmittance for sunlight is τ_{ss}. The resulting DHRF of the combination water - bottom is called r_{sd}, and the bi-hemispherical reflectance factor (BHRF) is r_{dd}. To generate input spectra of the bottom reflectance, the sub model BSM (brightness-shape-moisture) is applied. This model is based on the statistical Global Soil Vectors (GSV) approach of Chongya and Hongliang (2012) and more recently also used by Verhoef et al. (2018). This also implies that vegetated sea-bottoms are not yet considered in the current approach. The model has four input variables, dry soil brightness, two spectral shape variables, and the volumetric soil moisture percentage. In this particular application, only the dry soil brightness variable was varied to generate spectra of constant shape. Dry soil brightness in this context is formally defined as the square root of the sum of the three squared weight coefficients applied to the basis spectra to fit a given soil dry spectrum. Changing soil brightness affects the whole soil spectrum proportionally, while the spectral shape is preserved. The so-called irradiance reflectance just beneath the water surface is:

$$R(0^-) = \frac{r_{sd} E_s(0) + r_{dd} E_d^-(0)}{E_s(0) + E_d^-(0)} \tag{5.4}$$

where $E_S(0)$ and $E_d^-(0)$ are the direct solar irradiance and the diffuse downward irradiance incident at the top of the water layer, respectively. To include the effect of the water-air interface, we finally estimate the water-leaving remote sensing reflectance by Mobley (2003):

$$R_{rs} = \frac{0.52 R(0^-)}{Q - 1.7 R(0^-)} \tag{5.5}$$

In the turbid medium scattering model for the water layer, *a* similarity transform (Van de Hulst, 1980) was applied in such a way that all forward scattering greater than the backscatter coefficient was ignored, so that effectively isotropic scattering results. Accordingly, the beam extinction coefficient *c* in (m^{-1}) was reduced to:

$$c = a + 2b_b \tag{5.6}$$

where a is the absorption coefficient and b_b the backscattering coefficient. This means that the forward scattering peak due to Mie scattering by particles in the water is ignored and treated as the light that is not scattered at all. The transformed single scattering albedo ω is given by:

$$\omega = 2b_b / c = \frac{2b_b}{a + 2b_b} \tag{5.7}$$

The similarity transform, effectively resulting in an isotropic scattering approximation, simplifies the description of radiative transfer in the layer in matrix-vector form to:

$$\frac{\mathrm{d}}{c\mathrm{d}z}\begin{pmatrix} E_s \\ E^- \\ E^+ \end{pmatrix} = \begin{pmatrix} k & 0 & 0 \\ -s' & \alpha & -\sigma \\ s & \sigma & -\alpha \end{pmatrix}\begin{pmatrix} E_s \\ E^- \\ E^+ \end{pmatrix} = \begin{pmatrix} k & 0 & 0 \\ -\tfrac{1}{2}\omega k & \kappa-\omega & -\omega \\ \tfrac{1}{2}\omega k & \omega & -(\kappa-\omega) \end{pmatrix}\begin{pmatrix} E_s \\ E^- \\ E^+ \end{pmatrix} \tag{5.8}$$

where z is the metrical depth, E_s is the direct solar flux, E^- is the downward diffuse flux, E^+ is the upward diffuse flux, k is the extinction coefficient for direct sunlight, and κ the one for diffuse light. The extinction coefficients for diffuse and direct light are given by $\kappa = 2$, and $k = 1/\mu_w$, respectively, where μ_w is the cosine of the under water solar zenith angle. A generic solution of Eq. (5.7) can be formulated in matrix-vector form by:

$$\begin{pmatrix} E_s(\mathrm{b}) \\ E^-(\mathrm{b}) \\ E^+(\mathrm{t}) \end{pmatrix} = \begin{pmatrix} \tau_{ss} & 0 & 0 \\ \tau_{sd} & \tau_{dd} & \rho_{dd} \\ \rho_{sd} & \rho_{dd} & \tau_{dd} \end{pmatrix}\begin{pmatrix} E_s(\mathrm{t}) \\ E^-(\mathrm{t}) \\ E^+(\mathrm{b}) \end{pmatrix} \tag{5.9}$$

where (b) and (t) stand for the bottom and the top of the layer, respectively. The direct transmittance of the layer is given by $\tau_{ss} = \exp(-kcd)$, where d is the metrical thickness of the water layer. The other reflectance and transmittance quantities are given in Appendix A. We conducted a series of simulations with the developed WSB model to investigate the sea-bottom effect on the R_{rs} spectra at the sea surface level. The used values of the variables in the R_{rs} simulations by the WSB model are presented in Table 5.2.

Table 5.2. The variables, units and their corresponding values for simulations of R_{rs} spectra using the WSB model.

Variable	Unit	Values
Chla	mg m^{-3}	0 100
SPM	g m^{-3}	0 50
CDOM	m^{-1}	0
Bottom albedo		0.1 0.3 0.5
Water depth	m	0 .05 .1 .2 .4 .6 .8 1 1.2 1.4 1.6 2 5 20 50

The resulting R_{rs} spectra using the WSB model are presented on a logarithmic scale in Fig. 5.2.

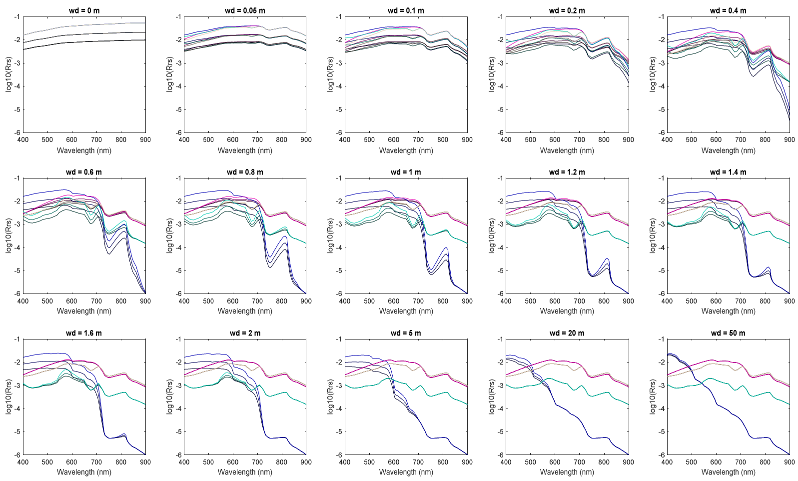

Figure 5.2. Spectra of 10log(R_{rs}) generated by the WSB model for fifteen water depths (wd), three bottom albedos (ba), two concentrations of Chla (mg m^{-3}), and two of SPM (g m^{-3}) including clear water. Water depth (wd) is indicated above each graph: clear water in blue, high Chla in green, high SPM in red, both high in yellow. Line brightness modulated by bottom albedo.

From Fig. 5.2 it is obvious that depending on water turbidity all parts of the spectrum are affected by bottom albedo. For clear water, the influence of bottom albedo (in the blue-green parts of the spectrum) could reach the surface, affecting thereby R_{rs}, for water depths up to 50 m. However, in the near infrared (wavelengths > 750 nm), the R_{rs} spectra are unaffected by bottom albedo for water depths > 2 m. There, the shape of the spectrum is completely determined by the absorption of water itself (Ruddick et al., 2006), although the magnitude of the spectrum is still dependent on the scattering due to the Chla and SPM concentrations together. Plotted logarithmically, this gives a series of spectra that are shifted parallel in the vertical direction. For clear water with a depth > 2 m, the slope of the spectrum between 750 nm and 900 nm is slightly larger than for turbid waters, but other simulations (not shown here) revealed that for low concentrations of Chla or SPM the spectral shape was practically the same as for high concentrations. So, with the exception of absolutely pure water, spectral shapes in this region are nearly invariant, regardless of WCCs. This phenomenon was termed "similarity spectrum" by Ruddick et al. (2006), and normalization of NIR spectra by the reflectance at one wavelength (*e.g.,* 750 nm) gives nearly a single normalized spectrum that is independent of WCCs.

5.4.2. The Near-Infrared Bottom Effect Index (NIBEI)

As it was found in Fig. 5.2 that for depths of less than 2 m the spectral shapes start deviating from the ones for deeper waters, optically shallow waters can be discriminated from optically deep waters by detecting deviations from the expected similarity spectrum. A first obvious candidate index for this is the ratio of the reflectances at 750 nm and 900 nm, which measures the spectral slope over this interval. From inspection of Fig. 5.2 one can observe that this slope is constant for waters deeper than 2 m, but for optically shallow waters it first increases sharply, reaches a maximum at about 0.4 m depth and finally declines to less than the deep water level. The sharp increase of the ratio is believed to be caused by a rising reflectance due to the bottom effect beginning at 750 nm, while at 900 nm the water layer is still optically deep. This ratio (750 nm / 900 nm) is very sensitive to the bottom effect in the NIR and therefore it was called NIBEI, the near infrared bottom effect index. With respect to the location of band centers of 700 nm and 900 nm in MERIS and OLCI images, separately, the NIBEI is defined as follows:

Table 5.3. The NIBEI formula for satellite images.

Satellite	750 nm	900 nm	NIBEI for satellite images[1]
MERIS	band-10	band-15	TOA radiance (band-10)/TOA radiance (band-15)
OLCI	band-12	band-19	TOA radiance (band-12)/TOA radiance (band-19)

[1] NIBEI formula = the ratio of TOA radiance values at spectral bands of 700nm/900nm.

It should be noted that the NIBEI values are constant for reflectances (Fig. 5.2), but at the TOA level, they are influenced by the atmospheric gain and path radiances. Per image, the TOA NIBEI is most influenced by visibility and SZA. Therefore, the NIBEI values are not constant for different satellite images and vary considering the date and atmospheric condition of each image, separately. However, in the future, it might even be possible to derive the best atmospheric correction from the requirement that NIR spectra for deep waters must have a fixed shape, regardless of WCCs. In that way, it would be possible to apply a fixed value for NIBEI (after atmospheric correction) for all images. However, it will remain a much bigger challenge to differentiate the combination of effects of the sea-bottom, WCCs, and atmospheric properties from radiance spectra alone. Therefore, it is suggested here to follow an intermediate approach by flagging optically shallow waters as objects that are too complex for further spectral analysis and to estimate WCCs only from pixels that have been identified as optically deep waters.

5.4.2.1. The implication of the NIBEI

We applied the NIBEI to distinguish the optically shallow waters from optically deep waters using MERIS and OLCI images over the Dutch Wadden Sea. To do this, first, we generated a NIBEI map for each image using the NIBEI formula described in Table 5.3. Next, we determined a NIBEI threshold to distinguish contaminated sea-bottom pixels from optically deep waters using these NIBEI maps. As explained in section 5.4.2, an image-based inspection was needed to determine the NIBEI threshold per each image, separately. However, determining the right NIBEI threshold per image could be done quickly and easily using the simple spectral band ratio of the NIBEI described in Table 5.3. By applying these NIBEI thresholds to OLCI and MERIS images, we generated the maps of discriminated optically shallow/deep pixels using Matlab. We presented such maps using two MERIS and OLCI images captured during high and low tidal phases, respectively. The reason to choose these images in different tidal phases was to investigate the application of the proposed NIBEI to detect TOA radiances (pixels) that were contaminated with the bottom effect in low and high tidal phases. We obtained the corresponding tidal phase information (high or low tide) for each image overpass in the study area from the Den Helder station also located at the western inlet of the Dutch Wadden Sea. The date and tidal information of these images are provided in Table 5.4.

Table 5.4. Images characteristics, tidal phases, the NIBEI, and land-mask thresholds.

Satellite	Date	SZA	Tidal phase[1]	NIBEI threshold [3]
MERIS	14-08-2002	41°	high	NIBEI values > 4
MERIS	19-04-2009	43°	low	NIBEI values > 2.8
OLCI	05-05-2018	39°	high	NIBEI values > 3.6
OLCI	06-06-2018	36°	low	NIBEI values > 3.1

[1] The phase of the tide (high: flood or low: ebb) at satellite overpass in the Dutch Wadden Sea.

The generated maps optically deep/shallow waters by applying the NIBEI using these four images are presented in Fig. 5.3.

5.4.2.2. Improving the reliability of WCC retrievals by applying the NIBEI

We evaluated the effect of applying the NIBEI in increasing the reliability of WCC retrievals from MERIS and OLCI images over the study area. To do this, first, we generated maps of the TOA radiances spectral residual errors (i.e., RMSE (W m^{-2} sr^{-1} μm^{-1}) between the observed and the best fits of modeled TOA radiances) per each MERIS and OLCI image, separately (Fig. 5.4). To model TOA radiances, we used a coupled water-atmosphere model named as 2SeaColor-MODTRAN (Arabi et al., 2016). The details of applying this model are described in the next section.

Next, we compared the spatial variation of the calculated TOA radiances spectral residual errors between the distinguished optically deep and shallow waters with and without applying the NIBEI using the generated RMSE (Wm^{-2}

sr^{-1} μm^{-1}) maps. Statistical analysis was also performed for this evaluation. The results of this statistical analysis are presented in section 5.2. The goodness-of-fit between the modeled and observed TOA radiances was based on R^2, RMSE, NRMSE, and RRMSE.

5.4.3. Modeling TOA radiances

To simulate TOA radiances using the coupled 2SeaColor-MODTRAN model, first, a LUT of R_{rs} data was generated by the 2SeaColor model for different combinations of WCCs (described in detail in section 5.4.3.1). Apart from that, a LUT of atmospheric parameters was generated by MODTRAN for different combinations of aerosol type and visibility (described in detail in section 5.4.3.2). By coupling these 2SeaColor-MODTRAN LUTs, a bigger LUT of TOA radiances was generated per each image, separately. The coupling of the two LUTs took place at the pixel level. However, the best spectral fitting match was found by considering only the first five visibilities that would generate non-negative reflectances in all bands and three aerosol types. Below we explain how the coupled 2SeaColor-MODTRAN model was used to model TOA radiances for MERIS and OLCI images.

5.4.3.1. LUT processing for generating R_{rs} values

The LUT of R_{rs} values by the 2SeaColor model was generated using Eq. (5.1a) considering various combinations of WCCs and for the specific SZA value for each satellite image, separately. The variation ranges of WCCs for these R_{rs}-LUTs is described in Table 5 as follows:

Table 5.5. The used ranges and units of WCCs in the R_{rs} LUTs by the 2SeaColor model.

Variable	Unit	Values	Step
Chla concentration	mg m^{-3}	0 - 100	5
SPM concentration	g m^{-3}	0 - 100	5
CDOM absorption at 440 nm	m^{-1}	0 - 1.5	0.5

We used the same water models described in Table 2 proposed by Arabi et al. (2018) for the 2SeaColor model parametrization considering the optical characteristics of different water constituents in the Dutch Wadden Sea. The generated LUT of R_{rs} values by the 2SeaColor model was later coupled to the MODTRAN-based atmospheric properties to model TOA radiances as described in the following subsection.

5.4.3.2. LUT processing for generating atmospheric parameters

The LUTs of atmospheric parameters (i.e., L_0, G and S) by MODTRAN were generated considering various combinations of visibility and aerosol type in combination with the environmental variables and illumination geometry of each satellite image, separately. The environmental variables in the form of the concentrations of O_3, H_2O, and CO_2 were obtained from Global Reference

Networks considering the region of interest, time and date of the satellite image. The illumination-observation geometry in the form of SZA, the VZA and RAA were extracted from MERIS and OLCI image directly. Other input variables for running MODTRAN were determined following Table 3 in Arabi et al. (2016). For more detailed information about MODTRAN, readers are referred to MODTRAN 5.2.1 user's manual by Berk et al. (2011). The variation ranges of visibility and aerosol type for these atmospheric parameters LUTs is described in Table 5.6 as follows:

Table 5.6. The used visibility range and aerosol types in atmospheric properties LUTs.

Atmospheric property	Unit	Variable
Visibility	km	4 - 100
Aerosol-type	-	Rural, Maritime, Urban

We defined the visibility increments considering that a change in lower visibilities (*e.g.,* 4 km) has much more effect on the TOA radiances than a change at higher visibilities (*e.g.,* 40 km). Therefore we used Inverse Visibility (IV) to obtain almost perfect linear increments in AOT (aerosol optical thickness). Based on this method, values of IV were set equal to 100 divided by the actual visibility (100 / Vis). We ran MODTRAN with the values (1, 2, 3, .., 25 for IV and therefore with the corresponding actual visibilities (100, 50, 33.3, …, 4 km).

To compensate possible biases in sensor gain values, after the sampling of MODTRAN spectra with the respective sensor's spectral response functions, we modified the values of L_0 and G to correct for the differences between the solar irradiance database used by the European Space Agency (ESA) and the default one used by MODTRAN. The ESA uses the extraterrestrial solar irradiance data by Thuillier et al. (2003), while in MODTRAN the corresponding data are from a different source (Kurucz, 1995). The performed analysis showed that the differences between the two sources of solar irradiance spectra were substantial and caused discrepancies, especially at the shorter wavelengths. Therefore, we used a correction factor for all MERIS and OLCI bands to modify the calculated MODTRAN parameters L_0 and G according to the solar irradiance values used by ESA. During the LUT generation, TOA radiances in the sensor's bands are calculated as follows:

$$L_{\mathrm{TOA}} = L_0 + \frac{Gr}{1 - Sr} \tag{5.10}$$

where L_{TOA} is the modeled TOA radiance value (W m^{-2} sr^{-1} μm^{-1}), and r is the hemispherical water-leaving reflectance (=πR_{rs}) calculated by 2SeaColor.

5.4.4. Generating WCCs and atmospheric properties maps

After evaluating the importance of applying the NIBEI, we generated the atmospheric properties, and WCC maps using the coupled 2SeaColor-MODTRAN LUT applied to optically deep waters pixels of MERIS and OLCI images. The simultaneous retrieval of WCCs and atmospheric properties was performed by spectrally fitting of the modeled TOA radiances (using RMSE) to observed TOA radiances for all bands except for bands 11 and 13 for MERIS and OLCI respectively. These bands are located in the O_2-A absorption region and could give erroneous results due to spectral sampling errors of MERIS and OLCI (Arabi et al., 2016). To speed up the computation and limit the combined LUT size, for every pixel and aerosol type, only five visibilities were selected from the atmospheric LUT. These visibilities were chosen to be less than the minimum required visibility for which the modeled L_0 was less than or equal to the measured TOA radiance in all bands. This approach is equivalent to assuming only non-negative reflectances.

Nonetheless, it dramatically increased the speed of computation when applied using MatLabR2017B on a personal PC [Processor: Intel (R) cORE (tm) i7 - 4700 MQ, CPU: 2.40 GHz, RAM: 7.88 GB]. In total, the average number of pixels per image was equal to 70,000. The total number of LUT cases for each pixel is 15 (5 visibility, 3 aerosol types) times the number of water cases (in total 21 × 21 × 4 = 1764 cases). The computation time to generate each map was thirteen minutes. In this approach six output maps were produced, containing aerosol type, visibility, Chla concentration, SPM concentration, CDOM absorption, and the RMSE spectral error.

5.4.5. Validating atmospheric properties and WCCs retrievals

We validated the accuracy of the coupled 2SeaColor-MODTRAN LUT-based retrievals at the NJS which is located at the optically deep water of the Dutch Wadden Sea (water depth > 5 m) (Wernand, 2011). For this, we used the inverse of Eq. (5.9) to estimate the water-leaving reflectances from TOA radiances (Verhoef and Bach, 2003) by using the known MODTRAN atmospheric parameters L_0, G and S. We used 14 MERIS-matchups and 17 OLCI-matchups concurrent with in-situ Chla (mg m^{-3}), SPM (g m^{-3}) and R_{rs} (sr^{-1}) measurements collected under the condition of SZAs < 60° at the NJS (Arabi et al., 2018). Since the NJS is located close to the shore, for every image, the darkest pixel from 5 by 5 pixels around the location of this station was extracted first using SNAP software. By selecting the darkest pixel from the 5 × 5 neighborhood centered on the NJS, we excluded cloudy and land pixels, as well as water pixels close to the shore that was possibly influenced by an adjacency effect due to the near land area. An underlying assumption in our approach was that the water of the darkest pixel had the same composition as the water found at the location of the NJS. However, since the water current is mostly strong near the Marsdiep inlet close to the NJS, we were confident that the water was well-mixed, and local gradients in water properties were small (Arabi et al., 2016). The results of this evaluation are presented in sections 5.5.3 and 5.5.4.

5.5. Results

Fig. 5.3 presents the optically shallow waters distinguished from optically deep waters by applying the NIBEI on the images described in Table 5.4. The image dates and the tidal phase are indicated above each image. The detected optically shallow waters by the NIBEI are in grey, the land regions are in black, and optically deep waters are in dark-blue color.

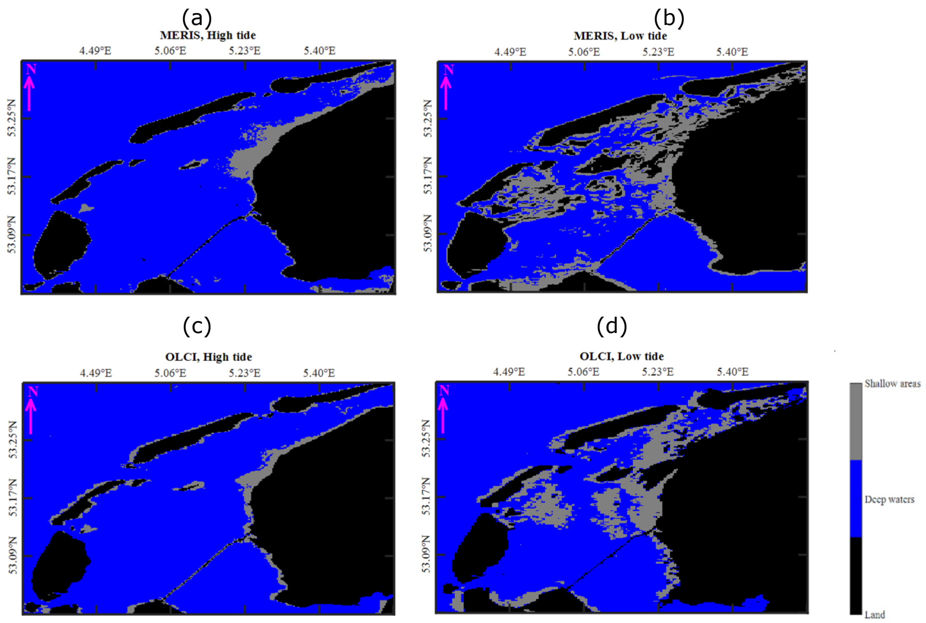

Figure 5.3. The generated maps of optically deep waters and the detected optically shallow waters by applying the NIBEI over the Dutch Wadden Sea and the IJsselmeer lake from; (a) the MERIS image captured during high tidal phase on 14-08-2002; (b) the MERIS image captured during low tidal phase on 19-04-2009; (c) the OLCI captured during high tidal phase on 05-05-2018; (d) the OLCI image captured during low tidal phase on 06-06-2018.

As can be seen from the above maps (in lat-long projection), pixels of optically shallow water, detected by the NIBEI, contain larger regions of the study area during the low tidal phase for both MERIS and OLCI images (Fig. 5.3 (b), (d)).

5.5.1. Improving the reliability of WCC maps

Fig. 5.4 shows the generated maps of spectral residual errors (RMSE) between the best fits of observed and modeled TOA radiances using the coupled 2SeaColor-MODTRAN (described in section 5.4.3) with and without applying the NIBEI for the same images described in Table 5.4.

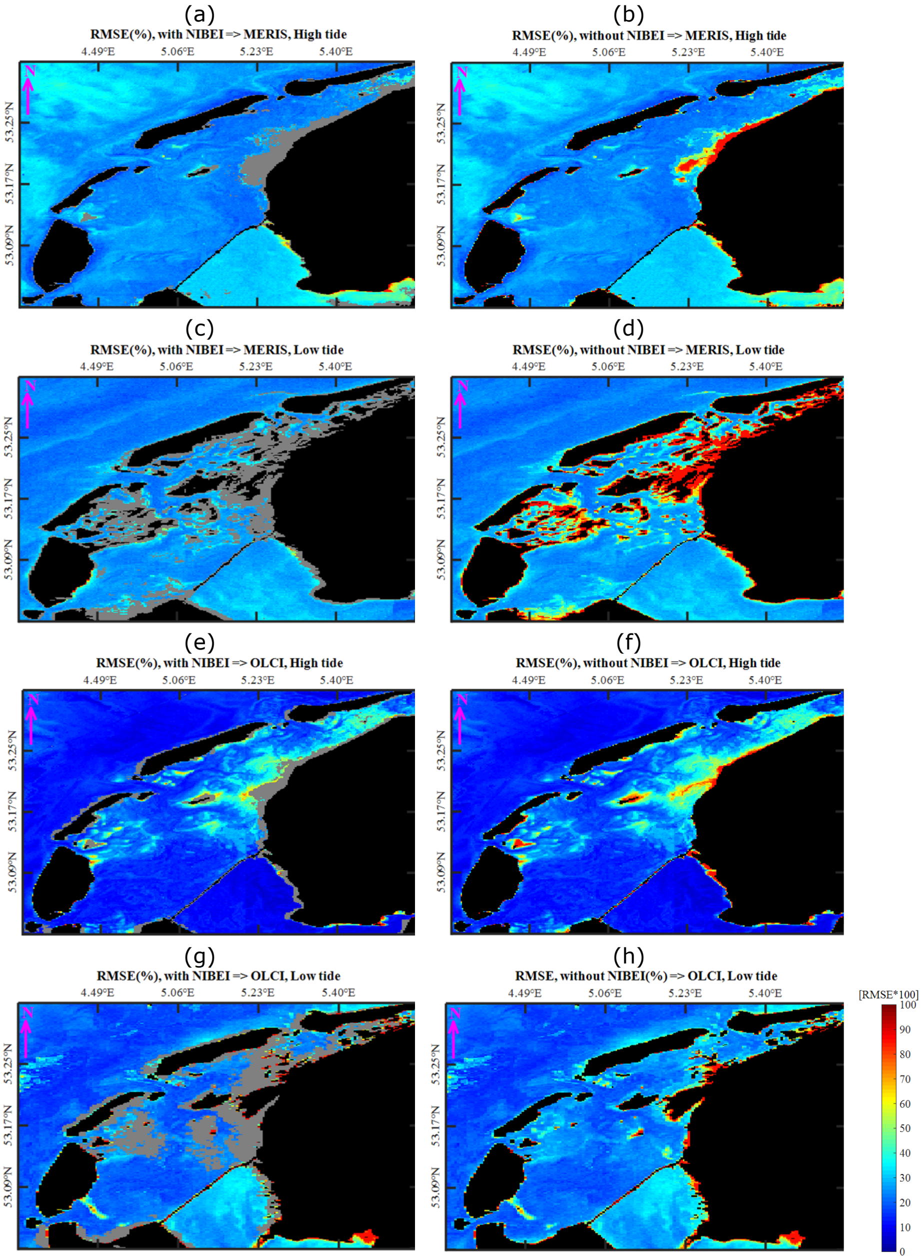

Figure 5.4. The generated maps of the TOA radiances spectral residual errors (RMSE) (Wm^{-2} sr^{-1} µm^{-1}) between the best fits of 2SeaColor-MODTRAN modeled and observed TOA radiances over the Dutch Wadden Sea and the IJsselmeer lake; first row: the MERIS image captured during high tidal phase on 14-08-2002 (a) with and (b) without applying the NIBEI; second row: the MERIS image captured during low phase on 19-04-2009 (c) with and (d) without applying the NIBEI; third row: the OLCI image captured during high tidal phase on 05-05-2018 (e) with and (f) without applying the NIBEI; fourth row: the OLCI image captured during low tidal phase on 06-06-2018 (g) with and (h) without applying the NIBEI.

As Fig. 5.4 (a) shows, the estimated TOA radiances spectral residual errors (RMSE (W m^{-2} sr^{-1} μm^{-1})) for the MERIS image captured during the high tidal phase, do not exceed ~ 30% in the different parts of the image after removal of optically shallow waters using the NIBEI. However, these errors reach their maxima (shown in bright-red color) of ~ 100% at the same locations of optically shallow waters if the NIBEI is not implemented in the same image in Fig. 5.4. (b). This outcome is even more apparent for the MERIS image captured during the low tidal phase when the optically shallow waters, detected by the NIBEI, cover larger areas in Fig. 5.4 (c). As a result, a considerable part of the Dutch Wadden Sea shows very high spectral residual errors (~ 100%) if the NIBEI is not implemented on the MERIS image in Fig. 5.4 (d). The same applies to OLCI images captured during high and low tidal phases, respectively. Consequently, the retrieved WCCs (Chla, SPM, and CDOM concentration) are questionable over these optically shallow waters due to very high spectral residual errors while the NIBEI is not implemented on the images. Further investigations showed that for each image similar aerosol types and visibilities were present over the detected shallow and optically deep waters (Figs. 5.6 and 5.7). Therefore it can be concluded that the effect of the sea-bottom is the main reason for the model's failure to accurately simulate TOA radiances over the optically shallow waters (Arabi et al., 2018; Yu et al., 2016).

Fig. 5.5 presents the spectral agreement between the modeled TOA radiances against the observed ones for MERIS and OLCI images at three band centers of 490 nm, 550 nm, and 665 nm as follows:

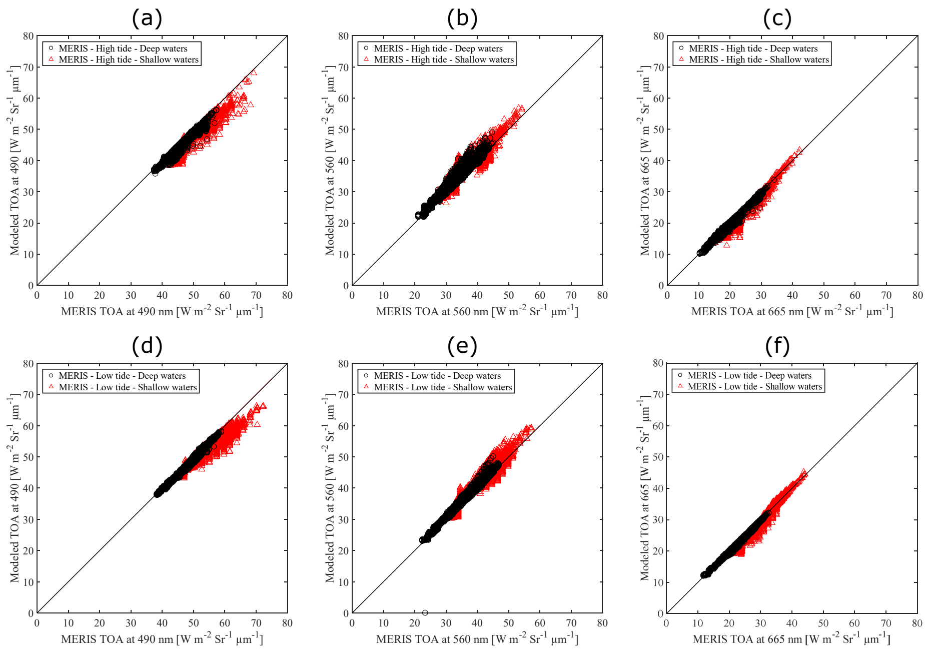

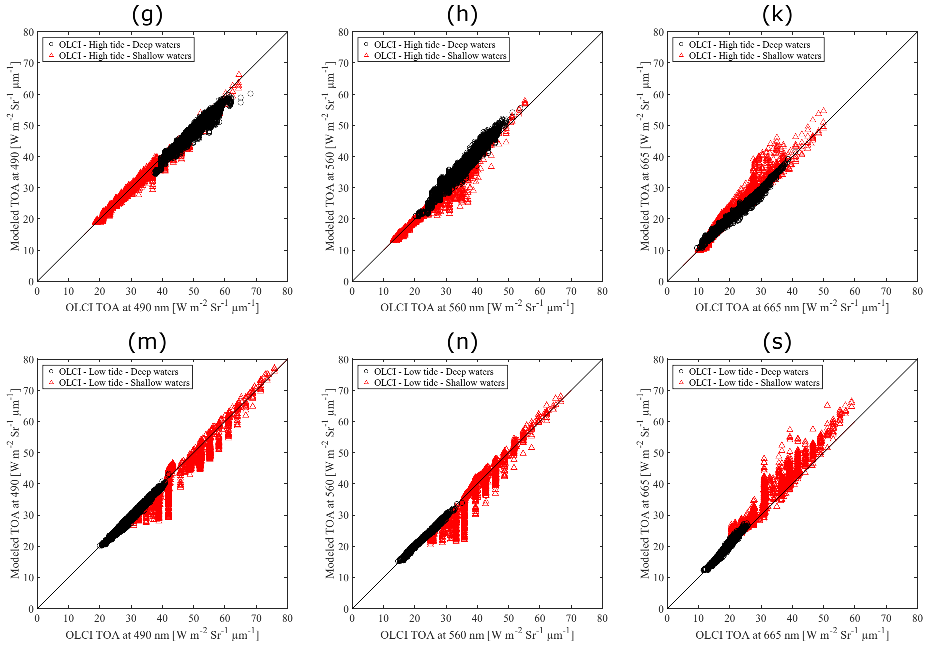

Figure 5.5. Comparison between the 2SeaColor-MODTRAN model's best-fit spectra and observed TOA radiances (Wm^{-2} sr^{-1} μm^{-1}) over the study area for the band centres of first column: 490 nm; second column: 560 nm; and third column: 665 nm, and from first row: the MERIS image captured during high tidal phase on 14-08-2002; second row: the MERIS image captured during low tidal phase on 19-04-2009; third row: the OLCI image captured during high tidal phase on 05-05-2018; fourth row: the OLCI image captured during low tidal phase on 06-06-2018.

As Fig. 5.5 shows, the accuracy of modeled TOA radiances against the observed ones decreases over the optically shallow waters in comparison to optically deep waters for both MERIS and OLCI images during high and low tidal phases, respectively. The related error statistics of this assessment are presented in Tables 5.7, 5.8, 5.9 and 5.10.

Table 5.7. Evaluation of the 2SeaColor-MODTRAN model's best-fit spectra against observed TOA radiances over the study area from the MERIS image captured during high tidal phase on 14-08-2002.

Statistical analysis	R^2		RMSE		NRMSE (%)		RRMSE (%)	
wavelength/ satellite	deep	shallow	deep	shallow	deep	shallow	deep	shallow
490 nm	0.97	0.85	0.52	1.45	2.60	5.10	1.20	2.86
560 nm	0.98	0.83	0.80	1.60	2.33	5.70	2.65	4.10
665 nm	0.99	0.89	0.41	1.08	1.72	3.36	2.51	3.49

Table 5.8. Evaluation of 2SeaColor-MODTRAN model's best-fit spectra against observed TOA radiances over the study area from the MERIS image captured during low tidal phase on 19-04-2009.

Statistical analysis	R^2		RMSE		NRMSE (%)		RRMSE (%)	
wavelength/ satellite	deep	shallow	deep	shallow	deep	shallow	deep	shallow
490 nm	0.99	0.79	0.38	1.43	1.83	5.38	0.81	2.56
560 nm	0.99	0.84	0.51	1.47	2.08	5.73	1.54	3.39
650 nm	0.99	0.90	0.23	1.06	1.10	3.10	1.20	2.49

Table 5.9. Evaluation of 2SeaColor-MODTRAN model's best-fit spectra against observed TOA radiances over the study area from the OLCI image captured during high tidal phase on 05-05-2018.

Statistical analysis	R^2		RMSE		NRMSE (%)		RRMSE (%)	
wavelength/ satellite	deep	shallow	deep	shallow	deep	shallow	deep	shallow
490 nm	0.95	0.89	0.86	2.03	1.96	3.08	1.83	3.05
560 nm	0.96	0.88	0.98	2.14	2.45	4.22	2.32	4.73
665 nm	0.98	0.89	0.53	2.38	1.68	5.43	2.99	7.87

Table 5.10. Evaluation of 2SeaColor-MODTRAN model's best-fit spectra against observed TOA radiances over the study area from the OLCI image captured during low tidal phase on 06-06-2018.

Statistical analysis	R^2		RMSE		NRMSE (%)		RRMSE (%)	
wavelength/ satellite	deep	shallow	deep	shallow	deep	shallow	deep	shallow
490 nm	0.99	0.86	0.35	2.70	1.58	6.00	1.29	5.53
560 nm	0.99	0.87	0.27	2.64	1.32	6.34	1.35	6.51
665 nm	0.99	0.86	0.30	2.39	2.11	6.21	1.86	6.58

As Tables 5.7, 5.8, 5.9 and 5.10 show, there is a strong agreement between the modeled TOA radiances and the observed ones for all three selected bands (490 nm, 560 nm and 665 nm) over the optically deep waters of the Dutch Wadden Sea for both low and tidal phases using MERIS and OLCI images, respectively (R^2 > 0.95, RMSE < 1, NRMSE ~ 2.5%, RRMSE ~ 2.5%). However, the agreement between the modeled TOA radiances and the observed ones decreases over the optically shallow waters for both low and tidal phases using MERIS and OLCI images (R^2 < 0.90, RMSE > 1, NRMSE ~ 4%, RRMSE ~ 5%). Therefore, it can be concluded that applying the NIBEI together with water retrieval algorithms to satellite images enables excluding all pixels with unreliable WCC retrievals due to high spectral residual errors. In other words, excluding the optically shallow waters from consideration by applying the NIBEI leads to increasing the reliability of WCC retrievals for the rest of the study area (identified as optically deep waters by the NIBEI). It should be noted that this conclusion does not necessarily mean that applying the NIBEI leads to an increase in the accuracy of the WCCs retrievals in optically deep waters. Since the accuracy of the WCC retrievals is dependent on other factors such as the suitability of the applied atmospheric properties and the water retrieval algorithm, it is independent of the NIBEI performance. In the next section, we generate WCCs and atmospheric properties maps using the coupled 2SeaColor-MODTRAN model over the masked optically shallow waters of the Dutch Wadden Sea and validate the accuracy of the WCCs retrievals in the NJS located in optically deep waters of the study area.

5.5.2. The generated maps of atmospheric properties

The generated maps of aerosol types and visibility using the coupled 2SeaColor-MODTRAN model from MERIS and OLCI images are presented in Figs. 5.6 and 5.7. For these maps, the aerosol types rural, maritime and urban are shown in green, blue and red color, respectively. As before, the optically shallow waters detected by the NIBEI are shown in grey, and the land regions are shown in black color, respectively. The location of the NJS is shown by a pink circle in the Western-South of each map (53° 00' 06"N; 4° 47' 21"E). For every group of generated maps, the legend is shown in the last image.

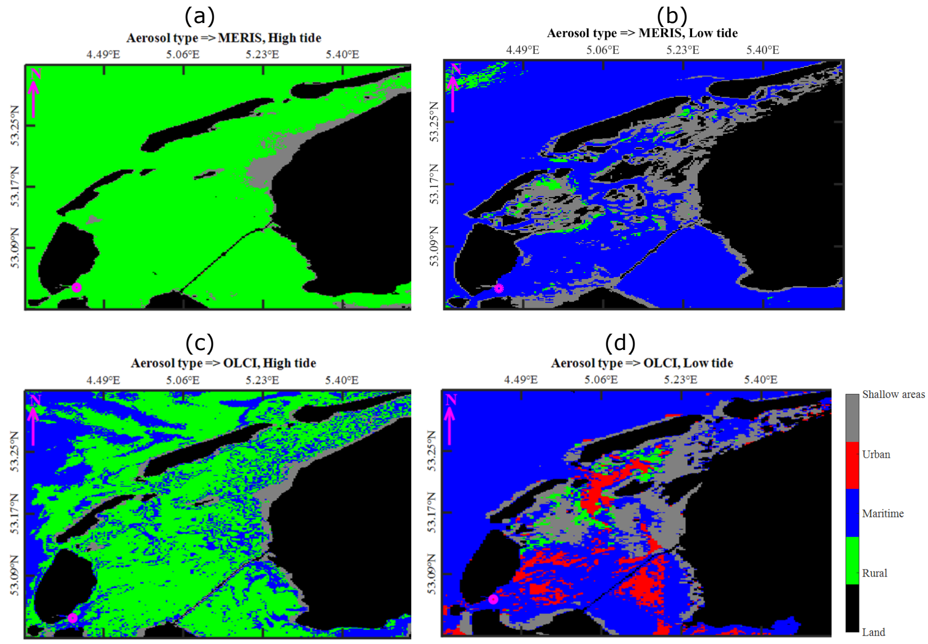

Figure 5.6. The generated maps of aerosol type (rural, maritime, urban) using the coupled 2SeaColor-MODTRAN model over the Dutch Wadden Sea and the IJsselmeer lake from (a) the MERIS image captured during high tidal phase on 14-08-2002; (b) the MERIS image captured during low tidal phase on 19-04-2009; (c) the OLCI image captured during high tidal phase on 05-05-2018 (d) the OLCI image captured during low tidal phase on 06-06-2018.

As can be seen from these maps, the aerosol type varies for each image by date. The dominant aerosol type is maritime for the images captured in April and June in Figs. 5.6 (b) and (d), while most parts of the images are diagnosed as the rural aerosol type for the images captured in August and May in Figs. 5.6 (a) and (c). Moreover, the aerosol type is homogeneous over the study area in Figs. 5.6 (a) and (b) while they are spatially varied in Figs. 5.6 (c) and (d). Overall, the rural and maritime aerosol type are mostly observed over the study area for all images, and the maritime aerosol type is mainly seen in the neighborhood of the North Sea (Figs. 5.6 (b), (c) and (d)). The urban aerosol type is only identified at some internal parts of the Dutch Wadden Sea and partly in the IJsselmeer Lake in Fig. 5.6 (d). Below the generated maps of retrieved visibility over the study are presented.

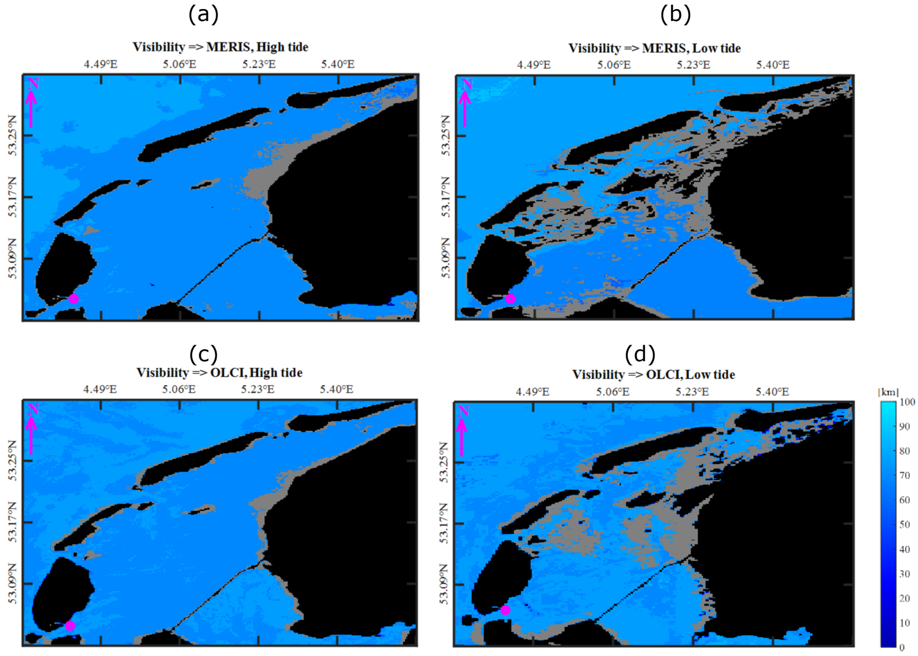

Figure 5.7. The generated visibility (km) maps using the coupled 2SeaColor-MODTRAN model over the Dutch Wadden Sea and the IJsselmeer lake from (a) the MERIS image captured during high tidal phase on 14-08-2002; (b) the MERIS image captured during low tidal phase on 19-04-2009; (c) the OLCI image captured during high tidal phase on 05-05-2018 (d) the OLCI image captured during low tidal phase on 06-06-2018.

The generated visibility (km) maps show that the visibility range varies between 10 km and 50 km for all dates. Moreover, the visibility varies spatially while higher visibilities are observed over the North Sea (40 km - 50 km) in comparison to the Dutch Wadden Sea (10 km - 40 km) for all images. Especially for the OLCI image in Fig. 5.7 (d), some local haze variation can be seen in internal parts of the Dutch Wadden Sea.

Below we present the validation results between in-situ hyperspectral measurements at the NJS and atmospherically corrected TOA radiances using the determined aerosol type and visibility by the model for each matchup, separately. It should be noted that in this TOA radiance approach, the atmospheric correction is not needed since the sensor radiances are simulated and compared to the measured radiance signals in the spectral bands of the sensor to retrieve surface and atmospheric properties simultaneously.

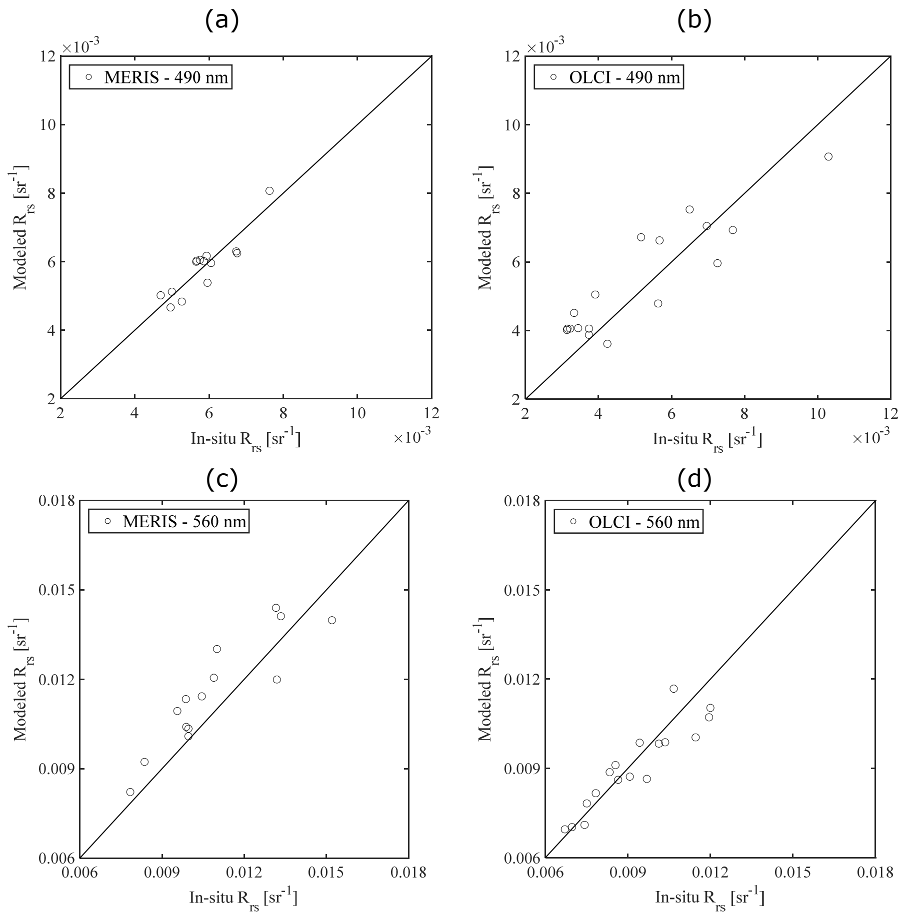

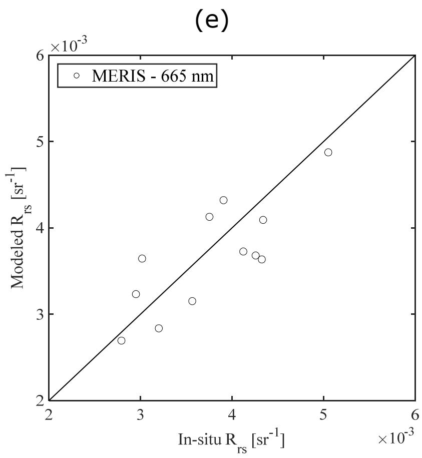

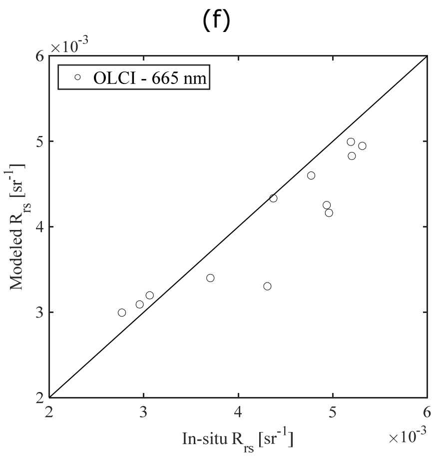

Figure 5.8. First column: comparison between MERIS-atmospheric corrected R_{rs} and in-situ R_{rs} values (sr^{-1}) for fourteen matchups at the NJS between 2008 and 2010 at MERIS band centers of (a) 490 nm, (c) 560 nm and (e) 665 nm; second column: comparison between OLCI-atmospheric corrected R_{rs} and in-situ R_{rs} values (sr^{-1}) for seventeen matchups at the NJS since April 2018 till present time at OLCI band centers of (b) 490 nm, (d) 560 nm and (f) 665 nm.

Table 5.11 presents a detailed statistical analysis of this evaluation:

Table 5.11. Models' performance evaluation in atmospheric correction part.

Statistical analysis	R^2		RMSE		NRMSE (%)		RRMSE (%)	
Band centre/ Satellite	MERIS	OLCI	MERIS	OLCI	MERIS	OLCI	MERIS	OLCI
490 nm	0.79	0.80	0.0003	0.0007	13	9	6	13
560 nm	0.78	0.82	0.0008	0.0005	10	9	7	5
665 nm	0.78	0.86	0.0004	0.0003	12	9	11	10

The results of this evaluation show reasonable agreement between the in-situ and atmospherically corrected water-leaving reflectances with respect to identified visibility and aerosol type for both MERIS and OLCI images (R^2 ~ 0.80, RMSE < 0.001). Therefore, it can be stated that the coupled model is accurate enough to atmospherically correct TOA R_{rs} from OLCI and MERI images.

5.5.3. Generating WCC maps

Below are the generated maps of Chla concentration (mg m^{-3}), SPM concentration (g m^{-3}), CDOM absorption at 440 nm (m^{-1}) for the same MERIS and OLCI images.

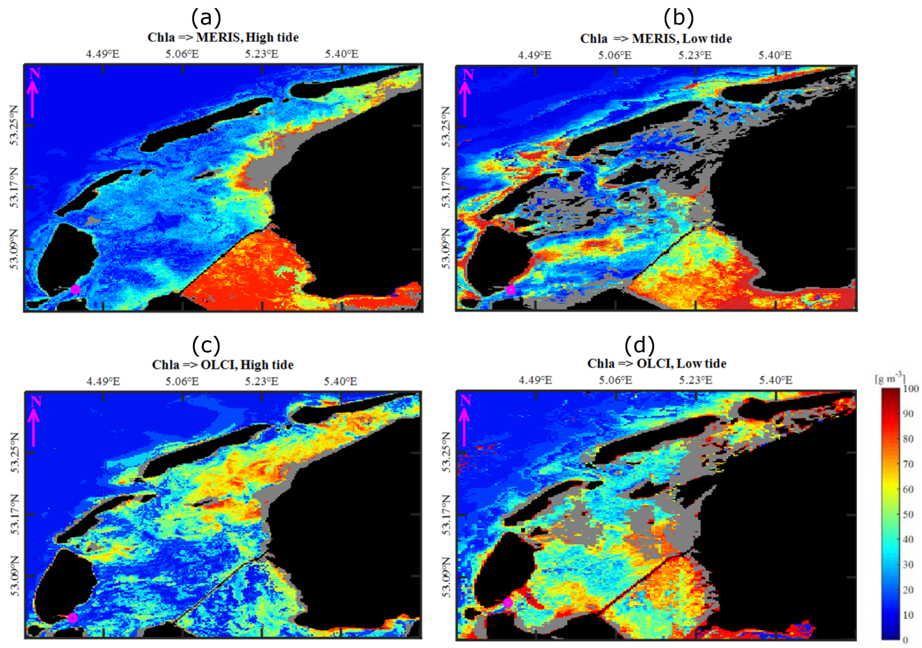

Figure 5.9. The retrieved Chla concentration (mg m^{-3}) maps using the coupled 2SeaColor-MODTRAN model over the Dutch Wadden Sea and the IJsselmeer lake from (a) MERIS image captured during high tidal phase on 14-08-2002; (b) MERIS image captured during low tidal phase on 19-04-2009; (c) OLCI image captured during high tidal phase on 05-05-2018 (d) OLCI image captured during low tidal phase on 06-06-2018.

As can be seen from Fig. 5.9, the variation range of Chla concentrations is similar on all dates (0 to 100 (mg m^{-3})). The retrieved Chla concentrations mainly show their maximum estimates nearby the coasts, surrounding islands of the Dutch Wadden Sea and the IJsselmeer lake (~ 100 (mg m^{-3})). These values decrease while moving from the shores to the internal parts of the Dutch Wadden Sea (~ 60 (mg m^{-3})) and reach their lowest amounts in the external parts of the Dutch Wadden Sea in the vicinity of the North Sea (< 20 (mg m^{-3}]) for all dates. However, spatial and temporal variability of Chla concentrations is observed on various dates. For example, more areas of the IJsselmeer lake show higher values of Chla estimates (~ 100 (mg m^{-3})) in April and August (Figs. 5.9 (a) and (b)) in comparison to May and June (Figs. 5.9 (c) and (d)). The accuracy of MERIS retrievals against the collected in-situ measurements at the NJS is presented in Fig. 5.10. For OLCI images, there were no matching in-situ measurements of Chla concentration (mg m^{-3}) to validate the retrievals.

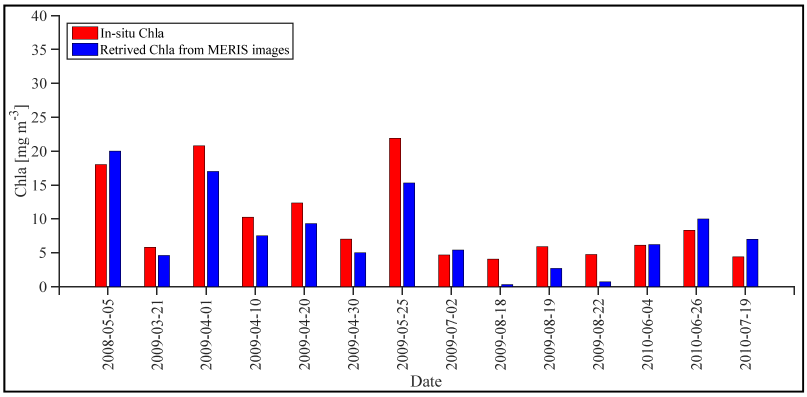

Figure 5.10. The comparison of the MERIS-retrieved (blue bars) and in-situ measurements (red bars) of Chla concentrations (mg m^{-3}) for fourteen MERIS matchups at the NJS between 2008 and 2010.

In Fig. 5.10, the X-axis shows the date of each MERIS-in-situ matchups and the Y-axis shows the values of measured and retrieved Chla concentrations (mg m^{-3}). Below the scatter plot of this evaluation is presented.

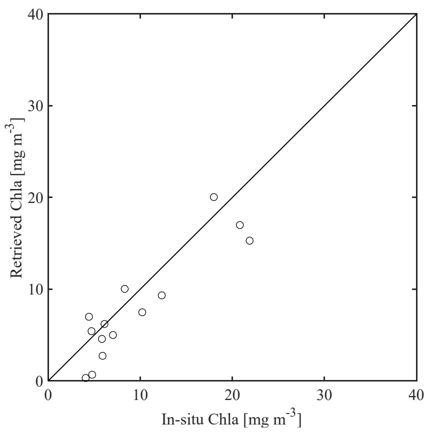

Figure 5.11. The Comparison between MERIS-retrieved and in-situ Chla concentrations (mg m^{-3}) for fourteen matchups at the NJS between 2008 and 2010.

Chla retrievals from MERIS images for a period of three years (2008 - 2010) shows reasonable agreement with in-situ measurements (R^2 = 0.79, RMSE = 27.72%, NRMSE = 14.91%, RRMSE = 27.72). The RMSE < 30% appear reasonable enough, as compared with the validation of the SeaWiFS Chla data product for global open ocean waters with a relative RMSE of about 58% (Le et al., 2013). Therefore, it is concluded that the accuracy of generated Chla maps using the coupled 2SeaColor-MODTRAN is reasonable enough over the optically deep waters of the Dutch Wadden Sea. Fig. 5.12 presents four maps of retrieved SPM concentrations (g m^{-3}) over the study area using the same MERIS and OLCI image as follows:

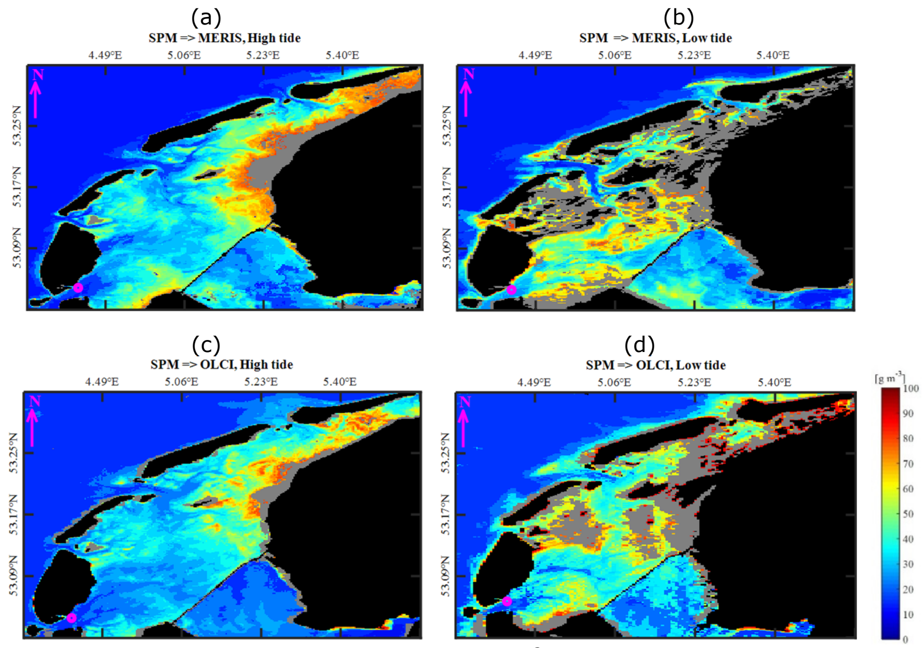

Figure 5.12. The retrieved SPM concentration (g m^{-3}) maps using the coupled 2SeaColor-MODTRAN model over the Dutch Wadden Sea and the IJsselmeer lake from (a) MERIS image captured during high tidal phase on 14-08-2002; (b) MERIS image captured during low tidal phase on 19-04-2009; (c) the OLCI image captured during high tidal phase on 05-05-2018 (d) OLCI image captured during low tidal phase on 06-06-2018.

As can be seen from Fig. 5.12, the retrieved SPM concentration maps show the same variation range (0 - 90 (g m^{-3})) for all dates. However, the spatial variability of these estimates varies according to tidal phase variations. For example, most parts of the Dutch Wadden Sea are covered with high SPM values nearby the coasts and islands (60 - 100 (g m^{-3})) during the low tidal phase in Figs. 5.12 (b) and (d). The spread of high SPM concentrations decreases during the high tidal phase while the high level of SPM has only observed nearby the Eastern-North coasts of the study area in Figs. 5.12 (a) and (c). The SPM concentrations reach their lowest values in the proximity of the North Sea for all dates (0 - 20 (g m^{-3})). Below the accuracy of the retrievals against the collected in-situ measurements of SPM at the NJS is presented. However, there were no matching in-situ measurements to validate these retrievals using OLCI images over the Dutch Wadden Sea at the time when this manuscript was written.

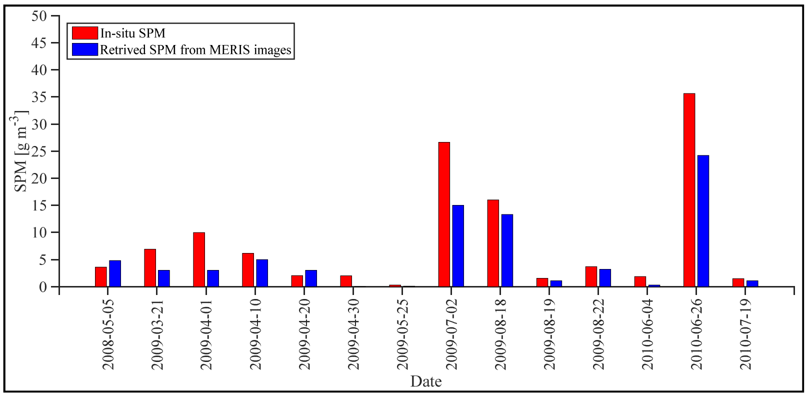

Figure 5.13. The comparison of the MERIS-retrieved (blue bars) and in-situ measurements (red bars) of SPM concentration (g m^{-3}) for fourteen MERIS matchups at the NJS between 2008 and 2010.

In Fig. 5.13, the X-axis shows the date of each MERIS matchup at the NJS and the Y-axis shows the values of in-situ SPM and retrieved Chla concentration from MERIS images at the location of the NJS. Below the scatter plot of this evaluation is presented.

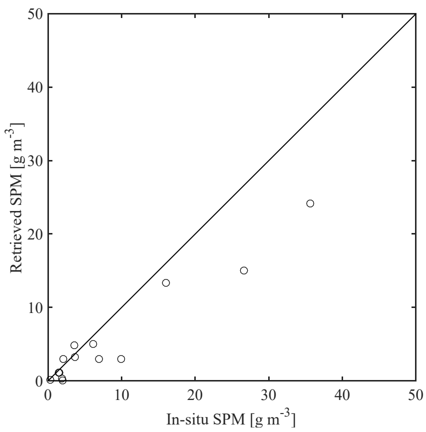

Figure 5.14. Comparison between MERIS-retrieved and in-situ SPM concentration (g m^{-3}) for fourteen matchups at the NJS between 2008 and 2010.

As the results of this evaluation shows, the retrieved estimated SPM concentrations (g m^{-3}) showed very good agreement with in-situ measurements (R^2 = 0.92, RMSE = 18.7%, NRMSE = 5.29%, RRMSE = 22.2%). Therefore, it is concluded that the accuracy of generated SPM maps using the coupled 2SeaColor-MODTRAN is reasonable enough over the optically deep waters of the Dutch Wadden Sea.

Overall, considering the turbid nature and complex spatial heterogeneity of the Wadden Sea, the performance of the coupled 2SeaColor-MODTRAN model should be regarded as encouraging and satisfactory. Not only is there a reasonable agreement between the coupled model's retrievals with in-situ measurements at the NJS, but also the generated WCC maps are within the range of measured WCCs on the ground reported by other researchers (Cadée and Hegeman, 2002; Hommersom, 2010a; Reuter et al., 2009; Tillmann et al., 2000).

5.5.4. Discussion

In many coastal areas, the sea-bottom effect contributes to the observed water leaving reflectances at the water surface level and accordingly to the TOA radiances at satellite level (Lee and Carder, 2002). This can interfere with the correct retrieval of WCCs from hyperspectral or satellite images depending on local water depth and transparency of the water (Lee et al., 1999; Martinez and Calway, 2012). Although bathymetry maps can be used to determine the shallowness of water in remote sensing studies of coastal areas (Pattanaik et al., 2015), these maps are not always available for all regions (Giardino et al., 2012). On the other hand, the effect of the sea-bottom varies depending on water turbidity and/or on water depth variation in tidal areas (Giardino et al., 2014; Maritorena et al., 1994; Mgengel, 1991). Therefore, using bathymetry maps cannot always help to improve the accuracy of WCC products over turbid tidal areas.

In this paper, we extended the 2SeaColor model by incorporating the sea-bottom effect for modeling of the above water reflectance as a function of water constituents' concentrations (Chla, SPM, CDOM), bottom albedo and water depth. The improved model, called Water - Sea Bottom (WSB), was used to better understand the effect of bottom albedo on field and satellite observations of ocean color. Using the developed WSB model, we assessed the influence of the sea-bottom on the water leaving reflectances for different combinations of Chla, SPM and CDOM concentration, water depth and bottom albedo. We found that all parts of the water leaving reflectance spectra are affected by water depth in various ways. However, in the NIR, the spectral shapes were nearly insensitive to the WCCs and spectra only increase in magnitude with water turbidity and the bottom albedo (Fig. 5.2). The results of this investigation are similar to ones obtained from measurements in a study conducted by Ruddick et al. (2006). As the main outcome of this investigation, we defined the novel index NIBEI to distinguish optically shallow waters (contaminated by sea-bottom effects) from optically deep waters. We later tested the application of applying the NIBEI on MERIS and OLCI at two aspects of i) generating shallow vs. optically deep water maps and ii) generating more reliable WCCs maps.

The results show that the NIBEI successfully discriminated sea-bottom contaminated waters from optically deep waters using MERIS and OLCI images (section 5.1). By generating these shallow vs. optically deep water maps using the NIBEI (Fig. 5.3), one can be made aware of the location of possible contamination by sea-bottom effects and identify waters to be excluded from consideration. Such products have an important application for the appropriate selection of in-situ measurements locations for the validation of different algorithms. As shown in Fig. 5.2, in the blue-green the sea-bottom can even have an influence on remote sensing observations for water depths up to 50 m if the water is clear enough. Note, however, that for turbid waters the bottom depth will have less influence than for clear waters. Therefore, it is essential to accurately determine the location of optically deep waters by not only considering the actual water depth maps (Fig. 5.1 (right)) but also by discriminating optically shallow waters using the spectral index NIBEI (Fig. 5.3). Otherwise, there is a chance that the WCC algorithm retrievals fail to be in good agreement with in-situ measurements due to the sea-bottom effect in these areas.

Moreover, the results showed that applying the proposed NIBEI led to generate more reliable WCCs maps using MERIS and OLCI images by excluding contaminated sea-bottom effects pixels from consideration (section 5.5.2). Reliable WCC maps (Figs. 5.9 and 5.12) over the complex shallow waters of the Dutch Wadden Sea can provide very significant information for the environmental decision makers concerning maintenance and conservation of this vital coastal area (Doerffer and Fischer, 1994; Eleveld et al., 2008; Peters et al., 2005; Pitarch et al., 2016). This also creates an excellent opportunity for the long-term spatio-temporal monitoring of this study area considering the availability of MERIS (2002 - 2012) and OLCI (2018 - present) images. However, the improvement in accuracy of WCCs retrievals by applying the NIBEI was out of the scope of this study and is recommended for future researches to define a stronger NIBEI.

Since our efforts in this paper were centered on applying the proposed NIBEI on MERIS and OLCI images over the Dutch Wadden Sea, it is still unknown how broadly applicable this index will be and to what extent our findings could be generalized. Thus, we suggest testing the applicability of the proposed NIBEI for other coastal areas using various ocean color remote sensors having suitable bands in the NIR region.

5.6. Conclusion

A new model called WSB was developed to incorporate the sea-bottom effect into R_{rs} simulations using radiative transfer modeling. From the analysis and validations of this study, it is concluded that:

1) The addition of the bottom layer to the 2SeaColor model enables to simulate the bottom effect on the observed water leaving reflectance values and facilitated the development of the NIBEI.
2) The NIBEI accurately discriminates optically shallow water from optically deep waters using MERIS and OLCI images.
3) The exclusion of optically shallow waters from the image increases the reliability of the derived WCCs in the optically deep waters.
4) Generating reliable WCC maps over the complex waters of the Dutch Wadden Sea as in this study is a significant achievement following the Water Framework Directive regulations from the European Union force (Environment Directorate-General of the European Commission, 2000).

Appendix A: Water layer optical properties in the WSB model

In the WSB model, a numerically safe solution of radiative transfer is applied that has been adapted from the 4SAIL vegetation canopy reflectance model (Verhoef et al., 2007). The numerical safety refers to the treatment of the possible singularity occurring when $k = m$, where m is the eigenvalue or the diffusion exponent of the two-stream system. Since the extinction coefficient k depends only on the solar zenith angle, and m depends on the spectral absorption properties of the medium, in many cases, the possibility exists that a combination of solar zenith angle and wavelength occurs under which this singularity can accidentally come to expression in the form of numerical instability.

Radiative transfer in water can be described with a similarity transformation that forces quasi-isotropic scattering, which means that only two scattering coefficients are needed, namely σ and s, the hemispheric (back)scattering coefficients for incident diffuse hemispheric light and direct sunlight, respectively. In this case, the diffusion exponent is found from:

$$m=\sqrt{\kappa(\kappa-2\omega)}=2\sqrt{1-\omega} \quad . \tag{A1}$$

The infinite reflectance is given by

$$r_\infty=\frac{\omega}{\kappa-\omega+m}=\frac{\omega}{2-\omega+2\sqrt{1-\omega}} \tag{A2}$$

In terms of $x = b_b/a$, one can write

$$r_\infty=\frac{\omega}{2-\omega+2\sqrt{1-\omega}}=\frac{\frac{2b_b}{a+2b_b}}{2-\frac{2b_b}{a+2b_b}+2\sqrt{1-\frac{2b_b}{a+2b_b}}}=\frac{2b_b}{2(a+2b_b)-2b_b+2\sqrt{a(a+2b_b)}} \tag{A3}$$

$$=\frac{b_b/a}{1+b_b/a+\sqrt{(1+2b_b/a)}}=\frac{x}{1+x+\sqrt{(1+2x)}}$$

From this we also find

$$1+r_\infty=\frac{1+2x+\sqrt{(1+2x)}}{1+x+\sqrt{(1+2x)}} \;;\; 1-r_\infty=\frac{1+\sqrt{(1+2x)}}{1+x+\sqrt{(1+2x)}} \;;$$
$$\frac{1+r_\infty}{1-r_\infty}=\sqrt{(1+2x)} \quad\Rightarrow\quad r_\infty=\frac{\sqrt{(1+2x)}-1}{\sqrt{(1+2x)}+1} \tag{A4}$$

To distinguish both infinite reflectances, we write $r_{dd}^\infty = r_\infty$. For the infinite DHRF we find

$$r_{sd}^\infty=\frac{s(1+r_\infty)}{k+m}=\frac{\dfrac{b_b}{\mu_w(a+2b_b)}\dfrac{2\sqrt{1+2x}}{\sqrt{1+2x}+1}}{\dfrac{1}{\mu_w}+m}=\frac{\dfrac{x}{\mu_w(1+2x)}\dfrac{2\sqrt{1+2x}}{\sqrt{1+2x}+1}}{\dfrac{1}{\mu_w}+\dfrac{2}{\sqrt{1+2x}}}=\frac{\dfrac{2x}{\sqrt{1+2x}+1}}{\sqrt{1+2x}+2\mu_w} \tag{A5}$$
$$=\frac{\dfrac{2x}{\sqrt{1+2x}+1}\dfrac{\sqrt{1+2x}-1}{\sqrt{1+2x}-1}}{\sqrt{1+2x}+2\mu_w}=\frac{\sqrt{1+2x}-1}{\sqrt{1+2x}+2\mu_w}$$

The other important quantities of the model are given without derivation:

$$J_1=\begin{cases}\dfrac{\mathrm{e}^{-mcd}-\mathrm{e}^{-kcd}}{k-m} & (|k-m|>=10^{-3})\\ \tfrac{1}{2}cd(\mathrm{e}^{-mcd}+\mathrm{e}^{-kcd})[1-\tfrac{1}{12}(k-m)^2(cd)^2] & (|k-m|<10^{-3})\end{cases} \tag{A6}$$

$$J_2=\frac{1-\mathrm{e}^{-(k+m)cd}}{k+m} \tag{A7}$$

$$\rho_{dd}=r_\infty\frac{1-\mathrm{e}^{-2mcd}}{1-r_\infty{}^2\mathrm{e}^{-2mcd}} \;;\quad \tau_{dd}=\frac{1-r_\infty{}^2}{1-r_\infty{}^2\mathrm{e}^{-2mcd}}\mathrm{e}^{-mcd} \tag{A8}$$

$$\rho_{sd}=s(1+r_\infty)\frac{J_2-r_\infty\mathrm{e}^{-mcd}J_1}{1-r_\infty{}^2\mathrm{e}^{-2mcd}} \;;\quad \tau_{sd}=s(1+r_\infty)\frac{J_1-r_\infty\mathrm{e}^{-mcd}J_2}{1-r_\infty{}^2\mathrm{e}^{-2mcd}} \tag{A9}$$

The function J_1 was designed to intercept the (near) singularity occurring when *k* approaches *m*. From Eq. (A6) one can see that not only the case of the exact singularity is handled, but also a narrow region around it, where | *k* – *m* | < 10^{-3}. This guarantees a completely smooth behavior of this function, without any sign of numerical instability.

Chapter 6 Concluding remarks and prospects

Monitoring of water quality is a crucial subject for the world's population as inconsistencies in water consumption combined with environmental variations influence coastal aquatic ecosystems and fresh waters. This dissertation concentrates on the capabilities of optical remote sensing to be applied for monitoring of water quality in complex shallow coastal waters and discusses how to translate the recorded remote sensing observations of in-situ measurements and satellite images into the validated and quantified environmental information products fundamental for water quality management applications.

6.1. Summary of conclusions

In this dissertation we have provided an overview of the main challenges and problems of optical remote sensing of ocean color in shallow coastal waters to identify the methods that have been used to tackle these problems till now; and to define the methods and algorithms which have been applied in this study to overcome these problems **(Chapter 1)**;

Using the RT hydro-optical model of 2SeaColor makes it possible to accurately retrieve WCCs at water surface level using time series of in-situ hyperspectral measurements. The 2SeaColor model inversion against time series of in-situ hyperspectral measurements under the condition of SZA $< 60^{\circ}$ is very promising for retrieving WCCs from in-situ measurements under different water turbidity conditions in highly turbid coastal waters **(Chapter 2)**.

By coupling 2SeaColor model simulations to the RT atmospheric model MODTRAN (the coupled 2SeaColor-MODTRAN model), one can simulate TOA spectral radiance data comparable to satellite-observed TOA radiances, and therefore one can retrieve the WCCs and atmospheric properties simultaneously from satellite images. Applying the coupled 2SeaColor-MODTRAN model on MERIS images makes it possible to retrieve WCCs directly from TOA radiances rather than from atmospherically corrected TOA reflectance data and shows considerable improvement in both phases of atmospheric correction and WCC retrieval in comparison to the standard MERIS C2R processor in the presence of local haze variation and high turbidity in coastal waters. **(Chapter 3)**.

Applying the validated 2SeaColor and 2SeaColor-MODTRAN models on 15-years of diurnal time series of in-situ hyperspectral measurements and multi-sensor satellite images of MERIS, MSI, and OLCI, respectively, makes it suitable for long-term monitoring of water quality in complex coastal waters of the Wadden Sea. Moreover, using the coupled 2SeaColor-MODTRAN model in a pixel-by-pixel approach makes it possible to generate simultaneous maps of WCCs and atmospheric properties from multi-sensor satellite images of MERIS, MSI, and OLCI for long-term spatio-temporal monitoring of WCCs at the Wadden Sea. However, the reliability of spatial variations in retrieved WCCs in the optically shallow waters of the study area remains questionable due to the sea-bottom effect **(Chapter 4).**

By developing the innovative near-infrared bottom effect index (NIBEI), one can accurately distinguish the optically shallow waters from optically deep waters from multispectral images of MERIS and OLCI. By excluding the contaminated bottom-effect pixels from consideration by applying the NIBEI in water retrieval algorithms, one can increase the reliability of generated WCC maps by the coupled 2SeaColor-MODTRAN model over the shallow waters of the Dutch Wadden Sea **(Chapter 5)**.

6.2. Implications

The RT hydro-optical model 2SeaColor is capable of accurately retrieving WCCs from time series of in-situ hyperspectral measurements collected on a daily basis over multiple years under different water turbidity conditions, tidal phase and SZAs (up to 60°) for the shallow tidal waters of the Dutch Wadden Sea. This is significant since this validated RT hydro-optical model can be applied for long-term monitoring of WCCs without the need for tuning empirical coefficients from field measurements in the complex coastal region. Moreover, the RT model of the 2SeaColor, that has been validated for dealing with complex coastal waters can be readily adapted to be applied to multi-variable retrievals in open ocean waters. Currently, there is a growing interest in the retrieval of additional water component information from water surface level than only the Chla concentration (as the main phytoplankton pigment) in ocean waters. Therefore, the use of the 2SeaColor model in open oceans has great potential to improve the accuracy of retrieved pigment concentrations, as it turns out that the assumed relationship between Chla and all the other water constituents breaks down **(Chapter 2)**.

The coupled RT atmospheric-hydro-optical model 2SeaColor-MODTRAN can be applied to simulate satellite radiance data accurately, and by model inversion one can simultaneously retrieve WCCs, visibility and aerosol type from satellite images under the various conditions of high turbidity and local haze presence. This approach is capable of generating accurate maps of WCCs and atmospheric properties and of monitoring water quality in a straightforward operational way. This is significant since satellite remote sensing of water quality in the optically complex waters of the Wadden Sea is very challenging. This is due to the presence of fair concentrations of water constituents and their tidal and seasonal variations, besides the presence of cloud and local haze variations due to the climatological conditions in this region. Moreover, the proposed coupled modeling method can be readily adapted for performing multi-sensor time-series studies, achieving a much denser temporal sampling than would be possible with a separate single sensor. This has an important implication for multi-sensor time series synergy studies in quantitative remote sensing of coastal waters. Moreover, all the above considerations suggest that improvements to coastal water algorithms will be of direct benefit to open oceans as well since in these waters it is also challenging to decouple the atmospheric effect from the ocean water component in the presence of spatial haze variations and absorbing aerosols **(Chapter 3)**.

The retrieval of WCCs by the coupled 2SeaColor-MODTRAN model inversion of TOA radiance data from multi-sensor satellite images, combined by using in-situ surface reflectance, is the most reliable approach to accurately track long-term variation of water surface properties in different seasons, SZAs, water turbidity and atmospheric conditions over the complex waters of the Wadden Sea. This is significant since the combination of optical remote sensing observations of multispectral sensors and in-situ hyperspectral measurements can give their integrated contributions for monitoring of time series of retrieved water surface components. These outputs have remarkable applications for recognizing anomaly events in the area, and the established long-term WCC retrievals may serve as baseline information to continuously monitor the estuary's eutrophic state for sustainable management of water resources at this complex water. This is significant in response to the obligation of the Water Framework Directive regulations from the European Union to member states to monitor all their coastal areas (Environment Directorate-General of the European Commission, 2000). Moreover, these outputs can be beneficial for both the application-oriented and academic sectors to understand the water quality response to climate change, human impact, etc. Of particular interest when analyzing the variability in the WCC trends retrieved from in-situ measurements and satellite images is whether any significant decreasing trend from 2003–2018 might indicate the effect of prior nutrient reduction management actions. This has significant implications for identifying positive anomaly events and may act as an alert for management actions. Obviously, climatic variability needs to be considered carefully when interpreting the long-term data trends and when making management decisions **(Chapter 4)**.

By applying the new NIBEI index to multispectral satellite images and generating the shallow vs. optically deep water maps, one can be made aware of the location of possible contamination by sea-bottom effects and identify waters to be excluded from consideration. This is significant since, in remote sensing of shallow coastal areas, it is essential to accurately determine the location of optically deep waters by not only considering the actual water depth maps but also by discriminating optically shallow waters. Otherwise, there is a chance that the WCC algorithm retrievals fail to be in good agreement with in-situ measurements due to the sea-bottom effect in these areas. Indeed, these distinguished optically shallow/deep maps have an important application for the appropriate selection of in-situ measurements locations for the validation of different algorithms. Moreover, applying the proposed NIBEI leads to generate more reliable WCCs maps using multispectral satellite images by excluding contaminated sea-bottom effects pixels from consideration. Providing these products over the complex shallow waters of the Dutch Wadden Sea is crucial as they contain significant information for the environmental decision makers concerning maintenance and conservation of this vital coastal area. This also creates an excellent opportunity for the long-term spatio-temporal quantitative water quality monitoring in this study area considering the availability of MERIS (2002 - 2012) and OLCI (2018 - present) images.

6.3 Challenges and future research

The research recommendations provided here are established based on different sections of this dissertation aiming to improve the optical remote sensing of water quality in future studies as follows:

Global water quality monitoring in aquatic ecosystems and coastal areas is in a pressing need. In parallel, there are increasing efforts in collecting high quality in-situ hyperspectral measurements using advanced instruments and airborne drones for quantitative monitoring of water quality in complex coastal waters. In principle, the developed coupled models are universally applicable, but SIOPs are regionally dependent and must be parameterized each time the retrieval method is applied to a new region for which the most suitable SIOPs are still unknown. Therefore it is also recommended to obtain information on the various ranges of possible SIOPs and their corresponding spatial/temporal distribution in order to apply the 2SeaColor model established based on possible measures of SIOPs and their spatial ranges in different coastal areas **(Chapter 2)**.

Systematically correcting the satellite-recorded TOA radiances for atmospheric contamination to automatic retrieval of WCCs from atmospherically corrected TOA radiances is one of the greatest challenges in global satellite remote sensing of coastal waters to automatic and timely monitoring of coastal waters. On the other hand, the availability of multi-sensor satellite images at a high temporal frequency is a great opportunity for continued monitoring of water quality at large spatial scales by using coupled RT atmospheric-hydro-optical models. Therefore it is recommended to apply and validate the coupled 2SeaColor-MODTRAN model for simultaneous retrieval of atmospheric and water properties in other parts of the world using various ocean color remote sensors to understand how broadly applicable this coupled model will be and to what extent these findings could be generalized. However, to apply this method to other regions, some additional information (*e.g.,* availability of regionally valid SIOPs, ranges of water constituent concentrations, the spectral response functions of the desired sensor, etc.) should be considered properly **(Chapter 3).**

A global and precise in-situ water quality monitoring programme is recommended to support the use of remote sensing observations at both water surface and TOA level providing validation and parameterization data. To meet this objective, uncertainties of collected in-situ measurements are needed to be determined, and quality control procedures and calibration should be considered carefully, and corresponding in-situ measurement protocols should be followed. That is also recommended to assemble and use the worldwide in-situ (*e.g.,* SIOPs, WCCs, and airborne/drone hyperspectral measurements) information collected by scientists, researchers, organizations, etc., to be used for validation and calibration of these water retrieval models using remote sensing observations in support of global monitoring of coastal water programs. The established and validated algorithms using worldwide in-situ hyperspectral and WCC measurements may also serve in the processing of future satellite images using oncoming satellite missions **(Chapter 4).**

Reliable long-term WCC maps from multi-sensor satellite images in a denser temporal resolution and tracking long-term variations of these constituents from in-situ hyperspectral measurements over complex shallow waters are very important water quality products for water quality managers and coastal planners. Therefore it is recommended to consider satellite monitoring of coastal waters as a part of a multidisciplinary method to link scientific outputs to water managers' needs and requirements. It is also recommended that the scientific community of water quality considers the main requirements of environmental and water management agencies besides stakeholders needs in the conceptualization phase of their projects to provide most beneficial products for both sides of the science community and aquatic ecosystem managers. This is considerable to efficient improve utilization of satellite-derived products such as long-term generated WCC maps **(Chapters 4,5)**.

It is recommended to improve the physical-based Near-Infrared bottom effect index NIBEI in order to obtain information about the type of sea bottom (*e.g.,* sandy, muddy, grown with vegetation, etc.) and to correct for bottom effects and the atmosphere in time series of multispectral satellite images (*e.g.,* MERIS, OLCI). It is also recommended to promote using the NIBEI implication in different image processing software programs (*e.g.*, SeaDAS, ErDAS, SNAP, ENVI) to be used for multi-spectral satellite image processing (e.g., OLCI, MSI, GOCI, MERIS) over shallow tidal areas in order to improve the reliability of water constituent retrievals from satellite images by flagging shallow water observations **(Chapter 5)**.

Bibliography

Albert, A., Mobley, C., 2003. An analytical model for subsurface irradiance and remote sensing reflectance in deep and shallow case-2 waters. Opt. Express. https://doi.org/10.1364/OE.11.002873

Allan, T.D., 2008. Remote sensing of the European seas: A historical outlook, Remote Sensing of the European Seas. https://doi.org/10.1007/978-1-4020-6772-3_2.

Ambarwulan, W., Salama, M.S., Mannaerts, C.M., Verhoef, W., 2011. Estimating specific inherent optical properties of tropical coastal waters using bio-optical model inversion and in situ measurements: case of the Berau estuary, East Kalimantan, Indonesia. Hydrobiologia 658, 197–211.

Ambarwulan, W., Verhoef, W., Mannaerts, C.M., Salama, M.S., 2012. Estimating total suspended matter concentration in tropical coastal waters of the Berau estuary, Indonesia. Int. J. Remote Sens. 33, 4919–4936. https://doi.org/https://doi.org/10.1080/01431161.2011.583289

Arabi, B., Salama, M.S., Wernand, M.R., Verhoef, W., 2016. MOD2SEA: A Coupled Atmosphere-Hydro-Optical Model for the Retrieval of Chlorophyll-a from Remote Sensing Observations in Complex Turbid Waters. Remote Sens. 722. https://doi.org/10.3390/rs8090722

Arabi, B., Salama, M.S., Wernand, M.R., Verhoef, W., 2018. Remote sensing of water constituent concentrations using time series of in-situ hyperspectral measurements in the Wadden Sea. Remote Sens. Environ. 216, 154–170. https://doi.org/10.1016/j.rse.2018.06.040

Arnone, R., Babin, M., Barnard, A.H., Boss, E., Cannizzaro, J.P., Carder, K.L., Chen, F.R., Devred, E., Doerffer, R., Du, K., Hoge, F., Kopelevich, O. V, Platt, T., Poteau, A., Roesler, C., Sathyendranath, S., 2006. Reports of the International Ocean-Colour Coordinating Group Remote Sensing of Inherent Optical Properties : Fundamentals, Tests of Algorithms, and Applications, IOCCG Report 5. https://doi.org/10.1006/jmbi.1998.2073

Attila, J., Koponen, S., Kallio, K., Lindfors, A., Kaitala, S., Ylöstalo, P., 2013. MERIS Case II water processor comparison on coastal sites of the northern Baltic Sea. Remote Sens. Environ. 128, 138–149. https://doi.org/10.1016/j.rse.2012.07.009

Babin, M., Morel, A., Fournier-Sicre, V., Fell, F., Stramski, D., 2003. Light scattering properties of marine particles in coastal and open ocean waters as related to the particle mass concentration. Limonology Oceanogr. 48, 843–859. https://doi.org/10.4319/lo.2003.48.2.0843

Bartholdy, J., Folving, S., 1986. Sediment classification and surface type mapping in the Danish Wadden Sea by remote sensing. Netherlands J. Sea Res. 20, 337–345. https://doi.org/10.1016/0077-7579(86)90001-3

Bashir, Z., 2016. Modeling the influence of biological activity on fine sediment transport in the Dutch Wadden Sea. Mater thesis. Deltares and University of Twente. 1–95.

Bayat, B., Van der Tol, C., Verhoef, W., 2016. Remote sensing of grass response to drought stress using spectroscopic techniques and canopy reflectance model inversion. Remote Sens. 8, 557. https://doi.org/10.3390/rs8070557

Beltrán-Abaunza, J.M., Kratzer, S., Brockmann, C., 2014. Evaluation of MERIS products from Baltic Sea coastal waters rich in CDOM. Ocean Sci. 10, 377–396.

Berk, A., Anderson, G.P., Acharya, P.K., Shettle, E.P., 2011. MODTRAN 5.2. 1 user's manual. Spectr. Sci. Inc., Air Force Res. Lab.

Brando, V.E., Dekker, A.G., 2003. Satellite hyperspectral remote sensing for estimating estuarine and coastal water quality. IEEE Trans. Geosci. Remote Sens. 41, 1378–1387.

Brando, V.E., Anstee, J.M., Wettle, M., Dekker, A.G., Phinn, S.R., Roelfsema, C., 2009. A physics based retrieval and quality assessment of bathymetry from suboptimal hyperspectral data. Remote Sens. Environ. 113, 755–770. https://doi.org/10.1016/j.rse.2008.12.003

Bresciani, M., Giardino, C., Lauceri, R., Matta, E., Cazzaniga, I., Pinardi, M., Lami, A., Austoni, M., Viaggiu, E., Congestri, R., Morabito, G., 2016. Earth observation for monitoring and mapping of cyanobacteria blooms. Case studies on five Italian lakes. J. Limnol.

Bricaud, A., Morel, A., Prieur, L., 1981. Absorption by dissolved organic matter of the sea (yellow substance) in the UV and visible domains. Limnol. Oceanogr. 26, 43–53. https://doi.org/10.4319/lo.1981.26.1.0043.

Brockmann, C., Stelzer, K., 2008. Optical Remote Sensing of Intertidal Flats. Remote Sens. Eur. Seas. Springer, Dordr.

Bukata, R.P., Jerome, J.H., Kondratyev, A.S., Pozdnyakov, D. V, 1995. Optical properties and remote sensing of inland and coastal waters. CRC press.

Bulgarelli, B., Zibordi, G., 2003. Remote sensing of ocean colour: Accuracy assessment of an approximate atmospheric correction method. Int. J. Remote Sens. https://doi.org/10.1080/01431160304985.

Cadée, G.C., 1982. Tidal and seasonal variation in particulate and dissolved organic carbon in the western dutch Wadden Sea and Marsdiep tidal inlet. Netherlands J. Sea Res. 15, 228–249. https://doi.org/10.1016/0077-7579(82)90006-0

Cadée, G.C., 1996. Accumulation and sedimentation of Phaeocystis globosa in the Dutch Wadden Sea. J. Sea Res. 36, 321–327. https://doi.org/10.1016/s1385-1101(96)90799-6

Carder, K.L., Steward, R.G., Paul, J.H., Vargo, G.A., 1986. Relationship between chlorophyll and ocean color costituents as thy affect remote-sensing models. Limnol. Oceanogr. 31, 403–413.

Carder, K.L., Cattrall, C., Chen, F.R., 2002. MODIS clear water epsilons (ATBD 21, v6). Ocean Color web page, 1-4.

Carpintero, M., Polo, M.J., Salama, M.S., 2015. Simultaneous atmospheric correction and quantification of suspended particulate matter in the

Guadalquivir estuary from Landsat images. Proc. Int. Assoc. Hydrol. Sci. 368, 15–20. https://doi.org/10.5194/piahs-368-15-2015.

Casal, G., Furey, T., Dabrowski, T., Nolan, G., 2015. Generating a Long-Term Series of Sst and Chlorophyll-a for the Coast of Ireland. ISPRS - Int. Arch. Photogramm. Remote Sens. Spat. Inf. Sci. XL-7/W3, 933–940. https://doi.org/10.5194/isprsarchives-XL-7-W3-933-2015

Casey, B., 2007. Water and bottom properties of a coastal environment derived from Hyperion data measured from the EO-1 spacecraft platform. J. Appl. Remote Sens. 1, 011502. https://doi.org/10.1117/1.2822610

Ceyhun, Ö., Yalçin, A., 2010. Remote sensing of water depths in shallow waters via artificial neural networks. Estuar. Coast. Shelf Sci. https://doi.org/10.1016/j.ecss.2010.05.015

Chang, T.S., Joerdel, O., Flemming, B.W., Bartholomä, A., 2006. The role of particle aggregation/disaggregation in muddy sediment dynamics and seasonal sediment turnover in a back-barrier tidal basin, East Frisian Wadden Sea, southern North Sea. Mar. Geol. 235, 49–61. https://doi.org/http://dx.doi.org/10.1016/j.margeo.2006.10.004

Chaves, J.E., Werdell, P.J., Proctor, C.W., Neeley, A.R., Freeman, S.A., Thomas, C.S., Hooker, S.B., 2015. Assessment of ocean color data records from MODIS-Aqua in the western Arctic Ocean. Deep Sea Res. Part II Top. Stud. Oceanogr. 118, 32–43.

Chen, X., Li, Y.S., Liu, Z., Yin, K., Li, Z., Wai, O.W.H., King, B., 2004. Integration of multi-source data for water quality classification in the Pearl River estuary and its adjacent coastal waters of Hong Kong. Cont. Shelf Res. https://doi.org/10.1016/j.csr.2004.06.010.

Chen, C., Tang, S., Pan, Z., Zhan, H., Larson, M., Jönsson, L., 2007. Remotely sensed assessment of water quality levels in the Pearl River Estuary, China. Mar. Pollut. Bull. https://doi.org/10.1016/j.marpolbul.2007.03.010.

Chongya, J., Hongliang, F., 2012. Modeling soil reflectance using a global spectral library San, in: AGU Fall Meeting. San Francisco, p. 100101.

Chybicki, A., 2017. Mapping South Baltic Near-Shore Bathymetry Using Sentinel-2 Observations. Polish Marit. Res. 24, 15–25. https://doi.org/10.1515/pomr-2017-0086

Creutzberg, F., 1961. On the orientation of migrating elvers (Anguilla vulgaris turt.) in a tidal area. Netherlands J. Sea Res. 1, 257–338. https://doi.org/10.1016/0077-7579(61)90007-2

CWSS, 2008. Nomination of the Dutch-German Wadden Sea as World Heritage Site. Common Wadden Sea Secretariat.

Dasgupta, S., Singh, R.P., Kafatos, M., 2009. Comparison of global chlorophyll concentrations using MODIS data. Adv. Sp. Res. 43, 1090–1100. https://doi.org/10.1016/j.asr.2008.11.009

Dekker, A.G., Vos, R.J., Peters, S.W.M., 2001. Comparison of remote sensing data, model results and in situ data for total suspended matter (TSM) in the southern Frisian lakes. Sci. Total Environ. 268, 197–214. https://doi.org/10.1016/S0048-9697(00)00679-3

Doerffer, R., Fischer, J., 1994. Concentrations of chlorophyll, suspended matter, and gelbstoff in case II waters derived from satellite coastal zone color scanner data with inverse modeling methods. Geophys. Res. Ocean. 99, 7457–7466. https://doi.org/10.1029/93JC02523

Doerffer, R., Schiller, H., 2007. The MERIS Case 2 water algorithm. Int. J. Remote Sens. 28, 517–535.

Doxaran, D., Froidefond, J.M., Castaing, P., Babin, M., 2009. Dynamics of the turbidity maximum zone in a macrotidal estuary (the Gironde, France): Observations from field and MODIS satellite data. Estuar. Coast. Shelf Sci. 81, 321–332. https://doi.org/10.1016/j.ecss.2008.11.013

Doxaran, D., Ruddick, K., McKee, D., Gentili, B., Tailliez, D., Chami, M., Babin, M., Reintegration, E., Spatiales, C.N. d'Etudes, Programme, B.S.P.O.S.-2, 2009. Spectral variations of light scattering by marine particles in coastal waters, from visible to near infrared 54, 1257–1271.

Doxaran, D., Lamquin, N., Park, Y.-J., Mazeran, C., Ryu, J.H., Wang, M., Poteau, A., 2014. Retrieval of the seawater reflectance for suspended solids monitoring in the East China Sea using MODIS, MERIS and GOCI satellite data. Remote Sens. Environ. 146, 36–48. https://doi.org/10.1016/j.rse.2013.06.020

Duan, H., Ma, R., Simis, S.G.H., Zhang, Y., 2012. Validation of MERIS case-2 water products in Lake Taihu, China. GIScience Remote Sens. 49, 873–894.

Dube, T., 2012. Primary Productivity of Intertidal mudflats in the Wadden Sea: A Remote Sensing Method. MSc Thesis, The Faculty of Geo-Information Science and Earth Observation, The University of Twenete, URL: https://www.itc.nl/library/papers_2012/msc/wrem/dube.pdf.

Duntley, S.Q., 1941. The Optical Properties of Diffusing Materials. Journal of the Optical Society of America. 61–70.

Duntley, S.Q., 1963. Light in the Sea. Journal of the Optical Society of America. 214–233, 53. https://doi.org/10.1364/JOSA.53.000214

Eleveld, M. a., Pasterkamp, R., van der Woerd, H.J., Pietrzak, J.D., 2008. Remotely sensed seasonality in the spatial distribution of sea-surface suspended particulate matter in the southern North Sea. Estuar. Coast. Shelf Sci. 80, 103–113. https://doi.org/10.1016/j.ecss.2008.07.015

Eleveld, M.A., Van der Wal, D., Van Kessel, T., 2014. Estuarine suspended particulate matter concentrations from sun-synchronous satellite remote sensing: Tidal and meteorological effects and biases. Remote Sens. Environ. 143, 204–215. https://doi.org/10.1016/j.rse.2013.12.019

Fettweis, M., Nechad, B., Van den Eynde, D., 2007. An estimate of the suspended particulate matter (SPM) transport in the southern North Sea using SeaWiFS images, in situ measurements and numerical model results. Cont. Shelf Res. 27, 1568–1583.

Friedrichs, A., Busch, J.A., van der Woerd, H.J., Zielinski, O., 2017. SmartFluo: A method and affordable adapter to measure chlorophyll a fluorescence with smartphones. Sensors (Switzerland).

Garaba, S.P., Zielinski, O., 2015. Remote Sensing Applications : Society and Environment An assessment of water quality monitoring tools in an estuarine system. Remote Sens. Appl. Soc. Environ. 2, 1–10. https://doi.org/10.1016/j.rsase.2015.09.001.

Garcia, R.A., Lee, Z., Hochberg, E.J., 2018. Hyperspectral shallow-water remote sensing with an enhanced benthic classifier. Remote Sens. 10. https://doi.org/10.3390/rs10010147.

Gemein, N., Stanev, E., Brink-spalink, G., Wolff, J.-O., Reuter, R., 2006. Patterns of suspended matter in the East Frisian Wadden Sea : Comparison of numerical simulations with MERIS observations. Eur. Assoc. Remote Sens. Lab. eProceedings 5, 180–198.

Giardino, C., Candiani, G., Bresciani, M., Lee, Z., Gagliano, S., Pepe, M., 2012. BOMBER: A tool for estimating water quality and bottom properties from remote sensing images. Comput. Geosci. 45, 313–318. https://doi.org/10.1016/j.cageo.2011.11.022

Giardino, C., Bresciani, M., Cazzaniga, I., Schenk, K., Rieger, P., Braga, F., Matta, E., Brando, V.E., Brando, V.E., 2014. Evaluation of multi-resolution satellite sensors for assessing water quality and bottom depth of Lake Garda. Sensors (Switzerland) 14, 24116–24131.

Gitelson, A.A., Dall'Olmo, G., Moses, W., Rundquist, D.C., Barrow, T., Fisher, T.R., Gurlin, D., Holz, J., 2008. A simple semi-analytical model for remote estimation of chlorophyll-a in turbid waters: Validation. Remote Sens. Environ. 112, 3582–3593. https://doi.org/10.1016/j.rse.2008.04.015

Gordon, H.R., Brown, O.B., Evans, R.H., Brown, J.W., Smith, R.C., Baker, K.S., Clark, D.K., 1988. A semianalytic radiance model of ocean color. Geophys. Res. Atmos. 93, 10909–10924.

Gordon, H.R., Wang, M., 1994. Retrieval of water-leaving radiance and aerosol optical thickness over the oceans with SeaWiFS: a preliminary algorithm. Appl. Opt. 33, 443–52.

Gould, R.W., Arnone, R. A, Martinolich, P.M., 1999. Spectral dependence of the scattering coefficient in case 1 and case 2 waters. Appl. Opt. 38, 2377–83. https://doi.org/10.1364/ao.38.002377

Goyens, C., Jamet, C., Schroeder, T., 2013. Evaluation of four atmospheric correction algorithms for MODIS-Aqua images over contrasted coastal waters. Remote Sens. Environ. 131, 63–75.

Halliday, E., McLellan, S.L., Amaral-Zettler, L.A., Sogin, M.L., Gast, R.J., 2014. Comparison of bacterial communities in sands and water at beaches with bacterial water quality violations. PLoS One. https://doi.org/10.1371/journal.pone.0090815

Harvey, E.T., Kratzer, S., Philipson, P., 2014. Satellite-based water quality monitoring for improved spatial and temporal retrieval of chlorophyll-a in coastal waters. Remote Sens. Environ. 158, 417–430. https://doi.org/10.1016/j.rse.2014.11.017

Hegeman, J., Cade, G.C., 2002. Phytoplankton in the Marsdiep at the end of the 20th century ; 30 years monitoring biomass , primary production , and Phaeocystis blooms 48, 97–110.

Hommersom, A., Peters, S., Wernand, M.R., de Boer, J., 2009. Spatial and temporal variability in bio-optical properties of the Wadden Sea. Estuar. Coast. Shelf Sci. 83, 360–370.

Hommersom, A., 2010. Dense Water and Fluid Sand: Optical properties and methods for remote sensing of the extremely turbid Wadden Sea. PhD Thesis, The Institute for Environmental Studies (IVM), Vrije Universiteit Amsterdam, URL: http://hdl.handle.net/1871/15939.

Hommersom, A., Peters, S.W.M., Van Der Woerd, H.J., Eleveld, M.A., Wernand, M.R., de Boer, J., 2010. Tracing Wadden Sea water masses with an inverse bio-optical and endmember model, in: EARSeL E-Proceedings.

Hommersom, A., Peters, S.W.M., van der Woerd, H.J., Eleveld, M.A., Wernand, M., Boer, J. de, others, 2010a. Tracing Wadden Sea masses with an inverse bio-optical and end-member model. EARSel eProceedings 9.

Hommersom, A., 2010b. Modeling the influence of biological activity on fine sediment transport in the Dutch Wadden Sea. https://doi.org/http://hdl.handle.net/1871/15939

Hommersom, A., Wernand, M.R., Peters, S., de Boer, J., 2010b. A review on substances and processes relevant for optical remote sensing of extremely turbid marine areas, with a focus on the Wadden Sea. Helgol. Mar. Res. 64, 75–92. https://doi.org/10.1007/s10152-010-0191-6

Hommersom, A., Researcher, I., 2015. A case study on the use of Hydropt in the Wadden Sea. report, Institute Environ. Stud. (IVM), VU Univ. Boelelaan 1085, 1081 HV Amsterdam, Netherlands.

Hu, C., Carder, K.L., Muller-Karger, F.E., 2000. Atmospheric correction of SeaWiFS imagery over turbid coastal waters: A practical method. Remote Sens. Environ. 74, 195–206. https://doi.org/10.1016/S0034-4257(00)00080-8

Hu, C., Lee, Z., Ma, R., Yu, K., Li, D., Shang, S., 2010. Moderate resolution imaging spectroradiometer (MODIS) observations of cyanobacteria blooms in Taihu Lake, China. J. Geophys. Res. Ocean. 115, 1–20. https://doi.org/10.1029/2009JC005511

IOCCG, 2000. Remote Sensing of Ocean Colour in Coastal, and Other Optically-Complex, Waters. Reports of the International Ocean-Colour Coordinating Group, No. 3, IOCCG, Dartmouth, Canada.

Jamet, C., Loisel, H., Kuchinke, C.P., Ruddick, K., Zibordi, G., Feng, H., 2011. Comparison of three SeaWiFS atmospheric correction algorithms for turbid waters using AERONET-OC measurements. Remote Sens. Environ. 115, 1955–1965. https://doi.org/http://dx.doi.org/10.1016/j.rse.2011.03.018

Kirk, J.T.O., 1994. Light and photosynthesis in aquatic ecosystems. Mar. Biol. Assoc. United Kingdom 74, 987.

Kneizys, F.X., Shettle, E.P., Abreu, L.W., Chetwynd, J.H., Anderson, G.P., W.O., G., J.E.a, S., S.a., C., 1988. Users Guide to LOWTRAN 7. Environ. Res.

Kristensen, P., Bøgestrand, J., 1996. Surface Water Quality Monitoring, Topic report. European Environment Agency.

Lawford, R., Strauch, A., Toll, D., Fekete, B., Cripe, D., 2013. Earth observations for global water security. Curr. Opin. Environ. Sustain. https://doi.org/10.1016/j.cosust.2013.11.009.

Le, C., Hu, C., English, D., Cannizzaro, J., Chen, Z., Feng, L., Boler, R., Kovach, C., 2013a. Towards a long-term chlorophyll-a data record in a turbid estuary using MODIS observations. Prog. Oceanogr. 109, 90–103. https://doi.org/10.1016/j.pocean.2012.10.002

Le, C., Hu, C., English, D., Cannizzaro, J., Kovach, C., 2013b. Climate-driven chlorophyll-a changes in a turbid estuary: Observations from satellites and implications for management. Remote Sens. Environ. 130, 11–24. https://doi.org/10.1016/j.rse.2012.11.011

Lee, Z., Carder, K.L., Arnone, R.A., 2002a. Deriving inherent optical properties from water color: a multiband quasi-analytical algorithm for optically deep waters. Applied Optics. 5755–5772. 41. https://doi.org/10.1364/AO.41.005755

Lee, Z., Carder, K.L., Chen, R.F., Peacock, T.G., 2001. Properties of the water column and bottom derived from Airborne Visible Infrared Imaging Spectrometer (AVIRIS) data. J. Geophys. Res. Ocean. 106, 11639–11651. https://doi.org/10.1029/2000JC000554

Lee, Z., Carder, K.L., Mobley, C.D., Steward, R.G., Patch, J.S., 1999. Hyperspectral remote sensing for shallow waters. 2. Deriving bottom depths and water properties by optimization. Appl. Opt. 38, 3831–3843. https://doi.org/10.1364/AO.38.003831

Lee, Z., Carder, K.L., Mobley, C.D., Steward, R.G., Patch, J.S., 1998. Hyperspectral remote sensing for shallow waters. I. A semianalytical model. Appl. Opt. 37, 6329–6338. https://doi.org/10.1364/AO.37.006329

Lee, Z., Du, K., Voss, K.J., Zibordi, G., Lubac, B., Arnone, R.A., Weidemann, A., 2011. An inherent-optical-property-centered approach to correct the angular effects in water-leaving radiance. Appl. Opt. 50, 3155. https://doi.org/10.1364/AO.50.003155

Li, H., He, X., Bai, Y., Chen, X., Gong, F., Zhu, Q., Hu, Z., 2017. Assessment of satellite-based chlorophyll-a retrieval algorithms for high solar zenith angle conditions. J. Appl. Remote Sens. 11, 12004. https://doi.org/https://doi.org/10.1117/1.JRS.11.012004

Li, J., Yu, Q., Tian, Y.Q., Becker, B.L., 2017. Remote sensing estimation of colored dissolved organic matter (CDOM) in optically shallow waters. ISPRS J. Photogramm. Remote Sens. 128, 98–110.

Loisel, H., Vantrepotte, V., Jamet, C., Dat, D.N., 2013. Challenges and New Advances in Ocean Color Remote Sensing of Coastal Waters. Oceanogr. Res. 1–38. https://doi.org/10.5772/56414

Long, R., 2011. The Marine Strategy Framework Directive: A new European approach to the regulation of the marine environment, marine natural resources and marine ecological services. J. energy Nat. Resour. law 29(1), 1–44. https://doi.org/10.1080/02646811.2011.11435256

Ly, J., Philippart, C.J.M., Kromkamp, J.C., 2014. Phosphorus limitation during a phytoplankton spring bloom in the western Dutch Wadden Sea. J. Sea Res. 88, 109–120. https://doi.org/10.1016/j.seares.2013.12.010

Lyzenga, D.R., 1978. Passive remote sensing techniques for mapping water depth and bottom features. Appl. Opt. 17, 379. https://doi.org/10.1364/AO.17.000379

Majozi, N.P., Salama, M.S., Bernard, S., Harper, D.M., Habte, M.G., 2014. Remote sensing of euphotic depth in shallow tropical inland waters of Lake Naivasha using MERIS data. Remote Sens. Environ. 148, 178–189. https://doi.org/10.1016/j.rse.2014.03.025

Malenovský, Z., Rott, H., Cihlar, J., Schaepman, M.E., García-Santos, G., Fernandes, R., Berger, M., 2012. Sentinels for science: Potential of Sentinel-1, -2, and -3 missions for scientific observations of ocean, cryosphere, and land. Remote Sens. Environ. 120, 91–101. https://doi.org/http://dx.doi.org/10.1016/j.rse.2011.09.026

Malthus, T.J., Mumby, P.J., 2003. Remote sensing of the coastal zone: An overview and priorities for future research. Int. J. Remote Sens. https://doi.org/10.1080/0143116031000066954

Maritorena, S., Morel, A., Gentili, B., 1994. Diffuse reflectance of oceanic shallow waters: Influence of water depth and bottom albedo. Limnol. Oceanogr. 39, 1689–1703. https://doi.org/10.4319/lo.1994.39.7.1689

Martinez-carranza, J., Calway, A., 2012. Remote Sensing of Bathymetry: An Investigation into the Effect of Bottom Reflectance on Passive Upwelling Spectral Irradiance 5210–5215.

Matthews, M.W., Matthews, M.W., 2011. A current review of empirical procedures of remote sensing in inland and near-coastal transitional waters 1161. https://doi.org/10.1080/01431161.2010.512947

Matthews, M.W., Bernard, S., Robertson, L., 2012. An algorithm for detecting trophic status (chlorophyll-a), cyanobacterial-dominance, surface scums and floating vegetation in inland and coastal waters. Remote Sens. Environ. https://doi.org/10.1016/j.rse.2012.05.032

McInnes, R.J., 2018. Sustainable development goals, in: The Wetland Book: I: Structure and Function, Management, and Methods. https://doi.org/10.1007/978-90-481-9659-3_125

McKinna, L.I.W., Fearns, P.R.C., Weeks, S.J., Werdell, P.J., Reichstetter, M., Franz, B.A., Shea, D.M., Feldman, G.C., 2015. A semianalytical ocean color inversion algorithm with explicit water column depth and substrate reflectance parameterization. J. Geophys. Res. Ocean. 120, 1741–1770. https://doi.org/10.1002/2014JC010224

Mélin, F., Zibordi, G., Berthon, J.F., 2007. Assessment of satellite ocean color products at a coastal site. Remote Sens. Environ. 110, 192–215.

Mélin, F., Vantrepotte, V., Clerici, M., D'Alimonte, D., Zibordi, G., Berthon, Canuti, E., 2011. Multi-sensor satellite time series of optical properties and chlorophyll-a concentration in the Adriatic Sea. Prog. Oceanogr. 91, 229–244. https://doi.org/https://doi.org/10.1016/j.pocean.2010.12.001

Mgengel, V., Spitzer, R.J., 1991. Application of remote sensing data to mapping of shallow sea-floor nearby Netherlands. Int. J. Remote Sens. 57(5):473-479.

Mobley, C.D., Gentili, B., Gordon, H.R., Jin, Z., Kattawar, G.W., Morel, A., Reinersman, P., Stamnes, K., Stavn, R.H., 1993. Comparison of numerical models for computing underwater light fields. Appl. Opt. https://doi.org/10.1364/AO.32.007484.

Mobley, C.D., 1994. Light and water: Radiative transfer in natural waters. Academic press. https://doi.org/http://www.jstor.org/stable/26231610

Mobley, C.D., 2003. Effects of optically shallow bottoms on upwelling radiances: Bidirectional reflectance distribution function effects. Am. Soc. Limnol. Oceanogr. 48, 337–345.

Moradi, M., Kabiri, K., 2015. Spatio-temporal variability of SST and Chlorophyll- a from MODIS data in the Persian Gulf. Mar. Pollut. Bull. 98, 14–25. https://doi.org/10.1016/j.marpolbul.2015.07.018.

Morel, A., Gentili, B., 1993. Diffuse reflectance of oceanic waters. II Bidirectional aspects. Applied optics. 6864–6879. 32. https://doi.org/10.1364/AO.32.006864

Morel, A., Maritorena, S., 2001. Bio-optical properties of oceanic waters: A reappraisal. Geophys. Res. 106, 7163–7180. https://doi.org/10.1029/2000JC000319.

Mueller, J.L., Brown, S.W., Clark, D.K., Johnson, B.C., Yoon, H., Lykke, K.R., Flora, S.J., Feinholz, M., Souaidia, N., Pietras, C., Stone, T.C., Yarbrough, M.A., Kim, Y.S., Barnes, R.A., 2004. Ocean optics protocols for satellite ocean color sensor validation, Revision 5, Volume VI: Special topics in ocean optics protocols, Part 2. Ocean Color web page VI, 35.

Niedermeier, A., Hoja, D., Lehner, S., 2005. Topography and morphodynamics in the German Bight using SAR and optical remote sensing data. Ocean Dyn. 55, 100–109.

O'Reilly, J.E., Maritorena, S., Mitchell, B.G., Siegel, D. a., Carder, K.L., Garver, S. a., Kahru, M., McClain, C., 1998. Ocean color chlorophyll algorithms for SeaWiFS. J. Geophys. Res. 103, 24937.

O’Reilly, J., Maritorena, S., 2000. Ocean color chlorophyll a algorithms for SeaWiFS, OC2, and OC4: Version 4. SeaWiFS postlaunch 8–22.

Orlandi, M., Marzano, F.S., Cimini, D., 2018. Remote sensing of water quality indexes from Sentinel-2 imagery : development and validation around Italian river estuaries 20, 19808.

Pahlevan, N., Sarkar, S., Franz, B.A., Balasubramanian, S. V., He, J., 2017. Sentinel-2 MultiSpectral Instrument (MSI) data processing for aquatic science applications: Demonstrations and validations. Remote Sens. Environ. 201, 47–56. https://doi.org/10.1016/j.rse.2017.08.033

Pasterkamp, R., Van der Woerd, H.J., Peters, S.W.M., Eleveld, M.A., 2003. Validation of MERIS Level 2 products in the North Sea : Dutch results for 2002-2003. Environ. Stud. 51, 2–11.

Pause, M., Schweitzer, C., Rosenthal, M., Keuck, V., Bumberger, J., Dietrich, P., Heurich, M., Jung, A., Lausch, A., 2016. In situ/remote sensing integration to assess forest health-a review. Remote Sens. 8. https://doi.org/10.3390/rs8060471.

Peters, S.W.M., 2001. MERIMON-2000: MERIS for water quality monitoring in the Belgian-Dutch-German coastal zone. Netherlands Remote Sensing Board BCRS.

Peters, S.W.M., Woerd, H. Van Der, Pasterkamp, R., 2004. Chl maps of the Dutch coastal zone : a case study within the REVAMP project. Institute for Environmental Studies (IVM), The Vrije Universiteit, Amsterdam.

Peters, S.W.M., Eleveld, M., Pasterkamp, R., van der Woerd, H., Devolder, M., Jans, S., Park, Y., Ruddick, K., Block, T., Brockmann, C., Doerffer, R., Krasemann, H., Röttgers, R., Schönfeld, W., Jorgensen, P. V, Tilstonde, G., Martinez-Vicente, V., Moore, G., Sorensen, K., Hokedal, J., Johnson, T.M., Lomsland, E.R., Aas, E., 2005. Atlas of Chlorophyll-a concentration for the North Sea (based on MERIS imagery of 2003). Institute for Environmental Studies (IVM), The Vrije Universiteit, Amsterdam.

Petzold, T., 1972. Volume Scattering Functions for Selected Ocean Waters. Scripps Inst. Ocean. SIO Ref. 72-78.

Philippart, C.J.M., Beukema, J.J., Cadée, G.C., Dekker, R., Goedhart, P.W., Van Iperen, J.M., Leopold, M.F., Herman, P.M.J., 2007. Impacts of nutrient reduction on coastal communities. Ecosystems 10, 95–118. https://doi.org/10.1007/s10021-006-9006-7

Philippart, C.J.M., Van Iperen, J.M., Cadee, G.C., Zuur, A.F., 2010. Long-term Field Observations on Seasonality in Chlorophyll-a Concentrations in a Shallow Coastal Marine Ecosystem, the Wadden Sea. Estuaries and Coasts 33, 286–294. https://doi.org/10.1007/s12237-009-9236-y

Philippart, C.J.M., Salama, M.S., Kromkamp, J.C., Van der Woerd, H.J., Zuur, A.F., Cadée, G.C., 2013. Four decades of variability in turbidity in the western Wadden Sea as derived from corrected Secchi disk readings. Sea Res. 82, 67–79. https://doi.org/10.1016/j.seares.2012.07.005

Pitarch, J., 2017. Biases in ocean color over a Secchi disk 25, 1124–1131.

Pitarch, J., Bellacicco, M., Volpe, G., Colella, S., 2016a. Use of the quasi-analytical algorithm to retrieve backscattering from in-situ data in the Mediterranean Sea. Remote Sens. Lett. 7, 591–600.

Pitarch, J., Volpe, G., Colella, S., Krasemann, H., Santoleri, R., 2016b. Remote sensing of chlorophyll in the Baltic Sea at basin scale from 1997 to 2012 using merged multi-sensor data. Ocean Sci. https://doi.org/10.5194/os-12-379-2016

Pitarch, J., Ruiz-Verdú, A., Sendra, M.D., Santoleri, R., 2017. Evaluation and reformulation of the maximum peak height algorithm (MPH) and application in a hypertrophic lagoon. J. Geophys. Res. Ocean. https://doi.org/10.1002/2016JC012174

Pope, R.M., Fry, E.S., 1997. Absorption spectrum (380-700 nm) of pure water. II. Integrating cavity measurements. Appl. Opt. 36, 8710–8723. https://doi.org/10.1364/AO.36.008710

Poremba, K., Tillmann, U., Hesse, K.-J., 1999. Distribution patterns of bacterioplankton and chlorophyll-a in the German Wadden Sea. Helgol. Mar. Res. 53, 28–35. https://doi.org/10.1007/PL00012135

Reid, P.C., Lancelot, C., Gieskes, W.W.C., Hagmeier, E., Weichart, G., 1990. Phytoplankton of the North Sea and its dynamics: A review. Netherlands J. Sea Res. https://doi.org/10.1016/0077-7579(90)90094-W

Reuter, R., Badewien, T.H., BartholomÄ, A., Braun, A., Lübben, A., Rullkötter, J., 2009. A hydrographic time series station in the Wadden Sea (southern North Sea). Ocean Dyn. 59, 195–211. https://doi.org/10.1007/s10236-009-0196-3

Ridderinkhof, H., Zimmerman, J.T.F., Philippart, M.E., 1990. Tidal exchange between the North Sea and Dutch Wadden Sea and mixing time scales of the tidal basins. Netherlands J. Sea Res. 25, 331–350. https://doi.org/10.1016/0077-7579(90)90042-F

Ruddick, K.G., Ovidio, F., Rijkeboer, M., 2000. Atmospheric correction of SeaWiFS imagery for turbid coastal and inland waters. Appl. Opt. 39, 897–912.

Ruddick, K.G., De Cauwer, V., Park, Y.-J., Moore, G.F., 2006. Seaborne measurements of near infrared water-leaving reflectance: The similarity spectrum for turbid waters. Limnol. Oceanogr. 51, 1167–1179. https://doi.org/10.4319/lo.2006.51.2.1167

Ryu, J.H., Kim, C.H., Lee, Y.K., Won, J.S., Chun, S.S., Lee, S., 2008. Detecting the intertidal morphologic change using satellite data. Estuar. Coast. Shelf Sci. https://doi.org/10.1016/j.ecss.2008.01.020

Salama, M.S., Monbaliu, J., Coppin, P., 2004. Atmospheric correction of Advanced Very High Resolution Radiometer imagery. Remote Sens. 25, 1349–1355. https://doi.org/10.1080/01431160310001592283

Salama, M.S., Stein, A., 2009. Error decomposition and estimation of inherent optical properties. Appl. Opt. 48, 4947–4962. https://doi.org/10.1364/AO.48.004947

Salama, M.S., Dekker, A., Su, Z., Mannaerts, C.M., Verhoef, W., 2009. Deriving inherent optical properties and associated inversion-uncertainties in the Dutch Lakes. Hydrol. Earth Syst. Sci. 13, 1113–1121. https://doi.org/10.5194/hess-13-1113-2009

Salama, M.S., Shen, F., 2010. Stochastic inversion of ocean color data using the cross-entropy method. Opt. Express 18, 479–499. https://doi.org/10.1364/OE.18.000479

Salama, M.S., Shen, F., 2010. Simultaneous atmospheric correction and quantification of suspended particulate matters from orbital and geostationary earth observation sensors. Estuar. Coast. Shelf Sci. 86, 499–511. https://doi.org/10.1016/j.ecss.2009.10.001

Salama, M.S., Mélin, F., Van der Velde, R., 2011. Ensemble uncertainty of inherent optical properties. Opt. Express 304, 16772–16783. https://doi.org/10.1364/OE.19.016772

Salama, M.S., Radwan, M., van der Velde, R., 2012b. A hydro-optical model for deriving water quality variables from satellite images (HydroSat): A case study of the Nile River demonstrating the future Sentinel-2 capabilities. Phys. Chem. Earth 50–52, 224–232. https://doi.org/10.1016/j.pce.2012.08.013

Salama, M.S., 2014. Roadmap Waterkwaliteit: helder beeld op troebel water. Den Haag, Enschede, Netherlands Sp. Off. (NSO), Univ. Twente Fac. Geo-Information Earth Obs. (ITC).

Salama, M.S., Verhoef, W., 2015. Two-stream remote sensing model for water quality mapping: 2SeaColor. Remote Sensing of Environment. 111–122. 157. https://doi.org/10.1016/j.rse.2014.07.022

Santer, R., Schmechtig, C., 2000. Adjacency effects on water surfaces: primary scattering approximation and sensitivity study. Appl. Opt. 39, 361–375. https://doi.org/10.1364/AO.39.000361

Sari, E., 2013. Bathymetric Modeling from Satellite Imagery via Single Band Algorithm (SBA) and Principal Components Analysis (PCA) in Southern Caspian Sea 7, 877–886.

Sathyendranath, S., others, 2000. Remote sensing of ocean colour in coastal, and other optically-complex, waters. IOCCG Rep. 3.

Saulquin, B., Fablet, R., Bourg, L., Mercier, G., d'Andon, O.F., 2016. MEETC2: Ocean color atmospheric corrections in coastal complex waters using a Bayesian latent class model and potential for the incoming sentinel 3 — OLCI mission. Remote Sens. Environ. 172, 39–49.

Schroeder, T., Behnert, I., Schaale, M., Fischer, J., Doerffer, R., 2007. Atmospheric correction algorithm for MERIS above case-2 waters. Int. J. Remote Sens. 28, 1469–1486.

Schroeder, T., Schaale, M., Fischer, J., 2007. Retrieval of atmospheric and oceanic properties from MERIS measurements: A new Case-2 water processor for BEAM. Int. J. Remote Sens. 28, 5627–5632. https://doi.org/10.1080/01431160701601774

Shen, F., Verhoef, W., 2010. Suppression of local haze variations in MERIS images over turbid coastal waters for retrieval of suspended sediment concentration. Opt. Express 18, 12653–62. https://doi.org/10.1364/OE.18.012653

Shen, F., Verhoef, W., Zhou, Y.X., Salama, M.S., Liu, X.L., 2010. Satellite Estimates of Wide-Range Suspended Sediment Concentrations in Changjiang (Yangtze) Estuary Using MERIS Data. Estuaries and Coasts 33, 1420–1429. https://doi.org/10.1007/s12237-010-9313-2

Shi, W., Wang, M., 2007. Detection of turbid waters and absorbing aerosols for the MODIS ocean color data processing. Remote Sens. Environ. 110, 149–161. https://doi.org/10.1016/J.RSE.2007.02.013

Siegel, D.A., Wang, M., Maritorena, S., Robinson, W., 2000. Atmospheric correction of satellite ocean color imagery: the black pixel assumption. Appl. Opt. 39, 3582–3591.

Sijtsma, F.J., Broersma, L., Daams, M.N., Hoekstra, H., Werner, G., 2015. Tourism Development in the Dutch Wadden Area: Spatial-Temporal Characteristics and Monitoring Needs. Environ. Manag. Sustain. Dev. 4, 217. https://doi.org/10.5296/emsd.v4i2.8561.

Smith, M.E., Bernard, S., O'Donoghue, S., 2013. The assessment of optimal {MERIS} ocean colour products in the shelf waters of the KwaZulu-Natal Bight, South Africa. Remote Sens. Environ. 137, 124–138. https://doi.org/http://dx.doi.org/10.1016/j.rse.2013.06.009

Staneva, J., Stanev, E. V, Badewien, T.H., Reuter, R., Flemming, B., Bartholoma, A., 2009. Hydrodynamics and sediment dynamics in the German Bight . A focus on observations and numerical modelling in the East Frisian Wadden Sea 29, 302–319.

Su, Z., Fernández-prieto, D., Timmermans, J., Chen, X., Hungershoefer, K., Roebeling, R., Schröder, M., Schulz, J., Stammes, P., Wang, P., Wolters, E., 2014. International Journal of Applied Earth Observation and Geoinformation First results of the earth observation Water Cycle Multi-mission Observation Strategy (WACMOS) 26, 270–285. https://doi.org/10.1016/j.jag.2013.08.002

Taylor, K.E., 2001. Summarizing multiple aspects of model performance in a single diagram. J. Geophys. Res. Atmos.

Tillmann, U., Hesse, K.J., Colijn, F., 2000. Planktonic primary production in the German Wadden Sea. J. Plankton Res. 22, 1253–1276. https://doi.org/10.1093/plankt/22.7.1253

Thuillier, G., Hersé, M., Labs, D., Foujols, T., Peetermans, W., Gillotay, D., Simon, P.C., Mandel, H., 2003. The solar spectral irradiance from 200 to 2400 nm as measured by the SOLSPEC spectrometer from the ATLAS and EURECA missions. Sol. Phys. https://doi.org/10.1023/A:1024048429145

UNEP, 2006. Marine and coastal ecosystems and human well-being: A synthesis report based on the findings of the Millennium Ecosystem Assessment. J. Bertrand Russell Arch.

Van der Wal, D., Pye, K., 2003. The use of historical bathymetric charts in a GIS to assess morphological change in estuaries. Hydrogr. J. https://doi.org/10.1111/1475-4959.04943

Van der Wal, D., Herman, P.M.J., Wielemaker-Van Den Dool, A., 2005. Characterisation of surface roughness and sediment texture of intertidal flats using ERS SAR imagery. Remote Sens. Environ. https://doi.org/10.1016/j.rse.2005.06.004

Van der Wal, Ysebaert, T., Herman, P.M.J., 2017. Response of intertidal benthic macrofauna to migrating megaripples and hydrodynamics 30, 1–4.

Van der Woerd, Hans, J., Dury, S., Pasterkamp, R., Hakvoort, H., Eleveld, M., Berg, G. Van Den, 2003. Water quality maps in the Western Scheldt estuary based on MERIS and CASI observations ; a comparison of products.

Van der Woerd, H., Pasterkamp, R., 2004. Mapping of the North Sea turbid coastal waters using SeaWiFS data. Can. J. Remote Sens. 30, 44–53. https://doi.org/10.5589/m03-051

Van der Woerd, H.J., Pasterkamp, R., 2008. HYDROPT: A fast and flexible method to retrieve chlorophyll-a from multispectral satellite observations of optically complex coastal waters. Remote Sens. Environ. 112, 1795–1807. https://doi.org/10.1016/j.rse.2007.09.001

Van der Woerd, H.J., Wernand, M.R., 2015. True Colour Classification of Natural Waters with Medium-Spectral Resolution Satellites: SeaWiFS, MODIS, MERIS and OLCI. Sensors 15, 25663–25680. https://doi.org/10.3390/s151025663.

Van Raaphorst, W., Philippart, C.J.M., Smit, J.P.C., Dijkstra, F.J., Malschaert, J.F.P., 1998. Distribution of suspended particulate matter in the North Sea as inferred from NOAA/AVHRR reflectance images and in situ observations. J. Sea Res. 39, 197–215. https://doi.org/10.1016/S1385-1101(98)00006-9

Verhoef, W., 1985. Earth observation modeling based on layer scattering matrices. Remote Sens. Environ. 17, 165–178. https://doi.org/10.1016/0034-4257(85)90072-0

Verhoef, W., Bach, H., 2003. Simulation of hyperspectral and directional radiance images using coupled biophysical and atmospheric radiative transfer models. Remote Sens. Environ. 87, 23–41. https://doi.org/10.1016/S0034-4257(03)00143-3

Verhoef, W., Bach, H., 2007. Coupled soil–leaf-canopy and atmosphere radiative transfer modeling to simulate hyperspectral multi-angular surface reflectance and TOA radiance data. Remote Sens. Environ. 109, 166–182. https://doi.org/https://doi.org/10.1016/j.rse.2006.12.013

Verhoef, W., van der Tol, C., Middleton, E.M., 2018. Hyperspectral radiative transfer modeling to explore the combined retrieval of biophysical parameters and canopy fluorescence from FLEX – Sentinel-3 tandem mission multi-sensor data. Remote Sens. Environ. 204, 942–963. https://doi.org/10.1016/j.rse.2017.08.006

Vries, I.D., Duin, R.N.M., Peeters, J.C.H., Bokhorst, M., Laane, R.W.P.M., 1998. Patterns and trends in nutrients and phytoplankton in Dutch coastal waters : comparison of time-series analysis, ecological model simulation, and mesocosm experiments 620–634.

Wang, Y., 1997. Satellite SAR imagery for topographic mapping of the tidal flat areas in the Dutch Wadden Sea. PhD thesis, Fac. Soc. Behav. Sci. 172. https://doi.org/http://hdl.handle.net/11245/1.134894

Wang, M., Bailey, S.W., 2001. Correction of sun glint contamination on the SeaWiFS ocean and atmosphere products. Appl. Opt. 40, 4790. https://doi.org/10.1364/AO.40.004790

Wang, M., Shi, W., 2005. Estimation of ocean contribution at the MODIS near-infrared wavelengths along the east coast of the U.S.: Two case studies. Geophys. Res. Lett. 32, 1–5. https://doi.org/10.1029/2005GL022917

Wang, M., 2007. Remote sensing of the ocean contributions from ultraviolet to near-infrared using the shortwave infrared bands: simulations. Appl. Opt. 46, 1535–1547. https://doi.org/10.1364/AO.46.001535

Wang, M., Shi, W., 2007. The NIR-SWIR combined atmospheric correction approach for MODIS ocean color data processing. Opt. Express 15, 15722–15733. https://doi.org/https://doi.org/10.1364/OE.15.015722

Wang, M., Son, S., Shi, W., 2009. Evaluation of MODIS SWIR and NIR-SWIR atmospheric correction algorithms using SeaBASS data. Remote Sens. Environ. 113, 635–644. https://doi.org/10.1016/j.rse.2008.11.005

Wang, M., Shi, W., Tang, J., 2011. Water property monitoring and assessment for China's inland Lake Taihu from MODIS-Aqua measurements. Remote Sens. Environ. 115, 841–854. https://doi.org/10.1016/j.rse.2010.11.012

Watson, J., Zielinski, O., 2013. Subsea optics and imaging. Elsevier.

Werdell, P.J., Bailey, S.W., Franz, B. a., Harding, L.W., Feldman, G.C., McClain, C.R., 2009. Regional and seasonal variability of chlorophyll-a in Chesapeake Bay as observed by SeaWiFS and MODIS-Aqua. Remote Sens. Environ. 113, 1319–1330.

Wernand, M.R., 2002. Guidelines for (ship-borne) auto-monitoring of coastal and ocean colour. Ocean Optics.

Wernand, M.R., 2011. Poseidon's paintbox: Historical Archives of Ocean Colour in Global - Change Perspective. Ph.D. Thesis, Univ. Utrecht, Netherlands. https://doi.org/https://dspace.library.uu.nl/handle/1874/212589

WFD, 2000. Directive 2000/60/EC of the European Parliament and of the Council of 23 October 2000 establishing a framework for Community action in the field of water policy. Off. J. Eur. Parliam. https://doi.org/10.1039/ap9842100196

Wimmer, C., Siegmund, R., Schwabisch, M., Moreira, J., 2000. Generation of high precision DEMs of the Wadden Sea with airborne interferometric SAR.

IEEE Trans. Geosci. Remote Sens. 38, 2234–2245. https://doi.org/10.1109/36.868881

Yang, C., Yang, D., 2015. An Improved Empirical Model for Retrieving Bottom Reflectance in Optically Shallow Water. IEEE J. Sel. Top. Appl. Earth Obs. Remote Sens. 8, 1266–1273.

Yanjiao, W., Peiqun, Z., Wenjie, D., Ying, Z., 2007. Study on Remote Sensing of Water Depths Based on BP Artificial Neural Network. Mar. Sci. Bull. 9, 26–35.

Yu, X., Salama, M.S., Shen, F., Verhoef, W., 2016. Retrieval of the diffuse attenuation coefficient from GOCI images using the 2SeaColor model: A case study in the Yangtze Estuary. Remote Sens. Environ. 109–119. 175. https://doi.org/10.1016/j.rse.2015.12.053

Yu, X., Shen, F., Liu, Y., 2016b. Light absorption properties of CDOM in the Changjiang (Yangtze) estuarine and coastal waters: An alternative approach for DOC estimation. Estuar. Coast. Shelf Sci. 181, 302–311. https://doi.org/10.1016/j.ecss.2016.09.004

Zibordi, G., Mélin, F., Berthon, J.F., 2006. Comparison of SeaWiFS, MODIS and MERIS radiometric products at a coastal site. Geophys. Res. Lett. 33, 1–4. https://doi.org/10.1029/2005GL025778

Zibordi, G., Berthon, J.F., Mélin, F., D’Alimonte, D., Kaitala, S., 2009. Validation of satellite ocean color primary products at optically complex coastal sites: Northern Adriatic Sea, Northern Baltic Proper and Gulf of Finland. Remote Sens. Environ. 113, 2574–2591.

Zibordi, G., Berthon, J.F., Mélin, F., D’Alimonte, D., 2011. Cross-site consistent in situ measurements for satellite ocean color applications: The BiOMaP radiometric dataset. Remote Sens. Environ. 115, 2104–2115. https://doi.org/10.1016/j.rse.2011.04.013

Zibordi, G., Ruddick, K., Ansko, I., Moore, G., Kratzer, S., Icely, J., Reinart, A., 2012. In situ determination of the remote sensing reflectance: An inter-comparison. Ocean Sci. 8, 567–586. https://doi.org/10.5194/os-8-567-2012

Zibordi, G., Mélin, F., Berthon, J.F., Canuti, E., 2013. Assessment of MERIS ocean color data products for European seas. Ocean Sci. 9, 521–533. https://doi.org/10.5194/os-9-521-2013

Zielinski, O., Brehm, R., 2007. Hyperspectral multi-parameter sensing for marine environmental security. Int. Ocean Syst. 11, 19–21.

Zielinski, O., Llinás, O., Oschlies, A., Reuter, R., 2002. Underwater light field and its effect on a one-dimensional ecosystem model at station ESTOC, north of the Canary Islands. Deep. Res. Part II Top. Stud. Oceanogr. https://doi.org/10.1016/S0967-0645(02)00096-6.

Zielinski, O., Busch, J.A., Cembella, A.D., Daly, K.L., Engelbrektsson, J., Hannides, A.K., Schmidt, H., 2009. Detecting marine hazardous substances and organisms: Sensors for pollutants, toxins, and pathogens. Ocean Sci. 5, 329–349. https://doi.org/10.5194/os-5-329-2009.

Author's biography and PhD publications

Behnaz Arabi obtained her BSc degree in Statistical Science and her MSc degree in Remote Sensing and Geographic Information System (RS - GIS) both from Shahid Beheshti University (SBU), Tehran, Iran. She did her PhD at Water Resource Department (WRS) of the Faculty of Geo-Information Science and Earth Observation (ITC), University of Twente, which resulted in this dissertation. Immediately after her PhD, she started her post-doc program at WRS, ITC, University of Twente. Her research interests focus on surface-atmosphere radiative transfer modeling, remote sensing of water quality, numerical inversion and optimization, satellite image processing, stochastic error analysis, GIS spatial analysis, and data visualization.

A list of Author's publications during her PhD at the University of Twente is as follows:

ISI Journal Articles:

Arabi, B., Salama, M.S., Wernand, M.R., Verhoef, W., 2016. MOD2SEA: A Coupled Atmosphere-Hydro-Optical Model for the Retrieval of Chlorophyll-a from Remote Sensing Observations in Complex Turbid Waters. Published in Remote Sensing journal. 2016, 8(9), 722., https://doi.org/10.3390/rs8090722.

Arabi, B., Salama, M.S., Wernand, M.R., Verhoef, W., 2018. Remote Sensing of Water Constituent Concentrations Using Time Series of In-situ Hyperspectral Measurements in the Wadden Sea. Remote Sensing of Environment, 2018, 216, 154–170, https://doi.org/10.1016/j.rse.2018.06.040.

Arabi, B., Salama, M.S., Pitarch, J., Verhoef, W., 2020. Integration of in-situ and multi-sensor satellite observations for long-term water quality monitoring in coastal areas. Remote Sensing of Environment Journal, 239 (2020) 111632. https://doi.org/10.1016/j.rse.2020.111632.

Arabi, B., Salama, M.S., van der Wal, Daphne., Pitarch, J., Verhoef, W., 2020. The impact of sea bottom effects on the retrieval of water constituent concentrations from MERIS and OLCI images in shallow tidal waters supported by radiative transfer modeling. Remote Sensing of Environment Journal, 237 (2020) 111596. https://doi.org/10.1016/j.rse.2019.111596.

International conferences Articles:

Arabi, B., Salama, M.S., Verhoef, W., 2016. Evaluation of Tidal Effect on Water Constituent Variations Using Optical Observations and Tide Gauge Recordings in the Dutch Wadden Sea. The 2018 IEEE International Geoscience and Remote Sensing Symposium (IGARSS 2018), Valencia, Spain, 22-27 July 2018.

Arabi, B., Salama, S., Bayat, B., and Verhoef, W., 2016. Monitoring of Water Quality in High Turbid Waters Using Coupled Atmospheric-hydro-optical Models and Remote Sensing Observations (Case study: The Wadden Sea). 2019 AGU Ocean Science Meeting, Louisiana, New Orleans, USA, 21-26 February 2016.

Arabi, B., Salama, S., and Verhoef, W., 2017. Phytoplankton Phenology in the Marsdiep Region of the Dutch Wadden Sea. Third International Ocean Colour Science Meeting, Lisbon, Portugal, 15-18 May 2017.

Arabi, B., Salama, S., van der Wal, Daphne., and Verhoef, W., 2019. Remote Sensing of Water Quality in the Wadden Sea. Boussinesq Lecture 2019, Amsterdam, the Netherlands, 17 October 2019.